



CORSO DI DOTTORATO DI RICERCA IN FISICA
XXXVII ciclo del corso di dottorato

**From the Asymptotic Giant Branch
to the Planetary Nebula phase.**
A study of the mass-loss and dust
production processes

Ph.D. candidate: Silvia Tosi

Supervisor: Prof. Paolo Ventura

Co-advisors: Dr. Flavia Dell'Agli, Dr. Devika Kamath

Coordinator: Prof. Giorgio Matt

Abstract

The asymptotic giant branch (AGB) phase, undergone by low- and intermediate-mass stars (LIMS), plays a crucial role in galactic dust production, though mechanisms that remain poorly understood. The post-AGB and planetary nebulae (PNe) phases provide valuable insights into LIMS evolution, as their spectra contain chemical signatures that trace nucleosynthesis and dust production, without the blending effects found in AGB spectra.

To enhance our understanding of LIMS, we selected a sample of 44 post-AGB stars and 9 PNe from the Magellanic Clouds and the Milky Way. These objects were characterized through SED analysis by collecting and analyzing relevant observational data, including chemical abundances, photometry, and spectra, spanning from ultraviolet to infrared wavelengths.

Our analysis enabled us to determine the amount of dust and gas surrounding each central star and estimate the progenitor mass for all sources. This was achieved by specifically extending the ATON stellar evolutionary tracks to the PN phase for this study. Furthermore, by linking these properties to the previous AGB phase, we were able to test existing theoretical evolutionary models for LIMS and recommend revisions where necessary. Specifically we suggest that the mass-loss rate at the tip of the AGB phase for metal-poor low-mass carbon stars must be $3 - 4 \times 10^{-5} M_{\odot}/\text{yr}$, which is 3–4 times higher than the typical values reported in the literature. Furthermore, contrary to previous findings, we propose that the dust observed around post-AGB stars was released when the central star’s effective temperature increased to approximately 3500–4000 K.

Additionally, we observed a positive correlation between the progenitor’s mass and the amount of dust in the post-AGB phase, and a similar trend for PNe, although modulated by the central star’s effective temperature, which may influence dust destruction. In contrast, the gas content in PNe was found to be inversely proportional to the progenitor’s mass. Moreover, we found that low-metallicity environments result in higher dust production in carbon-rich stars and lower amounts in oxygen-rich stars. Massive carbon stars ($1.5M_{\odot} \lesssim M \lesssim 2.5M_{\odot}$) were found to have dust layers closer to the central star compared to lower-mass carbon stars.

Future observations with the James Webb Space Telescope and Gaia astrometric data will expand our sample and provide more precise insights into the dust contributions from these sources.

Contents

Introduction	7
1 The evolution of the LIMS	11
1.1 From the main sequence to the asymptotic giant branch phase . . .	12
1.2 Asymptotic Giant Branch phase	14
1.2.1 Thermal pulse dynamics and the core-luminosity relation .	16
1.2.2 Third dredge-up	18
1.2.3 Hot bottom burning	21
1.2.4 Surface chemical evolution and its impact for dust formation	24
1.2.5 Mass-loss in AGB stars	27
1.3 Evolved evolutionary stages	27
1.3.1 Post-AGB phase	28
1.3.2 Planetary Nebula phase	30
1.4 ATON stellar evolution models	33
2 Dust formation during the evolved star phases	37
2.1 Dusty wind in the evolved stars	38
2.1.1 Dust formation	39
2.1.2 Wind dynamics	40
2.1.3 Dust production rate and optical depth	42
3 The evolution of the SED in the AGB-to-PNe transition	47
3.1 SED of the Post-AGB stars	48
3.1.1 Post-AGB modeling with DUSTY	50
3.2 SED of the Planetary nebulae	54
3.2.1 PNe modeling with CLOUDY	56
3.3 Reddening modeling	58
4 Post-AGB stars in the MCs	61
4.1 Shaping the SEDs of Post-AGB stars in the Magellanic Clouds . .	62
4.2 The progenitors of the post-AGB stars sample	67

4.2.1	Carbon stars	67
4.2.2	The oxygen-rich post-AGB stars in the MCs sample	73
4.3	A new methodology for testing mass-loss rates and dust production histories in evolved stars	74
4.4	Bridging theoretical models and observations in AGB and Post-AGB star evolution	77
4.4.1	Bright post-AGBs with carbon dust	79
4.4.2	Low-mass carbon stars	85
4.4.3	Carbon stars with sub-solar chemistry	88
4.4.4	A faint, dusty C-star	89
4.4.5	Oxygen-rich, faint post-AGB stars	90
4.5	An overall view of dust surrounding MCs post-AGB stars	92
5	Galactic post-AGB stars	93
5.1	Galactic carbon post-AGB stars	94
5.1.1	The SEDs analysis	94
5.1.2	Low-mass carbon stars	100
5.1.3	Mass-loss and dust formation during the late AGB phases of low-mass carbon stars	105
5.2	Galactic Oxygen-rich post-AGB stars	109
5.2.1	The characterization of the individual sources	110
5.3	Conclusions on the Post-AGB stars analysis in the MCs and the Milky Way	125
6	Planetary Nebulae	129
6.1	PNe in the LMC: SED analysis and characterization	130
6.2	Understanding the progenitor's mass	144
6.3	PNe in the LMC and their link to their previous history of dust production	153
6.4	The AGB–PN connection	157
6.5	The evolutionary link between the AGB, Post-AGB, and PN Phases: is a comprehensive overview possible?	163
6.6	Conclusion on PNe and the evolutionary bridge	166
7	Conclusions	169

Introduction

In the final stages leading to the white dwarf phase, low- and intermediate-mass stars ($0.8M_{\odot} \lesssim M \lesssim 8M_{\odot}$) evolve from the asymptotic giant branch (AGB, Herwig, 2005; Karakas & Lattanzio, 2014) to the PN stage (Iben, 1995; Kwitter & Henry, 2022), passing through the post-AGB phase (Van Winckel, 2003). During the AGB phase, stars eject their envelope almost entirely, reaching mass-loss rates up to $10^{-4} M_{\odot}/\text{yr}$ (Höfner & Olofsson, 2018; Decin, 2021). Thus, AGB stars play a crucial role in the cosmic lifecycle, enriching the interstellar medium (ISM) with newly synthesized elements (e.g. Romano et al., 2010; Vincenzo et al., 2016; Kobayashi et al., 2020). In their advanced phases, LIMS are also major dust producers (Boyer et al., 2012, 2015; Dell’Agli et al., 2015a,b; Zhukovska et al., 2008; Valiante et al., 2009; Schneider & Maiolino, 2024). The dense, cool winds in these stars create optimal conditions for molecules to condense into dust grains, which, once formed, are pushed by radiation pressure, accelerating the winds and dispersing material efficiently into the ISM (e.g. Bowen & Willson, 1991; Fleischer et al., 1992; Mattsson et al., 2010; Eriksson et al., 2014; Bladh et al., 2019a,b).

Several research groups have focused on modeling dust formation in the circumstellar envelopes of evolved stars. Pioneering studies in this field have advanced our understanding of dust condensation processes in AGB stars, offering valuable insights into the relationship between stellar winds and dust formation (Gail & Sedlmayr, 1985, 1999; Ferrarotti & Gail, 2006; Dorfi & Hoefner, 1991; Hoefner & Dorfi, 1992; Hoefner, Feuchtinger, & Dorfi, 1995; Höfner & Freytag, 2019). A significant advancement was achieved by applying the aforementioned dust growth and wind modeling to stellar evolution codes (Dell’Agli et al., 2019; Nanni et al., 2013, 2014; Ventura et al., 2012a,b, 2014, 2018). These studies enabled the first coupling of internal nucleosynthesis and mixing processes with a comprehensive model of dust formation throughout the AGB phase, providing a basis for dust yield predictions in LIMS and applications to galactic chemical evolution (e.g. Ginolfi et al., 2018; Calura et al., 2023; Palla et al., 2024). However, challenges remain in accurately modeling the AGB phase (e.g. Ventura et al., 2013; Karakas, 2010; Cristallo et al., 2015, 2011, 2009), due primarily to lim-

itations in first-principles descriptions of processes like convection and mass-loss (Ventura & D’Antona, 2005a,b; Ventura et al., 2018), which constrain model predictions.

To achieve a more reliable description, it is crucial to constrain the main properties of AGB stars through detailed comparisons with observations. This thesis proposes a novel approach within this context: by examining the later evolutionary stages, specifically the post-AGB and PN phases, it seeks to gain new insights into AGB evolution. Both stages represent the final outcomes of AGB evolution, providing valuable insights into the preceding AGB phase: without the spectral blending that typically affects AGB spectra, they allow for more precise information about their physical and chemical properties. Recent studies have used both post-AGB stars and PNe to trace nucleosynthetic signatures from the AGB phase (Kamath et al., 2023; Ventura et al., 2015, 2016, 2017; García-Rojas et al., 2018; Stanghellini et al., 2022). This thesis advances this approach, offering a comprehensive interpretation of observational data from the final AGB stages to the PN phase, with a particular focus on mass-loss and dust formation processes.

The primary methodology of this thesis involves modeling observations of post-AGB stars and PNe in both the Magellanic Clouds (MCs) and the Milky Way (MW) and comparing these with theoretical AGB models. This is achieved through a two-step procedure. First, was performed a detailed comparison of photometric data, spectra, and chemical abundances with results from spectral synthesis codes. This process enables the characterization of each star in the sample, allowing for the determination of key parameters such as stellar luminosity, effective temperature, surrounding dust mass, and, for PNe, the nebular gas mass. Then, the results of this analysis were evaluated against stellar evolution models to determine whether recent AGB models reliably reproduce the observed characteristics or require calibration. The selected evolutionary models have metallicities consistent with the observed $[\text{Fe}/\text{H}]$ and oxygen abundances of each object in our sample, which span $-1.5 \lesssim [\text{Fe}/\text{H}] \lesssim -0.1$ and $7.5 \lesssim 12 + \log(\text{O}/\text{H}) \lesssim 9$, respectively. This approach enables the reproduction of sources from different galaxies, each with distinct chemical enrichment histories, offering new insights into the role of metallicity in stellar evolution and dust production mechanisms. As a result, this study contributes to a deeper understanding of both galactic and cosmic chemical evolution.

The thesis is structured as follows: Chapter 1 provides a detailed review of the theoretical background on AGB, post-AGB stars and PNe, covering stellar evolution and nucleosynthesis. Chapter 2 discusses the theoretical components employed in this study, focusing on wind and stellar evolution models. Chapter 3 presents the techniques for spectral energy distribution (SED) analysis, from which stellar, gas, and dust parameters are derived for both post-AGB stars and PNe. The results of the SED analysis and the comparison with theoretical models,

focusing on mass-loss and dust formation in LIMS, are presented for the post-AGB samples of the MCs and MW in Chapters 4 and 5, respectively, and for the PNe in Chapter 6.

Chapter 1

The evolution of the LIMS

The life of stars is governed by nuclear reactions occurring within the inner regions of their structure. The longest evolutionary phases are represented by the burning of hydrogen and helium in the core, during which stars spend more than 98% of their evolutionary history (Kippenhahn & Weigert, 1990). Between these two stages lies a phase fueled by hydrogen burning in a shell surrounding the helium core formed during the prior hydrogen-burning stage. Following the central helium burning, the subsequent evolutionary path is highly dependent on the star's initial mass.

In the present work, we focus on LIMS, which are characterized by masses between $0.8 M_{\odot}$ and $8 M_{\odot}$. After central helium burning, these stars undergo the relatively brief yet critical AGB phase, before contracting towards the post-AGB and PNe phases and concluding their life as white dwarfs. Knowledge on the stellar structure and physical processes involved in the evolution of star of different masses and metallicities during these phases represents the building block for the understanding of the processes, such as mass-loss and dust production, that leads to the enrichment of the ISM.

In the following sections, we provide an overview of the evolutionary processes of LIMS, tracing their progression from formation on the Main Sequence (MS) to the final stages of their life cycle in the PN phase (see e.g. the complete evolution of a $1.0 M_{\odot}$ star with $Z = 4 \times 10^{-3}$, illustrated in Fig. 1.1). Furthermore, we examine the key phenomena governing the behavior and evolution of AGB stars, emphasizing the critical role of metallicity in shaping these processes, discussing how these characteristics emerge in the subsequent post-AGB and PN phases and offering a comprehensive depiction of each evolutionary stage.

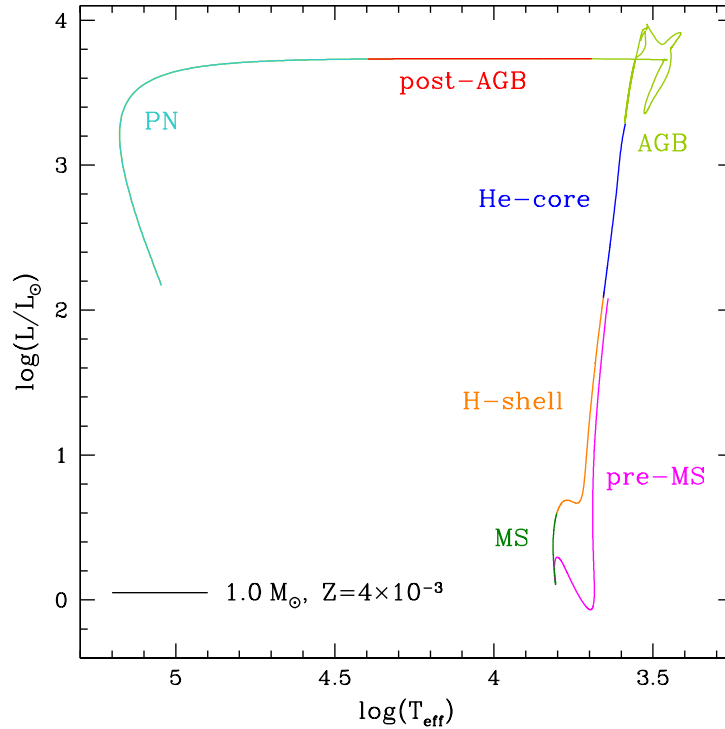


Figure 1.1: Hertzsprung–Russell diagram for $1.0 M_{\odot}$ calculated using the ATON stellar evolution code (Ventura et al., 1998). We note that all the stellar model diagrams presented in this thesis were produced using models derived from the ATON code.

1.1 From the main sequence to the asymptotic giant branch phase

The longest phase in the life of stars is the burning of hydrogen within their cores, known as the MS. The MS is characterized by the gradual conversion of hydrogen into helium in the core, accompanied by heating of the central regions and an increase in luminosity.

Hydrogen burning can occur via two different reaction network: for stars with a mass $M < 1.2 M_{\odot}$, ignite the proton-proton (p - p) chain; for more massive stars, which reach higher core temperatures ($\gtrsim 15 \times 10^6$ K), the dominant energy channel is the CNO cycle. Once the hydrogen is exhausted in the center of the star, combustion moves to an outer shell, close to the helium core. Subsequently, the

core contracts, elevating temperatures in its vicinity, thereby facilitating CNO cycle ignition. The discontinuity in molecular weight between the helium core and the hydrogen-rich outer regions, together with the need to maintain hydrostatic equilibrium, causes the envelope to expand: the star begins the process of cooling the outer regions and enters red giant branch (RGB) phase. This expansion favors the formation of an outer convective zone, which penetrates toward the inner regions until it reaches the hydrogen fusion shell. This convective episode is called the first dredge-up (FDU) and induces alterations in surface chemical composition, marked by an increase in ^{13}C and ^{14}N and a decrease in the abundance of ^{12}C and ^7Li (Abia et al., 2012) and an enrichment or reduction of the ^{17}O abundances according with the stellar mass. The expanded structure of the envelope leads the stars to undergo mass-loss processes, losing from 0.1 to 0.3 M_{\odot} . This mass-loss is especially critical for low-mass stars (below 2 M_{\odot}), and increase with the metallicity of the star (Tailo et al., 2021). Therefore, determining their mass in the subsequent evolutionary paths is not straightforward, as these are closely linked to the progenitor’s mass. To minimize uncertainties arising from RGB mass-loss, hereinafter we will refer to the progenitor’s mass at the onset of the AGB phase (discussed in the following Sec. 1.2) with “M”, while we will specify with “ M_{in} ” if we refer to the MS mass of the star.

During the RGB, the star evolves with increasing luminosity, while the inactive core contracts, releasing gravitational energy. Gradually, the central regions experience a rise in temperature, and when temperatures reach approximately ~ 100 MK, the onset of 3α reactions triggers the transformation of helium into carbon and oxygen. However, unlike hydrogen burning, the response of the star to helium ignition varies depending on its mass. For stars with masses exceeding 2 M_{\odot} , the central regions remain in a nearly ideal gas state, allowing for gradual core heating due to the contraction process, leading to a quiescent phase of helium burning. This phase, lasting approximately $\sim 10\%$ of the preceding one, results in a core composed of carbon and oxygen. On the contrary, stars with masses $M_{\text{in}} < 2 M_{\odot}$ progress along the RGB as their luminosity increases. The core becomes dense enough for electron degeneracy to take hold. Under these conditions, once temperatures reach ~ 100 MK, helium ignites in a violent “flash.” The substantial energy released by 3α ignition primarily serves to expand the outer regions of the star, causing a temporary extinction of CNO chain in the envelope. As the star’s overall luminosity decreases, the outermost regions contract in an attempt to rekindle CNO activity, leading to a more compact configuration compared to the previous giant phase. Eventually, helium ignition in the core removes degeneracy, enabling stable thermal conditions for helium burning. Gradual restoration of CNO combustion initiates a new evolutionary stage known as the horizontal branch (HB), where the star’s energy is sustained by central helium burning and CNO activity in the envelope.

For any value of the stellar mass, once the helium in the core is exhausted, the combustion front moves to a region close to the carbon-oxygen core, in a way that follows what has already been discussed in relation to the phases following the MS evolution. As the inert core contracts, the outer regions expand, prompting the extinction of CNO combustion and the sinking of the outer convective layer, termed the “second dredge-up” (SDU). While outer convection penetration is common to all stars, the reaching of the regions previously occupied by CNO nuclear activity, and the consequent change in the chemical composition of the surface, only affects stars with initial masses above $4 M_{\odot}$ (Ventura, 2010). The effects of the second dredge-up are an increase in the surface abundances of ${}^4\text{He}$, ${}^{12}\text{C}$, ${}^{13}\text{C}$, ${}^{14}\text{N}$, and a decrease in the concentrations of H, ${}^{16}\text{O}$, and ${}^{12}\text{C}$.

The mass of the CO core profoundly influences the subsequent evolutionary phases, as elaborated upon in the forthcoming Sections. A common fate among stars with masses $M_{\text{in}} \lesssim 8 M_{\odot}$ is the formation of an inert CO core, transitioning into a state of electron degeneracy due to gravitational contraction. This behavior is generally valid, with the exception of stars with masses $6 M_{\odot} \lesssim M_{\text{in}} \lesssim 8 M_{\odot}^*$, where carbon ignition occurs in an off-center zone under semi-electronic degeneracy conditions. Consequently, this leads to the formation of an inert and degenerate core composed of oxygen and neon (Siess, 2007, 2010).

1.2 Asymptotic Giant Branch phase

The evolutionary phases following the SDU are characterized by the contraction of the outer regions, triggered by the temporary extinction of the hydrogen-burning layer. This contraction process induces a rise in temperatures across the outer region of the star, leading to the reactivation of the CNO cycle. This marks the beginning of an evolutionary phase in which the star is fueled by the burning of hydrogen and helium in two layers above the core, constituting the AGB evolution. As shown in Fig. 1.2, during this phase, the structure of the star is composed of: (a) a nuclearily extinguished and degenerate core, made up of carbon and oxygen; (b) an internal shell, where 3α burning occurs; (c) an intershell zone, whose chemistry is determined by past CNO nuclear activity; (d) a more external shell, which will soon become the site of hydrogen burning; (e) the convective envelope.

*The above-mentioned mass range is debated within the astrophysical community, as it can vary significantly depending on the metallicity of the stars (Siess, 2007).

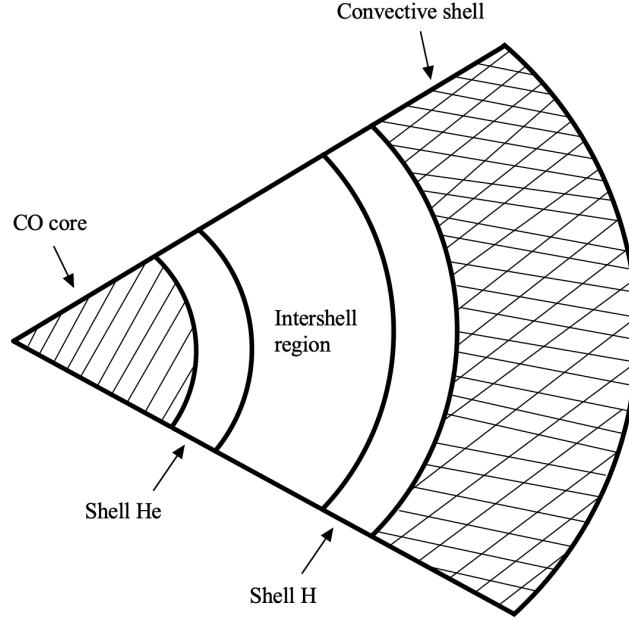


Figure 1.2: Internal structure of a typical AGB star, not in scale. Highlighted are the CO core, the convective envelope, the two layers where hydrogen and helium nuclear combustion take place, and the zone separating them, commonly called the “intershell”.

Table 1.1: Main evolutionary characteristics of LIMS, calculated for a $Z = 4 \times 10^{-3}$ case.

M_{in}/M_{\odot}	τ_{H} [yr]	τ_{He} [yr]	τ_{AGB} [yr]	$M_{\text{core}}/M_{\odot}$
0.80	1.45×10^{10}	9.31×10^7	1.54×10^6	0.522
0.90	9.11×10^9	9.20×10^7	1.47×10^6	0.527
1.00	5.94×10^9	9.18×10^7	1.34×10^6	0.531
1.25	2.71×10^9	9.00×10^7	1.28×10^6	0.537
1.50	1.62×10^9	9.00×10^7	1.36×10^6	0.542
2.00	7.70×10^8	2.37×10^8	3.76×10^6	0.492
2.50	4.39×10^8	1.10×10^8	1.31×10^6	0.585
3.00	2.80×10^8	6.12×10^7	4.69×10^5	0.710
4.00	1.44×10^8	2.43×10^7	2.58×10^5	0.833
5.00	8.78×10^7	1.35×10^7	1.52×10^5	0.897
6.00	6.11×10^7	8.41×10^6	6.26×10^4	0.998
7.00	4.51×10^7	5.61×10^6	4.81×10^4	1.23

Notes: τ_{H} denotes the duration of the hydrogen burning phase, τ_{He} the duration of the helium burning phase, τ_{AGB} the duration of the AGB phase, calculated from the first thermal pulse. $M_{\text{core}}/M_{\odot}$ is the core mass at the first thermal pulse.

Even though the AGB stage is very rapid compared to the previous evolutionary phases (see, e.g., the trend followed by stars with metallicity $Z = 4 \times 10^{-3}$, reported in Tab. 1.1), it is crucial for understanding the significant role of LIMS in galaxies. As previously mentioned, this importance arises primarily from their contributions to the enrichment of the ISM with elements synthesized during their evolution through various nucleosynthesis and mixing processes, which can profoundly alter the surface chemical composition of the star (Höfner & Olofsson, 2018).

In the following Sections we will describe the main phenomena active during the AGB phase. More attention will be dedicated to those processes that critically influence the AGB dust production.

1.2.1 Thermal pulse dynamics and the core-luminosity relation

The helium-burning region is extremely thin for reasons linked to the continuity of mass, due to the contact between the helium-burning shell and the highly degenerate and extremely dense CO core. The ignition of nuclear reactions in such a confined and dense space induces a pronounced thermal instability, which makes it impossible for electromagnetic radiation to transport the produced energy flux outward on a timescale comparable to that of the nuclear reaction in progress (Schwarzschild & Härm, 1965).

As hydrogen burning progresses, the mass of the helium-rich zone increases, leading to elevated density and pressure at the base of the intershell region. When the mass of the intershell region reaches a critical value, helium is ignited under unstable conditions, activating a thermonuclear runaway called a “helium shell flash.” The energy produced by the flash drives a convective region that extends from the He-burning shell to the H-burning zone. This homogenizes the chemical abundances in this region, and its efficiency depends on the core mass. Intershell convection recedes as the energy of the thermal pulse diminishes. The significant energy released during the thermal pulse does not reach the surface of the star. Instead, it causes the star to expand, cooling the material surrounding the helium-burning shell and extinguishing the hydrogen-burning shell, resulting in an energy deficit. As the hydrogen-nuclear fusion ceases, the envelope contracts until the hydrogen-burning shell reignites, rendering the helium-burning region inactive again. This initiates an extended period of stable hydrogen-shell burning, during which the mass of the intershell region gradually increases, eventually leading to the occurrence of the next thermal pulse.

Fig. 1.3 shows the evolution of the contribution to the luminosity from the different nuclear burning processes, namely L_{CNO} (orange line) and $L_{3\alpha}$ (blue line). Fig. 1.3 visually shows what happens when a thermal pulse begins: $L_{3\alpha}$ increases while L_{CNO} decreases rapidly; at the end of the thermal pulse, L_{CNO} increases

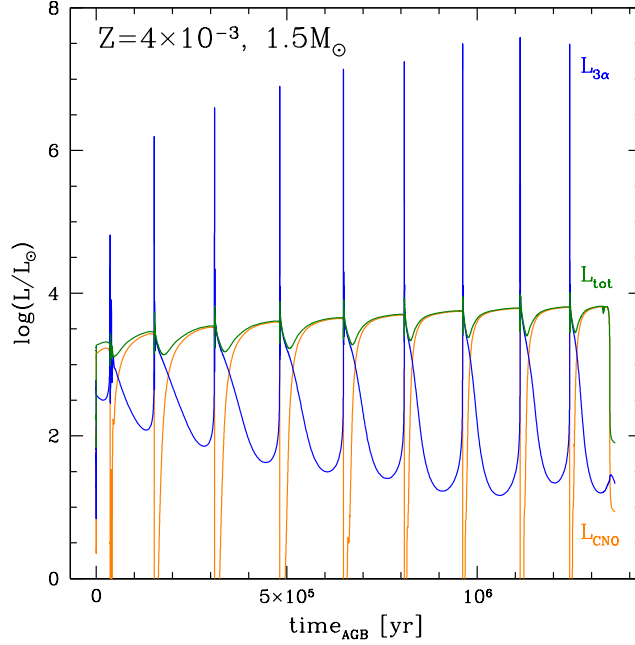


Figure 1.3: The time evolution of the contribution to the luminosity from the different nuclear burning processes. The orange lines denotes the luminosity from the CNO cycle (L_{CNO}), in blue the 3α ($L_{3\alpha}$) and in green the total luminosity (L_{tot}).

again. During this process, the total luminosity undergoes only marginal changes, consisting of a slight decrease as a consequence of the extinction of CNO burning. Indeed, L_{tot} (green line) corresponds to L_{CNO} during $\sim 90\%$ of the AGB phase, while for the remainder of the time, the main contribution to the total luminosity is provided by helium burning reactions.

Empirical constraints have shown that the total luminosity of AGB stars is strongly linked to the mass of their degenerate core (Paczynski, 1970). As described by the Paczynski relation (Eq. 1.1), the total luminosity, L_{tot} , exhibits an almost linear increase with the core mass, M_c , underscoring the fundamental role of the core in governing the evolutionary pattern of LIMS.

$$L_{\text{tot}} = 5.925 \times 10^4 \left(\frac{M_c}{M_\odot} - 0.52 \right) \quad (1.1)$$

The total luminosity is also closely related to mass-loss experienced by the star. Fig. 1.4 illustrates the AGB evolution of four different stellar masses ($0.7 M_\odot$, magenta line; $1.0 M_\odot$, blue line; $1.5 M_\odot$, orange line; and $2.0 M_\odot$, green line), all at

the same metallicity ($Z = 4 \times 10^{-3}$). As mentioned above, to avoid complications arising from uncertainties related to RGB mass-loss, in this and all subsequent diagrams, we refer to the progenitor’s mass at the start of the AGB phase. Furthermore, as mass-loss reduces stellar mass over time, longer evolutionary timescales correspond to lower current stellar masses. Therefore, in this figure and in those that follow, we use the current mass of the star as a proxy for time. The top panels of Figs. 1.4 show the evolution of luminosity, effective temperature and mass-loss rate for models with different initial masses; this is to give a general picture of the AGB evolution characteristics. The luminosity initially follows the trend with the core mass described in Eq. 1.1: the increase in the mass of the CO core, due to nuclear combustion, causes a gradual increase in luminosity. This behavior is inverted when the mass of the star is reduced significantly and the gravitational energy of the external layers is not sufficient anymore to maintain the same luminosity. The rise in luminosity of each star is affected by temporally depletion, due to thermal pulses (see also Fig. 1.3).

1.2.2 Third dredge-up

The third dredge-up (TDU) is a convective mixing mechanism that may occur after each thermal pulse, following the extinction of the 3α reaction and before the re-activation of the CNO shell. Specifically, during helium burning, an excessive amount of energy is released, making it impossible to transport to the surface via radiation. This leads to the formation of an intershell convective zone (ICZ) enriched with the products of 3α nucleosynthesis, primarily ^{12}C , along with a small amount of ^{16}O , between the two burning shells. Simultaneously, the expansion and cooling of the intershell region lead to deeper penetration of the outer convective envelope. If convection penetrates beyond the inactive H-burning shell, the material from the intershell region will be mixed into the outer envelope. In Fig. 1.5, a representation of the TDU mechanism is shown as a function of the time elapsed starting from the formation of the ICZ until the penetration of the convective envelope into the regions enriched in the elements produced during He burning.

In the bottom panels of Fig. 1.4, we can follow the effect of repeated TDU episodes on the surface chemical abundances. After each thermal pulse, the surface regions of the stars are enhanced by the products of the He burning, particularly ^{12}C (left bottom panel) and, in a softer way, of ^{16}O (see bottom panels Fig. 1.4). Stars with masses around $2 - 3 M_{\odot}$ conclude their AGB phase with a higher carbon surface abundances compared to their lower-mass counterparts. This is because their larger envelopes take longer to be ejected, allowing the star to undergo more TDU episodes. The greater the number of TDU episodes a star experiences, the higher the final surface carbon abundance.

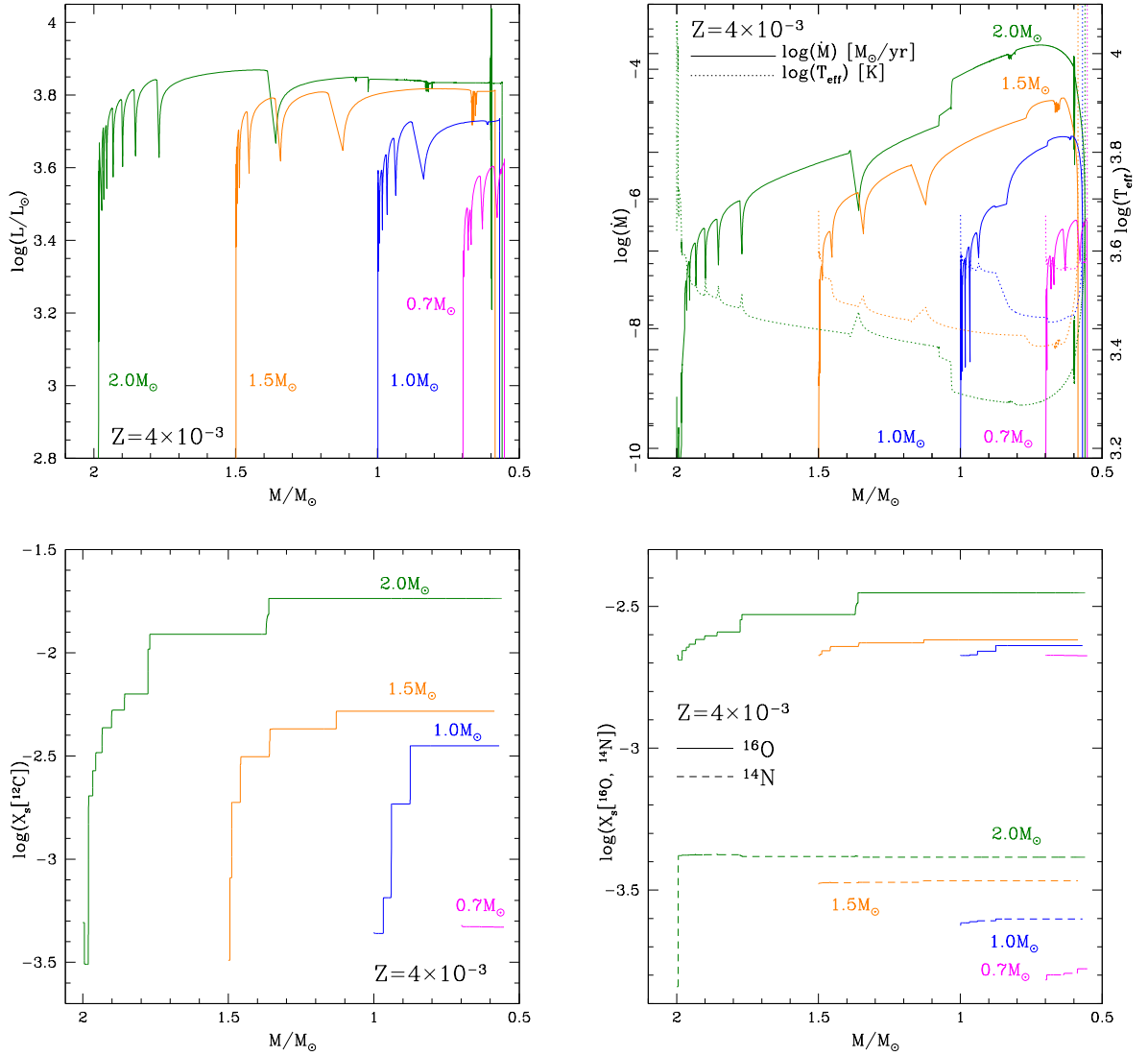


Figure 1.4: Variations in the physical and chemical properties of stars of different masses. In all the panels we represent four models at $Z = 4 \times 10^{-3}$: $2.0 M_{\odot}$ (in green line), $1.5 M_{\odot}$ (in orange), $1.0 M_{\odot}$ (in blue) and $0.7 M_{\odot}$. Top panels: luminosity (left panel), mass-loss rate and effective temperature (right) as functions of the current mass of the star, decreasing during the evolution. Bottom panels: surface abundance of ^{12}C (left panel), ^{16}O and ^{14}N (right panel) as functions of the current mass of the star, decreasing in the course of evolution.

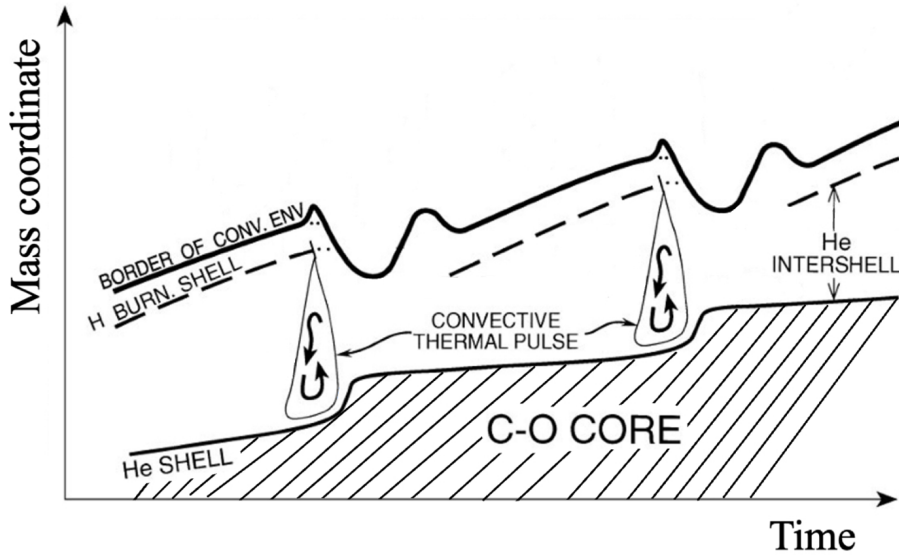


Figure 1.5: *Third dredge-up episodes represented during two consecutive thermal pulses. The time start from the formation of the intershell convective zone, followed by the deactivation of the hydrogen burning and the consequent penetration of the convective envelope. The figure is adapted with revisions from Busso et al. (1999).*

We also note that the TDU has the important role of progressively enriching the stellar surface in s-process elements. The latter is the process of neutron capture with the emission of gamma radiation (n, γ), which takes place on a long timescale, ranging from ~ 100 yr to $\sim 10^5$ yr for each neutron capture (Burbidge et al., 1957). The main neutron sources are the $^{13}\text{C}(\alpha, n)^{16}\text{O}$ reaction, active in radiative conditions during the interpulse period, and the $^{22}\text{Ne}(\alpha, n)^{25}\text{Mg}$ reaction, which is marginally activated within the convective shell produced by thermal pulses (Käppeler et al., 2011). This process leads to the formation of heavy elements, such as strontium, yttrium, zirconium, barium and lead, whose abundances will be used in the present thesis as traces of carbon-enrichment chemistry.

The top-right panel of Fig. 1.4 represents the variation in the effective temperature and mass-loss rate of low-mass stars. When the abundance of carbon nuclei per unit volume exceeds the abundance of oxygen nuclei ($\text{C}/\text{O} > 1$), there is a significant increase in the molecular opacity of the outer regions of the star (Marigo, 2002), which favors the expansion of the outermost stellar layers (Ventura & Marigo, 2009), causing a decrease in the effective temperature and an enhancement in the mass-loss rate.

The description of the evolutionary path through the TDU mechanism proves to be essential for the interpretation of the observations of LIMS, whose spectral distribution is profoundly altered by the high carbon surface abundance and by

the formation of large amounts of dust particles, facilitated by the high rates of mass-loss experienced. In Chapter 3, we will describe the observational effects of the TDU on the SED of evolved stars.

1.2.3 Hot bottom burning

For stars with core masses exceeding approximately $0.8 M_{\odot}$, the temperature gradients at the interface between the outer core and the inner envelope are steep enough to partially overlap the outer convective region with the hydrogen burning layer. This phenomenon results in temperatures at the base of the outer convective envelope (T_{bce}) of the order of 30–40 MK, sufficient for the activation of a proton-capture nucleosynthesis known as hot bottom burning (HBB, Boothroyd et al., 1995). The minimum mass exposed to HBB ranges from $3 M_{\odot}$ to $4\text{--}5 M_{\odot}$, depending on the convection efficiency and the metallicity (Ventura et al., 2013, 2018; Dell’Agli et al., 2018b).

Fig. 1.6 illustrates the AGB evolution of four massive AGB stars ($3.5 M_{\odot}$, blue line; $4.0 M_{\odot}$, orange line; $5.0 M_{\odot}$, green line and $6.0 M_{\odot}$, magenta line), all at the same metallicity ($Z = 4 \times 10^{-3}$), that activate the HBB. As shown in the top-left panel of this figure, the ignition of the proton-capture nucleosynthesis at the base of the convective envelope causes a significant enhancement in the luminosity of stars, beyond what the Paczyński relation predicts (Eq. 1.1). Radiation pressure instigates envelope expansion, leading to increased mass-loss rates (right panel, Fig. 1.6). The high radiation pressure prompts quick envelope loss, rendering stars experiencing HBB rapidly incapable of efficiently reigniting a hydrogen-burning shell. This will cause the lowering of the luminosity and the mass-loss rate after their initial rise (higher panel, Fig. 1.6).

On general grounds, the intensity of HBB increases with the mass of the star. As shown in the left panel of Fig. 1.7, higher-mass stars have larger core masses, leading to higher T_{bce} . However, the extent of nucleosynthesis as a function of mass is complex, as it depends on the delicate interplay between envelope temperatures and mass-loss rates (Ventura & D’Antona, 2011). In the latest evolutionary stages, when the envelope is largely reduced due to mass-loss, the HBB can be extinguished.

The bottom panel of Fig. 1.6 shows the main effect of HBB activation on the surface chemical abundance of massive AGB stars, which is the decrease in surface ^{12}C (left panel) and the parallel increase in ^{14}N content (right panel), both evidence for the effects of CN nucleosynthesis to which the innermost regions of the star’s envelope have evidently been exposed. We highlight the different behavior of the $3.5 M_{\odot}$ model, represented by the blue line in Fig. 1.6, which shows an enhancement of the ^{12}C before the decrease described above. This is because the stars that are close to the threshold required for the ignition of HBB

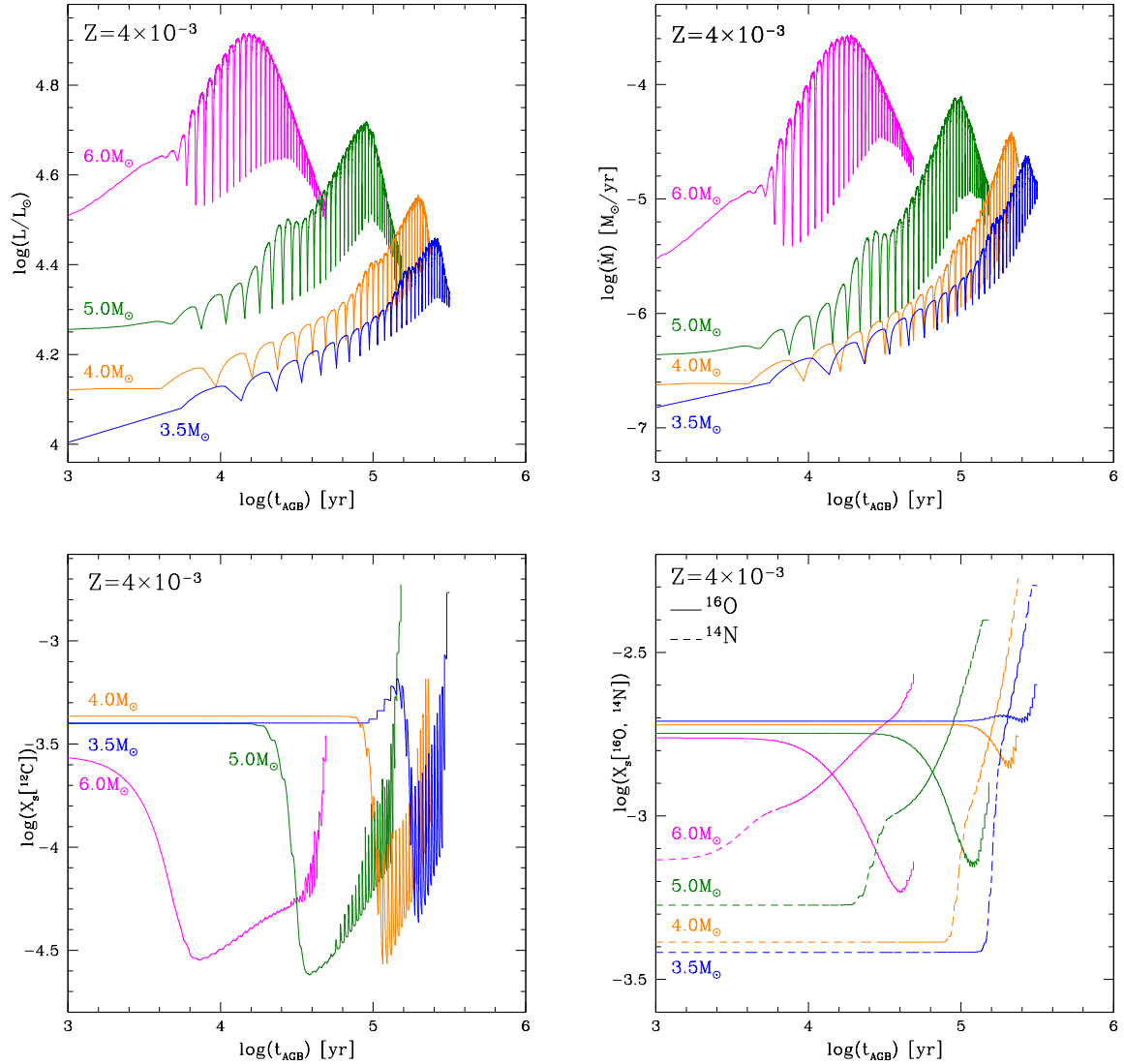


Figure 1.6: Variation in the physical and chemical properties of stars of different masses. We show four models at $Z = 4 \times 10^{-3}$: in blue $3.5 M_{\odot}$, in orange $4.0 M_{\odot}$, in green $5.0 M_{\odot}$ and in magenta $6.0 M_{\odot}$. Top panels: luminosity (left panel) and mass-loss rate (right panel) as functions of the time, calculated from the beginning of the AGB phase. bottom panels: Carbon (left panel), oxygen and nitrogen surface abundances (right panel) as functions of the time elapsed from the beginning of the AGB phase.

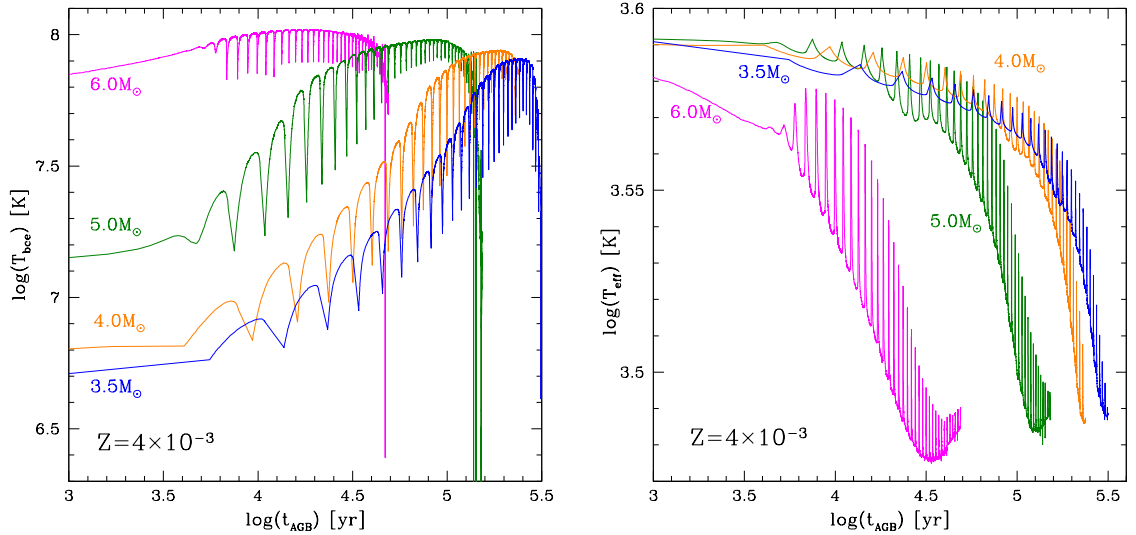


Figure 1.7: Temperature at the base of the convective envelope (left panel) and the star’s effective temperature (right panel) as functions of time elapsed since the beginning of the AGB phase. We show four models at $Z = 4 \times 10^{-3}$: in blue $3.5 M_{\odot}$, in orange $4.0 M_{\odot}$, in green $5.0 M_{\odot}$ and in magenta $6.0 M_{\odot}$.

have a surface chemistry that can be affected by both the HBB and the TDU. Oxygen depletion requires temperatures at the bottom of the convective envelope ($T_{\text{bce}} \sim 70 \text{ MK}$) that are higher than those needed to burn carbon ($\sim 40 \text{ MK}$). Since lower metallicity strengthens HBB (Dell’Agli et al., 2018a), significant depletion of surface oxygen abundance occurs only in massive, metal-poor AGB stars ($Z \leq 10^{-3}$), where the largest changes in the elemental mass fractions are observed.

Phenomena other than HBB can produce similar effects on the surface chemical abundance of the star, such as extra mixing (a hypothesis adopted to explain some post-AGB sources in Sec. 5.1.2 and Sec. 5.2.1) or the Cool Bottom Process (Busso et al., 2007; Wasserburg et al., 1995). The latter is not considered in this manuscript because, unlike HBB, its mechanism is not yet well understood by the scientific community, leaving many free parameters whose boundaries remain unclear (Palmerini et al., 2009).

1.2.4 Surface chemical evolution and its impact for dust formation

In the previous Sections we have described mixing and nucleosynthesis mechanisms responsible for the variation of the chemical composition of the envelope of AGB stars. How these processes evolve during this phase as a function of the mass and metallicity is particularly relevant to determine the chemical composition of the gas that will be ejected in the interstellar medium. In fact, they influence the chemical composition of the circumstellar envelope of these stars and therefore their capabilities of producing different dust species.

The mineral composition of the dust formed in AGB star winds depends on several factors, including the star’s surface chemical composition, influenced mainly by TDU and HBB, and the thermodynamic stability of different species (Höfner & Olofsson, 2018). The crucial parameter in this regard is the excess of carbon with respect to oxygen in the circumstellar envelope, due to the exceptional stability of the CO molecule, which absorbs entirely the less abundant element between carbon and oxygen. While a more complete description of the dust formation processes will be provided in the following Chapter, here we limit to describe the main compounds formed in the winds of AGB stars as a consequence of the variation of the C and O surface abundances with mass and metallicity.

As already introduced in Sec. 1.2.2, in those stars that experience repeated TDU episodes the surface carbon abundance can exceed that of oxygen, entering the so-called “carbon star” (or C-star) stage (see left panel of Figure 1.8). Carbonaceous dust are the dominant species in carbon-rich atmospheres. The following compounds form (see Sec. 2.1.1), listed in order of their thermodynamic stability: silicon carbide (SiC), solid carbon, and solid iron.

The C-star stage cannot be reached in stars that undergo too few TDU episodes, as they fail to accumulate enough carbon on their surface to exceed the oxygen abundance. Additionally, the C-star stage is prevented in stars experiencing strong HBB, which depletes surface carbon abundance (see Sec. 1.2.3). Oxygen-rich stars, characterized by $C/O < 1$ (see e.g., the right panel of Fig. 1.8 and the $0.7 M_{\odot}$ model in the left panel), form mainly silicate dust species such as olivine ($Mg_2xFe_{1-x}SiO_3$) and pyroxene ($Mg_xFe_{1-x}SiO_3$)[†], quartz (SiO_2), alumina dust (Al_2O_3), and solid iron. From a thermodynamic perspective (Sec. 2.1.1), alumina dust is the most stable compound, followed by olivine, pyroxene, and quartz. Stars undergoing HBB experience a depletion of surface carbon abundance due to nucleosynthesis processes. However, in some cases, this depletion is not strong enough to fully prevent the formation of carbon stars: the $3.5 M_{\odot}$ model depicted

[†]Olivine and pyroxene can form in different chain structures. The x parameters take into account their behaviour and it is a constant ranging between 1 and 0.

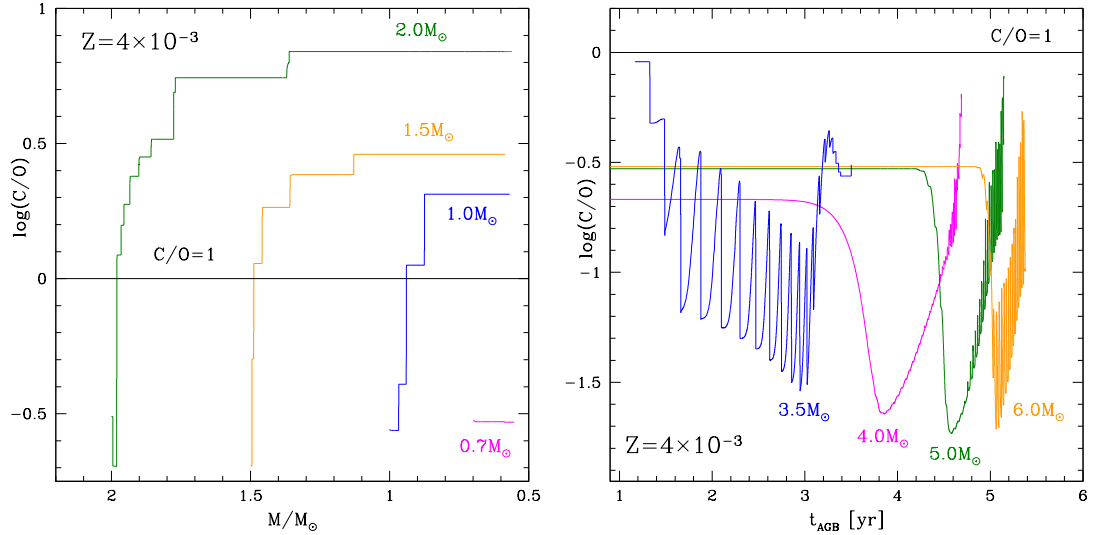


Figure 1.8: Surface carbon over oxygen abundances, reported as a function of the current mass (left panel) and the time elapsed after the beginning of the AGB phase (right panel). The models are at the same metallicity $Z = 4 \times 10^{-3}$. On the left panel are reported the $2.0 M_{\odot}$ (green line), $1.5 M_{\odot}$ (orange), $1.0 M_{\odot}$ (blue line) and $0.7 M_{\odot}$ (magenta) models. On the right panel are shown the $3.5 M_{\odot}$ (blue line), $4.0 M_{\odot}$ (magenta line), $5.0 M_{\odot}$ (green line) and $6.0 M_{\odot}$ (orange line) models.

by the blue line in the right panel of Fig. 1.8) represents a perfect example where this occurs. When the envelope is reduced, the T_{bce} and consequently the HBB nucleosynthesis efficiency is reduced, and final TDU episodes enrich the surface carbon abundance until turning the C/O to be greater than one.

The role of metallicity in AGB stars is essential for accurately modeling the contribution of AGB stars to the chemical enrichment of galaxies and the interstellar medium. Indeed, it significantly influences their evolution, nucleosynthesis, and dust production. In order to understand the impact of metallicity on the surface abundance of the star, in Fig. 1.9 carbon-rich and oxygen-rich models are compared for three different metallicities: $Z = 8 \times 10^{-3}$ (dashed line), 4×10^{-3} (full line), and 2×10^{-3} (dotted line).

- Given an initial mass $M > 3.5 M_{\odot}$, the lower the metallicity, the higher the core mass (see magenta line, left panel of Fig. 1.9), which results in higher T_{bce} during the AGB phase and thus more intense HBB phenomena. This will lead to a larger depletion of the surface carbon abundance, allowing

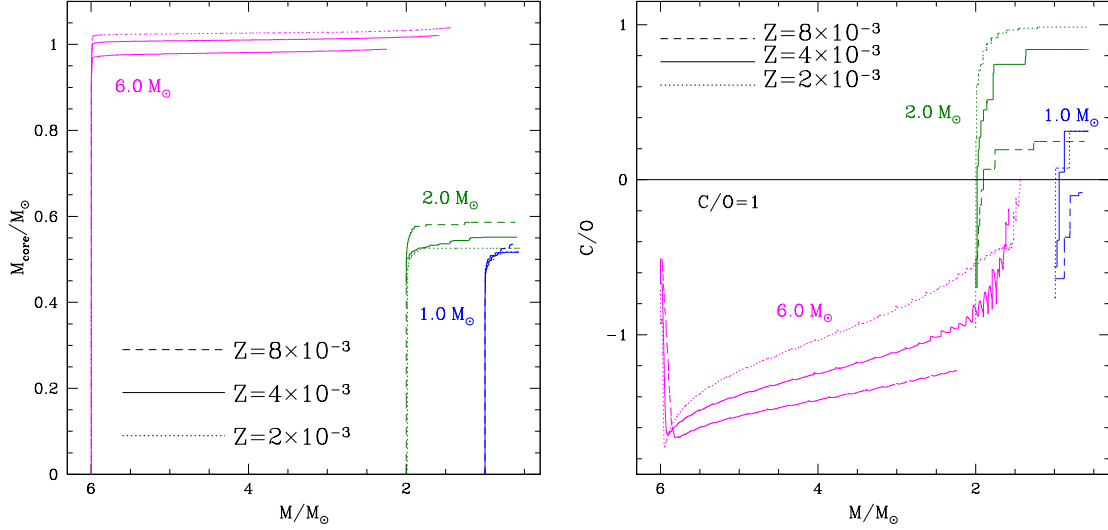


Figure 1.9: Core mass (left) and carbon over oxygen ratio (right) as a function of the current mass of the star. In both the panels are reported with three metallicity ($Z = 8 \times 10^{-3}$ with a dashed line, 4×10^{-3} with a full line and 2×10^{-3} with a dotted line), the $6.0 M_{\odot}$ (magenta), $2.0 M_{\odot}$ (green) and $1.0 M_{\odot}$ (blue) models.

for lower C/O (magenta line, right panel of Fig. 1.9), which favors the formation of silicate dust.

- For sources with masses between $1.0 M_{\odot}$ and $3 M_{\odot}$, the higher the metallicity, the higher the core mass (see blue and green lines, left panel of Fig. 1.9). In metal-rich environments, achieving the carbon-star stage can be more challenging due to the higher abundance of oxygen, requiring a larger number of TDU episodes to accumulate sufficient carbon on the surface to exceed the oxygen abundance (blue and green lines, right panel of Fig. 1.9). This is especially true for the low-mass sources (see e.g., the $1.0 M_{\odot}$ model in Fig. 1.9), whose C/O at the end of the AGB phase results close to one: assuming a different metallicity may result in $C/O > 1$ ($1.0 M_{\odot}$ at $Z = 4 \times 10^{-3}$ and $Z = 2 \times 10^{-3}$) or $C/O < 1$ ($Z = 8 \times 10^{-3}$).

1.2.5 Mass-loss in AGB stars

In Figs. 1.4 and 1.6 is shown how AGB stars evolution is characterized by low effective temperatures, typically around 3000 K or lower, and high luminosities, ranging from several thousand to tens of thousands of solar luminosities. This results in stellar radii that often extend several hundred times that of the Sun. Combined with their relatively low current masses, these stars exhibit surface gravities that are typically 4–5 orders of magnitude lower than those of sun-like stars. This low surface gravity exposes AGB stars to mass-loss from their loosely bound surface layers. Stellar pulsations create shock waves that dynamically lift the atmosphere. Then, radiation pressure on dust grains, which form in these levitated layers, drives the wind-acceleration process that facilitates the loss of the stellar envelope (Höfner & Olofsson, 2018).

As shown in the right panels of Figs. 1.4 and 1.6, mass-loss rates range from 10^{-8} to $10^{-5} M_{\odot}/\text{yr}$, though in some extreme cases rates as high as $10^{-4} M_{\odot}/\text{yr}$ or more have been observed. Observations indicate that AGB stars can reach such high mass-loss rates. Therefore, mass-loss itself becomes the primary process governing their evolutionary timescales and the extent of the nucleosynthesis and mixing processes (e.g. TDU episodes) that alter the surface chemical composition. Consequently, a thorough understanding of AGB evolution, including timescales, maximum luminosities, nucleosynthesis outcomes, and contributions to the ISM, requires an in-depth knowledge of the mass-loss process. Numerous mass-loss prescriptions have been proposed in the literature (see recent reviews by Höfner & Olofsson, 2018; Decin, 2021), each varying based on the star’s surface chemical composition and the specifics of the relationship (see Sec. 1.4 for those adopted in the present work). In this thesis, we will explore some of these mass-loss prescriptions, assessing their alignment with observational data and suggesting revisions when necessary.

1.3 Evolved evolutionary stages

In the first part of this Chapter, we highlighted the main physical and evolutionary processes that characterize the AGB phase. We emphasized how mechanisms such as nucleosynthesis, convection, and mass-loss, drive the evolution of these stars (Ventura & D’Antona, 2005a,b). We focused particularly on those processes that play a crucial role in dust production and the enrichment of the Universe.

Once LIMS reach the tip of the AGB phase (TAGB, i.e. the moment at which the mass-loss rate is the highest) and have lost most of their envelope, they undergo a structural transformation, evolving through the post-AGB and PN phases, transitioning from cool and expanded to compact and extremely hot. Since no fur-

ther mechanisms alter the surface chemical composition of the central star (CS) during contraction toward the white dwarf phase, the residual gas and dust surrounding the CS preserve the chemical imprint of the latest AGB evolutionary phases. For this reason, post-AGB and PN sources offer valuable insights into the late evolution of AGB stars.

In this second part of the Chapter, we will review the main structural and evolutionary characteristics of evolved stars as they traverse the Hertzsprung–Russell (HR) diagram from the TAGB to the PN phase. The main goal is to highlight the properties that characterize post-AGB stars and PN sources, while also deepening our understanding of the final stages of the AGB phase.

1.3.1 Post-AGB phase

After the last thermal pulse, the residual envelope of the star begins a contraction process, increasing the surface temperature of the star and entering what is known as the post-AGB stage. As discussed by Miller Bertolami (2016), defining the precise starting point of the post-AGB phase lacks rigidity, as it is contingent upon the core mass. In accordance with Iben & Renzini (1983), we define the conclusion of the AGB evolution as when the envelope mass falls below 1% of the total stellar mass, concurrently with an effective temperature exceeding ~ 6000 K. Throughout the post-AGB phase, stars adopt increasingly compact configurations, resulting in a rise in effective temperature up to approximately ~ 30000 K. This phase continues with constant luminosity during the contraction towards the white dwarf stage. This characteristic, for a fixed metallicity, enables a straightforward association between luminosity and the progenitor’s mass (see e.g., Fig. 1.10) and will be extensively utilized to characterize the post-AGB sample analyzed in Chapter 4, as well as in Sections 5.1 and 5.2.

The chemistry of post-AGB stars reflects the mechanisms that were active during AGB phase, such as TDU and HBB. Due to their higher effective temperatures compared to the previous evolutionary stage, the spectra of post-AGB stars are no longer affected by the blending effect caused by the presence of molecular lines typical of AGB sources. Instead, they are dominated by atomic transitions. This characteristic allows for an accurate determination of the photospheric chemical abundances of a wide range of elements, including CNO, alpha and Fe-peak elements, and s-process elements (see Kamath, 2020; Kamath et al., 2023, and references therein).

For what concern the dusty layer formed during the AGB phase, it is driven outward by radiation pressure, allowing it to reach a large distance from the central star (see Fig. 3.1, which will be presented in Sec. 3.1). This phenomenon offers an observational advantage, enabling the separation of emission contributions from the dusty layer and the star itself. The mineralogy of the dust in post-AGB

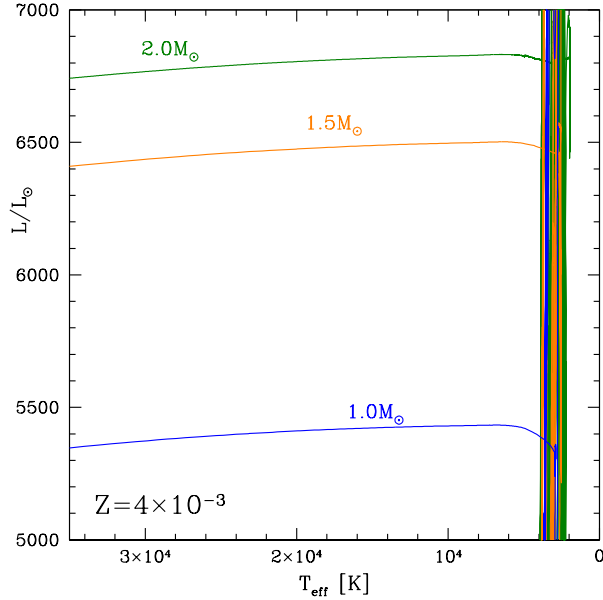


Figure 1.10: HR diagram zoomed into the post-AGB phase, for models with metallicity $Z = 4 \times 10^{-3}$. The different colours refers to different tracks. The masses are expressed at the beginning of the AGB phase and in blue is shown the $1.0 M_{\odot}$ model, in orange the $1.5 M_{\odot}$ and in green $2.0 M_{\odot}$.

stars reflects that formed during AGB evolution (see Sec. 1.2.4) and also provides evidence of very large molecules, probably excited by the ultraviolet (UV) emission produced by the circumstellar environment. Additional details on the spectral features observed in post-AGB sources will be provided in Sec. 3.1.

In order to achieve a reliable description of the transition from the AGB stage to the PNe phase is necessary to take into account the uncertainty on the evolutionary timescales. The major factors that contributes to these uncertainties include the mass of the H-rich envelope at which the model departs from the AGB and the intensity of the H-burning shell. Indeed the latter is affected by the phase of the thermal pulse cycle at which the star departs from the TAGB, which depends by e.g. the degeneracy level of the CO-core and intershell (Blöcker, 1995). Moreover, other mechanism can affect the evolutionary timescales treatment, as e.g. the speed of the reduction of the remaining H-rich envelope by winds and the prescription of winds during the early post-AGB phase, that will be largely discussed in the present thesis.

Several observations and studies have indicated the possibility of a late igni-

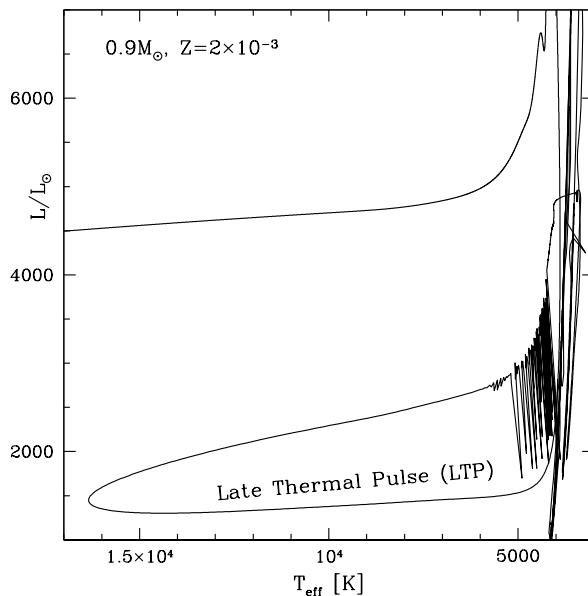


Figure 1.11: HR diagram for a $0.9M_{\odot}$ model with metallicity $Z = 2 \times 10^{-3}$ that experience a late thermal pulse during the post-AGB phase.

tion of helium shortly after the beginning of the contraction towards the post-AGB phase, a phenomenon known as a late thermal pulse (hereinafter late TP; Clayton & De Marco, 1997; Duerbeck et al., 2000; Van Winckel, 2003). The concept of helium ignition occurring after stars leave the AGB was initially proposed by Iben et al. (1983) and further investigated by Blöcker (2001). The latter investigated different scenarios characterized by the timing of the late TP ignition relative to the onset of the overall contraction, finding that during a late TP, the evolutionary tracks display an initial excursion towards the blue, followed by expansion towards the red, preceding the standard post-AGB contraction phase. In Fig. 1.11 we present a model star that underwent helium ignition immediately after the start of the overall contraction. During the occurrence of the loop, the luminosity of the star appears fainter than expected from the classical core mass-luminosity relation.

1.3.2 Planetary Nebula phase

During the transition from the AGB, the star's structure shifts from an expanded, giant-like configuration to a dwarf-like one. This change is driven by the reduc-

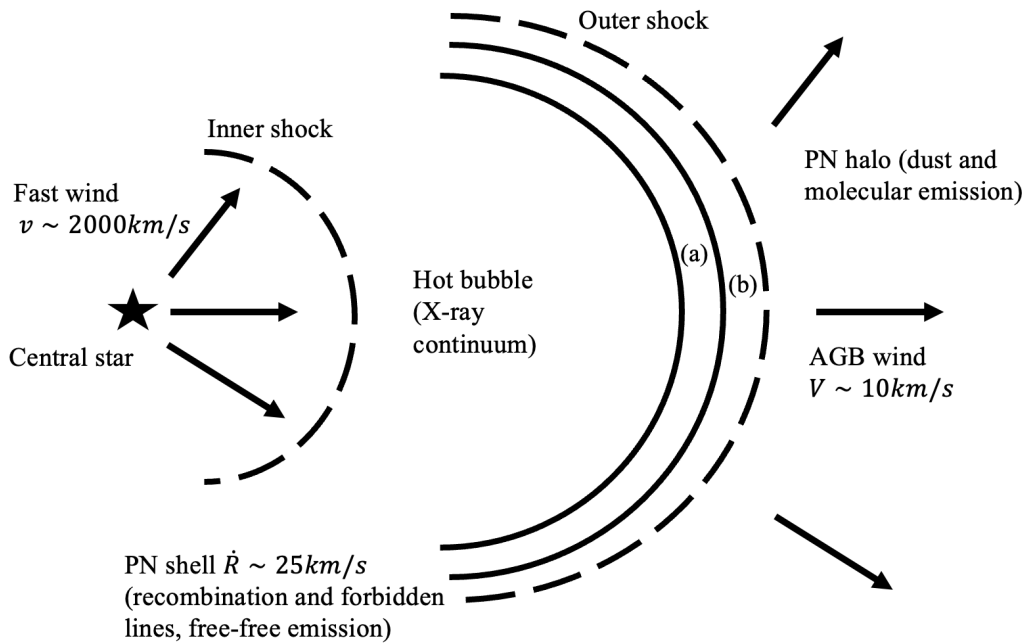


Figure 1.12: Schematic diagram of the structure of a planetary nebula. The fast wind of the central star sweeps the AGB wind, creating an X-ray bubble, a ionized region (a) and a neutral region (b). The figure is adapted with revisions from Kwok (2007).

tion of the hydrogen-rich envelope below the critical threshold required to sustain a giant-like structure (see Sec. 1.3.1). Consequently, the effective temperature increases until reaching a point where a cooling track begins, establishing a new equilibrium condition for the star.

The depletion of the envelope is primarily attributed to stellar winds active during the AGB and early post-AGB phases (Sec. 1.3.1). When the core becomes almost completely exposed and the mass-loss rate reaches approximately 10^{-8} M/yr , a new phase starts: the proto-planetary nebula. During this phase, a high-velocity wind called a “fast wind” is ejected, traveling at speeds around 2000 km s^{-1} (Kwok, 2007). The rapid movement causes it to collide with the inner edge of the AGB wind, gathering the pre-existing wind into a shell. Advancing at supersonic velocities relative to the preceding gas, the shell generates two shocks (illustrated with dashed lines in Fig. 1.12): an outer shock at the shell’s boundary and an inner shock where the fast wind encounters the slower-moving gas. If the fast wind is arrested by the inner shock, the temperature of the shocked gas increases, resulting in the formation of a hot bubble emitting X-rays (refer to Fig. 1.12). This hot bubble propels the shell outward, leading to expansion. Typical observed shell velocities are $\dot{R}_s \sim 10 - 30 \text{ km/s}$ (Volk & Kwok, 1985).

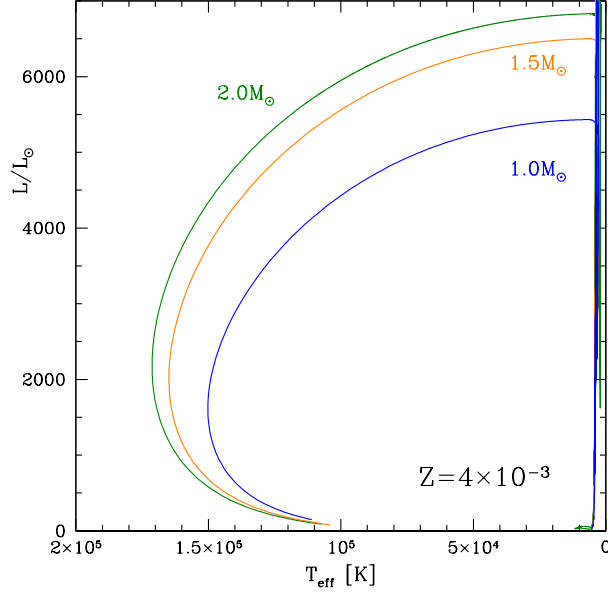


Figure 1.13: HR diagram zoomed into the planetary nebulae phase, for models with metallicity $Z = 4 \times 10^{-3}$. The different colours refers to different tracks. The masses are expressed at the beginning of the AGB phase and in blue is shown the $1.0M_{\odot}$ model, in orange the $1.5M_{\odot}$ and in green $2.0M_{\odot}$.

The formation of shock waves, combined with various other processes such as grain-grain collisions and sputtering, does not alter the mineral composition but can lead to the destruction of dust grains formed during the AGB phase. The impact of these mechanisms remains a debated topic in the scientific community (Natta & Panagia, 1981; Phillips & Ramos-Larios, 2008), but observational evidence highlights the presence of a diverse range of grain sizes, possibly indicating the fragmentation of larger grains into smaller ones (Osterbrock & Ferland, 2006). In this thesis, we aim to shed new light on this uncertain context by studying the amount of dust still present in PNe and connecting it to the previous history of dust production in the AGB phase (Chapter 6).

The PN phase begins when the effective temperature reaches a value ≥ 20000 K and continues along the cooling track towards the white dwarf stage (see Fig. 1.13). During this phase, the nebula is exposed to UV radiation from the CS (Kwok, 2000), which ionizes the surrounding gas. The extent of this ionization primarily depends on the intensity of the incident radiation field and the density of the nebula. The ionized region may either extend throughout the entire nebula, leading to a condition known as density-bounded PNe, where no neutral gas

remains, or be limited by the complete absorption of ionizing photons within the inner regions, resulting in residual gas neutrality termed radiation-bounded PNe (Rodríguez et al., 2009).

In the present thesis we will focus on the radiation-bounded nebulae, in which the ionized region (area (a) in Fig. 1.12) is succeeded by a photodissociation region (PDR, area (b) in Fig. 1.12), where far-ultraviolet (FUV) photons dominate the heating process (Tielens & Hollenbach, 1985). In both scenarios, some of the FUV radiation is absorbed by dust grains and large molecules, which induces photoelectric heating of small grains and larger molecules (Hollenbach & Tielens, 1997). This process is followed by thermal emission, manifesting as a dust continuum along with broad dust and molecular features observed in the infrared (IR) spectrum (Bandyopadhyay & Das, 2023).

As for the post-AGB sources, the chemical composition of PNe remains unaltered by other mechanisms, making them valuable for understanding AGB evolution. The study of the PN phase is particularly advantageous compared to the post-AGB phase due to its longer evolutionary timescale, increasing the likelihood of observing PNe compared to post-AGB objects (Bertolami Miller, 2016).

1.4 ATON stellar evolution models

The evolution of the LIMS presented in this work has been calculated using the ATON stellar evolution code, written in the late 1970s by Mazzitelli (1979) and currently used by the Rome group. A description of the most recent version of this code is given in Ventura et al. (1998). ATON integrates the 4 equations of stellar equilibrium (stellar luminosity, temperature, radius and mass), from the center of the star to the photosphere, according to the Henyey (or relaxation) method (Kippenhahn & Weigert, 1990): a numerical calculation technique that allows the determination of the profiles of the various fundamental physical quantities. Once the integration has been performed, ATON applies the time step to change the chemical composition and then proceeds with a new integration by relaxation. The code solves a matrix describing the effect of nuclear reactions, with a network of 30 chemical species, from hydrogen to silicon, and 64 nuclear reactions. In this way, the evolution of a star is described by a series of time steps, for each of which are determined the internal stratification of the structure and the global properties (luminosity, effective temperature, etc.).

The temperature gradient, within regions unstable to convection, is found via the Full Spectrum of Turbulence model (Canuto & Mazzitelli, 1991).

The formal borders of the convective regions are found via Schwarzschild criterion but the convective eddies are allowed to overshoot into radiatively stable regions, by imposing an exponential decay of velocities beyond the formal border:

the scale for the decay of velocities is $l = \eta H_p$, where η is a free parameter associated with the extension of the extra-mixed region. In agreement with the calibration given in Ventura et al. (1998) η is assumed to be equal to 0.02 during the evolution before the beginning of the TPs phase. This approach is consistent with results from numerical simulations (Freytag et al., 1996). Moreover, in the convective regions (including the overshoot zones), nuclear burning and chemicals mixing are self-consistently coupled by means of the diffusive method proposed by Cloutman & Eoll (1976).

The surface molecular opacities were adjusted to reflect changes in chemical composition resulting from carbon enrichment, following the methodology outlined by Marigo & Aringer (2009). As mentioned earlier in this Chapter, during the AGB phase, the star loses the majority of its envelope through stellar winds (see Sec. 1.2). The rate of mass-loss varies depending on the star's surface composition, requiring different prescriptions to accurately model this process. For the oxygen-rich phases in ATON is used the following formulation from Bloeker (1995):

$$\dot{M} \propto M^{-3.1} R L^{3.7} \quad (1.2)$$

while for carbon stars the one from Wachter et al. (2002, 2008):

$$\dot{M} \propto M^\alpha T_{\text{eff}}^\beta L^\gamma \quad (1.3)$$

In both the equation, T_{eff} , L , R , and M refer to the star's effective temperature, luminosity, radius, and mass, respectively. Within the metallicity range considered in this thesis ($10^{-3} \lesssim Z \lesssim 8 \times 10^{-3}$), the typical values for Wachter's parameters are $\alpha = -3$, $\beta = -7$ and $\gamma = +3$.

The selection of the Blocker and Wachter relations was made to ensure reliable prescriptions of the stars' radiative properties, which are essential for a detailed investigation of dust formation and the mass-loss mechanism. Adopting alternative prescriptions, such as more empirical ones (e.g. Guandalini et al., 2006), would influence the evolutionary timescales for the transition from the AGB to the post-AGB and PN stages, as well as the amount of material ejected and available for condensation into dust. However, as shown in Ventura et al. (2018), the use of different mass-loss rate prescriptions does not significantly affect dust properties in the low-mass regime ($M < 2.5 M_\odot$), where most of our sources are located (see Chapters 4, 5, and 6).

The formalism above described is adopted for calculations extended until the end of the AGB phase, when the envelope mass had dropped below a few tenths of a solar mass. Extending the computations into the post-AGB and PN phase required several modifications to the stellar evolution code, such as shorter time steps and temporarily freezing mesh rezoning for a limited number of models

following the onset of contraction. Numerical tests confirmed that the resulting post-AGB luminosity and surface chemistry were not dependent on the specific choices of time-step intervals (Marini et al., 2020).

Chapter 2

Dust formation during the evolved star phases

The presence of dust in the circumstellar envelopes of evolved stars has been extensively studied over the past several decades, both observationally and theoretically. Woolf & Ney (1969) were the first to suggest that solid particles exist in the circumstellar environments of these cool stars, based on their observations of emission bands between 10 and 14 μm . Around the same time, Gilman (1969) was the first to theoretically predict the composition of this dust by modeling the condensation of dust grains. The presence of dust plays a crucial role in accelerating stellar winds due to its high opacity around the peak wavelengths of the stellar SED. Radiation pressure on the dust grains propels them outward, and through dust-gas coupling, the gas is dragged along (Gehrz & Woolf, 1971; Gilman, 1972). These stellar winds can reach velocities of about 20–50 km s^{-1} in AGB stars, leading to highly variable mass-loss rates (see Sec. 1.2).

Both observational and theoretical studies indicate that AGB stars are significant contributors to the dust content of their host galaxies (Tielens, 2005; Boyer et al., 2012, 2015; Matsuura et al., 2013; Zhukovska et al., 2008; Schneider et al., 2014; Schneider & Maiolino, 2024), releasing dust into the environment that reflects the nucleosynthesis and mixing processes active during the AGB phase (see Sec. 1.2.4). These properties highlight the need to create models able to reproduce not only the evolution of the star, but also the dust production process and how it evolves during the AGB phase. For this reason, previous works by our team (e.g. Ventura et al., 2012a,b, 2014) have made an effort to include the dust production mechanism in the evolutionary tracks, using the schematization proposed by the Heidelberg group (Ferrarotti & Gail, 2006). These studies have been used to interpret the evolved stellar populations of the MCs (Dell’Agli et al., 2014b, 2015a,b) and the Local Group galaxies (Dell’Agli et al., 2016, 2018b, 2019), and to explore the possibilities offered in this area by the James Webb Space Telescope (JWST,

Marini et al., 2020, 2021).

In the following Sections we will describe the schematization adopted to model the dust growth and wind dynamics in our models. We will point the accent on: a) which dust species are expected to be formed as a function of the mass of the star, b) how the dust formation and mass-loss processes are interconnected, c) how the dust production rates increase towards the end of the AGB phase, especially for the dominant AGB sources of dust, i.e. carbon stars. The latter two points will represent the main reasons why finding constraints to these processes (dust production and mass-loss) from the subsequent evolutionary stages proves to be important for a global understanding of the dust budget from AGB stars.

2.1 Dusty wind in the evolved stars

The outer atmospheric layers of AGB stars provide a favorable environment for dust production and the subsequent radiative acceleration of these newly formed dust grains. The chemical composition of the dust reflects the evolutionary pattern followed by the stars (see Sec. 1.2.4): in the oxygen-rich environment ($C/O < 1$), species that require the presence of free oxygen, such as silicates (olivine, pyroxene, quartz), are favored; whereas in the carbon-rich environment ($C/O > 1$), all available oxygen is bound in the CO molecule, and consequently, the most favored species are solid carbon and SiC. In both cases, iron can condense.

In association with the evolutionary description of the CS, ATON's models follow the evolution of the dusty layer formed during the AGB phase (Ventura et al., 2014). The dust formation process in the environment of AGB stars was described in a series of papers by the Heidelberg group (Gail & Sedlmayr, 1999; Ferrarotti & Gail, 2001, 2002, 2006; Zhukovska et al., 2008; Zhukovska & Gail, 2009). In this thesis, we adopt the prescription outlined in Ventura et al. (2012a), which integrates the AGB models of ATON with the wind modeling approach proposed by Ferrarotti & Gail (2006). This framework is built upon a model of expanding wind, wherein the thermodynamic structure is determined by the physical parameters of the central object, such as effective temperature, surface gravity, and mass-loss rate. The wind behavior is described by two differential equations governing the radial variation of gas velocity and optical depth. The dust grains are assumed to form from the condensation of gaseous molecules present in the expanding winds, with an initial dimension of grains, a_0 , which is much smaller than the size reached by the various grains in the asymptotic regime. For this reason, the results of the simulations are almost independent of the choice of a_0 . Furthermore, an initial density of grains, $n_d = 3 \times 10^{-13}$, is assumed, which reflects the order of magnitude of the typical grain number densities in the outflows of AGB stars (Knapp, 1985).

In the following Subsection, we will describe the physics governing the formation and dynamics of the dust layer.

2.1.1 Dust formation

The temporal variation of the dust grain size for the i th dust species a_i is derived as a competition between the destruction rate J_i^{dec} and the growth rate J_i^{gr} :

$$\frac{da_i}{dt} = V_{0,i}(J_i^{gr} - J_i^{dec}) \quad (2.1)$$

$V_{0,i}$ is the volume of the nominal molecule in the solid. The growth rates per unit of time and the surface area are proportional to density n_i and the thermal velocity $v_{th,i}$, of the key species in the gas phase:

$$J_i^{gr} = \alpha_i n_i v_{th,i} \quad (2.2)$$

Where α_i is the sticking coefficient of the species i . The destruction rate, i.e. the vaporization rate of dust grains by thermal decomposition, is estimated from the vapour pressure of the key species ($p_{v,i}$) over the solid state, and it is proportional to the thermal velocity:

$$J_i^{dec} = \alpha_i v_{th,i} \frac{p_{v,i}}{kT} \quad (2.3)$$

As a general behavior, the destruction rate exceeds the growth rate in the regions close to the central star, which are characterized by too hot temperatures. Typical distances where dust formation can occur are at 3–4 stellar radii from the surface of the star, in which the temperature drops below 1000 K. The grain growth results in an increase in opacity, which, due to the strong radiation pressure of the star, will favor an acceleration of the wind, which will stop the dust formation. For this reason, dust formation and growth is expected to be efficient only at distances between ~ 3 and 10 stellar radii, and according to the growth rate, grains with different grain sizes and final velocities (Ventura et al., 2012a) can be formed.

The amount of dust formed depends by the “key element”, whose abundance is the minimum among all the elements necessary to form the corresponding dust aggregate. The abundance of the key element limits the quantities and dimensions of the dust grains of the species considered. Silicon is the key element for olivine, pyroxene, quartz, and SiC, whereas iron and carbon are the key elements for iron dust and solid carbon.

The fraction of gas condensed in dust is needed for the “ i ” species is:

$$f_i = \frac{4\pi(a_i^3 - a_{0,i}^3)}{3V_{0,i}} \frac{n_d}{\epsilon_k n_H} \quad (2.4)$$

a_i is the grain dimension, $V_0 = \frac{Am_H}{\rho_D}$ is the volume of the molecule given the ratio between atomic weight and the mass density of one mole ρ_D . ϵ_k is the number of free particles of the key element normalized to hydrogen $\epsilon_k = \frac{n_k}{n_H} = \frac{Y}{4X}$, where Y and X are the mass fractions of helium and hydrogen, respectively. n_H is the numerical density of hydrogen in the gas and n_k is the density of the k-element in the gas phase. The first one can be achieved from the mass density ρ , assuming that the gas is composed only of hydrogen and helium:

$$n_H = \frac{\rho}{(1 + 4\epsilon_{He})m_H} \quad (2.5)$$

2.1.2 Wind dynamics

The model used to determine the wind structure is based on a schematisation proposed by the Heidelberg group (Ferrarotti & Gail, 2006), according to which the dust forms in a stationary wind that expand radially from the photosphere of the star. We assume an isotropical expansion of the wind from the surface of the star. From the equation of momentum conservation we found the wind velocity v :

$$\frac{dv}{dr} = -\frac{GM_\star}{r^2}(1 - \Gamma) \quad (2.6)$$

where r is the radial distance from the center of the star, M_\star is the current mass of the star, and the relative weight of the effects of radiation pressure and gravity $\Gamma = kL_\star/4\pi cGM_\star$. In the expression for Γ , k is the flux-averaged extinction coefficient of the gas–dust mixture, which reflects the scattering and absorption processes of the photons released from the stellar photosphere by dust particles; L_\star is the luminosity of the star.

Therefore, the growth of dust grains and the dynamics of the wind are self-consistently coupled, as the determination of the size of the dust particles of the different species formed are required for the calculation of k . The flux-averaged extinction coefficient of the gas–dust mixture can be calculated as:

$$k = k_{gas} + \sum_i f_i k_{i,dust} \quad (2.7)$$

With $k_{gas} = 10^{-8}\rho^{2/3}T^3$ (Bell & Lin, 1994). The sum in Eq. 2.7 is extended to all the dust species considered: f_i represent the fractions of gaseous molecules condensed into dust and $k_{i,dust}$ represent their corresponding extinction coefficients. Assuming direct irradiation from the star’s photosphere, $k_{i,dust}$ can be expressed as the integral of the extinction coefficients at individual wavelengths, averaged over the Planck function corresponding to the effective temperature of the star:

$$k_{i,dust} = k_p(T_{eff}) = \frac{\int_0^\infty k_\nu B_\nu(T_{eff}) d\nu}{\int_0^\infty B_\nu(T_{eff}) d\nu} \quad (2.8)$$

In the case of opaque environments it is essential to take into account the effects of absorption and diffusion processes by the dust grains present. In this case, it is necessary to modify the expression 2.8 for the calculation of the average extinction coefficient by adding a term, whose importance increases with the opacity of the environment, describing the reprocessing of the electromagnetic radiation, calculated at the temperature of the envelope region considered T_\star (Gail et al., 2013):

$$k_{i,dust} = k_p(T_{eff})e^{-\tau_\star} + k_R(T_\star)(1 - e^{-\tau_\star}) \quad (2.9)$$

Where k_R is the average extinction coefficient calculated by Rosseland averaging, τ_\star is the local optical depth of the dust layer, obtained by integrating the columnar density of the gas ρ in the local dust layer over the relative absorption coefficients k_\star :

$$\tau_\star = \int_0^\infty \rho k_\star ds \quad (2.10)$$

If $\tau_\star \ll 1$, we get to the case $k_{i,dust} \sim k_p(T_{eff})$; otherwise, if $\tau_\star \gg 1$, the dominant contribution is $k_R(T_{eff})$. In the present work of thesis we will use the optical depth at the wavelength of $10 \mu\text{m}$ (Eq. 2.15) and the overall optical depth is calculated by summing all the contributions from the individual dust species and the largest contribution being given by those with the highest extinction coefficients (i.e. solid carbon or silicate dust).

By assuming fixed the dust mineralogy that is moving away from the stellar photosphere thanks to the pushing action of the radiation pressure of the star, the functional density profile of the dust will decrease reaching higher distances respect to the central star:

$$\rho(r) = \rho_{in}(r_{in}/r)^2 \quad (2.11)$$

From Eq. 2.6, when $\Gamma > 1$ the wind is accelerated by the radiation pressure exerted on the grains present, resulting in a variation of the wind density ρ . This is determined by the mass conservation equation, as a function of the rate of mass-loss of the star:

$$\dot{M} = 4\pi r^2 \rho v. \quad (2.12)$$

For what concerns the temperature profile of the gas in the wind, is used the relationship of Lucy (1971, 1976), which considers a geometric dilution factor and

a term that takes into account the effects of the re-processing of electromagnetic radiation by gas and dust:

$$T^4 = \frac{1}{2}T_{eff}^4 \left[1 - \sqrt{1 - \frac{R_\star^2}{r^2}} + \frac{3}{2}\tau_L \right]. \quad (2.13)$$

T_{eff} is the effective temperature of the star, R_\star the radius of the star, τ_L the optical depth, which is related to the gas density and extinction coefficient via the equation:

$$\frac{d\tau_L}{dr} = -\rho k \frac{R_\star^2}{r^2}. \quad (2.14)$$

The equation 2.14 comes from the knowledge of the grain sizes of the various dust species and of the radial stratification of the thermodynamic variables. We note that variations in dust mineralogy would result in changes to the τ value, primarily attributable to differences in their optical properties and, consequently, in the values of k .

The wind model used consists of two differential equations, which describe the behaviour of velocity (2.6) and optical depth (2.14). For velocity, an internal, partially arbitrary boundary condition is assumed to represent the velocity v_0 with which the wind enters the dust condensation region. For the optical depth we assume $\tau_L \rightarrow 0$ for $r \rightarrow \infty$. The relevant equations and the details of the numerical treatment are extensively described in several paper (see e.g. Ventura et al., 2012a, 2014).

2.1.3 Dust production rate and optical depth

In Tab. 2.1 are reported the chemical reactions from which the different dust compounds originate.

Species of dust	Reaction of formation
Olivine	$2xMg + 2(1-x)Fe + SiO + 3H_2O \rightleftharpoons Mg_{2x}Fe_{2(1-x)}SiO_4 + 3H_2$
Pyroxene	$xMg + (1-x)Fe + SiO + 2H_2O \rightleftharpoons Mg_xFe_{(1-x)}SiO_3 + 2H_2$
Quartz	$SiO + H_2O \rightleftharpoons SiO_2 + H_2$
Alumina	$Al_2O + H_2O \rightleftharpoons Al_2O_3 + 2H_2$
Iron	$Fe \rightleftharpoons Fe(s)$
Carbon	$C_2H_2 \rightleftharpoons 2C(s) + H_2$
Silicon Carbide	$2Si + C_2H_2 \rightleftharpoons 2SiC(s) + H_2$

Table 2.1: Relevant dust species that can be formed in the circumstellar envelope of the AGB stars and their formation reaction.

As shown in Figure 2.1, the dust production rate evolves over time since the beginning of the AGB phase, remaining active throughout this entire phase. That parameter directly depends by the mass-loss, which influence the wind density (Ferrarotti & Gail, 2006), thereby affecting the availability of gaseous molecules for condensation into dust.

The bottom panel of Figure 2.1 illustrates another proxy for the amount of dust formed during the AGB phase: the optical depth at a wavelength of $10 \mu\text{m}$ (Equation 2.15).

$$\tau_{10} = \pi \int_{r_{in}}^{r_{out}} n_d Q_{10} a^3 dr \quad (2.15)$$

a is the size of the dust grains, Q_{10} the extinction coefficient at $10 \mu\text{m}$, $n_d = C_{n_d} n_H \sim 1/r^2$ the number density, n_H and C_{n_d} are the seed density in volume units and the seed number in hydrogen units; r_{in} and r_{out} are the distances of the inner and outer borders of the region of the circumstellar envelope. It is important to note that due to the significantly different optical constants of silicates and carbonaceous dust species, a direct comparison between them is not possible.

According to the evolutionary history followed by the star, we can distinguish three different classes of LIMS:

- A. Stars progeny of low-mass stars, with $M \lesssim 1.0 M_{\odot}$, that during their evolution did not experience enough TDU before loosing their envelope to become carbon (see e.g. $0.7 M_{\odot}$ model in Fig. 1.8), and thus producing silicates-rich dust. Despite being characterized by relatively small mass-loss rates (see e.g. $0.7 M_{\odot}$ model in Fig. 1.4), resulting in a limited amount of dust production and optical depth (as demonstrated by the dust production in the $0.7 M_{\odot}$ model, Fig. 2.1), their understanding proves to be crucial since the initial mass function of the galaxies peaks in them.
- B. Intermediate-mass stars whose progenitor's masses are between $1.0 M_{\odot}$ and $3 M_{\odot}$, that achieve the carbon-star stage. For the carbon stars, the later stages of the AGB phase are particularly favorable for dust formation. Indeed, during each TDU, the surface carbon abundance increases, leading to a substantial rise in molecular opacities (Marigo, 2002). This expansion in structure is followed by an increase in the mass-loss rate (\dot{M}), particularly during the final interpulse phases, and the rate of dust production (which closely correlates with \dot{M} , see Fig. 2.1). Furthermore, the production of carbon dust is higher for stars characterized by higher masses: this is because sources with masses below $1.5 M_{\odot}$ experience few number of TDU before loosing their envelope (see Fig. 1.8), thus accumulating smaller amount of surface carbon abundance with respect to their more massive counterparts

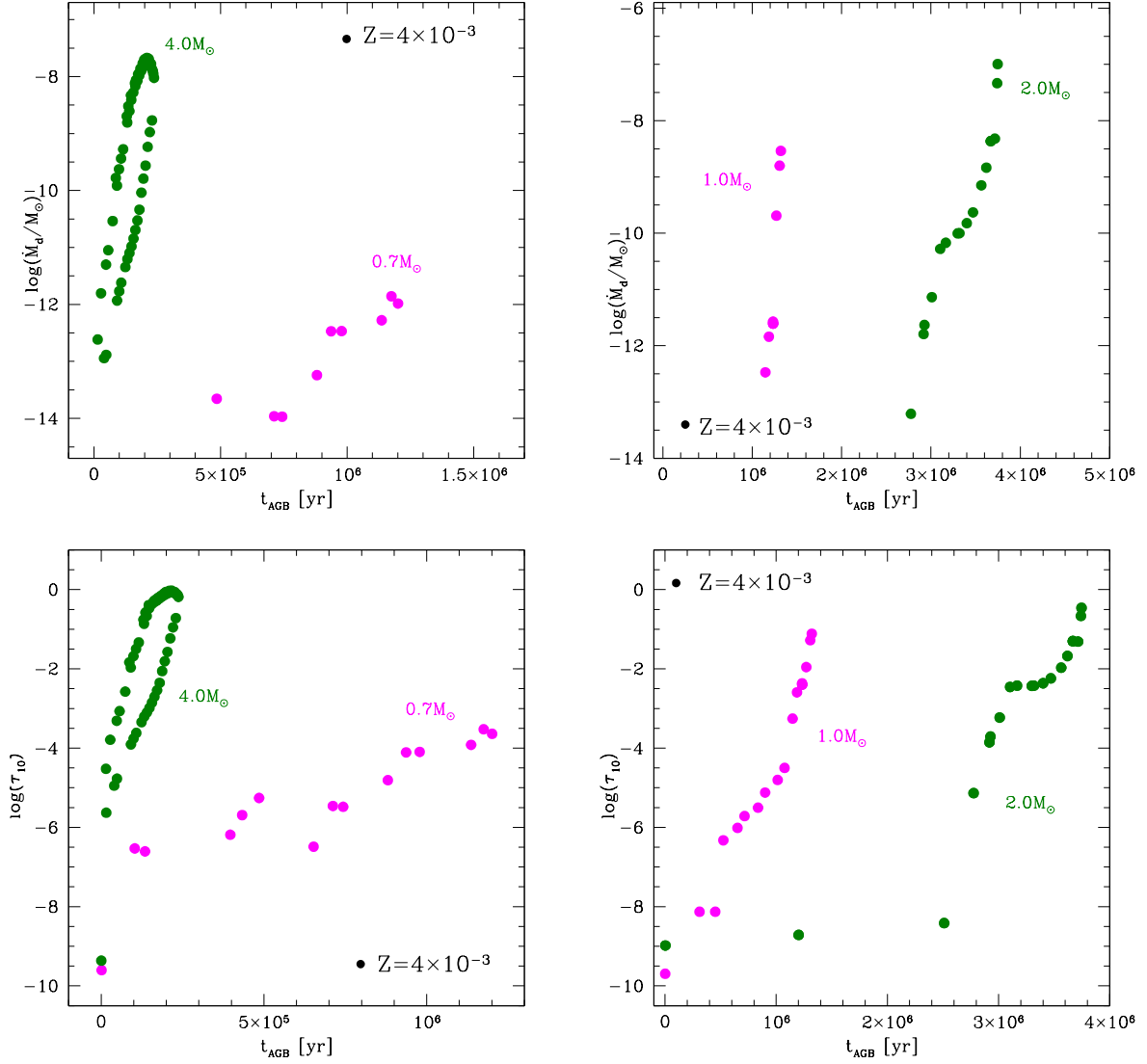


Figure 2.1: Dust production rate (top panels) and optical depth (bottom panels) as a function of the time elapsed since the beginning of the AGB phase. In the left panels are reported two oxygen-rich stars models with progenitor's masses equal to $4.0 M_\odot$ (green) and the $0.7 M_\odot$ (magenta); in the right panels the carbon-rich stars, showing the $1.0 M_\odot$ (magenta) and the $2.0 M_\odot$ (green) models.

(see left bottom panel Fig. 1.4). This behavior reflects into higher dust production rates and higher optical depth, for more massive objects (see Fig. 2.1).

- C. Stars characterized by masses higher than $3.5 M_{\odot}$, that experience strong HBB and thus with $C/O < 1$, producing silicate dust, mainly. In oxygen-rich stars, the peak of dust production coincides with the highest mass-loss rates, occurring when the HBB is most pronounced (Ventura et al., 2015), just before a significant portion of the envelope is shed. This lead to a dust production rate and an optical depth that follow the same trend (see Fig. 2.1) but we note that, by assuming a different mass-loss prescription, that behaviour could change. Indeed, e.g. in Marini et al. (2023) is shown that, by assuming the mass-loss rate from Vassiliadis & Wood (1993), the peak of the mass-loss increase with the period of rotation of the star and thus with its radius, leading to higher mass-loss rates at the end of the AGB evolution.

Several studies has shown that the larger (40–70%) contribution from AGB stars to dust budget of galaxies in the local Universe is determined by the C-star, characterized by masses $1.5 M_{\odot} \lesssim M \lesssim 3 M_{\odot}$, which are currently evolving through the very final AGB phases (Boyer et al., 2012, 2015; Dell’Agli et al., 2016, 2018b, 2019). For this reason, understanding dust production during the last interpulses and finding consistency with IR excess observed in post-AGB and PNe is crucial for assessing the dust yields of individual stars and the overall contribution of these objects to dust production in the host system. In the present thesis we will extensively discuss the dust formation process active during the end of the AGB phase, finding constraints for the mass-loss prescription and treatment usually used in the literature.

Chapter 3

The evolution of the SED in the AGB-to-PNe transition

Studying the SED of AGB stars can be a valuable tool for gaining a better understanding of the dust production processes active in these objects. The dust formed in the circumstellar envelope shapes the SED, providing indication on the nucleosynthesis and mixing processes occurred during the AGB phase. Indeed, in Sec. 1.2.4, we saw how the mineralogy of the dust is affected by TDU and HBB.

The IR emission from AGB stars serves as a real-time indicator of ongoing dust production. In the left panel of Fig. 3.1, the typical spectrum of an AGB star at the beginning of the AGB phase, when the dusty layer has not yet formed, is shown with a dotted line. The solid line in the left panel of Fig. 3.1 represents the same AGB star at a later stage when the dusty layer has formed, causing a shift of the star's emission to redder wavelengths. At this stage, the freshly formed dusty layer is close to the central star, at distances where dust formation can occur, i.e., around 3–4 stellar radii (see Sec. 2.1). The dust emission can dim partially or totally the photospheric emission from the star, challenging even more the determination of the stellar parameters and surface chemical abundances in these cool stars.

The infrared features observed depend on the dust mineralogy surrounding the star. Stars that have undergone multiple TDU episodes, transitioning to a carbon-rich stage, typically exhibit featureless emissions attributed to amorphous carbon (Sloan & Egan, 1995). Additionally, in some cases, a feature at $11.3\ \mu\text{m}$ can be seen, attributed to the presence of SiC (Speck et al., 1997), and/or a $30\ \mu\text{m}$ bump, whose carrier is often linked to MgS (Lombaert et al., 2012) but remains unidentified so far. M-type stars, dominated by an oxygen-rich composition, are mainly characterized by silicate dust in the amorphous form, which produces features at ~ 9.7 and $18\ \mu\text{m}$ (Sloan et al., 2003). In these environments, it is also possible to see other features, such as the $13\ \mu\text{m}$ feature due to the presence of

alumina dust (Al_2O_3) and crystalline silicate dust, characterized by emission at 11, 23, 28, 33 μm (Blommaert et al., 2014).

If dust forms in a sufficient quantity and the optical properties favor this mechanism, the dusty layer is then accelerated by the star’s radiation pressure, reaching increasingly larger distances from the stellar photosphere. Since no other mechanism significantly alters the surface chemical composition of LIMS after the AGB phase, it is possible to see the fingerprints of AGB evolution from the study of post-AGB stars and PNe. In this thesis (Tosi et al., 2022, 2023, 2024; Dell’Agli et al., 2022, 2023a) we aimed to characterize a broad sample of post-AGB stars and PNe using available observational data, such as photometry, spectroscopy, and surface chemical abundances, to constrain the primary physical parameters of the CS (luminosity and effective temperature) and chemical parameters (gas and dust chemical composition). The final goal was to compare this information with parameters derived from stellar evolution models, finding constraints on mass-loss and the dust formation process in previous evolutionary stages.

In the next Sections, we present the evolution of the SED of LIMS during the post-AGB and PN phases, explaining the methodology used to study the sample selected for the present thesis.

3.1 SED of the Post-AGB stars

The post-AGB stars provide an ideal environment for studying the surface chemical abundances of a broad range of elements, such as C, N, O, α elements, Fe-peak elements, and *s*-process elements (Kamath, 2020; Kamath & Van Winckel, 2022, and references therein). This is because their effective temperatures, ranging from 7000 K to 30000 K (see Sec. 1.3), are sufficiently high to avoid the blending effects caused by molecular lines typical of AGB stars (García-Hernández et al., 2006, 2009). Instead, their spectra are dominated by atomic transitions, which facilitate more accurate measurements of surface chemical abundances (De Smedt et al., 2016).

The study of the central star and the detached circumstellar environment is further enabled by the double-peaked shape of the SED of post-AGB stars, often referred to as “shell-type”. Based on radial velocity monitoring studies, this morphology is typical of sources that have undergone single-star evolution* (Van Winckel, 2003; Kamath et al., 2014, 2015). This morphology results from two primary factors: the increase in effective temperature relative to the AGB phase,

*The optically visible post-AGB sources typically associated with binary evolution do not show the characteristic two distinct flux peaks in the mid-IR. These stars, referred to as “disc-sources”, display a pronounced near-IR excess, suggesting that the circumstellar dust is located close to the central star, near the sublimation temperature (Van Winckel, 2003; Kamath et al., 2022).

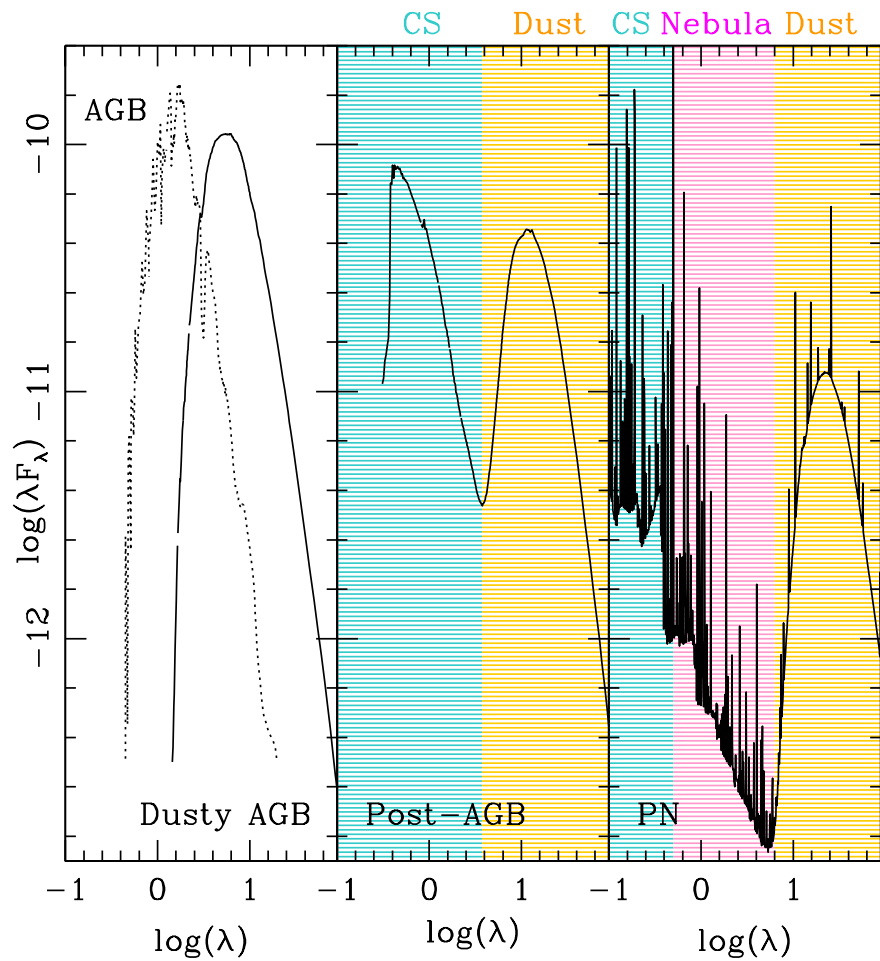


Figure 3.1: An example of SED of a dusty AGB star (left panel), post-AGB star (central panel) and planetary nebula (right panel). The dashed line represent the spectrum of the star of the dusty AGB star, showed without the contribution of the dust. On the central and right panel are also reported main contributors to the emission, i.e. CS (cyan area), dust (yellow area) and nebula (magenta area).

which shifts the central object’s emission into the UV wavelengths, and the detachment of the dusty layer from the star, resulting in progressively lower dust temperatures and shifting the peak of dust emission to the mid-IR region. This enables a clear distinction between dust emission (yellow area in the central panel of Fig. 3.1) and stellar emission (cyan area in the central panel of Fig. 3.1), producing the characteristic double-peak shape.

The mineralogy of dust in post-AGB stars reflects that of dust formed during AGB evolution (see Sec. 1.2.4). In many cases, stars that produced carbon dust exhibit signatures of *s*-process enhancement (Kamath et al., 2022) and show the presence of the 21 μm and 30 μm features in their SEDs (Kwok & Zhang, 2013). The 21 μm feature remains unidentified, though it seems associated with complex hydrocarbons (Volk et al., 2020), while the 30 μm feature is likely attributed to MgS grains (Goebel & Moseley, 1985; Sloan et al., 2014). A series of unidentified features in their spectra are associated with polycyclic aromatic hydrocarbons (PAHs) or with very small hydrogenated amorphous carbon grains (HACs, Buss et al., 1993) in the range of 3 – 12 μm , as well as with fullerenes (C60 and C70, Cami et al., 2010; Sloan et al., 2014); however, the origins of these features are still debated. In contrast, oxygen-rich sources show no evidence of *s*-process or carbon enrichment but exhibit silicate features in both amorphous and crystalline forms, along with the Al₂O₃ feature.

3.1.1 Post-AGB modeling with DUSTY

To produce synthetic SEDs of post-AGB stars for comparison with observational data points, we used the DUSTY radiative transfer code described in Nenkova et al. (2000). This code calculates the SED emerging from the star by accounting for the reprocessing of radiation released from the photosphere by a dusty region isotropically distributed around the point-like source. A summary of the code’s input and output parameters is provided in Tab. 3.1.

The starting point of the SED analysis is the input radiation entering the dusty layer, for which we used the Kurucz-Castelli atmosphere models (Castelli & Kurucz, 2003), available across a wide range of metallicities ([Fe/H] from -4 to 0.5), effective temperatures (3500 K to 50000 K), and surface gravity values ($\log(g)$ from 0.0 to 5.0 dex)[†]. The extensive grid of Castelli atmosphere models ensures a reliable representation of all the post-AGB sources considered in this study. Since our post-AGB sample lacks UV/optical spectra, our analysis is not sensitive to specific stellar features that might contribute in that spectral region (see Chapter 4 and 5). As a result, our findings remain unaffected by the choice of stellar

[†]The spectra can be downloaded from:
<http://svo2.cab.inta-csic.es/theory/newov2/index.php?models=Kurucz2003a11>

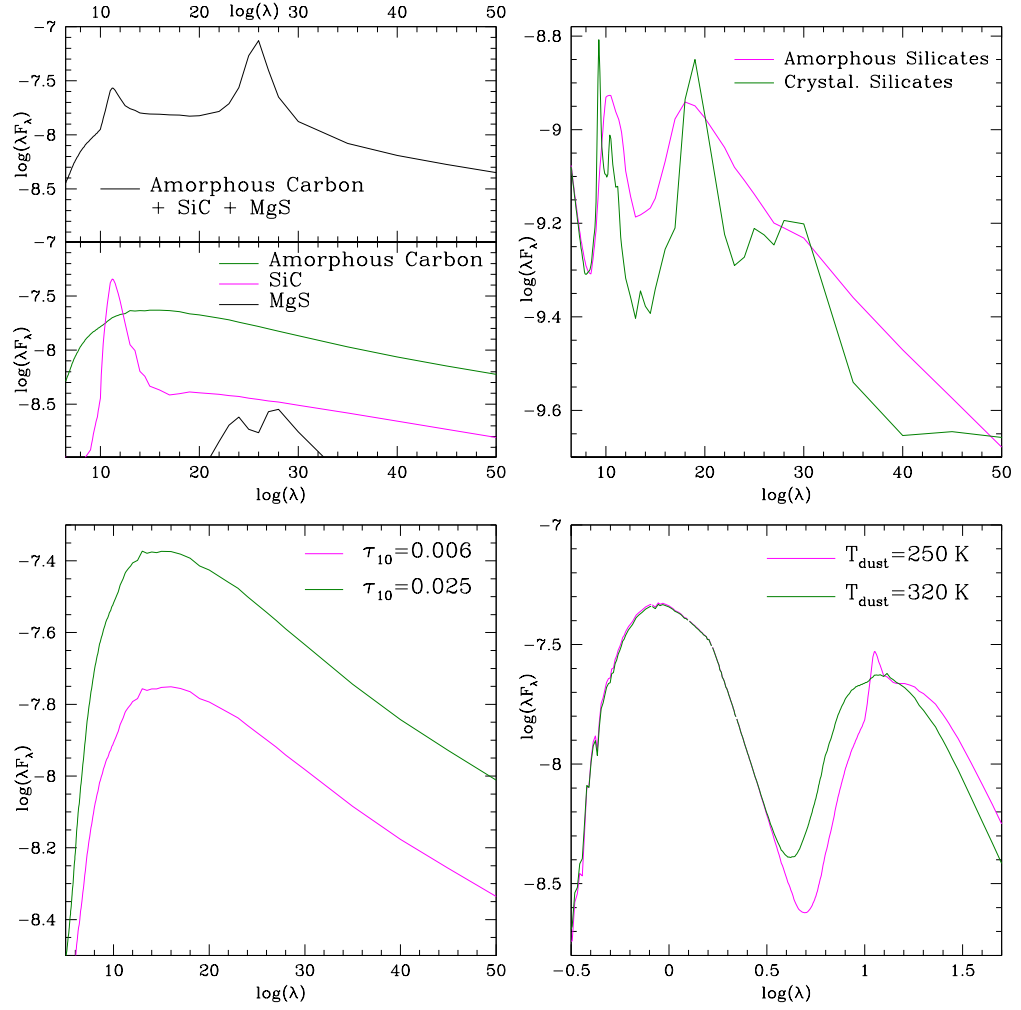


Figure 3.2: Synthetic spectra obtained using the transfer radiative code *Dusty*. λ is expressed in micron, λF_λ in erg/s/cm^2 . The panels represents the effect on the synthetic spectrum of the dust mineralogy (top panels, on the left the carbonaceous species, on the right the oxygen-rich dust), different dust temperatures (lower right), optical depth (lower left). In the top left panel is divided as follow: the top plot show the SED obtained assuming the presence of amorphous carbon, SiC and MgS; the lower display the individual contribution of each component.

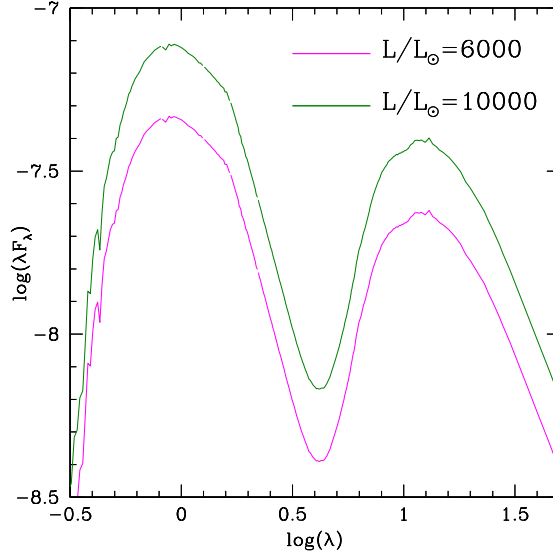


Figure 3.3: Synthetic spectra obtained using the transfer radiative code *Dusty* adopting different stellar luminosities. λ is expressed in micron, λF_λ in erg/s/cm².

atmosphere model.

Furthermore, to model the post-AGB stars we specified an a priori exponentially decreasing density distribution with a profile proportional to r^{-2} , where r represents the radial distance from the central star. For the dust grain sizes, we assumed asymptotic values of $0.12 \mu\text{m}$ for solid carbon, $0.07 \mu\text{m}$ for SiC, and $0.08 \mu\text{m}$ for silicates. These values were chosen for consistency with the typical grain sizes derived from the dust formation model described in Section 2.1.1 (e.g. Ventura et al., 2014, 2018).

We iteratively adjusted the input parameters to produce synthetic SEDs that satisfactorily match the observations. This process allowed us to derive stellar luminosity and dust properties through the following methodology:

- We considered both oxygen-rich and carbon-rich dust scenarios (right and top left panels of Fig. 3.2, respectively). For M-type stars, we explored the possible presence of amorphous silicates (magenta line) using the optical constants of Ossenkopf et al. (1992), and in low-temperature environments, crystalline silicates (green line) using the optical constants of Jaeger et al. (1994). For C-rich stars, we modeled the SED assuming amorphous carbon dust (green line) with the ACAR[‡] optical constants of Zubko et al. (1996).

[‡]The ACAR (Amorphous Carbon ARgon) optical constants are obtained producing amorphous

For high-metallicity sources, we further examined the contribution of SiC (magenta line) using the optical constants of Pegourie (1988). Additionally, for one object with available IR spectrum data, we included MgS dust (black line) using the optical constants of Hofmeister et al. (2003).

It is important to note that distinguishing between crystalline and amorphous silicates is possible using photometric data due to their narrow features, which significantly affect the flux between 10 and 30 μm (see top right panel, Fig. 3.2). As it will be discussed in Chapter 4, these features cause a steep decline in the photometric bands, observable through filters like WISE 4 and MIPS. Similarly, for carbonaceous sources, photometric data can indicate the presence of MgS dust, whose features affect the flux between 20 and 30 μm , influencing observational filters such as WISE 4 (see Sec. 5.1). However, for a comprehensive and accurate study of the aforementioned features, particularly for significant features where photometric data alone are insufficient (such as SiC), spectral data are essential. Spectral analysis offers the necessary detail to accurately identify and characterize all dust components, whether in oxygen-rich or carbon-rich environments.

- We evaluate the optical depth τ_{10} (see Eq. 2.15 for the definition) of the dust surrounding each source by analyzing the height of the IR peak (see lower left panel, Fig. 3.2).
- The minimum between the peak of the SED due to the star and that of the dust, usually found in the 3 – 6 μm spectral region, allows for the determination of the dust temperature at the inner boundary of the dusty region, T_d (see lower right panel, Fig. 3.2).
- By adjusting the synthetic SED to match the observed SED profile in the optical/near-IR region, it is possible to determine the luminosity of the star (see Fig. 3.3).

Once the dust mineralogy is determined, the dust temperature can be derived with an accuracy of approximately 10–20 K. When WISE, IRAC, and MIPS photometric data are available, the optical depth can be determined with a precision of 10 – 15%. The luminosity of the stars is primarily established from the near-IR spectrum, with an uncertainty within 10%.

carbon grains from arc discharge between amorphous carbon electrodes in an Ar atmosphere at 10 mbar (Zubko et al., 1996).

Table 3.1: *Input and output parameters of the transfer radiative code Dusty and the spectral synthesis code Cloudy.*

DUSTY	Input	Output
	Stellar atmosphere	L/L_{\odot}
		dust mineralogy
		τ_{10}
		T_d
CLOUDY	Input	Output
	Stellar atmosphere	T_{eff}
	Observed abundances	L/L_{\odot}
	N_h	ΔR
	R_{in}	M_{gas}
		dust mineralogy
		δ
		T_d

Notes: T_{eff} and L/L_{\odot} are the effective temperature and the luminosity of the star, τ_{10} the optical depth, T_d the dust temperature, ΔR the thickness of the nebula, M_{gas} the mass of gas that makes up the nebula, δ the dust-to-gas ratio.

3.2 SED of the Planetary nebulae

As discussed in Sec. 1.3.2, PNe consist of three main components, each contributing distinctively to the SED. The CS primarily emits in the UV range, producing a stellar continuum (cyan area, right panel, Fig. 3.1). In contrast, dust emissions dominate the IR wavelengths (yellow area, right panel, Fig. 3.1), while the optical and mid-infrared regions primarily reflect contributions from the ionized nebula (magenta area, right panel, Fig. 3.1).

The emission peak from the central star shifts toward bluer wavelengths compared to the preceding post-AGB phase, reflecting the excursion in the H–R diagram discussed in Sec. 1.3.2, which results from the increasing effective temperature. In contrast, the dusty layer exhibits lower temperatures due to its greater distance from the central star, influenced by radiation pressure, leading to a shift in the IR emissions toward redder wavelengths. Between the CS and dust emission, the nebular component contributes primarily in the mid-IR/optical regions and displays a characteristic step-like profile, as anticipated in Sec. 3.2, resulting from various processes (Brown & Mathews, 1970): (1) recombination of electrons onto H^+ ions, (2) bremsstrahlung (free-free transitions) of electrons in the Coulomb fields of hydrogen and helium ions, (3) recombination of electrons onto

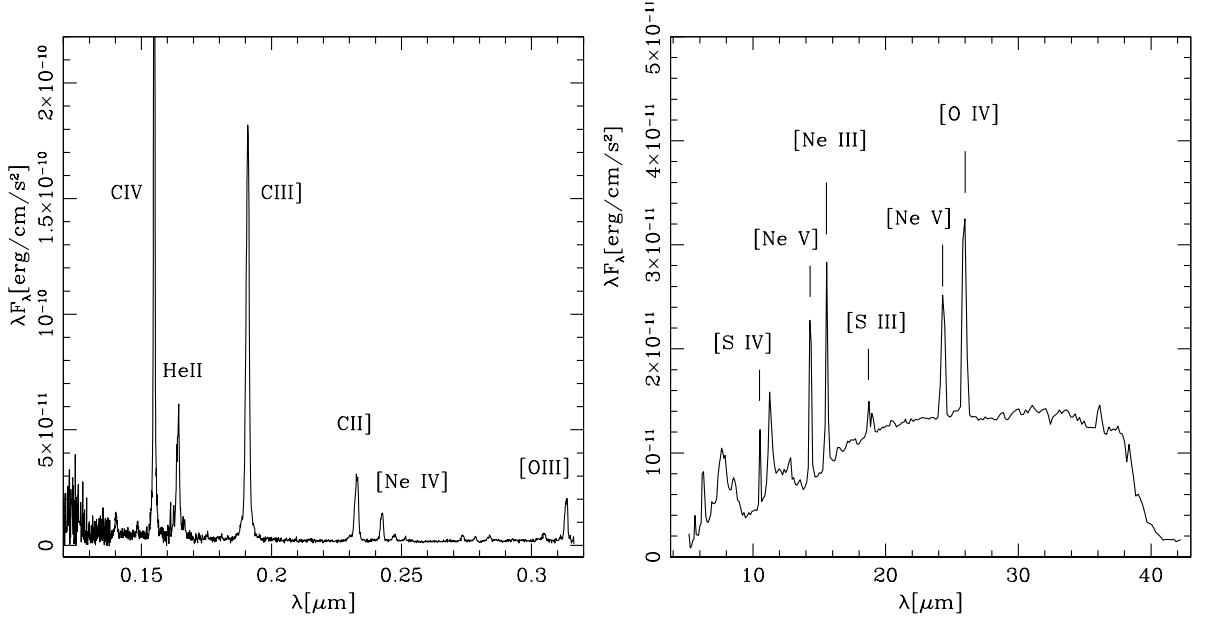


Figure 3.4: Example of a SED of a PN, in which are marked the most prominent emission lines. Both spectra correspond to SMP LMC 71 and will be discussed in detail in Chapter 6. The left panel presents the HST/STIS UV spectrum from Stanghellini et al. (2005), while the right panel shows the Spitzer/IRS spectrum from Stanghellini et al. (2007).

excited states of helium ions, and (4) two-quantum emission produced by hydrogen atoms.

The high effective temperature of the central star results in an SED characterized by numerous narrow emission lines, each providing significant information about the nebular structure. The intensity of these lines is primarily determined by the ionization parameter of the nebula, which increases with the luminosity of the CS but is inversely related to the hydrogen density and the distance from the source, corresponding to the size of the nebula (Osterbrock & Ferland, 2006). As will be discussed in Chapter 6, two of the most relevant lines for the present study are He II, detectable only in environments where the effective temperature exceeds 80000 K, providing important constraints on the CS’s effective temperature (Villaver et al., 2003), and [O III], which constrains the size of the nebula (Osterbrock & Ferland, 2006). A comprehensive list of key observable emission lines in PNe is provided in Fig. 3.4, with further details in Sec. 3.2.1.

These emission lines enable the determination of chemical abundances within PNe (Kwitter & Henry, 2022). In addition to these narrow lines, the spectra also feature broader signatures attributed to dust. Similar to post-AGB sources, PNe

exhibit clear signs of dust produced during the AGB phase, along with larger molecules such as C_{60} and C_{70} , HACs, and PAHs. Furthermore, PNe display features currently under investigation by the scientific community, such as broad peaks around 8, 12, and $17 \mu\text{m}$ (Kwok, 2022).

3.2.1 PNe modeling with CLOUDY

To take into account the extended morphology of the PNe and the photoionization of the gas, we used the code CLOUDY (v22.02, Ferland et al., 2017) to produce the synthetic spectrum to be compared with the observational data. The CLOUDY code works by dividing a cloud into a set of thin concentric shells referred to as zones that are selected to have thicknesses small enough to consider the physical conditions across them constant.

We specified the physical conditions of the central source, nebula, and dust in the input of the photoionization code (see Tab. 3.1).

- For the CS, we used two sets of models of stellar atmosphere. The most used is Rauch (2003), which is a grid of non-LTE, line-blanketed, plane-parallel, hydrostatic models that cover a range of effective temperatures from 50000 to 1000000 K and gravity factors from 5 to 9. For the few sources outside that grid, we used the non-LTE, line-blanketed, and wind-blanketed model of Pauldrach et al. (2001). In this case, the grid ranges from effective temperatures of 25000 to 50000 K, gravity factors from 3 to 4, and considers two stellar metallicities: $Z = 1 \times Z_{\odot}$ and $0.5 \times Z_{\odot}$. For the gas chemical composition, we applied the Aller & Czyzak (1983) and Khromov (1989) schematization.
- We modeled the nebula with a spherical shape and with a constant hydrogen density N_{H} , chosen to reproduce the observed electron density N_{e} (the higher N_{H} , the higher N_{e}). We parameterized the PNe to achieve an electron temperature T_{e} consistent with the observational constraints. We also imposed an inner radius of the nebula, R_{in} , consistent with the observed photometric radii, R_{phot} , of the nebulae. In particular, according to the ionization schematization given in Osterbrock & Ferland (2006), we assume that R_{in} is 0.7 times R_{phot} , which is directly correlated to the observed radii of [OIII].
- Regarding the dust modeling, we selected different dust species, choosing the ones most appropriate to reproduce the dust features visible in the IR spectra. For the different dust species, we used the CLOUDY built-in optical constants, namely the real and imaginary parts of the complex refractive index, $n + ik$, from Rouleau & Martin (1991) for amorphous carbon, Laor

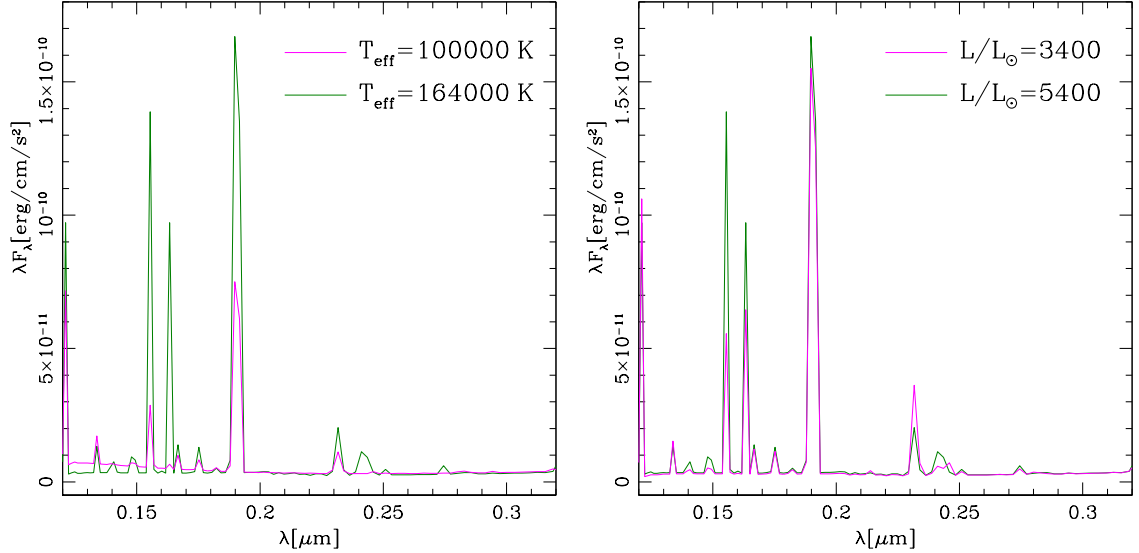


Figure 3.5: Exploration of the effect of the variation of the effective temperature (left panel) and luminosity (right panel) on the synthetic SED obtained by using the transfer radiative code CLOUDY.

& Draine (1993) for SiC, Ferland et al. (2017) for PAHs, and Martin & Rouleau (1991) for graphite and amorphous silicates. The grain size distribution used to model the carbon-rich dust (CRD) and the oxygen-rich dust (ORD) PNe is the interstellar medium one described in Mathis et al. (1977), which ranges from 0.005 to 0.25 μm . The only exception is PAHs, for which the scheme of Abel et al. (2008) and the 15C atoms described in CLOUDY, ranging from 0.0004 to 0.0011 μm , are applied.

Similarly, with the methodology described for the post-AGB sources, from the SED analysis of the SED, it is possible to derive critical information on the structure of the nebula, CS, and dust component:

- From the intensity of the emission lines in the UV region of the spectrum, we can determine the characteristics of the central star, i.e., the luminosity and the effective temperature (see Fig. 3.5).
- The thickness of the nebula ΔR can be primarily inferred from the mid-IR cascade (see lower right panel, Fig. 3.6), which is directly linked to the nebular gaseous mass, M_{gas} (the higher ΔR , the higher M_{gas}).

- From the comparison of the observational data in the IR wavelength with the synthetic spectrum, we can determine (1) the dust mineralogy (top panel of Fig. 3.6, left panel for carbonaceous dust, right panel for amorphous silicates), (2) the dust-to-gas ratio, δ (a proxy for the amount of dust present in the PN, reported in the lower left panel of Fig. 3.6), and (3) the dust temperature, T_d , which is determined self-consistently using the photoionization model.

The photoionization models are computed to reproduce the entire spectrum from the UV to the IR, constraining the contribution from all three main components of the PN: CS, nebula, and dust. This goal is much more challenging than reproducing only part of the spectra, as done in the majority of the works published in the literature. Therefore, to achieve a satisfactory agreement between the model and the SED, a certain level of flexibility is needed to estimate uncertainties. Our approach was to systematically vary each parameter while keeping the others fixed until the synthetic photometry deviated by 20% from the observed values.

3.3 Reddening modeling

In the present work of the thesis, we produced synthetic SEDs that accurately reproduce the observed spectra of post-AGB stars and PNe. To achieve a correct description of the SED, it was necessary to account for the degree of reddening, $E(B-V)$.

For the stars of the MCs we have used the value of $\log A_\lambda/A_v = 0.45$ reported in (Gordon et al., 2003). Moreover, for the post-AGB sources we selected $E(B-V)$ values to be consistent with Kamath et al. (2015, 2022).

As an opposite procedure to the reddening of the flux described above, it is possible to de-redden the observed spectra. We preferred to apply this methodology for the PNe, following the treatment of Stanghellini et al. (2005). This choice allowed us to reduce the number of free parameters to consider while remaining consistent with previous findings. Taking into account the Galactic foreground and the MCs extinction, and assuming negligible internal extinction within the nebulae, the de-reddened flux I_λ can be defined as:

$$I_\lambda = I_\beta \frac{F_\lambda}{F_\beta} 10^{cf_\lambda} \quad (3.1)$$

Where F_λ is the observed flux, f_λ is the reddening function at wavelength λ and c the target-dependent logarithmic extinction at H_β , which includes an LMC component and a foreground Galactic:

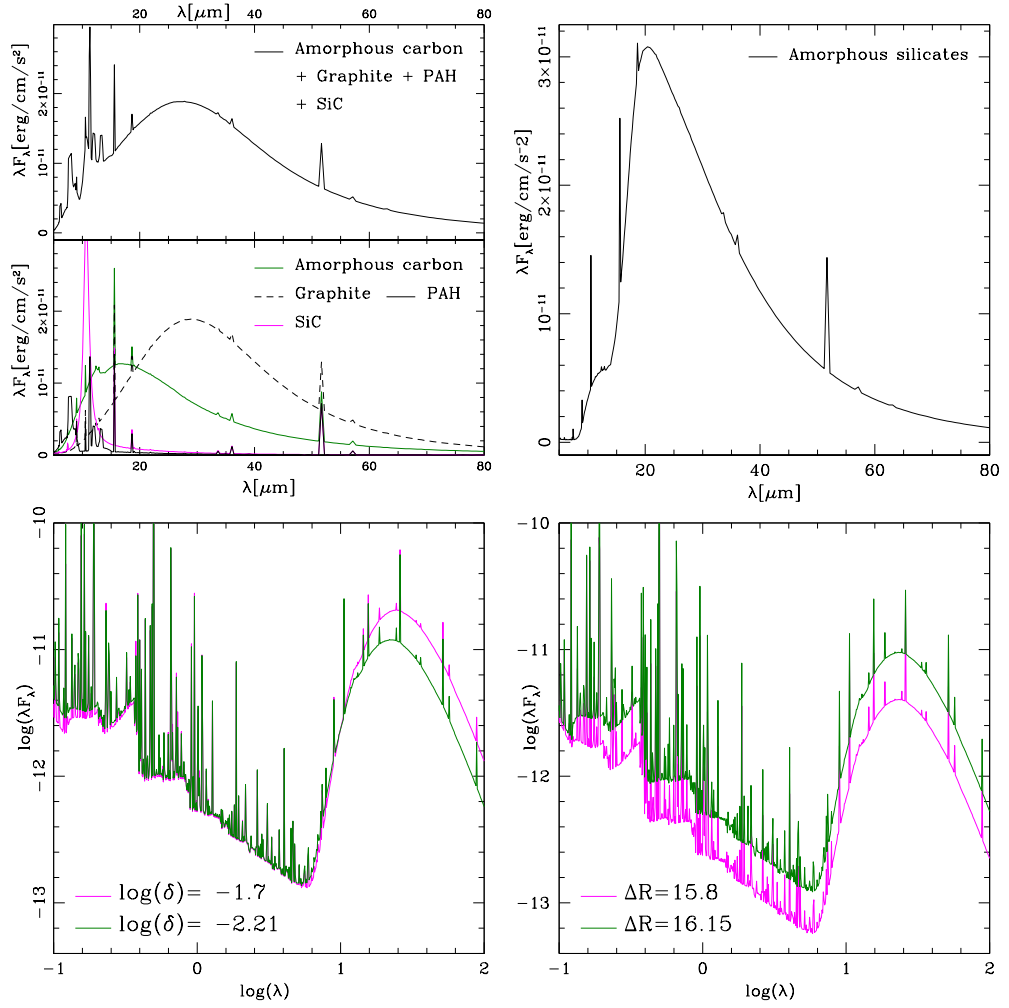


Figure 3.6: Synthetic spectra obtained using the transfer radiative code *Cloudy*. λ is expressed in micron, λF_{λ} in erg/s/cm^2 . The panels represents the effect on the synthetic spectrum of the dust mineralogy (top panels, on the left the carbonaceous species, on the right the oxygen-rich dust), different dust-to-gas ratio (lower left), thickness of the nebula (lower right). In the top left panel is divided as follow: the top plot show the SED obtained assuming the presence of amorphous carbon, graphite, SiC and PAH; the lower display the individual contribution of each component.

$$cf_{\lambda} = c_G f_{\lambda,G} + c_{LMC} f_{\lambda,LMC} \quad (3.2)$$

Where $f_{\lambda,G}$ and $f_{\lambda,LMC}$ are the Galactic and LMC extinction law, c_G is the reddening constant for the Galactic foreground in the direction of the LMC, c_{LMC} is the reddening constant for the LMC.

We note that all UV spectra and photometry of the PNe analysed in the present thesis are corrected for Galactic foreground and LMC extinction following the relationship 3.1 and 3.2, in agreement with Stanghellini et al. (2005).

Chapter 4

Post-AGB stars in the MCs

In the initial Chapters of this thesis, we highlighted the crucial role of the late AGB phase in contributing to the dust budget of LIMS. We also discussed how signatures of AGB nucleosynthesis and dust production remain evident in the SEDs of more evolved stars.

This Chapter presents our analysis of a broad sample of post-AGB stars in the MCs, studied to characterize each source and reconstruct their evolution and dust production during the AGB phase. The potential of post-AGB stars as tracers of earlier phases has been demonstrated through sources identified in the MCs by Kamath et al. (2014, 2015, hereafter K14 and K15). The known distances and low extinction in these galaxies provide an ideal setting for this approach, which is further supported by an extensive dataset of optically visible post-AGB stars in the MCs. Single post-AGB stars were selected based on radial velocity analysis and their shell-type SED*.

We used observational data to characterize each post-AGB source, comparing results with SED modeling performed via the radiative transfer code DUSTY (Sec. 3.1.1), which yielded key parameters such as luminosity, dust composition, optical depth, and dust temperature at the inner boundary. These characterizations were linked to theoretical models to derive information on progenitor mass and age, with new evolutionary tracks calculated and extended beyond the post-AGB phase using the ATON stellar evolution code (see Sec. 1.4).

This Chapter also introduces new methodologies developed in this thesis. By combining individual object characterizations with extended evolutionary tracks into the PNe phase, we investigate (1) the timing of the AGB-to-post-AGB transition, (2) the outflow dynamics from the dust formation epoch to the present, and (3) the mass-loss rates near the end of the AGB and during the central star's

*As discussed in Sec. 3.1, the SEDs of post-AGB stars can also exhibit a “disk-type” profile, which is typically associated with binary evolution (Kamath et al., 2014, 2015, 2023). For this reason, we have excluded such stars from our analysis.

contraction into the post-AGB phase.

In the following Sections, we present the results of this new methodology applied to post-AGB stars in the MCs, with most findings published in Tosi et al. (2022).

4.1 Shaping the SEDs of Post-AGB stars in the Magellanic Clouds

We started our analysis by selecting nine sources from the LMC and four from the SMC that likely followed single-star evolutionary paths. This selection resulted in sources with shell-type SEDs, making them suitable for modeling using the radiative transfer code DUSTY (Sec. 3.1.1), through which we derived stellar and dust parameters. The complete sample of MCs sources and the classification into shell-type and disc-type was initially established by K14 and K15 based on a preliminary study of their SEDs. Building on this work, the SEDs used in this thesis were constructed using the following photometric data: U, V, B, R, and I bands obtained from either Massey’s U, B, V, R CCD survey of the MCs (Massey, 2002), the LMC stellar catalogue (Zaritsky et al., 2004), or the Guide Star Catalogue Version 2.3.2 (Lasker et al., 2008); IRAC (3.6, 4.5, 5.8, and $8\mu\text{m}$) and MIPS (24.0, 70.0, and $160.0\mu\text{m}$) bands from the SAGE-LMC survey; J, H, and K bands (1.24, 1.66, and $2.16\mu\text{m}$ Skrutskie et al., 2006); and WISE W1, W2, W3, and W4 bands (3.4, 4.6, 12, and $22\mu\text{m}$ Wright et al., 2010). Additionally, for one of the sources (J004441.03), the Spitzer IR spectrum (Volk et al., 2011) was also included in the analysis.

When available, our study also incorporates observed carbon and oxygen abundances from Van Aarle et al. (2013) and De Smedt et al. (2015), derived through an analysis of the sources’ spectral lines. As will be discussed in Sec. 4.2, these abundances are crucial for inferring a more reliable characterization of the progenitor mass of the sources.

To achieve that purpose, we computed a series of synthetic SEDs with DUSTY, as described in Sec. 3.1.1, to be compared with the observed ones in order to find the best agreement between the two. To select appropriate atmosphere models from the ATLAS9 library (Castelli & Kurucz, 2003) we used the metallicity and effective temperature taken from K14 and K15 (reported in col. 2 and 3 of Tab. 4.1), calculated from a combination of a low and high resolution optical spectra. The comparison of the synthetic spectrum (black line) with the observational data (black dots) and the observed spectrum (dotted line) is presented in Figs. 4.1 and 4.2. We note that the error bars of the photometric data of the post-AGB stars in the SMC and the LMC are equal to the size of the symbols. In the cases where

multi-epoch observations for the same band are available, we show all the results in a vertical sequence, in conjunction with the central wavelength of the corresponding filter. For one source (J003643.94) we considered the possibility of the presence of SiC, reporting with a dashed line the result of the exploration (see middle right panel of Fig. 4.1). As will be discussed in Sec. 4.2, these abundances are crucial for inferring a more reliable characterization of the progenitor mass of the sources.

From the comparison of observational data with the synthetic spectrum it was possible to characterize the individual sources, following the methodology described in Sec. 3.1.1. Taking advantage of the knowledge of the distance[†], we determined the luminosity of each post-AGB star in the sample considered to be compared with the evolutionary tracks and determine the progenitor mass of each object, as described in the following Section.

Studying the signatures of dust features in the IR part of the SED (see Sec. 3.1), we found that 8 sources are surrounded by carbon dust, 5 by a mixture of amorphous and crystalline silicates, with the latter component accounting for $\sim 50\%$ of the total dust. Indeed, the use of a pure amorphous dust in the SED analysis procedure does not allow to reproduce the shape of the SED, independently of the optical constants adopted. This choice is consistent with the detection of crystalline silicates in AGB sources with optically thick dust envelopes in the Galaxy (Sylvester et al., 1999). Furthermore, the emission bands associated with crystalline silicates in evolved stars within the LMC have been extensively studied by Jones et al. (2014). Their research revealed (gas) mass-loss rates as low as $\sim 10^{-6} M_{\odot}/\text{yr}$, which align closely with the mass-loss rates observed in low-luminosity, oxygen-rich stars at the TAGB (see Sec. 4.4.5 below).

The quantities derived from SED analysis, namely the luminosities and the dust properties (i.e. the mineralogy, the optical depth, the dust temperature, and the distance from the center of the star of the inner border of the dust layer) are reported in Tab. 4.1. The last column gives the estimated mass of the progenitors at the beginning of the AGB phase (see next Section).

[†]Recent studies have provided precise measurements of the distances to both the LMC and the SMC using a variety of methodologies (e.g., Inno et al., 2013; Laney et al., 2012). Notably, some of the most recent measurements were obtained through the analysis of eclipsing binary systems. Specifically, Pietrzyński et al. (2019) determined the distance to the LMC to be 49.59 kpc, while Graczyk et al. (2020) derived a distance of 62.44 kpc for the SMC. In this thesis, we adopted distances of 50 kpc for the LMC and 62 kpc for the SMC to perform the SED analysis.

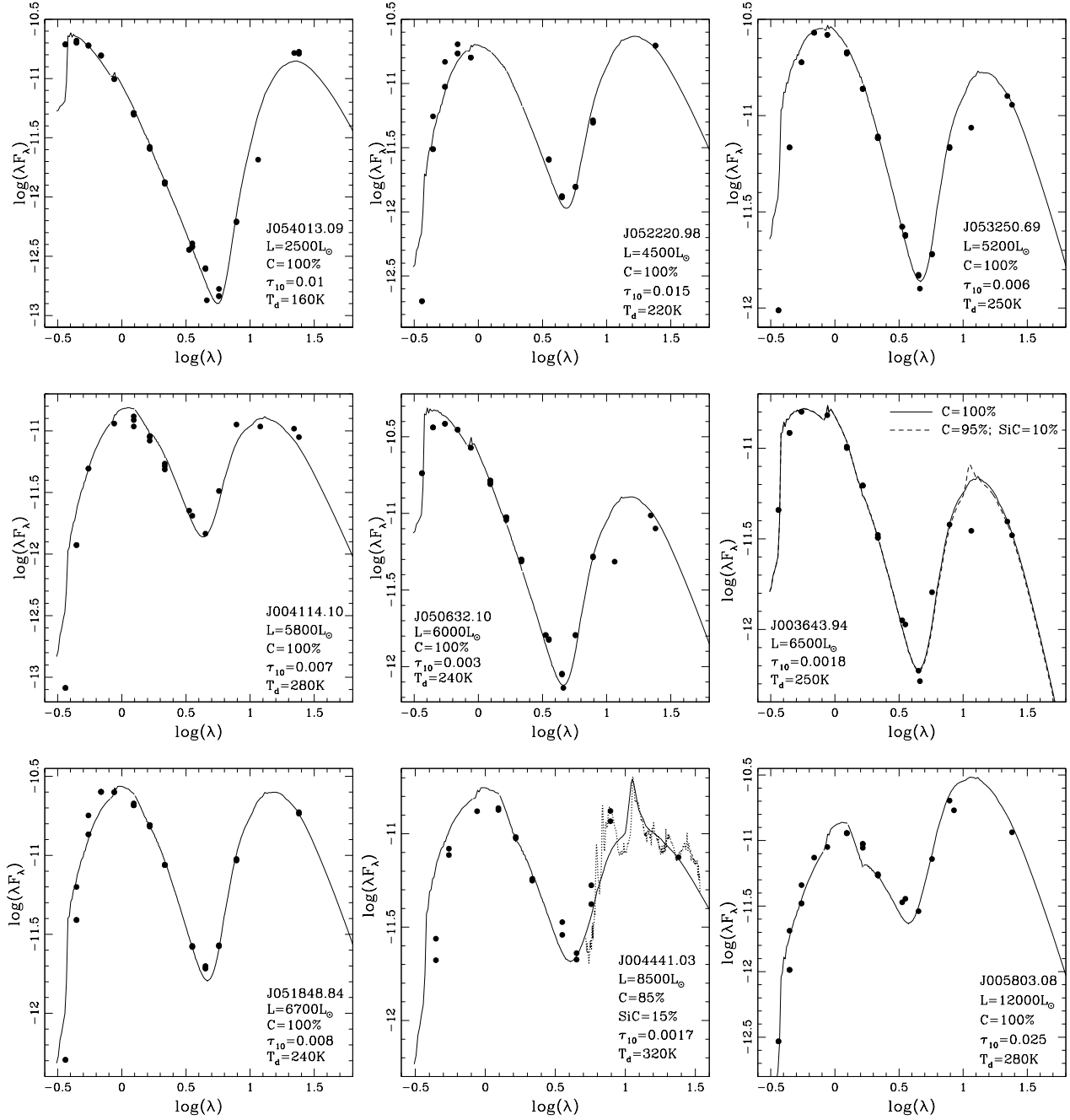


Figure 4.1: Optical and IR data (black dots) of SMC and LMC sources that we interpret as being surrounded by carbonaceous dust. The black lines show the synthetic SED obtained with the *DUSTY* code assuming amorphous carbon dust, while the dashed black line shows the combination of amorphous carbon and SiC. The dotted line in the middle panel of the bottom line shows the IR spectroscopy results from Volk et al. (2011).

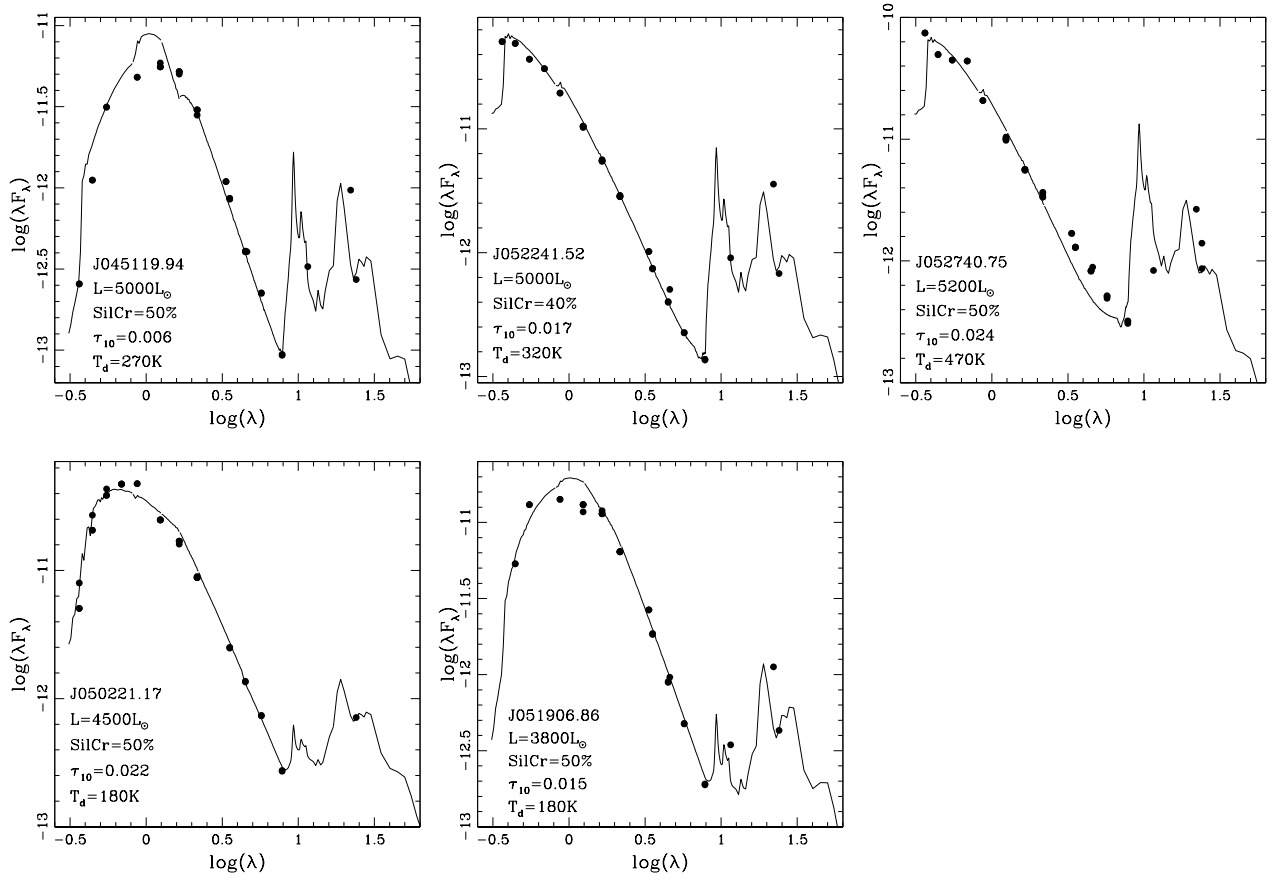


Figure 4.2: Optical and IR data (black dots) of SMC and LMC sources that we interpret as surrounded by silicate dust. The symbols used are the same as in Fig. 4.1. The fraction of silicate dust in the crystalline form is given in each panel.

Table 4.1: *Physical and dust properties of the LMC and SMC sources.*

ID	Sample	[Fe/H]	T _{eff} [K]	L/L _⊙	τ ₁₀	T _d [K]	R _{in} /R _⊙	M/M _⊙
Carbon-rich dust								
J052220.98-692001.5	LMC	-0.50	5750	4500	0.015	220	2.63 × 10 ⁵	0.9
J053250.69-713925.8	LMC	-1.10	6000	5200	0.006	250	2.06 × 10 ⁵	1.00
J004114.10-741130.1	SMC	-1.04	5750	5800	0.007	280	1.65 × 10 ⁵	1.00
J050632.10-714229.8	LMC	-0.40	7600	6000	0.003	240	2.74 × 10 ⁵	1.25
J003643.94-723722.1	SMC	-0.63	7500	6500	0.002	250	2.56 × 10 ⁵	1.50
J051848.84-700247.0	LMC	-1.00	6000	6700	0.008	240	2.62 × 10 ⁵	1.25
J004441.03-732136.0	SMC	-1.07	6000	8500	0.002	320	6.64 × 10 ⁴	2.00
J005803.08-732245.1	SMC	-1.03	6500	12000	0.025	280	1.20 × 10 ⁵	2.50
Oxygen-rich dust								
J045119.94-670604.8	LMC	-0.40	8250	5000	0.006	270	2.97 × 10 ⁴	0.80
J052241.52-675750.2	LMC	-0.50	8250	5000	0.017	400	2.26 × 10 ⁴	0.80
J052740.75-702842.0	LMC	-0.50	8250	5200	0.024	470	1.22 × 10 ⁴	0.90
J050221.17-691317.2	LMC	-0.60	5250	4500	0.022	180	5.45 × 10 ⁴	0.80
J051906.86-694153.9	LMC	-1.30	5500	3800	0.015	180	5.13 × 10 ⁴	0.65

Notes: *The quantities listed in the various columns are the following: 1: Source ID; 2: Galaxy of the sample; 3, 4: Metallicity and effective temperature derived spectroscopically by K14 and K15; 5-8: Luminosity, optical depth at 10 μm, dust temperature, and distance separating the central star from the inner border of the dusty region, found via SED analysis; 9: Mass of the progenitor at the beginning of the AGB phase, deduced via comparison of the derived luminosity with results from post-AGB evolution modeling. In the text we abbreviate the source ID to the first part of the name (e.g. J052220.98-692001.5 → J052220.98).*

4.2 The progenitors of the post-AGB stars sample

After the SED characterization, we considered the position of the stars on the HR diagram using the values of effective temperature and luminosity listed in Tab. 4.1. We then compared these positions with the evolutionary tracks of model stars of different masses, with metallicities consistent with those reported in Col. 2 of Tab. 4.1. This approach is suitable for post-AGB stars due to the unique morphology of their tracks, which run almost horizontally on the HR plane. The constant luminosity allows each star to be easily linked to the evolution of a specific stellar mass, once the metallicity is known, as it is in our case. The result of this comparison is shown in Fig. 4.3, where the different sources are represented with colored squares on the HR diagram (magenta for C-rich stars, green for the M-type sources), superimposed on the evolutionary tracks of $0.65 - 2.5 M_{\odot}$ stars (black lines)[‡]. Within the sample, we distinguish between metal-poor sources ($[\text{Fe}/\text{H}] \sim -1$), shown in the left panel of Fig. 4.3, which were compared with tracks of metallicity $Z = 2 \times 10^{-3}$; and higher-metallicity counterparts, which were compared with evolutionary sequences of metallicity $Z = 4 \times 10^{-3}$.

In the following paragraphs, we interpret the post-AGB stars in our sample, discussing carbon stars and oxygen-rich objects separately and grouping them according to their estimated age and metallicity. Where available, surface chemical abundances measured from high-resolution spectroscopy are compared with expectations from stellar evolution modeling, thus providing an additional test of our proposed interpretation. We note that in the following paragraphs, we will use an abbreviation for the source IDs by truncating them after the second digit following the decimal, in accordance with the notes provided in Table 4.1. Additionally, we will refer to sources with $[\text{Fe}/\text{H}] \sim -1$ as “metal-poor” and those with $[\text{Fe}/\text{H}] \sim -0.5$ as “sub-solar”.

4.2.1 Carbon stars

J053250.69 and J004114.10: low-mass, metal-poor carbon stars

J053250.69 and J004114.10 are the lowest-luminosity stars among the metal-poor objects surrounded by carbon dust. Based on their positions on the HR diagram, shown in the left panel of Fig. 4.3, we deduce that they descend from stars with masses around $1 M_{\odot}$.

For J053250.69, the presence of carbon dust is consistent with results from Van Aarle et al. (2013), indicating surface enrichment in carbon. The surface C/O

[‡]The masses considered here refer to the beginning of the AGB phase and do not account for possible mass-loss during the RGB ascent.

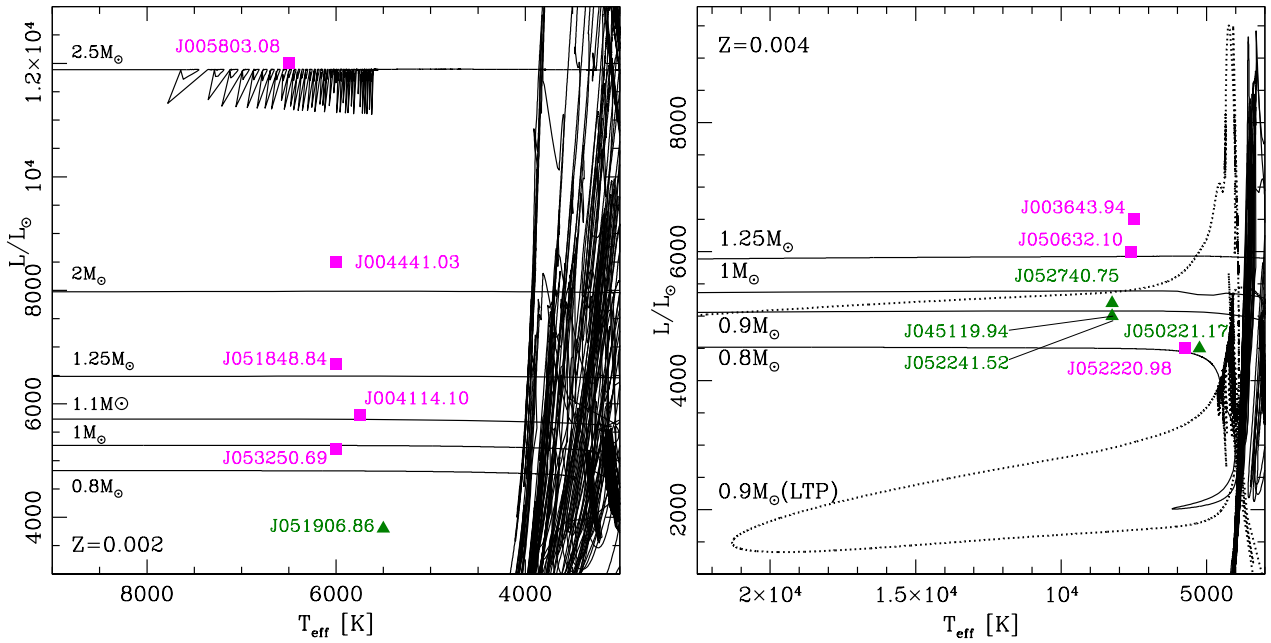


Figure 4.3: Post-AGB evolutionary tracks of model stars of metallicity $Z = 2 \times 10^{-3}$ (left panel) and $Z = 4 \times 10^{-3}$ (right). The dotted line in the right panel refers to a $0.9 M_{\odot}$ model star that experienced a late TP, shortly after the beginning of the contraction towards the post-AGB phase. The symbols indicate the observationally derived positions of the sources considered in this study, according to the effective temperatures given in K14 and K15, and the luminosities derived from the SED analysis (see Sec. 3.1.1 for the methodology). The squares and triangles refer to the sources surrounded by carbonaceous dust and silicates, respectively.

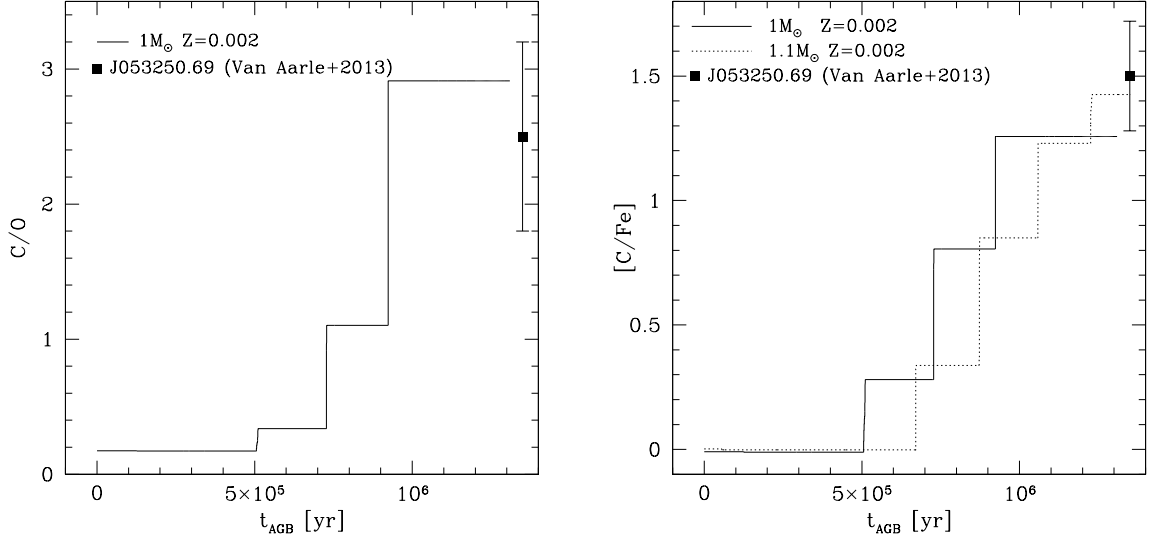


Figure 4.4: The comparison between the surface chemistry of J053250.69 and the time variation of chemical composition of low-mass model stars. The left panel displays the time evolution of the surface C/O ratio of a $1 M_{\odot}$, metal-poor model star during the AGB phase up to the post-AGB evolution. The black square and its error bar indicate the value measured by Van Aarle et al. (2013). The right panel shows the time evolution of the surface carbon of two model stars with masses $1 M_{\odot}$ (solid line) and $1.1 M_{\odot}$ (dotted line), compared to the results of Van Aarle et al. (2013).

ratio and $[C/Fe]^{\S}$ agree with results from stellar evolution modeling, as illustrated in Fig. 4.4, where the values reported in Van Aarle et al. (2013) are compared with the AGB-phase evolution of the C/O ratio and surface carbon content of a $1 M_{\odot}$ model star. The expected increase in surface $[O/Fe]$, approximately 0.1 dex, is 0.1 – 0.2 dex below the lower limit reported in Van Aarle et al. (2013).

Regarding J004114.10, spectroscopic data are currently unavailable. Based on its estimated luminosity, we predict that the progenitor star was approximately $0.1 M_{\odot}$ more massive than J053250.69. Consequently, we anticipate a higher degree of carbon enrichment, resulting in a final $[C/Fe]$ ratio of approximately 1.5 (see the right panel of Fig. 4.4).

Considering a mass-loss of $0.1 - 0.2 M_{\odot}$ during the RGB phase, we infer that both sources originated from metal-poor progenitors with masses in the range of

^{\S}The notation “[X/Fe]” represents the relative abundance of a chemical element X compared to iron, measured with respect to the same abundance ratio in the Sun: $[X/Fe] = \log\left(\frac{n_X}{n_{Fe}}\right)_{\star} - \log\left(\frac{n_X}{n_{Fe}}\right)_{\odot}$

1.2 – 1.3 M_{\odot} , formed approximately 3 Gyr ago.

J051848.84

For this source, we derive a luminosity $L \sim 6700 L_{\odot}$, consistent with the findings of De Smedt et al. (2015). This luminosity, as illustrated in the left panel of Fig. 4.3, corresponds to a star of approximately 1.25 M_{\odot} . The conclusion drawn in Sec. 4.1 that the star is surrounded by carbon dust aligns with the discussion in De Smedt et al. (2015), indicating enrichment in carbon with a [C/Fe] ratio of 1.2. The s-process enrichment reported by De Smedt et al. (2015) further suggests the occurrence of repeated TDU events.

The observed surface abundances of ^{12}C and ^{16}O agree with results from stellar evolution modeling, as shown in the top right panel of Fig. 4.5, where the findings of De Smedt et al. (2015) are compared with the evolutionary track of surface carbon and oxygen of a 1.25 M_{\odot} model star. Assuming a mass-loss of 0.1 M_{\odot} during the RGB phase, we infer that the progenitor of J051848.84 was initially a 1.3 – 1.4 M_{\odot} star, which formed approximately 2.5 Gyr ago.

J004441.03

This source has an estimated luminosity of 8500 L_{\odot} , making it one of the brightest objects in the sample under investigation. In the previous Section, we established that it is surrounded by carbon dust, a conclusion supported by findings from De Smedt et al. (2015), which highlight significant carbon and s-process enrichment. This interpretation is also consistent with its position on the HR diagram (see Fig. 4.3), suggesting a progenitor star of approximately 2 M_{\odot} . Notably, this is the first source discussed so far that did not undergo a helium flash; instead, core helium burning occurred under quiescent conditions of thermal stability.

Stars in the 2 – 3 M_{\odot} range are expected to undergo a series of TDU events, leading to substantial surface carbon enrichment. In agreement with this, studies by Dell’Agli et al. (2015a,b) indicate that sources in the LMC exhibit significant IR excesses that are consistent with the progeny of 2 – 3 M_{\odot} stars.

This interpretation is further supported by the findings of De Smedt et al. (2015), who report a high surface carbon mass fraction, [C/Fe] \sim 1.7. The results presented in the top right panel of Fig. 4.5 reinforce the robustness of our analysis, as the final surface abundances of both carbon and oxygen are fully consistent with those reported by De Smedt et al. (2015). The estimated age of J004441.03 is approximately 1 Gyr.

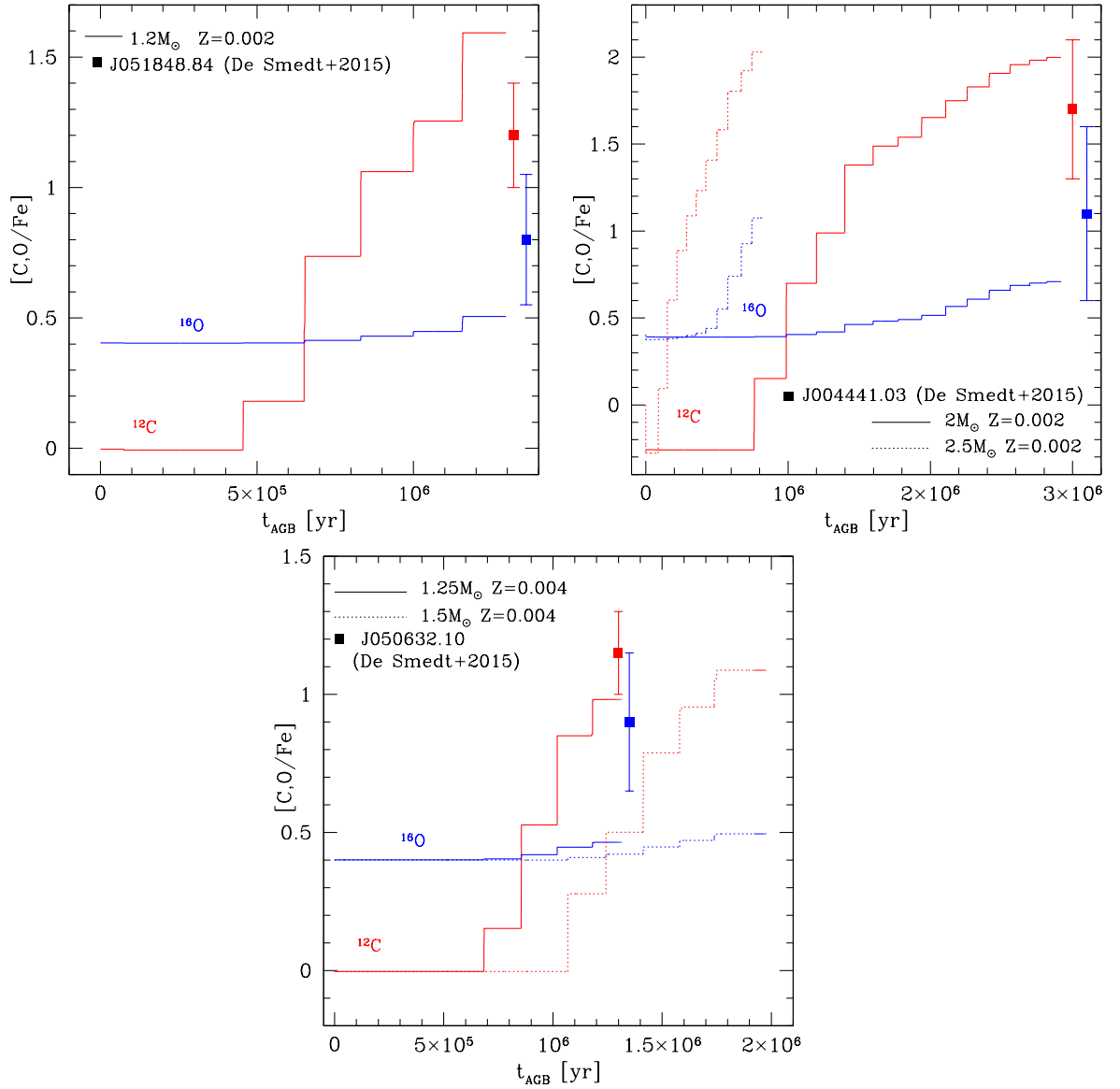


Figure 4.5: Time variation in the surface carbon (red line) and oxygen (blue) content during the AGB evolution of a $1.25 M_{\odot}$ (top left panel), $2 M_{\odot}$ and $2.5 M_{\odot}$ (top right panel) models star of metallicity $Z = 0.002$ and $1.25 M_{\odot}$ and $1.5 M_{\odot}$ of metallicity $Z = 0.004$ (lower left panel). The red and blue dots on the right side of the plane (with the corresponding error bars) indicate the results for J051848.84 (top left), J004441.03 (top right), and J050632.10 (bottom panel) from De Smedt et al. (2015).

J005803.08

This star is the brightest in the sample, with an estimated luminosity of approximately $12000 L_{\odot}$. Comparison with results from post-AGB evolution modeling in the left panel of Fig. 4.3 suggests that the progenitor of this source was a $2.5 M_{\odot}$ star. The expected evolution in surface chemistry for such a star, in terms of ^{12}C and ^{16}O mass fractions, is illustrated in the bottom panel of Fig. 4.5 with dotted lines.

Similar to the previously examined star, we anticipate that this source experienced multiple TDU events, resulting in a significant increase in surface carbon, achieving a final $[\text{C}/\text{Fe}]$ ratio exceeding 2. Additionally, the bottom panel of Fig. 4.5 indicates some enrichment in oxygen and an increase in s-process abundances.

J005803.08 has the highest mass among the sources analyzed here and formed most recently, with an estimated age slightly exceeding half a Gyr.

J050632.10 and J003643.94

From SED analysis (see Fig. 4.1), we find that both of these sources, with sub-solar chemical composition, are surrounded by carbon dust. This aligns with their estimated luminosities in the range of $6000 - 6500 L_{\odot}$, which, according to post-AGB modeling (see the right panel of Fig. 4.3), correspond to progenitors slightly above solar mass. Such stars are expected to undergo a sufficient number of TDU episodes to reach the carbon star stage.

In their study, Van Aarle et al. (2013) presented spectroscopic results for J050632.10, confirming carbon enrichment with $[\text{C}/\text{Fe}]$ slightly above unity. As illustrated in the bottom panel of Fig. 4.5, this is consistent with the expected carbon enrichment for $1.25 M_{\odot}$ stars of metallicity $Z = 0.004$, which is the derived mass of the progenitor of this source based on its luminosity. However, the anticipated oxygen enrichment is lower than indicated by Van Aarle et al. (2013), even under the assumption that the gas from which the star formed was significantly α -enhanced, with $[\alpha/\text{Fe}] = +0.4$.

J003643.94 is slightly brighter than J050632.10 (see right panel of Fig. 4.3), suggesting a higher mass progenitor of approximately $M \sim 1.5 M_{\odot}$. The results shown in the bottom panel of Fig. 4.5, which show the variation in surface ^{12}C and ^{16}O for the $1.25 M_{\odot}$ and $1.5 M_{\odot}$ cases, indicate that the final surface abundances of carbon and oxygen should be similar to those found for J050632.10.

According to our interpretation, J003643.94 formed approximately 2 Gyr ago, whereas J050632.10 is older, with an estimated age slightly above 3 Gyr.

J003643.94 is slightly brighter than J050632.10 (see right panel of Fig. 4.3), suggesting a higher mass progenitor of approximately $M \sim 1.5 M_{\odot}$. The results

shown in the bottom panel of Fig. 4.5, which show the variation in surface ^{12}C and ^{16}O for the $1.25 M_{\odot}$ and $1.5 M_{\odot}$ cases, indicate that the final surface abundances of carbon and oxygen should be similar to those found for J050632.10.

According to our interpretation, J003643.94 formed approximately 2 Gyr ago, whereas J050632.10 is older, with an estimated age slightly above 3 Gyr.

J052220.98: a (too) faint carbon star

The position of J052220.98 on the HR diagram, shown in the right panel of Fig. 4.3, suggests a progenitor mass of approximately $0.8 M_{\odot}$. However, this interpretation conflicts with our findings in Sec. 4.1, where we determined that this source is surrounded by carbon dust. Typically, carbon stars of similar metallicity to J052220.98 evolve to the post-AGB phase with luminosities exceeding $\sim 5000 L_{\odot}$, implying progenitors with masses $M > 0.9 M_{\odot}$.

One potential explanation for this seemingly anomalous behavior is that J052220.98 descended from a low-mass progenitor that experienced an exceptionally deep TDU event during its late evolutionary phases, resulting in significant carbon enrichment and transforming it into a carbon star. While this scenario remains plausible, we favor the hypothesis that this source underwent a late TP (see Sec. 1.3.1) shortly after beginning its contraction towards the post-AGB phase.

An illustrative example of such behavior is presented in the right panel of Fig. 4.3, where the gray dotted line corresponds to the evolution of a $0.9 M_{\odot}$ model star that underwent helium ignition immediately after the onset of overall contraction.

During this looping phase, the star's luminosity is lower than expected based on the classical core mass-luminosity relationship. Therefore, we propose that J052220.98 originated from a progenitor of $\sim 0.9 - 1 M_{\odot}$ that transitioned to the C-star stage during the AGB phase and is currently undergoing a looping phase similar to that shown in the figure, following a late TP event.

4.2.2 The oxygen-rich post-AGB stars in the MCs sample

Five of the sources examined here exhibit evidence of silicate dust in their surroundings, as indicated by the analysis presented in Sec. 4.1. These stars are marked with green triangles in Fig. 4.3. One possible explanation for these objects is that they originate from stars with masses $M > 3 M_{\odot}$ that underwent HBB during the AGB phase. HBB prevents surface carbon enrichment due to proton-capture activity at the base of the convective envelope, depleting surface ^{12}C (Sec. 1.2.3). However, this scenario can be ruled out in the current context, as such massive AGB stars are expected to enter the post-AGB phase with luminosities not below $16000 L_{\odot}$ (Sec. 1.2.3), significantly higher than those observed for the stars considered here, as depicted in Fig. 4.3.

An alternative explanation is that these sources are derived from low-mass stars that did not reach the carbon star stage. For a given metallicity, there exists a luminosity threshold that separates carbon stars from their lower-mass, and hence fainter, oxygen-rich counterparts (Sec. 1.2.4). At the onset of the AGB phase, these lower-mass stars consist of a degenerate core of approximately $\sim 0.5 M_{\odot}$ and a convective envelope of a few tenths of solar mass, which is lost via stellar winds before undergoing the necessary number of TDU events to become carbon stars. The luminosity threshold is sensitive to metallicity, with lower metallicity facilitating easier attainment of the C-star stage due to less oxygen in the star's envelope (Sec. 1.2.4). For example, at $Z = 0.002$, carbon stars should have $L > 4700 L_{\odot}$, while for $Z = 0.004$, the threshold luminosity is approximately $5200 L_{\odot}$.

The luminosities of the five sources exhibiting silicate dust in their surroundings fall within these aforementioned limits, as illustrated in Fig. 4.3. Specifically, J051906.86 and J050221.17 have luminosities significantly below the threshold values discussed above. Consequently, they are interpreted as originating from low-mass stars with initial masses at the onset of the AGB phase of $\sim 0.7 M_{\odot}$ (J051906.86) and $\sim 0.8 M_{\odot}$ (J050221.17), respectively. Assuming typical RGB mass-loss of $0.1 - 0.2 M_{\odot}$, these stars correspond to ages in the range of 8 – 10 Gyr, making them the oldest objects in the sample studied here.

Conversely, J052740.75, J045119.94, and J052241.52 are slightly brighter, with luminosities close to the threshold values discussed for the $Z = 0.004$ population. These luminosities correspond to progenitors of $\sim 0.85 M_{\odot}$ that formed between 6 and 8 Gyr ago. It is likely that they experienced some TDU events before losing their entire envelope, which may have resulted in surface carbon and s-process enrichment.

4.3 A new methodology for testing mass-loss rates and dust production histories in evolved stars

One of the aims of this study is to compare the mass-loss rates predicted by theoretical models and literature with the rates necessary to explain observations of evolved stars. In that regard, the characterization of individual sources presented in Sec. 4.2 allows us to determine the progenitor masses and, based on Fig. 4.6, the mass-loss rates during the TAGB (\dot{M}^{TAGB} , see Sec. 1.2.5). By scaling these rates with the effective temperature, we can estimate variations in mass-loss rates experienced by the stars during the contraction to the post-AGB phase.

Fig. 4.6 illustrates \dot{M}^{TAGB} as a function of the star's mass at the beginning of the AGB phase, calculated using stellar evolution models. \dot{M}^{TAGB} shows an

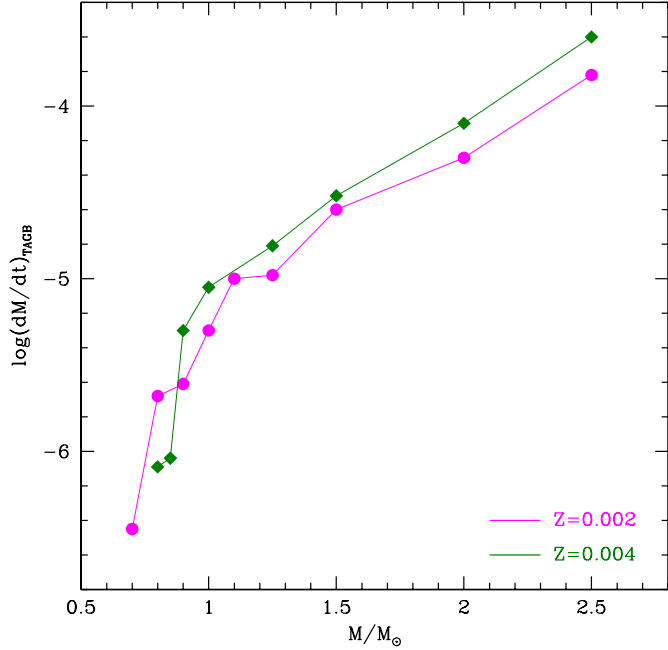


Figure 4.6: Mass-loss rate at the TAGB for stars of different mass, reported on the abscissa, and metallicity $Z = 0.002$ (magenta dots) and $Z = 0.004$ (green diamonds). The values shown in the diagram have been calculated using the ATON stellar evolution models.

increasing trend with stellar mass, due to the fact that higher-mass stars reach larger luminosities and radii (see Sec. 1.2), and also exhibits a steep rise at the threshold mass where the transition from M-type to C-type stars occurs. This rise is associated with an increase in surface molecular opacities due to the formation of C-rich molecules.

The comparison of the results reported in Fig. 4.6 with those described in Sec. 4.1 (in particular the derived values of τ_{10}) allows us to verify the agreement between \dot{M}^{TAGB} reported in Fig. 4.6 and the observational constraints, as well as to identify the evolutionary phase during which the dust responsible for the observed IR excess was released. For this purpose:

1. We focus on specific points along the evolutionary tracks (“onset” stage in Fig. 4.7) where the dust production mechanism may be active, leading to the formation of dust observed in the present day. Each of these points is characterized by an effective temperature ($T_{\text{eff}}^{\text{onset}}$) and an optical depth

(τ_{10}^{onset}), both of which can be derived from ATON (Sec. 1.4) under an assumed mass-loss prescription (Sec. 1.2.5). Consistent with previous studies (e.g., Van Hoof et al., 1997), we explore the possibility of ongoing dust production during the TAGB phase and following the onset of post-AGB contraction. However, as discussed in the next subsection, our observations of post-AGB sources indicate that dust formation ceases once effective temperatures exceed 4000 K. Therefore, we primarily consider scenarios in which dust formation ended either during the TAGB or in the early stages of post-AGB contraction, rather than during the current post-AGB phases.

2. Afterward, we calculate the optical depth characterizing the SED of the post-AGB phase (τ_{10}^{now}) for the stages where τ_{10}^{onset} was previously determined. According to Eq. 2.15, τ_{10}^{now} is primarily influenced by thermodynamic conditions, particularly density, at the distance $R_{\text{in}}^{\text{now}}$ from the star's center. Assuming an expanding shell of dust with a fixed width, where n_d scales as r^{-2} and both Q_{10} and a remain constant as the dust moves outward, τ_{10}^{now} scales as $1/R_{\text{in}}^{\text{now}}$. For the TAGB or different post-AGB phases, the assumption of solid carbon dust and silicates that form at a distance of approximately $10 R_{\star}$ (Dell'Agli, 2012)[¶] results in $\tau_{10}^{\text{onset}} \sim 1/(10 R_{\star})$. For dust currently surrounding the star at a distance $R_{\text{in}}^{\text{now}}$, $\tau_{10}^{\text{now}} \sim 1/R_{\text{in}}^{\text{now}}$. Therefore, the relation we seek is:

$$\tau_{10}^{\text{now}} \sim \tau_{10}^{\text{onset}} \times (R_{\text{in}}^{\text{onset}}/R_{\text{in}}^{\text{now}}) = \tau_{10}^{\text{onset}} \times (10 R_{\star}/R_{\text{in}}^{\text{now}}) \quad (4.1)$$

A basic schematization, not in scale, of the time evolution (Δt) from the AGB configuration of the star + dusty layer, to the nowadays observed structure (post-AGB phase) is reported in Fig. 4.7.

3. Comparing the optical depth values derived from Eq. 4.1 with those derived from the SED modeling reported in col. 5 of Tab. 4.1, allows us to test various hypotheses regarding the dust formation and mass-loss during the final AGB phases and the early post-AGB contraction, by analyzing the expansion velocities of the dust layer from its ejection to the present. These velocities are calculated based on the derived distance of the dusty region and the elapsed time, using AGB and post-AGB models. We assume that

[¶]The distance at which most of the carbon and silicate dust forms in this paper is assumed to be $10 R_{\star}$, consistent with the predictions of the ATON models. However, we acknowledge that a slightly lower value, around $\sim 5 R_{\star}$, remains plausible (Höfner & Olofsson, 2018). Such a change would result in a shift of approximately $\Delta \log(\tau_{10}) \sim 0.3$, without significantly affecting the conclusions discussed in the following Sections.

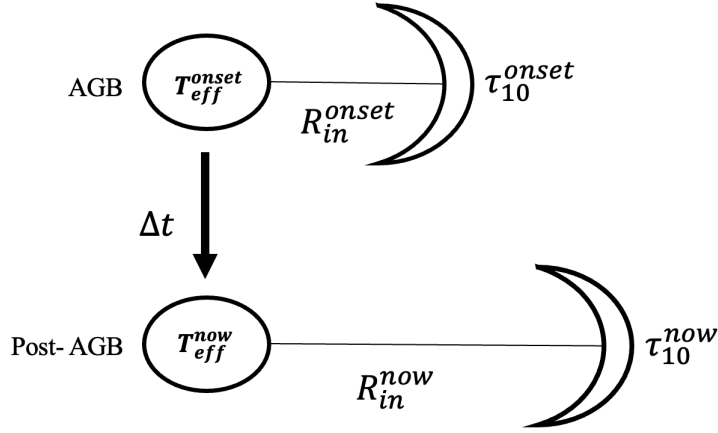


Figure 4.7: Time evolution of the stellar and dust characteristics from the AGB to the post-AGB phase. The post-AGB phase represents the configuration nowadays observed, in which the dusty layer achieved larger distances from the central star R_{in}^{now} and it is characterized by optical depth τ_{10}^{now} . The dust nowadays observed was released during the onset epoch, in which the dusty layer was characterized by a R_{in}^{onset} and τ_{10}^{onset} .

post-AGB wind velocities are comparable to AGB phase velocities, typically ranging from 10 to 30 km/s (He et al., 2014; Klochkova, Panchuk, & Tavalzhanskaya, 2015).

The approach described here will be used in the present thesis to derive the mass-loss rates that align with the observational constraints and the expected dynamical conditions. If our analysis provides no match between the AGB and the post-AGB configuration, we will model post-AGB evolution with varying mass-loss rates to determine when the dust responsible for the observed IR excess was released.

4.4 Bridging theoretical models and observations in AGB and Post-AGB star evolution

A summary of the results presented in Tab. 4.1 is shown in Fig. 4.8, which displays the τ_{10} of each source as a function of luminosity (left panel) and the distance of the inner edge of the dust layer from the center of the star (right panel). Various trends can be detected in the figure, correlating τ_{10} with stellar luminosity and dust mineralogy for stars of different metallicities.

For metal-poor carbon stars (represented by filled squares in the figure), we observe: a) a positive correlation between luminosity and optical depth (left panel),

with brighter stars exhibiting larger IR excesses; and b) an anti-correlation between luminosity and R_{in} , indicating that brighter stars have their dusty layers' inner borders closer to the surface. In contrast, the two highest-metallicity carbon stars, indicated by open squares in Fig. 4.8, exhibit significantly smaller optical depths compared to their lower-metallicity counterparts with similar luminosities.

Oxygen-rich stars behave differently from carbon stars. These stars have similar luminosities (see Fig. 4.8), with optical depths varying by a factor of roughly two around the average value $\tau_{10} = 0.02$. The right panel of Fig. 4.8 shows that the dusty zones for oxygen-rich stars are closer to the star compared to carbon stars.

To explain these trends and gain a more comprehensive understanding of dust production and propagation from the TAGB to what is currently observed in the post-AGB phase, we apply the methodology described in the previous Section to study a few objects in detail. The selected sources, J005803.08, J053250.69, and J050221.17, vary in luminosity and dust composition (see Sec. 4.2 for details). For each source, we examine whether the synthetic optical depth, τ_{10}^{onset} , calculated using the mass-loss prescription of Wachter et al. (2008) and assuming the dust observed during the post-AGB phase formed at the TAGB, aligns reasonably well with the optical depth τ_{10} derived from SED modeling. To assess this, we scale τ_{10}^{onset} using Eq. 4.1.

If agreement is not reached, we will first investigate whether assuming dust formation after the TAGB phase improves the alignment. If this adjustment is insufficient, we will also consider alternative mass-loss prescriptions. The results of this exploration are presented in various tables throughout the text (Tabs. 4.2 and 4.3). We begin with J005803.08, a bright carbon star that has undergone several TDU episodes, resulting in significant carbon enrichment in its surface layers (Sec. 4.4.1). Next, we examine J053250.69, which represents faint, low-mass carbon stars that reached the C-star stage during their final thermal pulses (Sec. 4.4.2). In Sec. 4.4.5, we discuss J050221.17, a low-mass, oxygen-rich star that did not become a carbon star due to insufficient TDU events, leaving it with a C/O ratio below 1. Following this, we provide a comprehensive analysis of two carbon stars with sub-solar chemical compositions (Sec. 4.4.3) and J052220.98, a low-luminosity carbon star (Sec. 4.4.4).

4.4.1 Bright post-AGBs with carbon dust

According to the discussion in Sec. 4.2.1, J005803.08 is the brightest source investigated in the MCs post-AGB sample, with a luminosity of approximately $12000 L_{\odot}$, indicating a progenitor mass of about $2.5 M_{\odot}$. This mass is close to the threshold required to initiate HBB, which destroys surface carbon and prevents the star from becoming a carbon star (Sec. 1.2.3). As the luminosity of the post-AGB

stars increases with initial mass (see Fig. 4.3), J005803.08 is among the brightest object in the sample with carbon-star chemistry.

The AGB evolution of massive carbon-rich stars has been studied in detail by Dell’Agli et al. (2015a) and more recently by Marini et al. (2021). These studies highlight the significant carbon accumulation in the surface regions and the intense dust production, particularly during the final AGB phases (see Sec. 1.2.4). Stellar evolution and dust-formation modeling suggest that at the TAGB, this class of stars experiences mass-loss rates slightly exceeding $10^{-4} M_{\odot}/\text{yr}$ and efficient dust production with rates on the order of a few $10^{-6} M_{\odot}/\text{yr}$. A thick dust shell composed mainly of solid carbon is expected to surround the star at the TAGB, with optical depths of $\tau_{10} \sim 5$ (Dell’Agli et al., 2021). At solar or sub-solar chemistries, SiC grains might significantly contribute to the overall extinction of radiation; however, this is not the case for J005803.08 due to its low metallicity.

The left panel of Fig. 4.9 illustrates the temporal evolution of the effective temperature for a $2.5 M_{\odot}$ model star with a metallicity similar to that of J005803.08, spanning from the late AGB phases through the contraction phase towards the post-AGB stage. The black line is derived using the mass-loss prescription from Wachter et al. (2008) along with the input physics outlined in Chapter 2, applied consistently across both the AGB and post-AGB phases. In this scenario, the elapsed time from the TAGB to the current evolutionary stage, marked by $T_{\text{eff}} = 6500 \text{ K}$ (value reported in col. 3, Tab. 6.3; dashed line in left panel Fig. 4.9), is approximately 5600 yr.

With the aim of connecting what is currently observed in the post-AGB phase with AGB modeling, in the right panel of Fig. 4.9, is reported the variation of the optical depth characterizing the dusty layer in the AGB phase (τ_{10}^{onset} , full line) and the post-AGB stage (τ_{10}^{now} , dotted line). The dashed orange line represents the optical depth derived for J005803.08 from the SED modeling reported in Tab. 4.1 ($\tau_{10} = 0.025$).

Starting from the AGB configuration (full line, right panel Fig. 4.9), we calculated the τ_{10}^{onset} at effective temperature intervals spaced equally by 500 K, ranging from the TAGB (3000 K) to five subsequent phases during the post-AGB period, reaching 5000 K (full symbols, right panel Fig. 4.9). τ_{10}^{onset} decreases as the star contracts (and the effective temperature increases) because the mass-loss rate diminishes, resulting in a less dense wind (see Eq. 2.12). Consequently, fewer gas molecules are available to condense into dust.

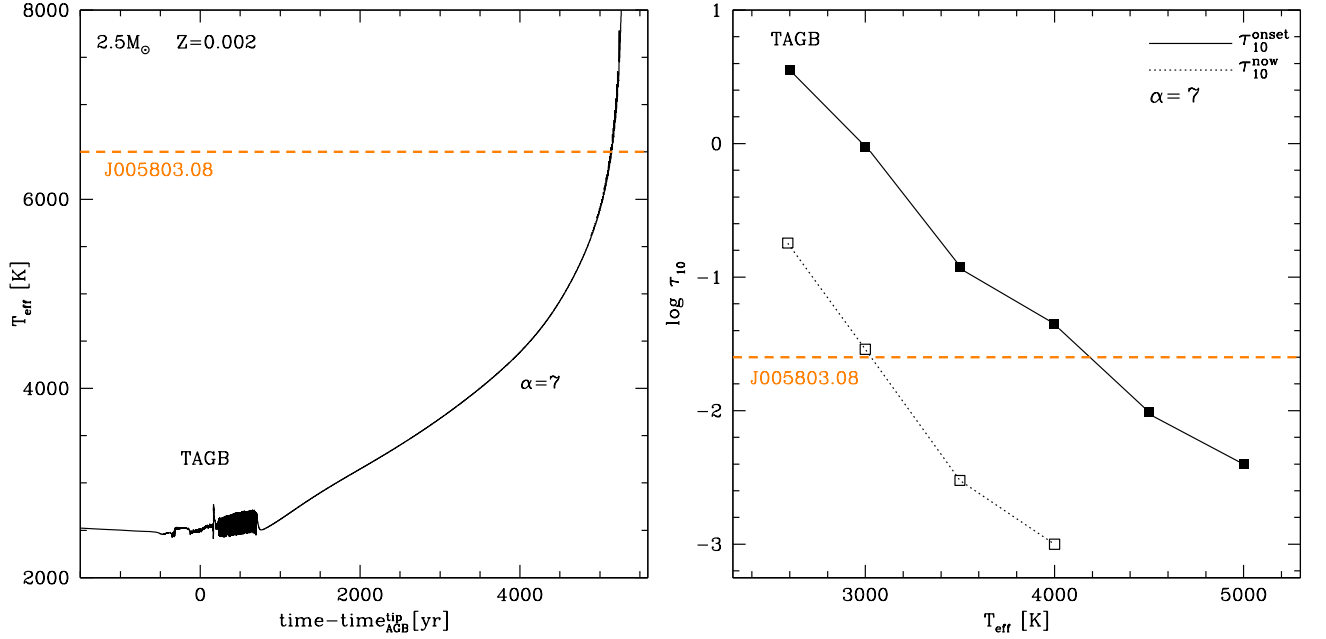


Figure 4.9:

Left panel: Time variation in the effective temperature of a $2.5 M_{\odot}$ model star, obtained assuming the mass-loss relation from Wachter et al. (2002, 2008) (Eq. 1.3). The times are counted from the beginning of the contraction of the AGB phase and are calculated up to the achievement of the value of the effective temperature of J005803.08 given in K14 and K15 (dashed orange line).

Right panel: Optical depth of a $2.5 M_{\odot}$ star model as a function of effective temperature. τ_{10}^{onset} (solid lines and filled circles) represents the optical depth of the dusty layer at the moment of its formation, calculated at different effective temperatures (full squares), starting from the TAGB (top left square) and through five subsequent phases, each characterized by an increased value of T_{eff} . τ_{10}^{now} (dotted lines and open symbols) represents the nowadays optical depth, which can be compared to the optical depth obtained for J005803.08 from the SED modeling (dashed orange line, $\tau_{10} = 0.025$, as reported in Tab. 4.1). τ_{10}^{now} is derived by scaling each value of τ_{10}^{onset} using Eq. 4.1, assuming a distance of the dusty layer as determined from the SED analysis ($R_{\text{in}} = 1.2 \times 10^5 R_{\odot}$).

Table 4.2: Time evolution of the dusty layer from the moment in which the dust was formed (onset, AGB phase) to the beginning of the contraction to the post-AGB phase (now) for a massive carbon star.

α	$\Delta t[\text{yr}]$	τ_{10}^{onset}	τ_{10}^{now}	$v[\text{km/s}]$
$T_{\text{eff}}^{\text{onset}} = 2600\text{K}, R_{\star}/R_{\odot} = 605$				
7 ^(A)	5600	3.6	0.18	0.5
$T_{\text{eff}}^{\text{onset}} = 3000\text{K}, R_{\star}/R_{\odot} = 400$				
7 ^(B)	3600	0.95	0.03	0.7
4	1500	1.26	0.04	1.8
3	1020	1.61	0.05	2.6
2	740	2.02	0.07	3.6
$T_{\text{eff}}^{\text{onset}} = 3500\text{K}, R_{\star}/R_{\odot} = 300$				
4	800	0.44	0.01	3.3
3 ^(C)	500	0.86	0.021	5.3
2 ^(C)	330	1.39	0.035	8.0
$T_{\text{eff}}^{\text{onset}} = 4000\text{K}, R_{\star}/R_{\odot} = 230$				
2 ^(C)	120	0.96	0.018	22

Notes: 1 – alpha parameter given in Eq. 4.2; 2 – time elapsed from the onset to the now stage; 3, 4 – Optical depth onset and obtained from Eq. 4.1, the latter to be compared with the optical depth of J005803.08, which is $\tau_{10} = 0.025$; 5 – wind velocity calculated as $R_{\text{in}}/\Delta t$.

^{A,B,C} refers to Case A, B and C discussed in the text (Sec. 4.4.1).

To calculate the time evolution from the AGB phase to the post-AGB (see also Fig. 4.7), we employed the methodology outlined in the previous Section to compute the corresponding τ_{10}^{now} for each considered phase.

Case A. Using Eq. 4.1 we calculated the τ_{10}^{now} (dotted line, right panel of Fig. 4.9) which we then compared to the τ_{10} derived from SED modeling of J005803.08 (col. 5, Tab. 4.1, i.e., $\tau_{10} = 0.025$, reported with a dashed line in the right panel of Fig. 4.9). This calculation assumes that the dust currently observed in the post-AGB phase was released at the TAGB phase, that the mass-loss prescription from Wachter et al. (2008) (Eq. 1.3) is applied, and that the inner boundary distance of the dust zone for J005803.08 (col. 7, Tab. 4.1, i.e., $R_{\text{in}} = 1.2 \times 10^5 R_{\odot}$).

As a result of this comparison, we are inclined to dismiss the possibility that the observed dust surrounding J005803.08 was released during the star’s evolution at the AGB tip for the following reasons: a) the expected optical

depth is approximately seven times higher than that derived from SED analysis ($\tau_{10}^{now} = 0.18$, Tab. 4.2, compared with $\tau_{10} = 0.025$, Tab. 4.1); and 2) estimating the average expansion velocity of the dust based on R_{in} and the elapsed time since the TAGB to the current evolutionary stage yields $v \sim 0.5$ km/s (Case A, col.5, Tab. 4.2), which is significantly lower than observed velocities (He et al., 2014; Klochkova, Panchuk, & Tavalzhanskaya, 2015).

Case B. Since assuming that the dust observed in the post-AGB phase was produced during the TAGB does not provide reasonable agreement between τ_{10}^{now} and the value derived from the SED analysis and does not align with the observational wind velocities, one possible solution is that the currently observed dust was released after the onset of contraction to the post-AGB phase, when the star’s effective temperature was approximately 3000 K. However, this possibility can also be dismissed because the elapsed time since this evolutionary phase is approximately 3600 yr, which, combined with the distance of the dusty layer, results in an average expansion velocity of below 1 km/s, still too slow (Case B, col.5, Tab. 4.2). Another reason to disregard this scenario is that if the winds and dust moved at a velocity of around 0.8 km/s, the dust produced at the AGB tip would now be located at a distance of approximately $2 R_{in}$, causing a noticeable bump in the star’s SED in the $25 - 30 \mu\text{m}$ range, which is not observed.

Since no satisfactory explanation could be derived for the observations of J005803.08, we explored alternative mass-loss rate laws. Starting with the mass-loss prescription from Wachter (Eq. 1.3, Wachter et al., 2008), we modified its slope beyond the TAGB phase by altering its dependency on effective temperature:

$$\dot{M} = \dot{M}^{\text{TAGB}} \times (T_{\text{eff}}/T_{\text{eff}}^{\text{TAGB}})^{-\alpha}, \alpha = 2, 3, 4. \quad (4.2)$$

We note that α is a parameter that defines how fast the mass-loss decreases after the contraction of the stars and in the standard Wachter et al. (2008) prescription equal to 7. In doing that we calculated new evolutionary simulations for the $2.5 M_{\odot}$ model star, starting from the AGB tip with \dot{M}^{TAGB} unchanged, and extending into the post-AGB phase with the modified \dot{M} . The results of these simulations are presented in the left panel of Fig. 4.10, illustrating the temporal evolution of effective temperature, and in the right panel of Fig. 4.10, where optical depths are color-coded to indicate different scenarios. In both figures, $\alpha = 4$ is reported with a red line, $\alpha = 3$ with a blue line, and $\alpha = 2$ with a green line.

These runs demonstrate that higher mass-loss rates lead to shorter evolutionary timescales, as the rate of contraction during the AGB to post-AGB transition is determined by the speed at which the remaining envelope is shed (Iben & Renzini,

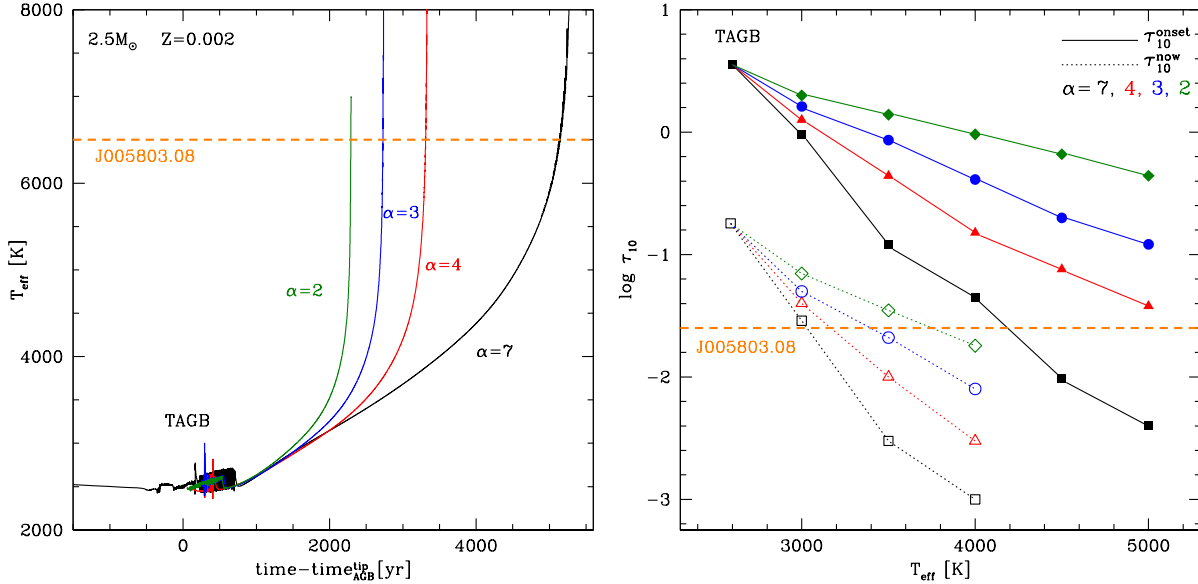


Figure 4.10: Same as 4.9. The black line shows the standard result obtained using the mass-loss formulation from Wachter et al. (2002, 2008). Colored tracks refer to results obtained using Eq. 4.2, by assuming that \dot{M} decreases as $T_{\text{eff}}^{-\alpha}$, with $\alpha = 2$ (green), 3 (blue), and 4 (red).

1983). The influence of mass-loss treatment on the timescales of the AGB to post-AGB transition has been studied extensively, with Van Hoof et al. (1997) showing that assuming a sustained high mass-loss rate after the contraction phase begins significantly accelerates the increase in effective temperatures for post-AGB stars.

Case C. Consistency between the predicted and observed IR excess (and therefore optical depth) is found in the scenarios where $\alpha = 2$ and $\alpha = 3$, assuming that the currently observed dust originated during the star’s contraction phase to an evolutionary stage characterized by effective temperatures ranging from 3500 to 4000 K. In these cases, the calculated average wind expansion velocities range from 5 to 20 km/s, aligning well with observational constraints (He et al., 2014; Klochkova, Panchuk, & Tavalzhanskaya, 2015). These velocities are sufficiently rapid that any dust ejected at the TAGB would have traveled distances of 5 to 20 R_{in} away from the central star by now, thereby not significantly affecting the SED in the $\lambda < 50 \mu\text{m}$ spectral region.

To summarize, the interpretation of the observations of J005803.08 suggests

that mass-loss rates slightly above $10^{-4} M_{\odot}/\text{yr}$ for bright carbon stars undergoing AGB evolution are consistent with the observed IR excess. This conclusion holds under the assumption that dust formation occurred when the effective temperatures reached approximately 3500 – 4000 K, and that the rate of mass-loss during the transition to the post-AGB phase scales as $T_{\text{eff}}^{-2,-3}$.

4.4.2 Low-mass carbon stars

J053250.69 is the faintest of the stars among our MCs sample, which we interpret as being surrounded by carbon dust (see Fig. 4.3), with the exception of J052220.98, which is discussed separately. In Sec. 4.2.1, we identified this object as originating from a low-mass progenitor with an initial AGB mass of approximately $1 M_{\odot}$, close to the minimum required to reach the C-star stage. As illustrated in Fig. 4.4, which depicts the time variation of surface C/O and [C/Fe] for a $1 M_{\odot}$ model star with similar metallicity to J053250.69, the C-star stage is attained during the final two thermal pulses. The mass-loss rate at the TAGB is estimated at $\dot{M}^{\text{TAGB}} \sim 10^{-5} M_{\odot}/\text{yr}$ (see Fig. 4.6). By studying this source, we explore the low-luminosity end of the carbon star population, providing a comprehensive view of the late-AGB and post-AGB evolution of carbon stars, alongside the analysis of J005803.08.

Table 4.3: Time evolution of the dusty layer from the moment in which the dust was formed (onset, AGB phase) to the beginning of the contraction to the post-AGB phase (now) for a low-mass carbon star.

α	$\Delta t[\text{yr}]$	τ_{10}^{onset}	τ_{10}^{now}	$v[\text{km/s}]$
$T_{\text{eff}}^{\text{onset}} = 3200\text{K}$				
7 ^(A)	15000	0.70	8.6×10^{-3}	0.3
$T_{\text{eff}}^{\text{onset}} = 4000\text{K}$				
7 ^(A)	5000	0.03	2.5×10^{-4}	1.0
2 ^(A)	1500	0.28	2.0×10^{-3}	3.0
$T_{\text{eff}}^{\text{onset}} = 4000\text{K}$ and $3 \times \dot{M}_{\text{tip}}$				
2 ^(B)	900	0.57	4.36×10^{-3}	10

Note: 1 – alpha parameter given in Eq. 4.2; 2- time elapsed from the onset to the now stage; 3, 4 – Optical depth onset and obtained from Eq. 4.1, the latter to be compared with the optical depth of J053250.69, which is $\tau_{10} = 0.006$; 5 – wind velocity calculated as $R_{\text{in}}/\Delta t$.

^{A,B} refers to Case A and B discussed in the text (Sec. 4.4.2).

Case A. Analogous to the analysis of J005803.08, we examined the TAGB and var-

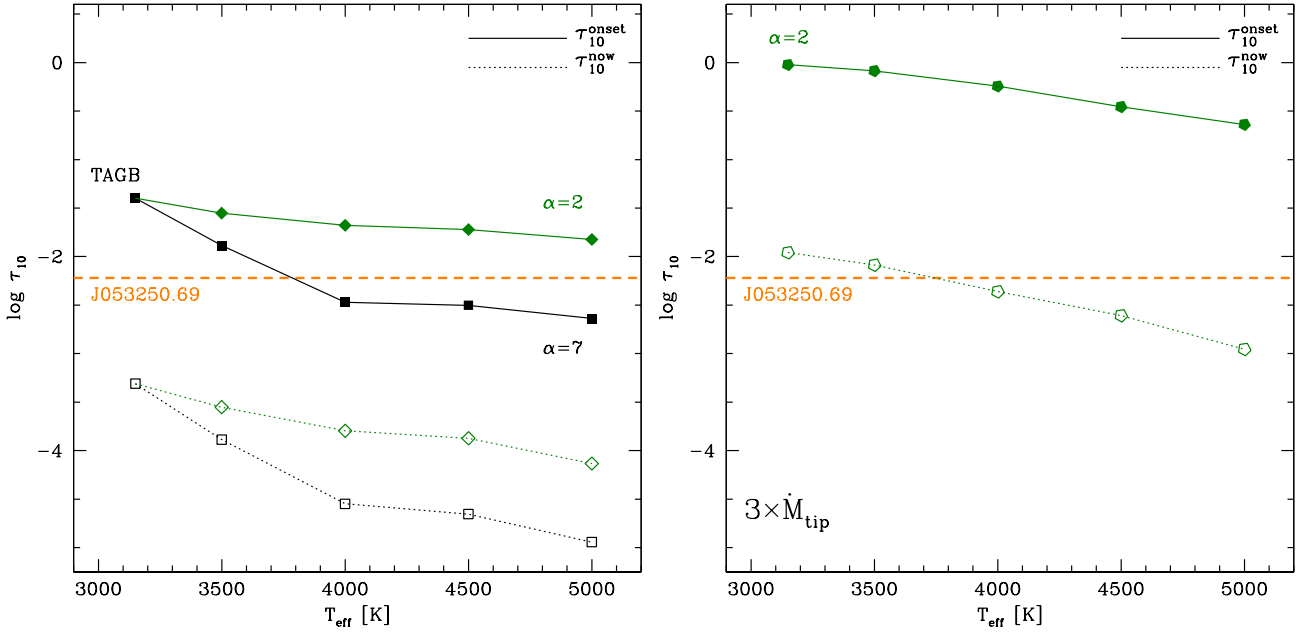


Figure 4.11: Optical depth variation as a function of the effective temperature. *Left panel:* τ_{10}^{onset} (solid lines and full dots) represent the optical depth that characterize a $1.0 M_{\odot}$ model star, when dust is freshly formed and still close to the star. This is computed at different stages of the AGB to post-AGB transition as represents by the squares, starting from the TAGB (top left square) and during the subsequent phases moving towards higher T_{eff} . Instead, τ_{10}^{now} (dotted lines and open symbols) is obtained using Eq. 4.1 adopting for each value of τ_{10}^{onset} , the distance of the dusty layer retrieved from the SED analysis ($R_{\text{in}} = 2.06 \times 10^5 R_{\odot}$). The dashed orange line represents the optical depth obtained for J053250.69 from the SED modeling ($\tau_{10} = 0.006$, reported in Tab. 4.1). *Right panel:* Same as the left panel, but assuming a mass-loss at the TAGB phase increased by a factor of three.

ious phases during the transition to the post-AGB for a $\sim 1 M_{\odot}$ model star. These phases were characterized by effective temperatures ranging from 3500 K to 5000 K, in 500 K increments. We employed the methods described earlier to calculate τ_{10}^{onset} for these stages. This analysis was applied to both the standard evolution of the $1 M_{\odot}$ model star used for J053250.69, utilizing the mass-loss prescription by Wachter et al. (2002, 2008), and to a scenario where the post-AGB mass-loss rate follows $\dot{M} = \dot{M}^{\text{TAGB}} \times (T_{\text{eff}}/T_{\text{eff}}^{\text{TAGB}})^{-2}$.

The results of this analysis are presented in Tab. 4.3 (Case A) and in the right panel of Fig. 4.11, which shows the optical depth values during the star's evolution from the TAGB to the post-AGB phase. Full symbols represent the optical depth at each evolutionary stage, while open symbols indicate the corresponding current optical depth, assuming the dust was released during those phases. Black squares and green diamonds denote results from standard evolution modeling and the $\dot{M} \sim T_{\text{eff}}^{-2}$ law, respectively.

Figure 4.11 reveals that the optical depths obtained are significantly smaller than those derived for J053250.69, with differences exceeding a factor of ten, regardless of the mass-loss treatment used for the post-AGB phase contraction. Another issue concerns the estimated velocities at which the dusty layer has moved away from the star since its release. According to the standard transition from the TAGB to the post-AGB phase, the time elapsed since the TAGB to the current phase is approximately 15000 yr. Combined with the dusty region's distance derived in Sec. 4.1, namely $2 \times 10^5 R_{\odot}$, this corresponds to an average expansion velocity of less than 1 km/s. Even if we assume dust release during a later phase, such as at 4000 K (though this is inconsistent with the estimated optical depth), the average expansion velocity would still not exceed 1 km/s.

The preliminary conclusion from this analysis is that the mass-loss rate at the TAGB for low-mass carbon stars is likely underestimated. A higher \dot{M}^{TAGB} is needed to achieve greater optical depths, compatible with the observed IR excess, and to shorten contraction timescales, ensuring the derived velocities align with observational evidence (He et al., 2014; Klochkova, Panchuk, & Tavalzhanskaya, 2015).

Based on these considerations, we computed additional evolutionary sequences starting from the TAGB, progressing through the contraction to the post-AGB phase, and reaching the effective temperature of J053250.69. In these calculations, \dot{M}^{TAGB} was artificially increased from the initial $\sim 10^{-5} M_{\odot}/\text{yr}$, and the mass-loss rate during the subsequent contraction phases was adjusted accordingly, either following the prescription by Wachter et al. (2002, 2008) or adopting the relationship $\dot{M} \sim T_{\text{eff}}^{-2}$.

Case B. The results obtained by increasing \dot{M}^{TAGB} by a factor of three and applying the $\dot{M} \sim T_{\text{eff}}^{-2}$ relationship during the following phases are shown as green pentagons in the right panel of Fig. 4.11 and in Case B of Tab. 4.3. Consistency between the derived and expected optical depth is achieved when assuming the dust responsible for the current IR excess was released when the star’s effective temperature was between 3500 and 4000 K. In this scenario, the time interval is reduced to 500–1000 yr, resulting in an average wind expansion velocity of 10–15 km/s.

We note that we focus on the $\alpha = 2$ case because using the mass-loss scaling with effective temperature described in Sec. 4.4.1 (Eq. 4.2), the only way to obtain an IR excess comparable to the observed one is by assuming that the dust was released while the star was at the TAGB. However, in that situation, the dust would have traveled for approximately 5000 yr, leading to an average expansion velocity of around 1 km/s.

Therefore, the observational interpretation of J053250.69 indicates that, to achieve consistency between the AGB and the post-AGB phases, it is necessary to enhance \dot{M}^{TAGB} by a factor of three. Moreover, in agreement with the previous case, it is required to assume the $\dot{M} \sim T_{\text{eff}}^{-2}$ relationship and that the dust observed today was released when the effective temperature was approximately 3500 – 4000 K.

4.4.3 Carbon stars with sub-solar chemistry

The sample of carbon stars studied here includes J050632.10 and J003643.94, two sub-solar metallicity stars with similar luminosities around $6000 L_{\odot}$ (see Tab. 4.1 and the right panel of Fig. 4.3). In Sec. 4.2.1, we suggest that these stars descend from $\sim 1 - 1.5 M_{\odot}$ progenitors, which evolved into carbon stars. Both stars, indicated by open squares in Fig. 4.8, deviate from the τ_{10} versus luminosity trend defined by low-metallicity carbon stars, having optical depths that are approximately two times smaller. Furthermore, the distances of the dusty regions from the central stars are the largest distances in the entire sample.

These differences can be partly explained by the fact that these two stars are the hottest among the carbon stars considered, as shown in Tab.4.1. This suggests they are in a more advanced post-AGB phase compared to the lower metallicity carbon stars, allowing the dusty layer to travel further and reach larger distances. However, these factors alone do not fully account for the low IR excess observed in the SEDs of J050632.10 and J003643.94. As shown in the right panel of Fig. 4.8, the distances of the dusty regions around these two sources are found to be $\sim 0.05 - 0.1$ dex higher than those in other carbon stars. Applying Eq. 4.1, we find that the corresponding differences in τ_{10}^{now} should not exceed 20 – 30%. To explain

the roughly two-fold difference in the derived optical depth, we must assume that dust formation during the late evolutionary phases was significantly less efficient.

The most plausible explanation for the lower dust formation in J050632.10 and J003643.94 during the late AGB phases is the smaller number of gaseous carbon molecules available to condense into solid particles in the surface regions. This is related to the small carbon excess relative to oxygen, a critical factor for solid carbon dust formation due to the high stability of CO molecules (Ferrarotti & Gail, 2006). The carbon excess is intrinsically larger in metal-poor stars ($Z \sim 0.004$), given their lower initial oxygen content, whereas it is smaller in stars with sub-solar chemistry, as in the two sources investigated here. This excess is also sensitive to any possible oxygen enrichment from the TDU events experienced.

This last point deserves particular attention. The results in Fig. 4.5 indicate negligible oxygen enrichment in the surface regions of these two stars. However, Van Aarle et al. (2013) report significant oxygen enrichment for J050632.10, implying a low carbon excess and consequently poor dust production. We conclude that the low IR excess observed in these two stars is related to their metallicity and oxygen enrichment, as evidenced by high-resolution spectroscopy results.

These findings have several implications that merit further investigation. First, the observations of J050632.10, similar to other post-AGB stars in the MW (K22), indicate significant surface oxygen enrichment, which current AGB phase modeling does not predict. Concerning the mass-loss description of carbon stars, the formalism must account for surface chemical composition, as the efficiency of radiatively driven winds in carbon stars is highly sensitive to carbon excess relative to oxygen. Lastly, in modeling carbon dust formation, it is recommended that the number density of seeds for dust grain growth, as suggested by Nanni et al. (2013, 2014), be dependent on carbon excess rather than assuming simple proportionality to hydrogen density, as is common in most current models.

4.4.4 A faint, dusty C-star

In the left panel of Fig. 4.8, we observe the anomalous position of J052220.98, which deviates from the general trend established by carbon stars. Despite having the lowest luminosity among the carbon stars in the sample, its optical depth, as derived in Sec. 4.1, is comparable to that of the brightest carbon stars.

In Sec. 4.2.1, we explored the possible origin of this object and suggested that it experienced a late-TP, which could explain its relatively low luminosity. If this hypothesis is correct, the dust formation modeling used for the other stars discussed so far would not be applicable due to the limited understanding of the mass-loss mechanisms that occur during and after a late TP as the star transitions to the post-AGB phase. We speculate that the significant IR excess observed in the SED of J052220.98 results from a rapid removal of the residual envelope, which

could have led to increased mass-loss rates and enhanced dust production.

4.4.5 Oxygen-rich, faint post-AGB stars

We consider J050221.17 representative of low-mass stars that did not reach the carbon star stage. As discussed in Sec. 4.2.2, this source descends from a low-mass progenitor, with an initial AGB phase mass around $0.8 M_{\odot}$. Stellar evolution modeling indicates that such low-mass stars, with metallicity similar to J050221.17, undergo four to five thermal pulses before their external envelope, initially around $0.3 M_{\odot}$, is lost, triggering the transition to the post-AGB phase. The surface chemistry remains substantially unchanged since the beginning of AGB evolution. Like the previously discussed carbon stars, the highest mass-loss rates, approximately $10^{-6} M_{\odot}/\text{yr}$, are reached at the AGB tip.

The dust formed in these stars' winds is mainly composed of silicates, with alumina dust contributing less than 10% (Dell'Agli et al., 2014a). Adopting the assumption described in Chapter 2, i.e. a mass-loss prescription from Blöcker (1995) (Eq. 1.2), we find that the optical depth at the AGB tip is $\tau_{10} = 0.5$.

Following the methodology applied to the carbon stars (Sections 4.4.1 and 4.4.2), we modeled dust formation in the stellar wind at several stages along the evolutionary track. Starting from the effective temperature at the TAGB around 3600 K we considered three additional points, each equally spaced in effective temperature: $T_{\text{eff}}^{\text{onset}} = 4000, 4500, 5000$ K. In line with the approach outlined in Section 4.3 used the stellar radii for each phase, along with the dust layer distance for J050221.17, $R_{\text{in}} = 5.45 \times 10^4 R_{\odot}$, to calculate the current optical depth via Eq. 4.1. The results, shown in Fig. 4.12, display the values of τ_{10}^{now} as a function of effective temperature.

The expected duration of evolution from the TAGB to the present is around 60000 years. Given the current distance of the dusty region from the central star, this implies that the dust particles have moved very slowly since their release, with average velocities below 0.1 km/s. This is the primary reason we believe it is highly unlikely that the dust responsible for the current IR excess was released while the star was at the TAGB. Another reason for this assumption is that the derived τ_{10}^{now} is significantly higher than reported in Tab. 4.1 ($\tau_{10} = 0.022$).

Indeed, the results in Fig. 4.12 suggest that consistency between the expected and derived τ_{10} is found if the dust was released when the effective temperature was in the 4000 – 4500 K range. In this case, the time elapsed since the dust was released would be much shorter, corresponding to average velocities of about 0.5–1 km/s. These velocities are lower than those found in the study of carbon stars' winds, which likely explains why the distance between the dusty cloud and the central object is smaller for M-type post-AGB stars compared to C-rich stars, as shown in the right panel of Fig. 4.8. The generally lower extinction coefficients of

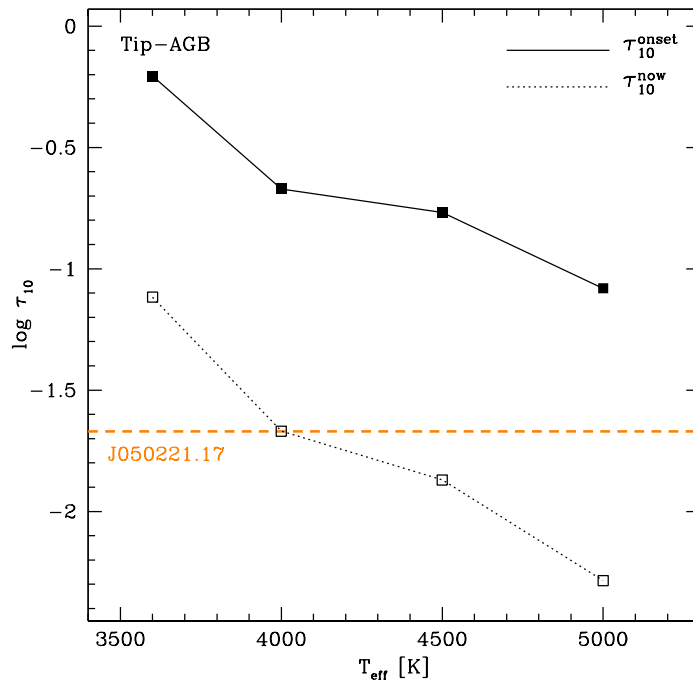


Figure 4.12: *Optical depth variation as a function of the effective temperature.* τ_{10}^{onset} (solid lines and full dots) represent the optical depth that characterize a $0.8 M_{\odot}$ model star, when dust is freshly formed and still close to the star. This is computed at different stages of the AGB to post-AGB transition as represents by the squares, starting from the TAGB (top left square) and during the subsequent phases moving towards higher T_{eff} . Instead, τ_{10}^{now} (dotted lines and open symbols) is obtained using Eq. 4.1 adopting for each value of τ_{10}^{onset} , the distance of the dusty layer retrieved from the SED analysis ($R_{\text{in}} = 5.45 \times 10^4 R_{\odot}$). The dashed orange line represents the optical depth obtained for J053250.69 from the SED modeling ($\tau_{10} = 0.022$, reported in Tab. 4.1).

silicates compared to carbonaceous dust species result in slower expansion velocities for dust in oxygen-rich stars compared to C-rich counterparts. Additionally, M-type stars are the faintest objects in the sample studied here, resulting in lower radiation pressure effects on the dust particles due to their lower luminosity.

4.5 An overall view of dust surrounding MCs post-AGB stars

In this Chapter, we analyzed 13 post-AGB stars from the MCs, performing a SED analysis to constrain the main properties of both the central star and surrounding dust. Our findings indicate that eight of these sources experienced multiple TDU episodes, showing clear signatures of carbon-rich dust. In contrast, five of the sources are low-mass stars that did not reach the carbon-star phase, instead exhibiting traces of silicate-rich dust.

By examining the relationship between optical depth and stellar luminosity (and thus mass), we identified a positive correlation: brighter carbon stars tend to have higher dust formation rates in the final AGB phases, and higher-luminosity stars transition more quickly into the post-AGB stage. Consequently, the time elapsed since the dust was released is shorter, so the dusty region is closer to the star's surface. Moreover, evidence suggests that the dust observed in the C-rich post-AGB sources was expelled after the star entered its general contraction phase, during which its effective temperature increased to approximately 3500–4000 K, and the mass-loss rates during the TAGB phase required to replicate the observed IR excesses of metal poor and low-mass sources are approximately three times higher than those predicted by stellar evolution models.

Oxygen-rich stars that did not reach the C-star stage display a narrower range of luminosities compared to their C-rich counterparts, preventing any significant trends from being detected. The dust-production rate during the late evolutionary phases of these stars is considerably lower than that of carbon stars. Consequently, the outflow experiences less acceleration, resulting in shorter distances from the dusty regions to the photosphere. Similarly to what was found for the C-rich sample, to achieve agreement between the dust observed nowadays and the AGB modeling, we suggest that the dust currently observed was produced after the beginning of the contraction of the star, when the effective temperature was approximately 3500–4000 K.

Carbon-rich post-AGB stars with sub-solar metallicity ($Z \sim 0.004$) show smaller IR excesses compared to their lower-metallicity counterparts. This is attributed to the scarcity of gaseous carbon molecules available for dust formation, which is linked to the high surface oxygen abundances.

Chapter 5

Galactic post-AGB stars

In this Chapter, we apply the methodology proposed in Chapter 4 to study a sample of 31 Galactic post-AGB stars, utilizing distance measurements from the early data release 3 (EDR3) of the ESA satellite Gaia (Bailer-Jones et al., 2021; Gaia Collaboration et al., 2021; Lindegren et al., 2021). We selected stars that likely evolved as single objects, gathering observational data available in the literature on their effective temperatures (Kamath et al., 2023, hereafter K23) and surface chemical composition (Reddy et al., 1999; Van Winckel & Reyniers, 2000; De Smedt et al., 2016; Pereira et al., 2011; Klochkova & Kipper, 2006; Reyneirs, 2000). Following the methodology outlined in Sec. 3.1.1, we performed SED modeling and determined the progenitor masses, comparing our results with the previous findings of K22.

Since the luminosity range of the target stars in this sample is significantly broader than that of the LMC sample (see the following subsections and also K22), the analysis of MW sources enables a more comprehensive investigation of the evolutionary properties of both oxygen- and carbon-rich stars. Indeed, the Galactic sample exhibits greater diversity compared to the LMC sample, encompassing a wide range of characteristics, from objects with significant IR excess to those with little to no circumstellar dust.

Through the analysis of MW post-AGB sources, our goal is to interpret the observed IR excess to investigate the timing of the AGB-to-post-AGB transition in carbon stars, the mass-loss rates near the end of the AGB phase and during the contraction of the central star, and the dynamics of the outflow from the moment the dust responsible for the current IR emission was formed until the present. The rich C-star sample provides an opportunity to study the role of mass and metallicity in AGB and post-AGB evolution, as well as in the dust formation process.

5.1 Galactic carbon post-AGB stars

The sample of carbon-rich post-AGB stars from the MW analyzed in this study consists of sources specifically selected for their *s*-process enrichment, a consequence of repeated TDU episodes (as detailed in Sec. 1.2.2), and for exhibiting the characteristic $21\ \mu\text{m}$ and $30\ \mu\text{m}$ features in their SEDs (Kwok & Zhang, 2013, see Sec. 3.1 for details). Additionally, we selected sources classified as single stars based on long-term radial velocity monitoring programs (K22; Hrivnak et al., 2017), with their effective temperatures and chemical abundances already investigated in the literature (K22; Reddy et al., 1999; Reyneers, 2000; Van Winckel & Reyniers, 2000; Klochkova & Kipper, 2006; Pereira et al., 2011; De Smedt et al., 2016). This selection resulted in a sample of 18 C-rich objects, for which an initial characterization of the progenitor mass was previously performed in K23.

Similarly with what performed for the MCs sample, we aim to interpret the observed IR excess to investigate (1) the timing of the AGB to post-AGB phase transition in carbon stars, (2) the mass-loss rates experienced near the end of the AGB phase and during the contraction of the central star to the post-AGB, and (3) the dynamics of the outflow from the time when the dust responsible for the currently observed IR emission was formed until the present. Furthermore, given the particularly diversity rich nature of this sample, it is possible to study the (4) role of mass and metallicity on AGB and post-AGB evolution and on the dust formation process. For this purpose, we followed the same method used for the MCs sources.

5.1.1 The SEDs analysis

The radiative transfer code DUSTY (Nenkova et al., 2000) was used to generate synthetic SEDs, which were then compared with the observed SEDs of individual stars, reconstructed using photometric data automatically collected from the Vizier database (Ochsenbein et al., 2000) by K22 and, when available, spectra from the Short Wavelength Spectrometer (SWS) of the *Infrared Space Observatory* (ISO; Sloan et al., 2003). The synthetic SEDs were initiated using the effective temperatures and metallicities provided in K22 (see Tab. 5.1), which guided the selection of appropriate atmosphere models from the ATLAS9 library (Castelli & Kurucz, 2003). These models provided the input radiation from the star entering the dusty regions.

In Sec. 3.1.1, we explored the possibility of deriving the stars' luminosities by reproducing the near-IR spectrum. Determining luminosity requires a distance, which is known for stars in the MC. For Galactic sources, distances can be estimated from *Gaia* EDR3 parallaxes, and we used the probabilistic distances from Bailer-Jones et al. (2021). We adopted the same classification used in K22, flag-

Table 5.1: Carbon MW post-AGB stars studied in the present work.

Source	ID	[Fe/H]	T _{eff} [K]	L/L _⊙ ^{K22}	[C/O]
IRAS 02229+6208	1	-0.45 ± 0.14	5952	9973 – 1611	–
IRAS 04296+3429	2	-0.62 ± 0.11	7272	5971 – 20082	–
IRAS 05113+1347	3	-0.49 ± 0.15	5025	1043 – 6731	2.42 ± 0.40
IRAS 05341+0852	4	-0.54 ± 0.11	6274	197 – 592	1.06 ± 0.30
IRAS 06530-0213	5	-0.32 ± 0.11	7809	2736 – 8178	1.66 ± 0.36
IRAS 07134+1005	6	-0.91 ± 0.20	7485	4955 – 6098	1.24 ± 0.29
IRAS 07430+1115	7	-0.31 ± 0.15	5519	14 – 30	1.71 ± 0.30
IRAS 08143-4406	8	-0.43 ± 0.11	7013	3927 – 5452	1.66 ± 0.39
IRAS 08281-4850	9	-0.26 ± 0.11	7462	5567 – 16692	2.34 ± 0.24
IRAS 12360-5740	10	-0.40 ± 0.15	7273	5178 – 7940	0.45 ± 0.20
IRAS 13245-5036	11	-0.30 ± 0.10	9037	7106 – 16800	1.11 ± 0.30
IRAS 14325-6428	12	-0.56 ± 0.10	7256	3758 – 6988	2.27 ± 0.40
IRAS 14429-4539	13	-0.18 ± 0.11	9579	1591 – 14624	1.29 ± 0.26
IRAS 19500+1709	14	-0.59 ± 0.10	8239	6194 – 8138	1.02 ± 0.17
IRAS 20000+3239	15	-1.40 ± 0.20	5478	9332 – 25218	–
IRAS 22223+4327	16	-0.30 ± 0.11	6008	1956 – 2499	1.04 ± 0.22
IRAS 22272+5435	17	-0.77 ± 0.12	5325	5234 – 6108	1.46 ± 0.26
IRAS 23304+6147	18	-0.81 ± 0.20	6276	6381 – 9386	2.8 ± 0.2

The columns are defined as follows: object name, source ID; metallicity and effective temperatures as listed in K22; luminosity from K22 (see their Table 1), obtained considering the upper and lower limits of the distances retrieved from Bailer-Jones et al. (2021); C/O from K22 (see their Table 3).

ging stars as either Q1 or Q2 based on whether the renormalised unit weight error (RUWE*) was below or above 1.4, respectively:

- For Q1 stars, the luminosity ranges were determined by fitting the SEDs, particularly by scaling the synthetic SED to match the near-IR spectrum, combined with the distance range given in K22. From these ranges, we selected the values most consistent with the interpretations of the individual sources from K23.
- For Q2 sources, we derived the luminosity by combining results from the SED analysis with the average distances given in K22. Unlike the Q1 case, for Q2 stars we also considered distances beyond the range used in K22 to ensure consistency between observations and modeling. This approach was particularly applied to three objects, discussed in Sec. 5.1.2, for which we invoked distances approximately two to 20 times higher than those in K22, justified by the large RUWE index of these objects.

The results of the analysis of each object in the sample are presented in Figs. 5.1 and 5.2. The black line is the synthetic spectrum and the black dots the photometric data, the error bars of which are equivalent to the size of the symbols used in the figures. When multi-epoch observations for the same band were available, all results are shown in a vertical sequence according to the central wavelength of the corresponding filter. Furthermore, when available, we compared the SED with the SWS spectra (Sloan et al., 2003, gray dotted line in Figs. 5.1 and 5.2), testing the presence of different dust species:

- SiC particles can be recognized in the observed SED of the C-rich MW stars, in fraction that can be reliably assessed only for stars with available spectra. We assume its presence in all the sources, in percentages between 5 and 30% but in some cases, this feature is partly overlapped with one associated with complex hydrocarbons, complicating the analysis.
- The SWS spectra also reveal the presence of the $30\mu\text{m}$ feature, which Goebel & Moseley (1985) proposed to originate from MgS particles around carbon stars. We tested the hypothesis that either pure MgS[†] (green line,

*The RUWE is defined as the magnitude and colour-renormalized square root of the reduced chi-squared statistic to the Gaia astrometric fit (Lindgren et al., 2021). A value of RUWE < 1.4 is often employed to select stars with accurate parallaxes and proper motions, while larger values could be a sign of binarity and, in general, of a poor astrometric fit (e.g. Belokurov et al., 2020; Penoyre et al., 2020).

[†]The hypothesis of MgS dust growing around SiC cores was proposed by Zhukovska et al. (2008) and applied extensively by Marini et al. (2021). The result reported with a blue line in Fig. 5.2 was obtained by assuming that the MgS mantle has the same width as the SiC core, around $0.07\mu\text{m}$ (Tosi et al., 2023).

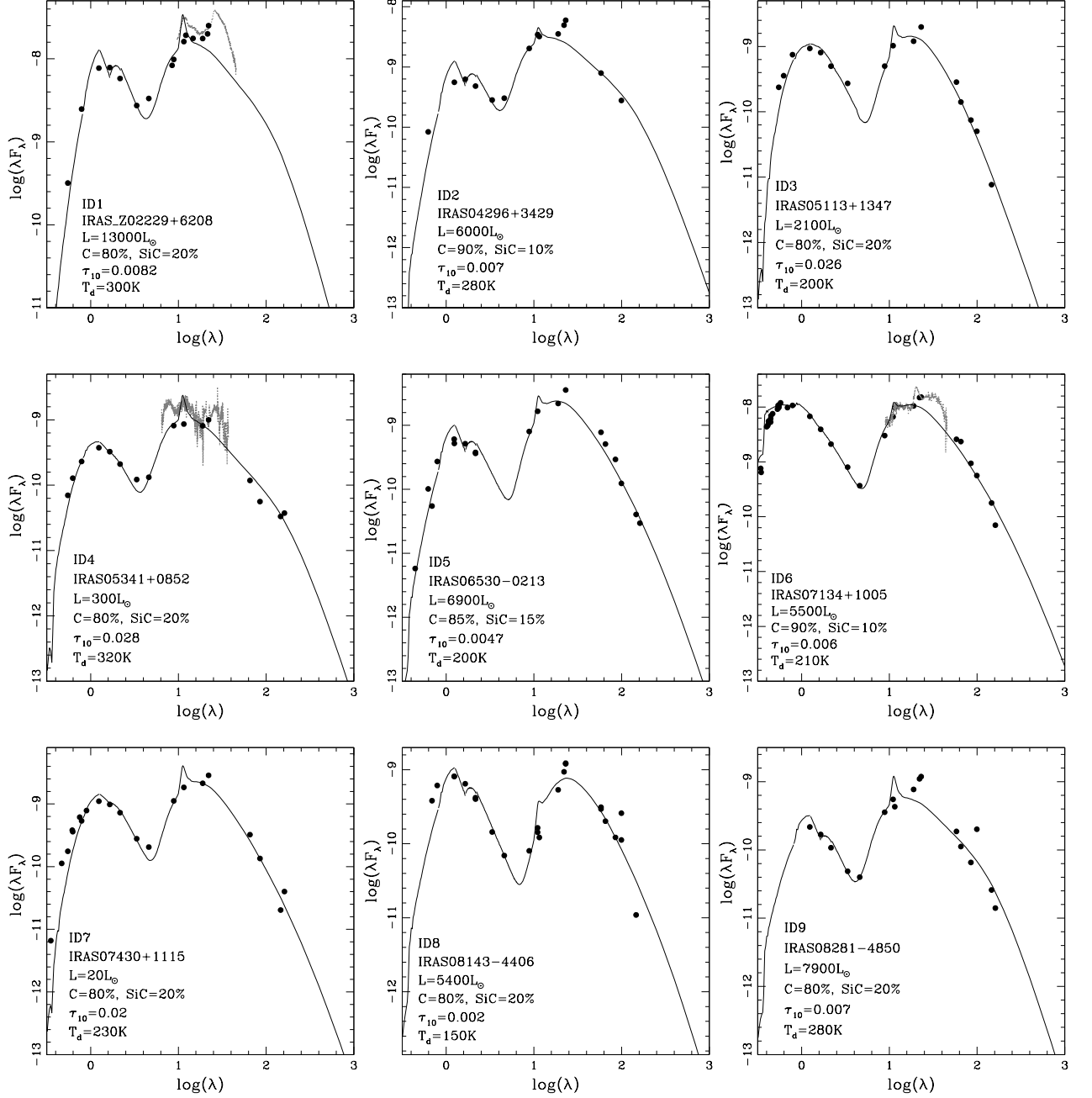


Figure 5.1: SED analysis of Galactic sources classified as single C-rich post-AGB stars, which we interpret as surrounded by carbonaceous dust in this study. The black dots are the observed optical and IR data from K22. The black lines are the best fit model obtained using the DUSTY code (see Sec. 1.4). The gray line shows the SWS spectra from Sloan et al. (2003), where available. The various panels show the stellar and dust parameters derived from this study for each source.

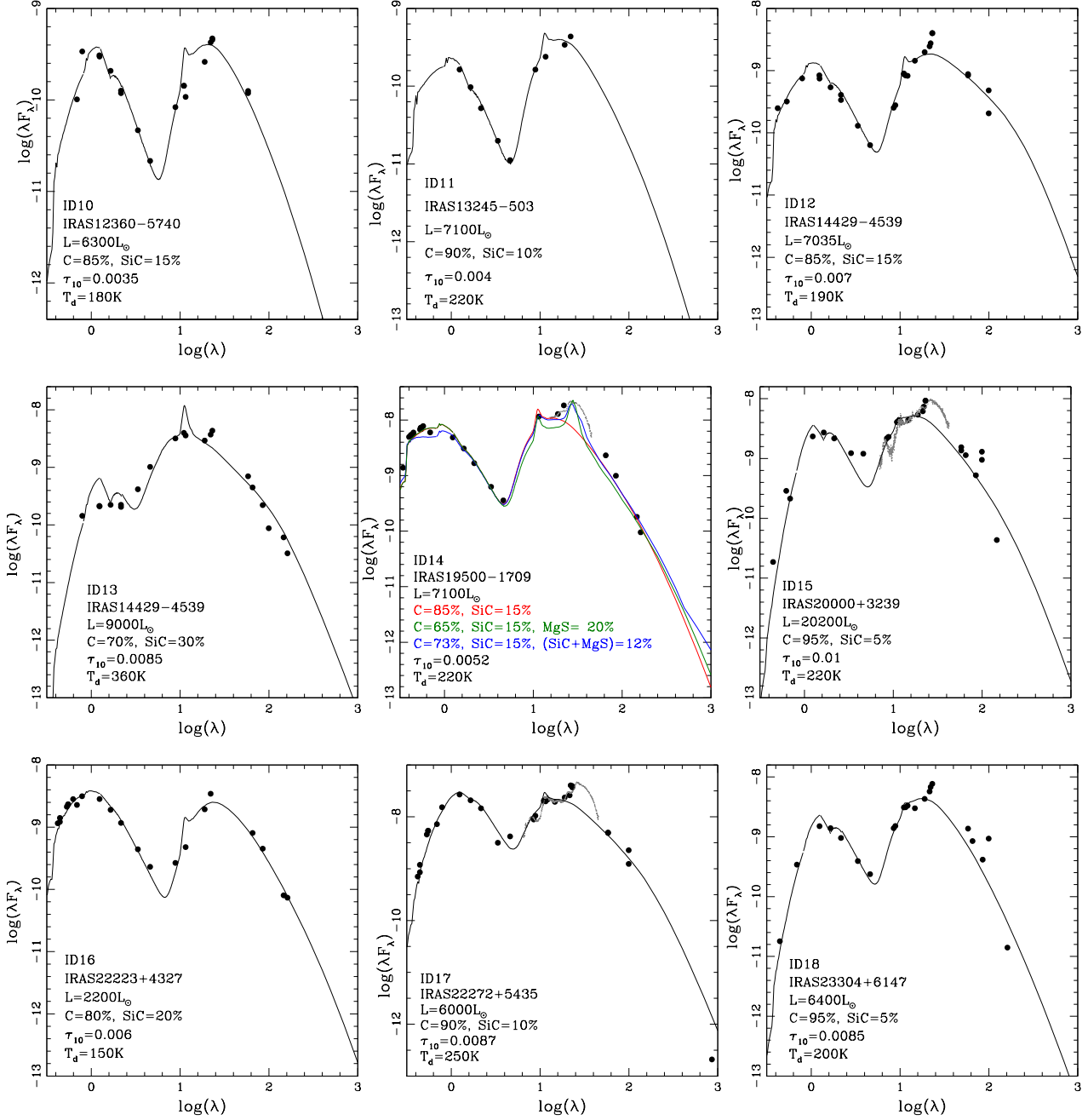


Figure 5.2: Same as in Fig. 5.1. The different lines in the middle panel indicate the synthetic SED obtained by assuming a SiC plus solid carbon dust mixture (red line), 12% of pure MgS dust (green line), 12% of hybrid dust with SiC core and MgS shell (blue line). The gray line shows the SWS spectra from Sloan et al. (2003).

Table 5.2: *Physical and dust properties of the C-rich MW post-AGB stars in this study.*

ID	L/L_{\odot}	τ_{10}	$T_d[\text{K}]$	R_{in}/R_{\odot}	flag
1	13000	0.0082	300	1.84×10^5	Q2
2	6000	0.007	280	1.74×10^5	Q2
3	2100	0.026	200	1.84×10^5	Q2
4	300	0.028	320	2.60×10^4	Q2
5	6900	0.0047	200	4.64×10^5	Q2
6	5500	0.006	210	3.68×10^5	Q1
7	20	0.020	230	1.39×10^4	Q2
8	5400	0.002	150	6.81×10^5	Q1
9	7900	0.007	280	1.94×10^5	Q2
10	6300	0.0035	180	4.81×10^5	Q1
11	7100	0.004	220	3.89×10^5	Q2
12	7035	0.007	190	5.22×10^5	Q2
13	9000	0.0085	360	1.20×10^5	Q2
14	7100	0.0052	220	3.73×10^5	Q1
15	20200	0.010	220	5.32×10^5	Q2
16	2200	0.006	150	4.93×10^5	Q2
17	6000	0.0087	250	1.90×10^5	Q1
18	6400	0.0085	200	4.22×10^5	Q2

Notes: *The columns are defined as follows (from left to right): 1: Source ID (from K22), 2: luminosity derived in the present study (see Sec. 5.2.1); 3-5: Optical depth at 10 μm , dust temperature, and distance separating the central star from the inner border of the dusty region, found via SED fitting; 6: The quality flag (Q1 or Q2), based on the Gaia EDR3 RUWE parameter. We note that the results of ID 3, ID 4, ID 7, and ID 16 are in agreement with the case B treatment illustrated in Sec. 5.1.2.*

middle panel Fig. 5.2) or MgS dust coated on SiC particles (blue line, middle panel Fig 5.2) could be responsible for this feature, improving the agreement between the synthetic and SWS spectra (see middle panel of Fig. 5.2). This result further supports the hypothesis that MgS particles are responsible for the $30\ \mu\text{m}$ feature. Further investigations using updated optical constants for MgS dust and a broader sample of post-AGB sources are needed before definitive conclusions can be reached. The results of the MgS investigation indicate that the estimated luminosity and overall optical depth of the individual sources are scarcely affected by the inclusion of MgS particles. This is because the luminosity is derived from the mid-IR flux (Sec. 1.4), while the optical depth is almost entirely due to solid carbon dust (top left panel, Fig. 3.2).

- Unlike the previous cases, we could not reproduce the SWS spectra in the regions around the features at $6.9\ \mu\text{m}$ and $15 - 21\ \mu\text{m}$, due to unknown carriers. Nevertheless, the inclusion of those features would not significantly alter the conclusions, as these features are weaker than the $30\ \mu\text{m}$ feature, less affecting the SED.

The results obtained from the SED analysis by using the methodology described in Sec. 3.1.1 are summarized in Tab. 5.2. It lists the luminosities and the dust properties derived with the present analysis (i.e., the mineralogy, optical depth, dust temperature, and distance from the center to the star of the inner border of the dust layer), the last column reports the quality flag of the distance as given in K22.

In the previous Section we studied the relationship between the optical depth τ_{10} (derived from SED analysis), the luminosity (L) of the stars, and the distance (R_{in}) of the inner border of the dusty region from the stellar surface (1) to characterize the individual sources in terms of the dust currently surrounding them and, (2) to establish a correlation between the current IR excess and the stars' evolutionary history. With the same aim, in Fig. 5.3 are illustrated the $\tau_{10} - L$ and $\tau_{10} - R_{\text{in}}$ trends for the stars in the C-rich MW sample.

In the following Subsection, we discuss the different groups of stars categorized by the mass and formation epoch of their progenitors and the amount of dust present in their surroundings.

5.1.2 Low-mass carbon stars

The most populated region in the $\tau_{10} - L$ plane (Fig. 5.3) features stars with luminosities ranging from $5000 L_{\odot}$ to $10000 L_{\odot}$ and optical depths of $\tau_{10} < 0.01$. The authors of K23 interpreted the sources in this region as descendants of stars

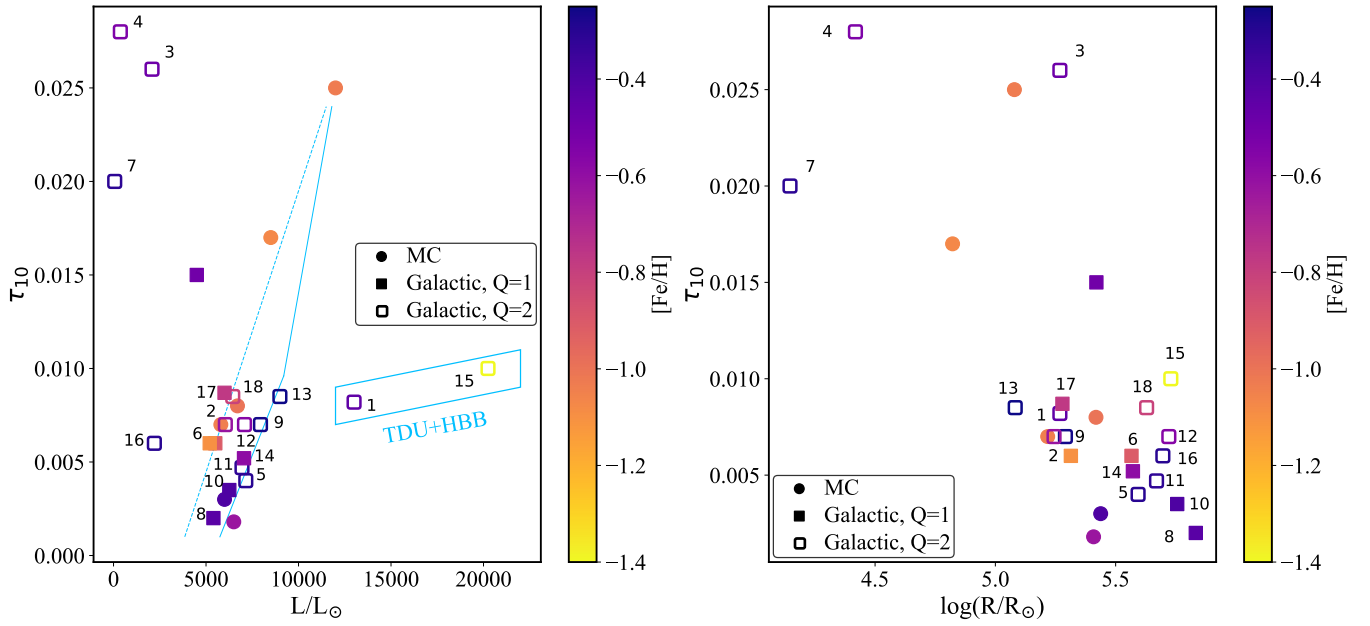


Figure 5.3: Optical depths at $10\ \mu\text{m}$ as a function of the luminosity of the star (left panel) and of the distance of the inner border of the dusty zone from the centre of the star (right panel). The physical and dust parameters are derived from the SED analysis (Tab. 5.2). The vertical color bar indicates the relative metallicity of the sources. The circular markers refer to the LMC stars studied by T22, the squares to the MW targets: the Galactic post-AGB stars marked as Q1 are reported with filled symbols, while those flagged as Q2 are reported with empty symbols. In the left panel, the central solid line and the multi-segment on the right represent the trend in the τ - L plane of the metal-poor and metal-rich objects, respectively.

with masses between $0.9 M_{\odot}$ and $1.5 M_{\odot}$ that reached the C-star stage in their final evolutionary phases, following an initial AGB lifetime as M-type stars.

The distribution of stars in this plane indicates that, for stars of similar metallicity, the optical depth generally increases with luminosity. This finding aligns with the analysis presented for the MCs sample (Chapter 4). Indeed, the higher mass-loss rates experienced by more massive objects (see Sec. 1.2 for details) drive this trend, as they lead to faster evolution of brighter stars during the AGB-post-AGB transition, bringing the dusty region closer to the stellar surface. This interpretation is further supported by the distribution of the same stars in the $\tau_{10} - R_{\text{in}}$ plane (Fig. 5.3), where, with the exceptions of sources ID 15 and ID 18 (both flagged as Q2), the distance of the dusty region from the star's surface is negatively correlated with luminosity.

Another notable result in the left panel of Fig. 5.3 is that stars of different metallicities define separate sequences. Metal-poor objects exhibit a more pronounced IR excess (hence higher optical depths) compared to their more metal-rich counterparts of similar luminosity. The more metal-rich sequence extends from luminosities of $\sim 5000 L_{\odot}$ and $\tau_{10} \sim 2 \times 10^{-3}$ (represented by source ID 8) to $L \sim 9000 L_{\odot}$ and $\tau_{10} \sim 8 \times 10^{-3}$ (ID 13). The metal-poor star sequence can be linked to the two bright metal-poor carbon stars studied in T22, easily identifiable in Fig. 5.3. In this case, luminosities range from 5000 to $12000 L_{\odot}$, and the variation in optical depth is $6 \times 10^{-3} < \tau_{10} < 2.5 \times 10^{-2}$ (Tab. 5.2).

The higher opacity of metal-poor stars can be attributed to two closely related causes (see also Sec. 4.2). First, for low-mass stars of similar luminosity but different chemical compositions, the surface abundance of ^{12}C upon entering the post-AGB phase is relatively independent of metallicity. However, metal-poor stars achieve a higher surface C/O ratio than their more metal-rich counterparts because they start with lower initial oxygen levels. This results in higher surface molecular opacities, leading to more expanded, lower surface gravity structures that favor a cooler, denser envelope. Consequently, the environment becomes more conducive to dust formation.

An additional reason for the higher IR excess observed in metal-poor stars is the greater carbon excess relative to oxygen (Ferrarotti & Gail, 2002, 2006). This is intrinsically higher in metal-poor stars due to their lower oxygen content, resulting in a higher quantity of carbon molecules available for the formation of solid carbon grains. Similar conclusions were reached by Lagadec & Zijlstra (2008) and Sloan et al. (2012).

Luminosity also plays a significant role. Brighter stars experience higher carbon enrichment at their surfaces before losing their envelopes. This is because their envelopes are more massive than those of lower-luminosity stars, and their inter-pulse periods are shorter, meaning less mass is lost between TP. At luminosities around $10000 L_{\odot}$, the amount of carbon accumulated in surface regions

(exceeding a 1% mass fraction) becomes significantly higher than oxygen, making the (C-O) excess largely independent of metallicity. Therefore, the separation in τ_{10} between metal-poor stars and their higher-metallicity counterparts decreases as luminosity increases. Consequently, post-AGB carbon stars with luminosities around $10000 L_{\odot}$ are expected to occupy the same regions of the $\tau_{10} - L$ plane as the two most opaque stars in the LMC, regardless of metallicity.

Stars experiencing hot bottom burning and third dredge-up

Stars ID 1 and ID 15 occupy the bottom-right region of the $\tau_{10} - L$ plane (Fig. 5.3), with luminosities of $15000 - 20000 L_{\odot}$ and optical depths of $\tau_{10} \sim 0.01$. The authors of K23 identified these stars as progeny of $3 - 3.5 M_{\odot}$ stars formed around 300 Myr ago, whose surface chemical compositions were altered by the combined effects of HBB and TDU. The interpretation for ID 1 and ID 15 given in K23 is based on their large luminosities, which are near the threshold required for the ignition of HBB, and on their significant nitrogen enhancement, a clear signature of CN (or CNO) processing. Stars whose surface chemistry is affected by both HBB and TDU are expected to show the largest nitrogen enrichment, as nitrogen is synthesized from both the ^{12}C initially present in the star and the primary ^{12}C convected to the surface by repeated TDU events (see Figs. 1.6 and 6.4).

The sources ID 1 and ID 15 diverge from the τ_{10} versus luminosity trend defined by their lower-mass counterparts and they are also characterized by optical depths smaller than those of the two brightest carbon stars in the LMC studied. This discrepancy is due to the lower carbon excess with which these stars enter the post-AGB phase, resulting from the effects of HBB, which reduces the amount of ^{12}C available in their surface regions (see K23 for further discussion on the expected evolution of surface ^{12}C in these stars)

The dust cloud around ID 1 is located at approximately $2 \times 10^5 R_{\odot}$, one of the smallest dust distances in the sample (Fig. 5.3). Given that ID 1 is one of the brightest sources, this supports the suggestion described in Sec. 4.4, that luminosity influences evolutionary timescales. Specifically, the transition of ID 1 from the late AGB to the post-AGB phase was significantly shorter than for most of the carbon stars in our sample.

The situation for ID 15 is more complex. The dusty region around ID 15 is located at about $6 \times 10^5 R_{\odot}$ (Col. 5, Tab. 5.2), one of the largest distances in the sample (see Fig. 5.3), despite ID 15 being the brightest star. This suggests that radiation pressure might also play a significant role. Brighter stars experience higher radiation pressures, which can trigger faster winds, causing the dust to be pushed further away from the stellar surface.

Overall, these observations indicate that the optical depth and dust distribution around post-AGB stars are influenced by a combination of factors, including

initial mass and radiation pressure.

Post-HB or bright carbon stars?

The sample of C-rich MW stars considered is completed by the sources ID 3, ID 4, ID 7, and ID 16, whose luminosities are significantly below the threshold required for AGB evolution. For this reason, the authors of K23 suggested that these sources might be post-HB objects that failed to reach the AGB phase. These stars may have lost their convective envelopes and started contracting before reaching the AGB phase. Following Schwab (2020), K23 proposed that the carbon and *s*-process enrichment observed in these stars resulted from deep mixing during the helium flash episode. We raise further questions regarding the origin of these stars because, as shown in the left panel of Fig. 5.3, all four of the least luminous stars exhibit high optical depths, among the highest in the sample. Therefore, we suggest the following scenarios:

- A. If these luminosities are accurate, it indicates that low-mass stars undergo a brief, intense episode of mass-loss before evolving to the blue side of the HR diagram. This intense mass-loss phase could create an overdensity region conducive to dust formation.
- B. Alternatively, the large optical depths observed for these stars could be due to underestimation of their distances. If their distances are indeed underestimated, their true luminosities would be significantly higher than the best values reported in K22. The Q2 flag for all four sources supports this consideration, indicating that their distances are highly uncertain.

We propose that the luminosities of these sources follow the same τ_{10} -L pattern traced by the carbon stars in the sample that did not experience any HBB (see Fig. 5.4, the result of that exploration is reported with dotted black line, followed by open black squares). In this context, ID 3 and ID 4 would share a similar origin to the brightest carbon stars in the LMC, with luminosities in the 12000 to 15000 L_{\odot} range. Therefore, these stars would have evolved from 2.5 – 3 M_{\odot} progenitors that experienced a series of TDU episodes, leading to significant surface enrichment of ^{12}C and *s*-process elements, consistent with the surface chemical composition derived from observations (K22).

For ID 4, the hypothesis B is further supported by the derived location of the dusty region around the star, which aligns with the bright carbon stars in the LMC. The situation for ID 3 is more complex, as the inner border of its dust layer is significantly farther away ($4.5 \times 10^5 R_{\odot}$) than that of its LMC counterparts.

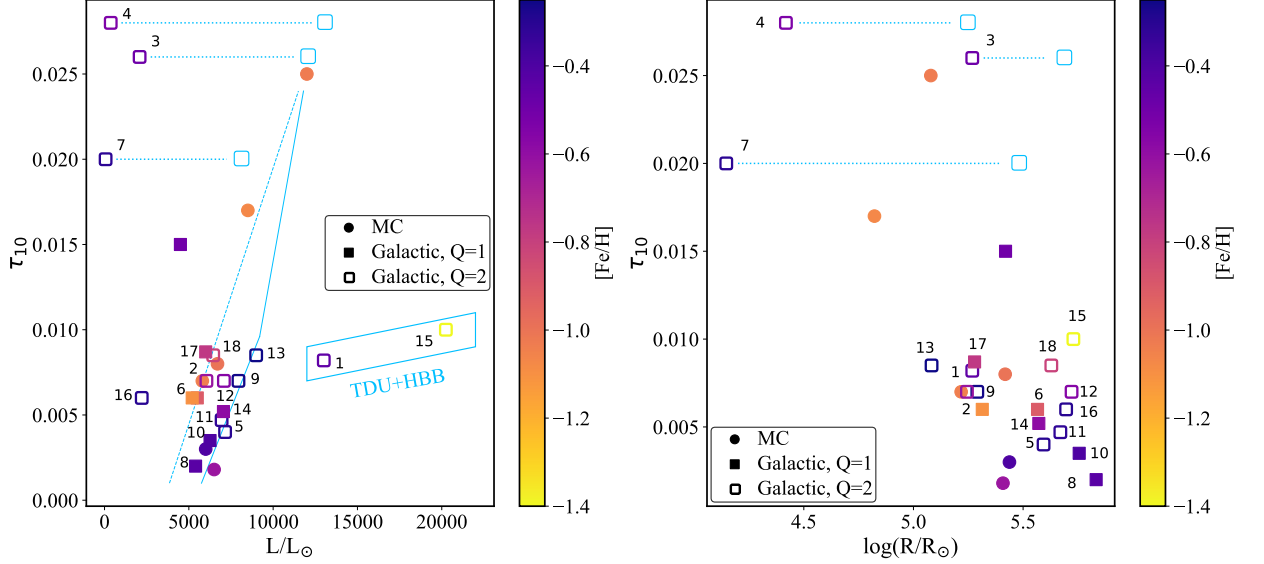


Figure 5.4: Same as Fig. 5.3. The light blue dotted lines, ending with a square, show the projection of the stars (ID4, ID3, ID7) obtained by changing the distance retrieved from Bailer-Jones et al. (2021) and thus the magnitude, according to the case B described in Sec. 5.1.2.

A similar interpretation applies to ID 7, with a luminosity of $\sim 8000 L_{\odot}$, which suggests a progenitor mass of approximately $2 M_{\odot}$. In this case, the dusty region is located $2.8 \times 10^5 R_{\odot}$ away from the stellar surface, as shown in the right panel of Fig. 5.3.

5.1.3 Mass-loss and dust formation during the late AGB phases of low-mass carbon stars

In this Section, we focus on the sources identified as the progeny of low-mass carbon stars (Sec. 5.1.2). Similar to the analysis conducted for the MCs sample (Sec. 4.4), we consider the hypothesis that dust was released during various stages of the contraction phase, soon after the TAGB. For each selected stage, we model dust formation following the scheme introduced by the Heidelberg group (Ferrarotti & Gail, 2006) and verify the consistency between the results obtained from dust formation modeling and SED analysis by considering two key points.

Specifically, for each evolutionary phase considered, we model dust formation to calculate the corresponding optical depth, τ_{10}^{onset} , which would characterize the

star if it were observed at the dust formation epoch (see Fig. 4.7). To ensure compatibility with the current optical depth derived from SED analysis, τ_{10}^{now} , we apply the scaling relation reported in Eq. 4.1. As detailed in Sec. 4.4, we evaluate the reliability of the hypothesis that dust was released at a given evolutionary phase by comparing τ_{10}^{now} , as derived from Eq. 4.1, with the values obtained from SED analysis, reported in Tab. 5.2.

This evaluation involves two main steps: (1) identifying the evolutionary stage (and therefore the effective temperature, assuming that the luminosity remains approximately constant) during which the dust responsible for the detected IR excess was released; and (2) deriving the velocity at which the wind would have traveled since the dust was released until the present epoch. This is done using $v = R_{\text{in}}/\Delta t$, where Δt represents the time interval required for the star's effective temperature to increase from the value at the considered evolutionary phase to the current value (see Fig. 4.7). This time interval is calculated based on stellar evolution modeling. We consider reliable only those evolutionary phases for which the derived velocities fall within the 5–20 km/s range, reflecting an uncertainty in the effective temperature of approximately 500 K.

In the following paragraph, we apply the methodology outlined in Sec. 4.4 to investigate sources ID 8 and ID 17, which exhibit the lowest and highest optical depths, respectively, within the subset examined in Sec. 5.1.2. The study of these stars provides insights into the evolution of low-luminosity post-AGB carbon stars with varying IR excesses. Given the limited investigation of ID 8 and ID 17 in K23, we initially interpret their evolution based on observed physical and chemical properties, followed by an analysis of the dust responsible for their current IR excess.

IRAS 22272 (ID 17): Past evolutionary history and the properties of the dust shell

The left panel of Fig. 5.5 illustrates the evolutionary track of a $1.25M_{\odot}$ model star with a metallicity of $Z = 4 \times 10^{-3}$, evolving from the post-helium flash phase to the white dwarf cooling sequence (Sec. 1.1). In the right panel of Fig. 5.5, the surface carbon abundance is shown to increase during two TDU events, occurring after the last two TP. The star's position on the HR diagram and the derived surface carbon content are consistent with a progenitor mass of approximately $1.25M_{\odot}$, supporting the interpretation of this source as presented in K23. This mass estimate suggests that ID 17 formed approximately 3–3.5 Gyr ago.

Regarding the dust surrounding the star, from the SED modeling we derive that its current location at a distance $R_{\text{in}} = 1.9 \times 10^5 R_{\odot}$ with an optical depth of $\tau_{10}^{\text{now}} = 8.7 \times 10^{-3}$ (see Col. 3 and 5, Tab. 4.1). The mass-loss rate during the TAGB phase, as derived from stellar evolution modeling, is approximately

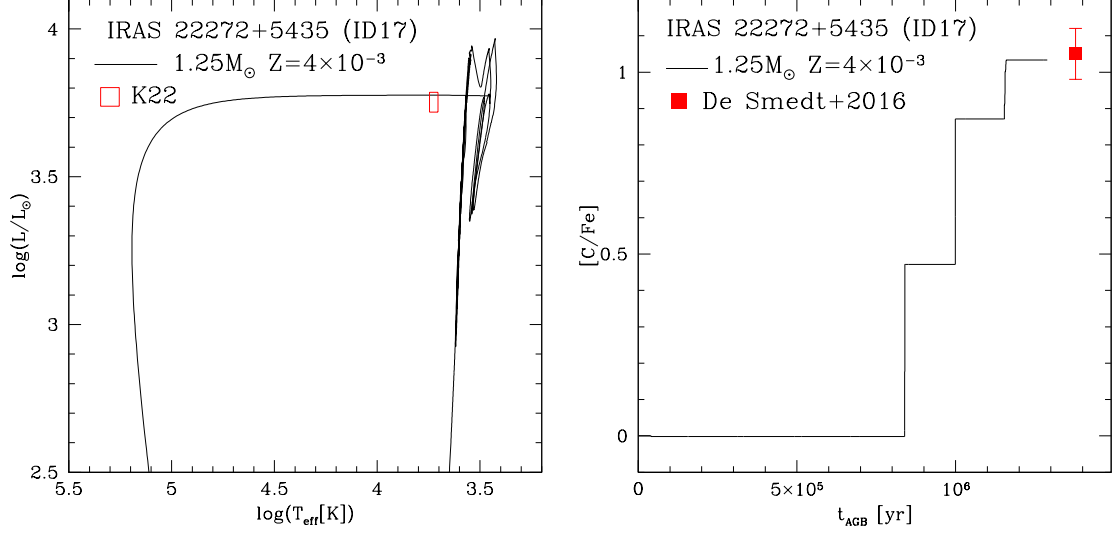


Figure 5.5: Evolutionary track of a $1.25 M_{\odot}$ star of $Z = 4 \times 10^{-3}$ (left panel) and the variation of the surface carbon of the same $1.25 M_{\odot}$ model star during the AGB phase (right panel). The red box in the left panel shows the effective temperature and luminosity (with corresponding error bars) given by K22 for ID 17, while the red data point in the right panel indicates the surface $[C/Fe]$ of ID 17.

$\sim 1.5 \times 10^{-5} M_{\odot}/\text{yr}$. The evolutionary sequence depicted in Fig. 5.5 follows the standard description of mass-loss by Wachter et al. (2008).

In the MCs sample, we found that dust around low-mass post-AGB stars was released when the effective temperature was around 3500 K. Modeling dust formation at this same evolutionary phase for ID 17 yielded an initial optical depth of $\tau_{10}^{\text{onset}} = 0.1$, which, after applying Eq. 4.1, corresponds to a current value of $\tau_{10}^{\text{now}} \sim 10^{-3}$. This value is significantly lower than the optical depth deduced from the SED analysis (8.7×10^{-3}).

In agreement with the MCs findings (Sec. 4.4.2), consistency among the observations is achieved by assuming that the mass-loss rate during the TAGB phase of ID 17 is approximately three times higher than previously estimated. This assumption leads to $\tau_{10}^{\text{onset}} = 0.9$ when $T_{\text{eff}} = 3500$ K, which, applying Eq. 4.1, corresponds to a current optical depth of $\tau_{10}^{\text{now}} = 8 \times 10^{-3}$, consistent with the result from the SED analysis. Under this assumption, the time required for the star to evolve from $T_{\text{eff}} = 3500$ K to the present epoch is approximately 300 yr. This timeframe aligns with the time required for the dust cloud to travel to its current location, assuming a velocity of 10 km/s.

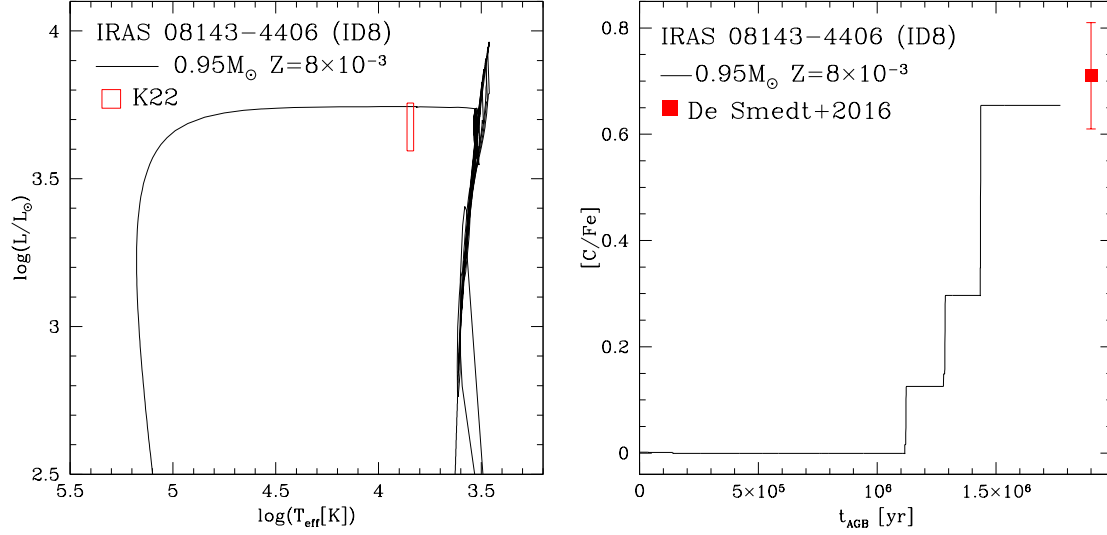


Figure 5.6: Evolutionary track of a $0.95 M_{\odot}$ star of $Z = 8 \times 10^{-3}$ (left panel) and the variation of the surface carbon of the same $0.95 M_{\odot}$ model star during the AGB phase (right panel). The effective temperature and luminosity are shown in the red box on the left. luminosity (with corresponding error bars) for ID 8 from K22, while the red data point in the right panel indicates the surface $[C/Fe]$ of ID 8.

The transition from the AGB to the post-AGB phase for IRAS 08143 (ID 8)

Fig. 5.6 depicts the HR diagram position and surface carbon abundance of ID 8, consistent with the evolutionary path of a $0.95 M_{\odot}$ model star with metallicity $Z = 8 \times 10^{-3}$, as interpreted in K23. Both observational data and stellar evolution modeling converge, indicating that this source formed approximately 11–12 Gyr ago. The final surface carbon content is a result of two TDU events occurring after the last two TP, totaling eight pulses throughout its evolutionary sequence.

The SED analysis for ID 8 yielded a current optical depth of $\tau_{10}^{\text{now}} = 2 \times 10^{-3}$ and placed the dusty region at a distance $R_{\text{in}} = 6.8 \times 10^5 R_{\odot}$ from the star, as detailed in Col. 3 and 5 of Tab. 4.1. According to stellar evolution modeling, during the TAGB phase, the star had an effective temperature $T_{\text{eff}} = 2650$ K, a stellar radius of $340 R_{\odot}$, and a mass-loss rate $\dot{M}^{\text{TAGB}} = 1.8 \times 10^{-5} M_{\odot}/\text{yr}$.

When applying the scaling relation between mass-loss rate and effective temperature proposed in Fig. 1.3, the estimated transition time from the TAGB phase at $T_{\text{eff}} = 7000$ K to the current stage is approximately 4000 yr. To account for the distance R_{in} inferred from the SED analysis, which suggests a current stage

effective temperature of around 7000 K, wind velocities of approximately 3 km/s would be required. However, a more plausible scenario is that the observed dust formed as the star began contracting, reducing its radius to $270 R_{\odot}$ and an effective temperature of 3000 K. In this case, the estimated crossing time would be about 1500 yr, implying more realistic wind velocities around 10 km/s.

Modeling the dust formation at the physical conditions corresponding to $T_{\text{eff}} = 3000$ K results in an optical depth of $\tau_{10}^{\text{onset}} = 0.4$. This initial condition leads to a current optical depth of $\tau_{10}^{\text{now}} = 1.8 \times 10^{-3}$, which is in satisfactory agreement with the results obtained from the SED analysis.

These findings are based on the mass-loss rate at the TAGB phase derived from standard evolutionary modeling. This approach contrasts with the analysis conducted earlier in this Section for ID 17 and, more broadly, with the conclusions concerning low-mass carbon stars of the MCs sample (Sec. 4.4.2), where a threefold increase in \dot{M}^{TAGB} was necessary to replicate the results obtained from SED analysis.

In conclusion, the mass-loss rates derived for low-luminosity carbon stars using the methodology of Wachter et al. (2008) are reliable for stars with solar or slightly sub-solar chemical compositions, particularly when the carbon excess relative to oxygen is minimal. However, this approach tends to underestimate the mass-loss rates for counterparts with metal-poor compositions at similar luminosities.

5.2 Galactic Oxygen-rich post-AGB stars

In this Section, we apply the methodology previously used for the MCs and C-rich MW sources to study 13 oxygen-rich stars. As with the carbon-rich sample, we specifically selected sources that likely evolved as single stars, ensuring their single-star evolution through long-term radial velocity monitoring programs (K22; Hrivnak et al., 2017).

The oxygen-rich nature, linked to $C/O < 1$, may origin from HBB nucleosynthesis or a number of TDU events insufficient to reach the carbon star stage (Sec. 1.2.4). The latter scenario was already identified for 5 sources in the LMC (Chapter 4), which are homogeneous in terms of luminosity and optical depth (Sec. 4.4.5). Since the luminosity of post-AGB stars is directly related to the mass of the progenitor (Fig. 1.10), the luminosity range of the target stars in this sample is significantly wider than that of the MCs sample (K22).

A first characterization of the progenitor mass has already been performed for most of the stars in K23, using the stellar evolution code ATON. In addition, a comprehensive set of surface abundances for these stars has been compiled by the authors of K22.

In analogy to Chapter 4 and Sec. 5.1, in the present thesis we aim to correlate the properties of the dust responsible for the observed IR excess with the dust production processes active during the prior AGB and early post-AGB phases. This involves modeling dust formation at the TAGB and during various evolutionary stages throughout the post-AGB phase. This approach seeks to establish consistency between the results from stellar evolution and dust formation modeling and the observations, and to determine when the dust currently observed was released.

5.2.1 The characterization of the individual sources

To study the oxygen-rich MW sample we applied the approach outlined in Sec. 3.1.1, which involves the comparison of the synthetic SED generated using DUSTY with the photometric data collected by K22 and, when available, the *Infrared Space Observatory* (ISO) spectra (Sloan et al., 2003). To construct the synthetic SED, we specify as input radiation the atmosphere models from ATLAS9 (Castelli & Kurucz, 2003), selecting the metallicity and effective temperatures as reported in Kamath et al. (2022, see columns 3 and 4, Tab. 5.3).

In analogy with what already discussed for the C-rich MW stars (Sec. 5.1), for determining the luminosity of Galactic objects is required to adopt a distance, that we selected within the range provided by Bailer-Jones et al. (2021). This range reflects into an uncertainty in the luminosity, that was explored by Kamath et al. (2022, see column 5, Tab. 5.1). For the present thesis, we chose the best value of the distance to ensure consistency between the entire observational framework of the individual stars (surface chemical abundances and dust mineralogy) and the results from stellar evolution and dust formation modeling. It is important to note that the accuracy of the distance measurement creates a natural distinction between stars labeled as Q1 ($\text{RUWE} < 1.4$) in K22, which will form the basis of most of our interpretation, and those flagged as Q2 ($\text{RUWE} \gtrsim 1.4$), whose distances are significantly more uncertain, leading to less reliable luminosity determinations (see Sec. 5.1.1 for more details). The RUWE quality flag for each source is provided in column 6 of Tab. 5.3.

The results of the SED analysis for the various sources considered are displayed in Fig. 5.7 and Fig. 5.8. In these figures, the black line represents the synthetic spectrum and the black dots correspond to the photometric data, with error bars equivalent to the size of the symbols used. When multi-epoch observations for the same band are available, all data points are shown in a vertical sequence according to the central wavelength of the corresponding filter. The gray dotted line represents the ISO spectrum.

The distribution of the observed IR data provides insights into whether the dust composition is purely amorphous silicate (optical constants from Draine & Lee, 1984) or contains a percentage of crystalline silicates (optical constants from

Table 5.3: *Physical and dust properties of the Galactic post-AGB stars targeted in this study, taken from the literature.*

Source	ID	[Fe/H]	T _{eff} [K]	L/L _⊙ ^{K22}	flag
IRAS 01259+6823	19	-0.6 ± 0.1	5510	220 – 646	Q1
IRAS 08187–1905	20	-0.6 ± 0.1	5772	2099 – 3286	Q2
SAO 239853	21	-0.8 ± 0.1	7452	13080 – 48520	Q2
HD 107369	22	-1.1 ± 0.1	7533	814 – 1010	Q1
HD 112374	23	-1.2 ± 0.1	6393	9961 – 11882	Q1
HD 133656	24	-0.7 ± 0.1	8238	4861 – 5690	Q1
HR 6144	25	-0.4 ± 0.1	6728	22212 – 30419	Q1
HD 161796	26	-0.3 ± 0.1	6139	5209 – 6322	Q1
IRAS 18025–3906	27	-0.5 ± 0.15	6154	975 – 12963	Q2
HD 335675	28	-0.9 ± 0.2	6082	7303 – 28359	Q2
IRAS 19386+0155	29	-1.1 ± 0.14	6303	4345 – 22765	Q2
IRAS 19475+3119	30	-0.24 ± 0.15	8216	5955 – 7545	Q1
HR 7671	31	-1.6 ± 0.1	6985	3449 – 3734	Q1

Notes: *The quantities listed in the various columns are the following: 1 - Object name; 2 - source ID (as reported in Kamath et al. 2022a); 3, 4: metallicity and effective temperatures, derived spectroscopically by K22; 6: luminosity from K22 (see their Table 1), obtained considering the upper and lower limits of the distances retrieved from Bailer-Jones et al. (2021); 8: the quality flag (Q1 or Q2), based on the Gaia EDR3 renormalized unit weight error parameter, taken from K22.*

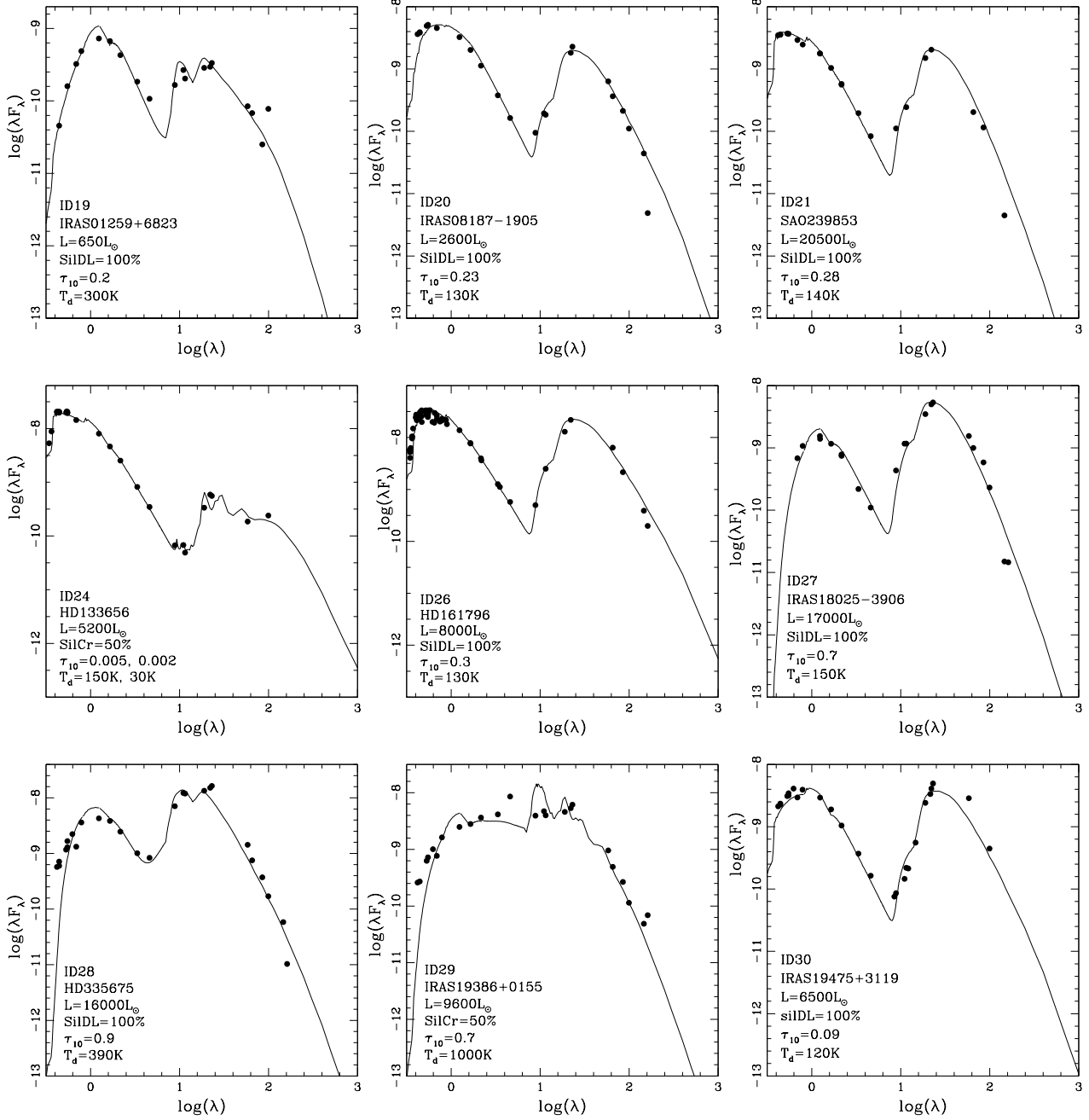


Figure 5.7: SED analysis of Galactic sources classified as single O-rich post-AGB stars, which we interpret as surrounded by oxygen-rich dust in this study. The black dots are the observed optical and IR data from K22. The black lines show the best-fit model obtained with the DUSTY code. The stellar and dust parameters derived from this study for each source are shown in the different panels.

Table 5.4: *Physical and dust properties of the Galactic post-AGB stars targeted in this study, derived in the present work of thesis.*

ID	L/L_{\odot}	τ_{10}	$T_d[\text{K}]$	R_{in}/R_{\odot}
19	650	0.2	300	6.30×10^3
20	2600	0.23	130	1.55×10^5
21	20500	0.28	140	3.80×10^5
22	900	$< 10^{-4}$	150	–
23	11000	$\leq 10^{-3}$	150	6.45×10^4
24	5200	0.005	150	2.00×10^5
25	25500	$< 10^{-4}$	120	–
26	8000	0.3	130	2.85×10^5
27	17000	0.7	150	3.60×10^5
28	16000	0.9	390	3.95×10^4
29	9600	0.7	1000	6.00×10^3
30	6500	0.09	120	4.15×10^5
31	3600	$< 10^{-4}$	30	–

Notes: *The quantities listed in the various columns are the following: 1 - source ID (as reported in Kamath et al. 2022a); 2: luminosity derived in the present study for the Galactic sources; 3-4: optical depth at 10 μm , dust temperature and distance separating the central star from the inner border of the dusty region, found via SED fitting.*

Jaeger et al., 1994). The specifics on the dust species adopted for each SED model are indicated in Fig. 5.7 and Fig. 5.8 adopting the nomenclature “SilDL” for amorphous silicates and “SilCr” for the crystalline silicates.

As a results of the SED investigation (see Sec. 3.1.1 for the methodology) we derived the quantities reported in Tab. 5.4: luminosity (col. 2), optical depth (col. 3), dust temperature (col. 4), and the inner border of the dusty region (col. 5).

To establish a correlation between the current IR excess and the stars’ evolutionary history, similar to the analysis performed for the C-star MW and MCs samples, we examine the $\tau_{10} - L$ and $\tau_{10} - R_{\text{in}}$ trend, shown in the left and right panels of Fig. 5.9. The color coding indicates the metallicity of each post-AGB star, as reported in column 3 of Tab. 5.3, while the full and open symbols represent Q1 and Q2 sources, respectively.

The left panel of Fig. 5.9 reveals a rough correlation between luminosity and optical depth for the sources with solar or sub-solar compositions: the stars are distributed along a diagonal band covering luminosities ranging from 4000 to 18000 L_{\odot} and optical depths from 5×10^{-3} to 0.9, with some exceptions dis-

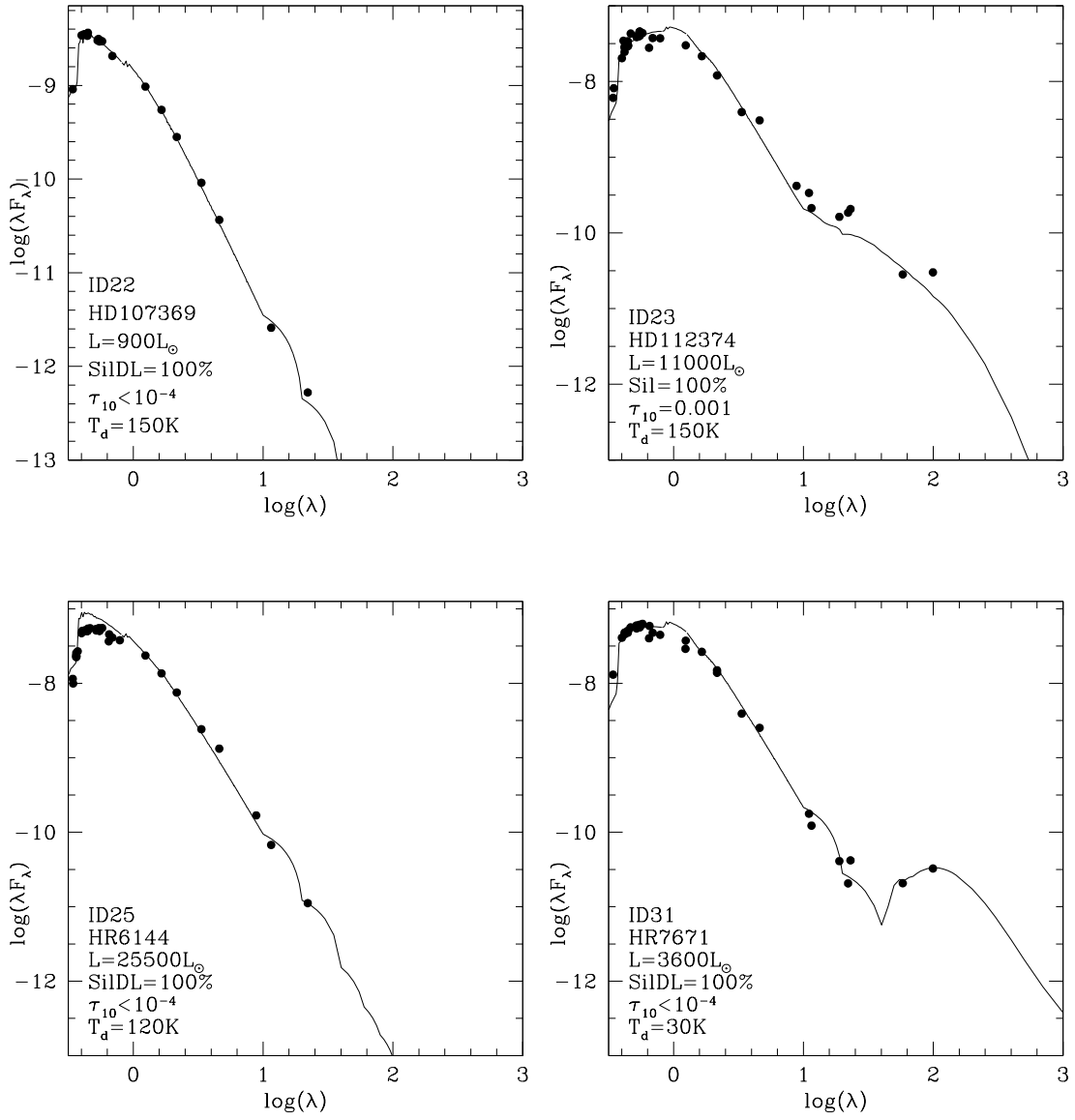


Figure 5.8: Same as Fig. 5.7, but for the “dust-free” sources, defined by $\tau_{10} < 10^{-3}$.

cussed in the next Subsections. Moreover, as highlighted in Fig. 5.9 by the blue contour, it is possible to distinguish different groups of stars sharing similar dust properties:

- **Dust-poor:** Low-mass stars that did not reach the C-star stage occupying the low-luminosity region shown in the right panel of Fig. 5.9. Considering silicate formation, it is not straightforward for radiation pressure to overcome the gravitational pull of the central star and accelerate the wind. In that context, the dust-poor sources exhibit a correlation between the distance of the dusty region from the star and its luminosity. This trend is evident in our analysis of the five MCs oxygen-rich stars (Chapter 4), along with ID 24 and ID 30, spanning from winds minimally influenced by radiation pressure to fully radiation-driven winds. The positive correlation between velocity and luminosity explains why dusty regions are farther from brighter stars.
- **Opaque:** Stars descending from massive AGBs experiencing HBB, characterized by optical depths that tend to be higher compared to low-mass counterparts of similar metallicity. This is attributed to greater dust production rates throughout the AGB phase, particularly during its final stages. However, analysis of the right panel of Fig. 5.9 reveals that the relationship between the distance of the dusty layer and luminosity is less straightforward compared to carbon stars in the MCs studied in Chapter 4.

This discrepancy is largely due to the inherent differences in extinction properties between carbon dust and silicates. Carbonaceous dust exhibits mean opacities approximately one order of magnitude higher than silicates under typical thermodynamic conditions for dust formation (see Fig. 10 in Ferrarotti & Gail, 2006). The substantial scattering and absorption coefficients of carbon dust favor significant acceleration of the outflow even with moderate dust quantities. Consequently, the current location of the dusty region is primarily influenced by the AGB to post-AGB phase transition timescale, thus linked to the luminosity of the star. When considering bright oxygen-rich stars that have undergone HBB, with luminosities around or above $2 \times 10^4 L_{\odot}$, radiation pressure is sufficiently strong to drive the wind.

In the subsequent Sections, we follow the categorization just mentioned, adding dust-free and peculiar objects, discussing each star composing the group separately and comparing the results of our analysis with the results of K23.

Opaque: Post-AGB stars that experienced HBB

K23 identified sources ID21 and ID27 as progeny of massive AGB stars that underwent HBB. This conclusion is drawn from their surface chemical composition,

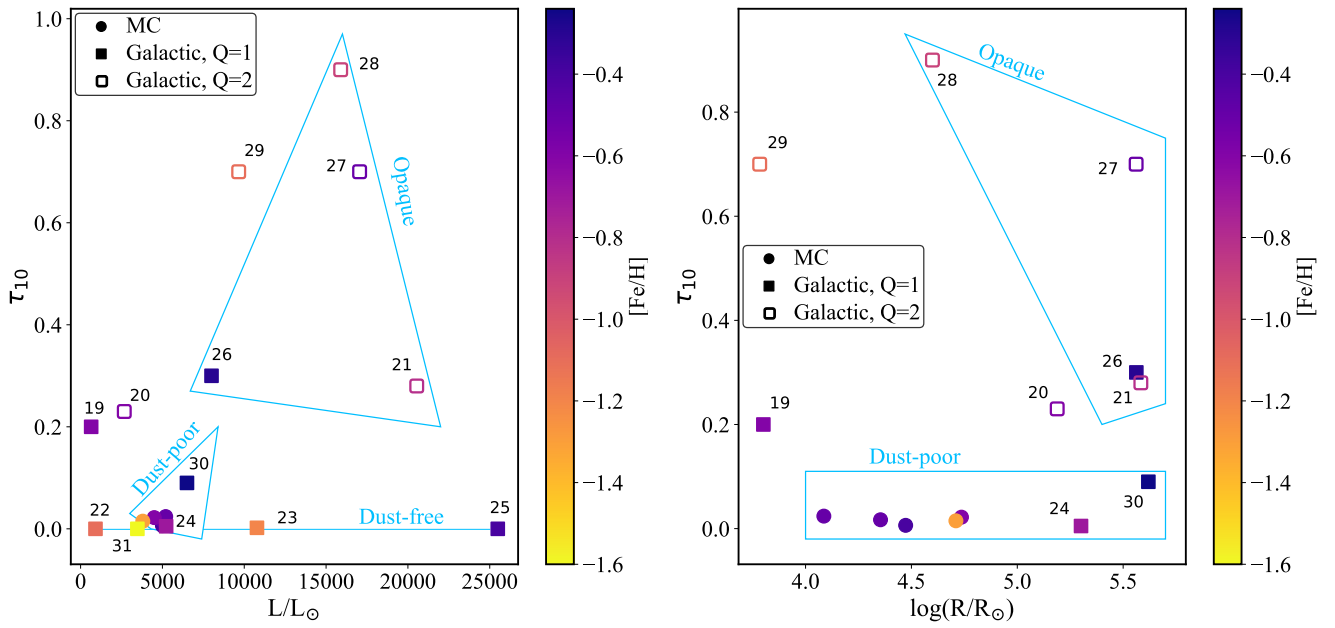


Figure 5.9: The optical depths at wavelength $\lambda = 10 \mu\text{m}$ derived from the SED analysis (Tab. 5.4) as a function of the luminosity of the star (left panel) and the distance of the inner edge of the dusty zone from the center of the star (right panel). The circle represents the MCs sources discussed in Chapter 4, while the squares represent the oxygen-rich galactic stars. The open and full squares refer to Q2 and Q1 RUWE, respectively. The color coding indicates the metallicity of each source, as given in Tab. 5.3.

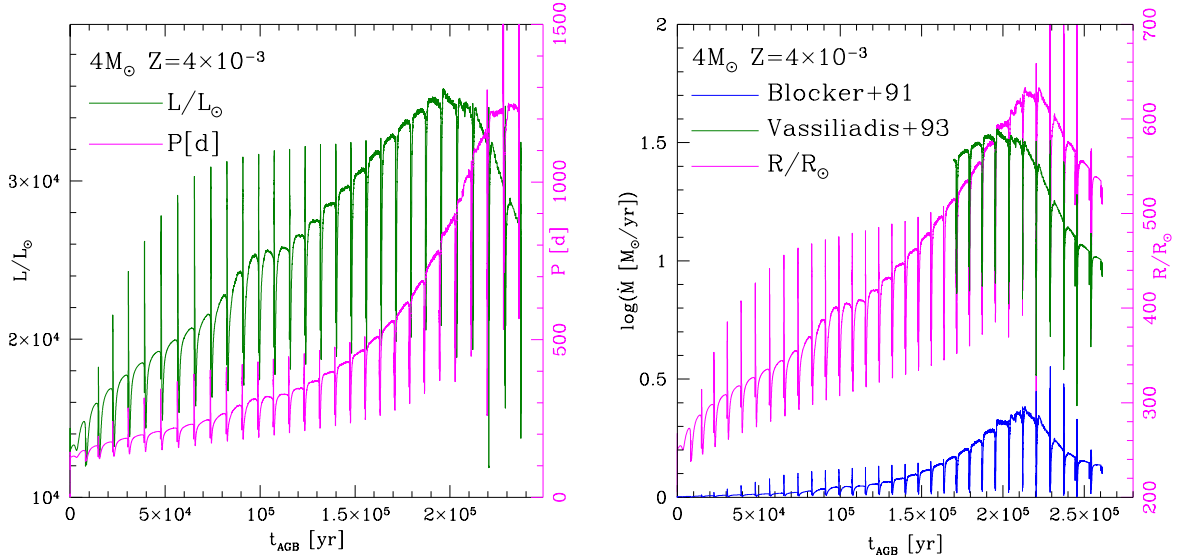


Figure 5.10: Evolution of a $4 M_{\odot}$ model star of metallicity $Z = 4 \times 10^{-3}$, in terms of the time variation of different physical quantities. The times on the x-axis are set to zero at the beginning of the AGB phase. The left panel shows the variation of luminosity (green line, scale on left y-axis) and pulsation period (magenta, scale on right). The right panel shows the evolution of the mass-loss rate modeled by Blocker & Schönberner (1991, blue line) and of the stellar radius (magenta, scale on the right). The green line in the right panel shows the mass-loss rate that would be obtained during the final AGB phase if the Vassiliadis & Wood (1993) prescription for mass-loss.

which exhibits nitrogen enrichment and slightly supersolar [C/Fe] ratios. Analyzing these sources provides an opportunity to study dust production by massive AGB stars, a topic not covered in the MCs sample (Chapter 4). Additionally, this approach is valuable for constraining the mass-loss experienced during the late AGB phases of stars undergoing HBB.

Unfortunately, both ID21 and ID27 have been flagged as Q2, resulting in highly uncertain distances and consequently uncertain luminosities. Regarding ID21, the post-HBB interpretation aligns with the luminosity range provided in K22. For ID27, however, the luminosity range given by K22 is approximately $1000 - 13000 L_{\odot}$, whereas post-HBB stars are expected to have luminosities above approximately $17000 L_{\odot}$. Given the Q2 flag, we suspect that the luminosity of ID27 given in K22 is underestimated.

For modeling ID 27, we adopted a $4 M_{\odot}$ model star with a metallicity of $Z = 4 \times 10^{-3}$, consistent with the metallicity reported by K22. As depicted with

the green line in the left panel of Fig. 5.10, this star reaches a peak luminosity of approximately $35000 L_{\odot}$, which decreases to around $22000 L_{\odot}$ during the final phases before contracting into the post-AGB evolution. Before entering the contraction phase, the model star exhibits an effective temperature of $T_{\text{eff}} = 3400 \text{ K}$, a radius of approximately $500 R_{\odot}$ (magenta line, right panel Fig. 5.10), a period of about 1200 days (magenta line, left panel Fig. 5.10), and a mass of $0.87 M_{\odot}$.

The mass-loss rate for the stars experiencing the HBB remains uncertain, with different theoretical models yielding significantly varying values and behaviors throughout the AGB evolution (see Sec. 1.2.5):

- A. When employing the mass-loss treatment by Blöcker (1995), which correlates \dot{M} tightly with luminosity (Eq. 1.2), it becomes evident that the highest mass-loss rates ($\dot{M} \sim 5 \times 10^{-5} M_{\odot}/\text{yr}$) coincide with peak luminosity phases (compare the time variations of luminosity and mass-loss rate in the left and right panels of Fig. 5.10, respectively) and also with the highest period.

Dust formation modeling based on this mass-loss rate, along with the given values of luminosity, effective temperature, and mass as well as the surface chemistry of the star, results in a TAGB optical depth of $\tau_{10} = 0.4$. Utilizing Eq. 4.1, which links the current optical depth to τ_{10} during the star's last dust release, we estimate the current optical depth to be $\tau_{10} \sim 5 \times 10^{-3}$. This value is significantly lower than the τ_{10} derived for ID 27, as reported in col. 3 of Tab. 4.1 ($\tau_{10} = 0.7$). This finding reinforces recent conclusions by Marini et al. (2023) that applying the mass-loss law from Blöcker (1995) during the final AGB phase presents challenges in interpreting the SED of dust-obscured AGB stars in the Galaxy. These stars are likely descendants of massive AGBs experiencing HBB and currently progressing through late AGB stages. On the other hand, Marini et al. (2023) discovered that using the Vassiliadis & Wood (1993) formulation provides a much more satisfactory explanation of observations for these types of sources.

- B. Applying the Vassiliadis & Wood (1993) prescription (green line, right panel Fig. 5.10), considering the values of $35000 L_{\odot}$, $T_{\text{eff}} = 3400 \text{ K}$, and a period of about 1200 day mentioned earlier, results in TAGB optical depths of $\tau_{10} \sim 5$, corresponding to current optical depths consistent with those found for ID 27 (see Tab. 4.1, $\tau_{10} = 0.7$). Applying these revised mass-loss rates during the very final AGB phases, we estimate the time elapsed between the AGB tip and the current epoch to be approximately $\sim 2000 \text{ yr}$. Moving to a later phase with an effective temperature of 3500 K , this duration decreases to about $\sim 400 \text{ yr}$. Assuming an average velocity of approximately $\sim 20 \text{ km/s}$, the distance traveled by the dust closely matches the value derived from SED analysis. This conclusion is independent of how

mass-loss is modeled throughout the entire AGB evolution. The treatment of mass-loss significantly affects the duration of the AGB phase and influences the number of TP experienced by the star. However, the conditions during the very final AGB stages, post-HBB cessation, are unaffected by the preceding AGB evolution. These conditions are primarily determined by the residual core mass at the onset of final contraction.

The derived optical depths from these sources align with the discussion above. For ID 27, from the SED analysis we calculate $\tau_{10} = 0.7$, while for ID 21 we obtain $\tau_{10} = 0.3$. The difference between the two stars is primarily attributed to the lower metallicity of ID 21 compared to ID 27, resulting in fewer available silicon atoms for dust formation.

The dust-poor stars

The stars ID 24 and ID 30 were determined by K23 to be low-mass stars that lost their envelopes after only a few TDU events and did not become carbon stars. In line with this interpretation, we see in the left panel of Fig. 5.9 that these two sources occupy the same region as the four LMC oxygen-rich stars discussed in the MCs sample. In Chapter 4, they were also identified as low-mass stars that had not reached the C-star stage.

Among this group, ID 30 stands out with the highest τ_{10} ($\tau_{10} = 0.09$). From an evolutionary point of view, this is due to higher luminosity and mass-loss rate at the end of the AGB phase (see Fig. 1.6 and Sec. 1.2.4). In fact, the luminosity range of ID 30 given in K22, specifically $5955 - 7545 L_{\odot}$, aligns with the interpretation provided in K23, but only when values close to the lower limit are considered (see Fig. 3 in K23).

To test whether a satisfactory agreement between the physical and dust parameters derived from observations and from SED analysis with the results from stellar evolution and dust formation modeling can be achieved, we investigated ID 30 in detail. Because the metallicity of this star is higher than the other low-luminosity sources for which we propose a similar origin (all of which share a sub-solar chemical composition), we considered solar metallicity models specifically calculated for the present investigation.

The left panel of Fig. 5.11 shows the evolutionary track of a $1.1 M_{\odot}$ model star of solar metallicity. We note that the mass refers to the beginning of the core helium-burning phase, from which the evolutionary run is started. The post-AGB luminosity of this model star is $\sim 6700 L_{\odot}$, which is within the luminosity range given by K22 (red box, left panel Fig. 5.11). This stellar model experiences ten TPs and only two TDU events. As shown in the right panel of Fig. 5.11, the surface carbon increases up to $[C/Fe] \sim 0.2$, consistent with the results given in K22,

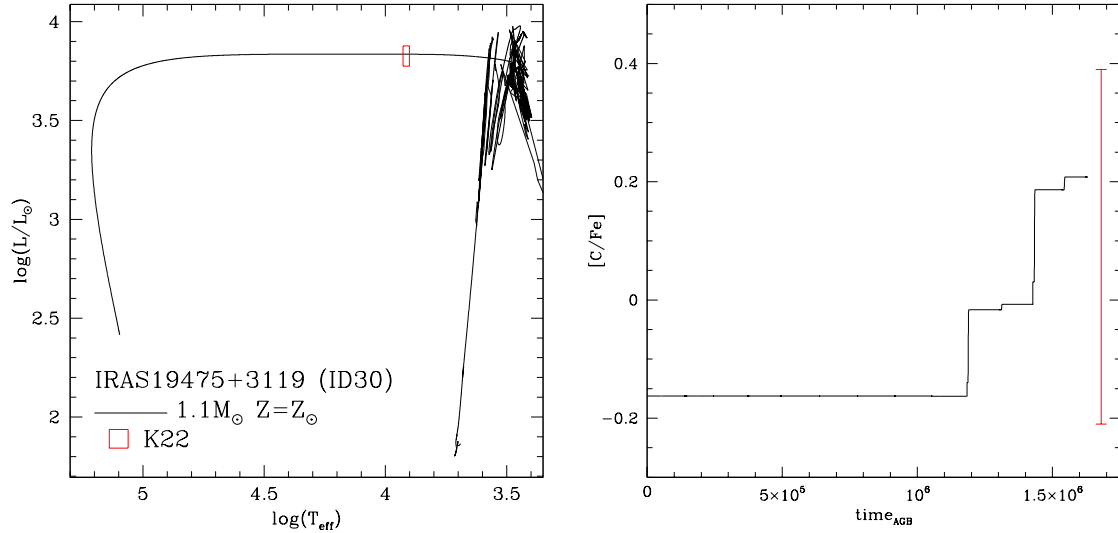


Figure 5.11: The excursion of the evolutionary track of a $1.1 M_{\odot}$ star of solar metallicity (left panel) and the variation of the surface carbon of the same $1.1 M_{\odot}$ model star during the AGB phase. The red box on the left panel shows the effective temperature and luminosity (with corresponding error bars) for ID 30 in K22, while the red vertical line in the right panel indicates the surface $[C/Fe]$ of ID 30.

far below the threshold required to convert the star into a carbon star. Assuming the star lost $0.1 M_{\odot}$ during the RGB phase, we derive an initial progenitor mass of $1.2 M_{\odot}$, corresponding to an age for ID 30 of approximately 6 Gyr. The uncertainty associated with the derivation of the post-RGB mass of ID 30 is small. Indeed, if we consider masses of around $1 M_{\odot}$, we find post-AGB luminosities smaller than the lower limit for ID 30 given in K22. Conversely, assuming a higher mass reflects in a larger number of TDU events respect those shown in the right panel of Fig. 5.11, eventually becoming a carbon star with significant s-process enrichment.

To achieve a comprehensive understanding of dust production and propagation from the TAGB to the present time, we followed the methodology adopted in Chapter 4 and Sec. 5.1.

The source ID 24 exhibits lower luminosity and metallicity compared to ID 30. Its post-AGB luminosity matches that of a $0.9 M_{\odot}$ star with a metallicity of $Z = 4 \times 10^{-3}$. Accounting for the loss of $0.1 - 0.2 M_{\odot}$ during the RGB phase, we estimate that this star formed 5-6 Gyr ago. The contraction time from the TAGB to the current effective temperature of $T_{\text{eff}} = 8238 \text{ K}$ is $2.5 \times 10^4 \text{ yr}$, while the

time from when $T_{\text{eff}} = 3500 \text{ K}$ to its current state is $2500 \times 10^4 \text{ yr}$. This timescale aligns with the distance of the dusty region derived from SED analysis, assuming the dusty layer traveled at a velocity of approximately 2 km/s .

Regarding ID30, the interpretation is more complex. Indeed, we considered the possibility that:

- A. The dust nowadays observed was released during the TAGB. For a $1.1 M_{\odot}$ model, this phase occurs when the star reaches a maximum size slightly exceeding $300 R_{\odot}$ before contracting during the post-AGB phase. At this stage, the star exhibits a mass-loss rate of approximately $2 \times 10^{-6} M_{\odot}/\text{yr}$, which is roughly twice that of low-luminosity oxygen-rich stars discussed in Chapter 4, due to its higher luminosity and greater metallicity.

Calculating the optical depth using Eq. 4.1, τ_{10} is estimated to be 0.5, significantly higher than values derived from SED analysis, thereby rejecting the idea that the dust observed today originated during the TAGB phase. Moreover, the possibility that the dust was released at the TAGB can be also disregarded on the basis of dynamical arguments. Indeed, the time required for the star to evolve from the TAGB to its current phase is approximately 10^4 yr . Combined with the distance of the dusty region ID 30 (reported in Tab. 4.1), this would imply velocities less than 1 km/s , inconsistent with observations and dynamical models of radiation-driven stellar winds.

- B. The observed IR excess was released when the effective temperature of the star reached 3500 K . In assuming that, from Eq. 4.1 we calculate $\tau_{10} \sim 0.1$, which corresponds with results shown in Fig. 5.7 and reported in Tab. 4.1. Considering that the time elapsed since the star's effective temperature was 3500 K to the present epoch is slightly less than 1 Kyr , and assuming an expansion velocity of 10 km/s , we estimate the current distance of the dusty layer to be approximately $4 \times 10^5 R_{\odot}$ from the central star. This estimation is consistent with the analysis derived from SED analysis (see the right panel of Fig. 5.9).

In the right panel of Fig. 5.9, we observe that ID 30's dusty region distance is similar to brighter, higher-mass counterparts like ID 21 and ID 27. Comparing with the five low-luminosity, oxygen-rich stars analyzed in Chapter 4 (depicted as gray triangles in Fig. 5.9), it is evident that the dust from ID 30 has traveled significantly farther, reaching distances that are 3 to 10 times greater.

In the stars discussed in Chapter 4, the production of dust was minimal, resulting in reduced effects from radiation pressure and outflow velocities on the order of a few km/s . Conversely, ID 30 produced dust in larger quantities, thereby experiencing stronger radiation pressure and consequently higher outflow velocities. Indeed, between ID 27 ($\sim 10^{-4} M_{\odot}/\text{yr}$) and ID 30 ($\sim 2 \times 10^{-6} M_{\odot}/\text{yr}$), there's

nearly a two-orders-of-magnitude disparity in mass-loss rates. Since outflow velocity is closely tied to mass-loss rate due to mass conservation principles, the outflow velocity in ID 30 is significantly higher than in low-mass counterparts, effectively counterbalancing differences in evolutionary timescales that influence the location of the dusty region.

This interpretation aligns with findings by Goldman et al. (2017), who observed a positive correlation between expansion velocities of oxygen-rich star outflows in the LMC and the Galaxy with their respective luminosities and metallicities. Given ID 30's higher luminosity and metallicity compared to its LMC counterparts, this correlation supports our analysis.

Dust-free stars

Sources ID 22 and 25, as investigated by K22, exhibit no IR excess (see Fig. 5.8), indicating the absence of dust in their surroundings and no dust production during the final stages of the AGB phase. These sources occupy the lower region of the plane shown in the left panel of Fig. 5.9, alongside ID 23 and ID 31, which show small IR excess corresponding to an optical depth of $\tau_{10} \leq 10^{-3}$. These sources are absent from the right panel of the figure, as the dusty layer could not be detected.

Regarding ID 22, 23, and 31, the lack of dust formation is attributed to their low metallicity (see col.3, Tab. 4.1), which prevents significant quantities of silicates and alumina dust from forming. This conclusion holds true across various progenitor masses and current luminosities. Specifically, it arises from the sensitivity of dust formation in the winds of oxygen-rich stars to metallicity, contrasting with the more robust dust production seen in carbon-rich stars (see for observational perspectives van Loon, 2000, for theoretical predictions Ferrarotti & Gail (2006) and Ventura et al. (2014)).

However, this explanation does not apply to ID 25, which has a metallicity of $[\text{Fe}/\text{H}] = -0.4$. The luminosity of ID 25, approximately consistent with a progenitor mass of $\sim 4 M_{\odot}$ as discussed in K23, is considered fairly reliable despite being flagged as Q1. Stars of similar masses and metallicities typically experience HBB during the AGB evolution, leading to the production of significant amounts of silicates in their circumstellar envelopes ($\sim 2 \times 10^{-3} M_{\odot}$ during the entire AGB phase, e.g. Ventura et al., 2014), which should be detectable presently. The presence of proton-capture nucleosynthesis is confirmed by the enhanced nitrogen content, with $[\text{N}/\text{Fe}]$ slightly below unity, and a high fraction of sodium, specifically $[\text{Na}/\text{Fe}] = +0.8$ (Luck et al., 1990).

One of the findings from Chapter 4 is that brighter stars typically exhibit higher optical depths compared to their lower luminosity counterparts, even when surrounded by the same type of dust. This is primarily due to shorter evolutionary timescales, especially during the transition from the AGB to the post-AGB phase,

resulting in dust being closer to the central object upon release. Considering these factors, the post-AGB classification of ID 25 appears highly improbable. Instead, it is more plausible that the original classification by Luck et al. (1990), as also discussed by Van Winckel (1997), remains valid: ID 25 is likely a supergiant, with enhanced surface levels of nitrogen and sodium resulting from meridional currents activated during its main sequence phase, influenced by stellar rotation (Limongi & Chieffi, 2018).

Low-luminosity stars as plausible AGB-manqué

As described in K22, ID 19 and ID 20 are currently evolving at luminosities below the threshold required to initiate the TP phase and K23 suggested that these objects originate from low-mass progenitors undergoing the post-HB phase. Specifically:

- ID 19 is classified as a Q1 star, with a luminosity well below the threshold required to enter the TP phase. This indicates it completed core helium burning as a giant, lost an envelope of a few $0.01 M_{\odot}$, and then evolved to the blue side of the HR diagram. The rapid contraction process, facilitated by the low envelope mass, led to its current effective temperature. This scenario is supported by the findings in the right panel of Fig. 5.9, where ID 19 is observed to have the closest dusty layer, located within 10^4 solar radii.
- ID 20 was classified as Q2 by K22, which suggests there may be some uncertainty regarding its luminosity. We speculate that the true luminosity could be around $4000 L_{\odot}$. If this hypothesis is correct, it implies that the star entered the AGB phase when its envelope mass was below $0.1 M_{\odot}$, which was subsequently lost rapidly, potentially during the first thermal pulse. This scenario aligns with the model proposed by Renzini (1989), which posits a relatively prolonged peak luminosity phase for very low-mass stars.

Regarding the dust observed nowadays, it was likely formed during the initial contraction to the blue phase when the effective temperatures did not exceed 4000 K. This interpretation aligns with results from stellar evolution modeling; however, the IR excess observed in ID 19 and ID 20, corresponding to $\tau_{10} = 0.2$ (see Fig. 5.9), is significantly higher than expected. Indeed, the mass-loss rates, slightly above $10^{-7} M_{\odot}/\text{yr}$, correspond to an optical depth below 0.05. Using Eq. 4.1, we calculate a current optical depth of $\tau_{10} \sim 0.01$, which is inconsistent with the values derived from SED analysis.

A potential solution involves considering the nitrogen abundance of ID 20 reported in K22. This value is consistent with predictions from HBB nucleosynthesis, particularly when considering the upper range of values. This suggests that ID 20 could descend from a massive AGB progenitor that experienced HBB.

Nevertheless, a more accurate determination of the parallax is necessary to better understand the nature of this object.

A few outliers

The subset of oxygen-rich stars identified by K22 as lacking s-process enrichment includes three sources for which a comprehensive understanding of their evolutionary and dusty properties remains challenging.

ID 26 stands out as a peculiar object due to its significant nitrogen enrichment despite its low luminosity. This source is classified as Q1 by K22, ensuring the reliability of the provided luminosity range. To explain the origin of this star, we suggest two possible scenarios. The first scenario, consistent with K23, considers ID 26 as a source that likely underwent deep mixing during the RGB phase, which, as shown in Fig. 3 of K23, could explain the observed enrichment in nitrogen and sodium. On the other hand, ID 26 exhibits a substantial infrared excess, with an optical depth of $\tau_{10} = 0.3$, one of the highest in our analysis of oxygen-rich sources. Deep mixing is not expected to influence dust production during the final evolutionary phases, which is crucial for determining the surrounding dust during the post-AGB phase. Given these dusty characteristics, another possible scenario associates ID 26 with a progenitor that experienced HBB. However, caution is warranted, as reported asymmetries in the dust distribution (Min et al., 2013) could challenge a straightforward interpretation based on the isotropic assumptions of the DUSTY code (Sec. 3.1.1). In summary, while the surface chemistry and dusty properties of ID 26 align with progenitors of masses above $\sim 3 M_{\odot}$ that underwent HBB and produced significant dust until the end of the AGB phase, its observed low luminosity is more indicative of a lower-mass progenitor.

ID 28's optical depth and the distance of its dusty layer from the star suggest it originates from an intermediate-mass progenitor, consistent with the upper limit of metallicity reported in Tab. 5.3. This categorization places this source among the outliers, as the nitrogen abundance derived by Şahin et al. (2011) appears inconsistent with expectations from HBB, which typically elevates surface nitrogen levels by ~ 1 dex.

ID 29 presents a high optical depth of $\tau_{10} = 0.7$. However, its luminosity, classified as Q2 by K22, is highly uncertain, with a range of $4300 L_{\odot} < L < 22800 L_{\odot}$. Furthermore, nitrogen and oxygen surface abundances are unavailable, complicating identification of the progenitor and interpretation of the IR excess. Another challenge is the potential presence of a disk around this source, which could invalidate the methodology employed in this analysis. Pereira et al. (2004) suggested, based on SED morphology, that ID 29 is surrounded by a dust disk, consistent with findings by Goldman et al. (2017). In agreement with that, ID 29 lacks the double-peak structure typical of spherically symmetric sources in

its SED (see Fig. 5.7), contributing to discrepancies between the model fit and observed data, particularly in the wavelength region below $\lambda \sim 11 \mu\text{m}$, regardless of the choice with regard to the percentage of crystalline silicate considered.

5.3 Conclusions on the Post-AGB stars analysis in the MCs and the Milky Way

We studied a sample of 44 single stars identified as post-AGB sources observed in the MCs and MW, with the goal of characterizing the mass, formation epoch of the progenitors, and the mineralogy of the dust responsible for the observed IR excess. The analysis is based on the combination of optical and near-IR data, which allowed us to trace the morphology of the SED.

The comparison between observations and synthetic SED modeling obtained via the radiative transfer code DUSTY allowed us to identify 26 stars surrounded by carbonaceous dust and 18 objects with silicates dust. The determination of luminosity, derived through the SED analysis process, led to the estimation of the initial mass of the progenitors based on the tight link between core mass and luminosity that characterizes post-AGB stars (see Sec. 1.2.1). For the post-AGB sources observed in the Galaxy, we used Bailer-Jones et al. (2021) distances from the *Gaia* EDR3.

As a result of the radiative transfer modeling, we determined the dust mineralogy around individual sources, the optical depth, and the distance of the dusty region from the central star. Specifically, we found that the dust observed in the post-AGB stars is strongly influenced by the progenitor mass, which is consistent with the understanding of the AGB dust production process (see Sec. 1.2.4):

- Within the mass range of the post-AGB sources analyzed in this thesis ($0.8 M_{\odot} \lesssim M \lesssim 4.0 M_{\odot}$), we observed that sources with larger progenitor masses are characterized by greater τ_{10} . For carbon stars, this is attributed to the fact that more massive progenitors experience a greater number of TPs compared to those with lower progenitor masses. This results in increased surface carbon abundance, higher mass-loss rates, enhanced dust production, and consequently higher τ_{10} . Similarly, more massive oxygen-rich stars are associated with more expanded envelopes and stronger radiation pressure, which further promotes mass-loss rates, dust production, and τ_{10} . An exception to this trend occurs in stars that undergo both TDU and HBB, that exhibit smaller IR excesses than carbon stars undergoing only TDU. This is because HBB reduces the carbon excess relative to oxygen, resulting in less carbonaceous dust (see $3.5 M_{\odot}$ model, Fig. 1.8).

- Higher progenitor’s mass, associated to higher mass-loss rates in massive carbon-rich stars lead to a faster reduction of their envelopes, keeping dust closer to the star. In contrast, lower-mass carbon-rich stars lose their envelopes more gradually, allowing dust to drift farther over time. However, in M-type stars, dusty shells remain closer to the central star compared to carbon stars, as radiation pressure on silicates is weaker than on carbon dust, resulting in slower winds.

The data retrieved from the SED modeling were used to reconstruct the evolutionary history from the late AGB phase to the present, allowing the calibration of the mass-loss rates and investigate the role of metallicity in dust production mechanisms. In particular, we found that the metallicity influence the dust production process, playing a crucial role in determining the composition and quantity of dust formed around different types of stars:

- Metal-poor sources ($[\text{Fe}/\text{H}] \lesssim -0.7$) from low-mass progenitors ($M \lesssim 1.0 M_{\odot}$) that did not reach the carbon-star stage exhibit little to no dust due to the scarcity of silicon and aluminum.
- Metal-rich carbon stars ($[\text{Fe}/\text{H}] \gtrsim -0.7$), with higher initial oxygen levels, have lower carbon-to-oxygen ratios, forming less dust compared to metal-poor stars of similar luminosity.

Investigating the mass-loss mechanisms in both carbon-rich and oxygen-rich stars, we focused on how these processes vary depending on the star’s evolutionary phase and chemical composition, finding that:

- To reproduce the observed IR excesses, mass-loss rates at the TP of the AGB phase of metal-poor ($[\text{Fe}/\text{H}] \lesssim -0.7$) carbon low-mass stars ($0.8 M_{\odot} \lesssim M \lesssim 1.5 M_{\odot}$) need to be approximately $4 - 5 \times 10^{-5} M_{\odot}/\text{yr}$, which is about three times higher than the rates predicted by standard evolution models by using the Wachter et al. (2002, 2008) prescription. However, the mass-loss rates expected for stars of similar mass but with a higher metallicity, align well with the observational data ($1 - 1.5 \times 10^{-5} M_{\odot}/\text{yr}$).

This highlights the need for refined modeling of mass-loss mechanisms in carbon stars, accounting for both evolutionary phase and surface chemical composition.

- For oxygen-rich stars, descendants of low-mass progenitors that did not become carbon stars ($M \lesssim 1.0 M_{\odot}$), theoretical models predict mass-loss rates at the AGB tip of about $10^{-6} M_{\odot}/\text{yr}$, in satisfactory agreement with observations. However, for oxygen-rich stars that experienced HBB ($M \gtrsim 3.5 M_{\odot}$),

the mass-loss rates from Vassiliadis & Wood (1993) better reproduce the observational data than the Blöcker (1995) prescription.

The results on mass-loss rates were obtained by comparing the expected wind velocities and optical depths with those derived from the SED modeling. This comparison prompted a deeper investigation into the efficiency of dust formation during the final evolutionary phases and the dynamics of outflows from central stars, helping to determine when the currently observed dust was released. The findings suggest that the dust surrounding post-AGB stars was primarily ejected after contraction into the post-AGB phase began, with effective temperatures rising to around 4000 K.

For most of the stars studied, the proposed interpretation is well-supported by high-resolution spectroscopy, which aligns closely with expectations from stellar evolution modeling. Comparing these observations with our SED analysis also allowed us to probe the distances of the Q2 sources i.e. the objects whose *Gaia* EDR3 parallaxes are more uncertain. To reconcile observational constraints with theoretical modeling, for few Q2 sources (ID3, ID4, ID7 and ID27) we recommend to increase the Bailer-Jones et al. (2021) distance.

The results described in the present Section are published in several peer-reviewed journals (T22,T23 Dell’Agli et al., 2022, 2023a). More accurate studies will be required by the forthcoming release of *Gaia* astrometric data, that will be crucial for expanding our Galactic sample of objects.

In future work, we will focus on obtaining robust observational evidence to further constrain the dust chemical composition of our target sample. High-resolution IR and mid-IR spectra from JWST, covering the $\sim 5\text{--}28\ \mu\text{m}$ wavelength range, will be especially valuable. These spectra will provide insights into the diverse features present in post-AGB stars, including atomic fine-structure lines, hydrogen lines, PAHs, crystalline and amorphous silicates, SiC, MgS, the enigmatic $21\ \mu\text{m}$ feature, alumina, C_2H_2 , SiS, SiO, TiO, and H_2O (Sloan et al., 2016; Gielen et al., 2011). Integrating these observations with our newly developed models will enhance our understanding of dust formation in the outflows of post-AGB stars.

Chapter 6

Planetary Nebulae

The study on post-AGB stars, presented in the previous Chapters, demonstrated the utility of comparing photometric and spectroscopic data with predictions from evolutionary models to characterize the main physical and chemical properties of evolved stars, reconstructing key aspects of the earlier evolutionary stages of these sources. By introducing a new methodology, we have been able to understand the history of mass-loss at the TAGB and soon after. We also have been able to understand when the dust still present around the post-AGB was formed and released. All these information provides crucial constraints for describing the evolutionary timescales of the transition towards the white dwarf phase.

In this regard, the PN phase offers a complementary perspective for studying LIMSs with respect to the post-AGB stage previously discussed. By comparing the chemical compositions of PNe with predictions from stellar evolution models, we can reconstruct the AGB history, including nucleosynthesis and mixing processes (Kamath et al., 2023; Ventura et al., 2015, 2016, 2017; García-Rojas et al., 2018; Stanghellini et al., 2022). Additionally, analyzing the SEDs of PNe allows us to retrieve information on the final mass-loss episodes and dust production during the AGB phase.

In this Chapter, we present the first comprehensive interpretation of the observational data available from the final AGB stages to the PN phase. We focus on objects from the LMC that likely evolved as single stars. The well-constrained distance of the LMC makes it an ideal laboratory for precise determinations of luminosities and initial stellar masses, which we performed using photoionization modeling. This approach enabled us to characterize the physical properties of the CS, nebular gas, and dust of each PN in the sample. Furthermore, we compared these physical characteristics and observed chemical abundances of PNe with a wide set of ATON stellar evolution models (Ventura et al., 1998) specifically extended to the PN phase. This comparative analysis allowed for a robust determination of the progenitor mass of the CS, thereby establishing the connection

between observed PNe and their past evolutionary history.

Our aim is to demonstrate that the simultaneous study of stars in different evolutionary phases along the same evolutionary sequence (in the luminosity- T_{eff} plane) provides valuable insight into the amount of dust produced during the AGB phase, the cessation of dust production, and the transport of dust away from the star. This approach offers a comprehensive view of the transition from the AGB, to the post-AGB, and finally to the PN phases, facilitating a deeper understanding of the production and evolution of dust during the late stages of a star’s life. The results of the analysis here described were published in Tosi et al. (2024) and Ventura et al. (2025).

6.1 PNe in the LMC: SED analysis and characterization

Our study focused on a selected sample of LMC PNe, leveraging the accurately known distances to these sources. We chose PNe with observed mid-IR spectra to directly assess the presence of dust within the nebula. Additionally, we collected UV spectra and photometric data spanning from UV to optical and IR wavelengths to construct comprehensive SEDs.

Table 6.1: *ID, coordinates, and morphology of the PNe studied in the present work.*

ID	R.A. (J2000.0)	Decl. (J2000.0)	Morphology ^{a,b,c,d}
SMP LMC 4	04 43 21.50	-71 30 09.5	Elliptical
SMP LMC 18	05 03 42.64	-70 06 47.8	Round
SMP LMC 25	05 06 24.00	-69 03 19.2	Round
SMP LMC 34	05 10 17.18	-68 48 23.0	Elliptical
SMP LMC 66	05 28 41.20	-67 33 39.0	Elliptical
SMP LMC 71	05 30 33.22	-70 44 38.4	Elliptical
SMP LMC 80	05 34 38.87	-70 19 56.9	Round
SMP LMC 81	05 35 20.92	-73 55 30.1	Round
SMP LMC 102	06 29 32.93	-68 03 32.9	Round

Notes: ^a Shaw et al. 2001; ^b Shaw et al. 2006; ^c Stanghellini et al. 1999; ^d Stanghellini et al. 2002;

The final sample of nine LMC PNe includes both round and elliptical PNe, specifically chosen to exclude close binary systems that might exhibit significant deviations from single-star evolution (Stanghellini et al., 2002b)*. This selection

*Observational evidence suggest that more complex structures, such as the bipolar morpholo-

Table 6.2: *Input parameters used for the spectral synthesis analysis.*

ID	$\log(\text{C}/\text{H})+12$	$\log(\text{O}/\text{H})+12$	$n_{\text{H}} [\text{cm}^{-3}]$	$\log(R_{\text{in}}/[\text{cm}])$
SMP LMC 4	$8.66^a \begin{smallmatrix} +0.1 \\ -0.1 \end{smallmatrix}$	$8.61^b \begin{smallmatrix} +0.1 \\ -0.1 \end{smallmatrix}$	3.55×10^3	17.56
SMP LMC 18	$8.37^a \begin{smallmatrix} +0.1 \\ -0.1 \end{smallmatrix}$	$\sim 7.87^b \begin{smallmatrix} +0.1 \\ -0.1 \end{smallmatrix}$	3.31×10^3	17.42
SMP LMC 25	$8.29^a \begin{smallmatrix} +0.1 \\ -0.1 \end{smallmatrix}$	$8.17^b \begin{smallmatrix} +0.1 \\ -0.1 \end{smallmatrix}$	1.51×10^4	17.08
SMP LMC 34	$8.13^a \begin{smallmatrix} +0.1 \\ -0.1 \end{smallmatrix}$	$8.46^c \begin{smallmatrix} +0.4 \\ -0.4 \end{smallmatrix}$	4.79×10^3	17.22
SMP LMC 66	$8.51^b \begin{smallmatrix} +0.1 \\ -0.1 \end{smallmatrix}$	$8.31^b \begin{smallmatrix} +0.1 \\ -0.1 \end{smallmatrix}$	2.51×10^3	17.45
SMP LMC 71	$8.90^a \begin{smallmatrix} +0.1 \\ -0.1 \end{smallmatrix}$	$8.63^b \begin{smallmatrix} +0.1 \\ -0.1 \end{smallmatrix}$	1.10×10^4	17.21
SMP LMC 80	$7.51^a \begin{smallmatrix} +0.1 \\ -0.1 \end{smallmatrix}$	$8.34^b \begin{smallmatrix} +0.1 \\ -0.1 \end{smallmatrix}$	7.94×10^3	17.04
SMP LMC 81	$7.16^a \begin{smallmatrix} +0.1 \\ -0.1 \end{smallmatrix}$	$8.25^b \begin{smallmatrix} +0.1 \\ -0.1 \end{smallmatrix}$	1.26×10^3	16.99
SMP LMC 102	$8.65^a \begin{smallmatrix} +0.1 \\ -0.1 \end{smallmatrix}$	$8.28^b \begin{smallmatrix} +0.1 \\ -0.1 \end{smallmatrix}$	900	17.57

Notes: 1– source ID, 2, 3–observed abundances of carbon and oxygen, 4– electron density, and the 5– inner radius of the nebulae. ^a Stanghellini et al. 2005; ^b Leisy & Dennefeld 2006; ^c Henry, Liebert & Boroson 1989

aligns with the spherical symmetry assumption of the photoionization model used in our analysis (Sec. 3.2.1).

Tab. 6.1 lists the names and coordinates of our targets, along with their morphology derived from *Hubble* Space Telescope (HST) images (Shaw et al., 2001, 2006; Stanghellini et al., 1999, 2002a). The photometric data were sourced from various catalogs, including UBV and IRAC data from Reid (2014) and Lasker et al. (2008), and WISE photometry from Cutri & et al. (2012). The mid-IR spectra were obtained from the *Spitzer* Infrared Spectrograph (IRS; LS07), and UV spectra from the HST/Space Telescope Imaging Spectrograph (STIS; Stanghellini et al., 2005, hereinafter LS05). All UV spectra and photometric data were corrected for Galactic foreground and LMC extinction (Sec. 3.3).

We generated synthetic spectra using the spectral synthesis code CLOUDY

gies has been associated to a binary evolution (Miszalski et al., 2009; Balick & Frank, 2002). For this reason we excluded them from our sample.

(v22.02; Ferland et al., 2017) to compare with the UV to mid-IR photometric and spectroscopic data of nine LMC PNe (see Fig. 3.4 for a description of the typical emission lines). The input parameters, described in Sec. 3.2.1, were chosen to be consistent with observational constraints. Specifically, carbon and oxygen abundances were scaled to match the observed measurements from LS05, Leisy & Dennefeld (2006), and Henry et al. (1989, columns 2 and 3, Tab. 6.2). The hydrogen density, n_{H} (column 4, Tab. 6.2), was selected to reproduce the electron density N_{e} reported in LS05. The inner radius, R_{in} , was derived by scaling the observed radii of [OIII] from Shaw et al. (2001).

We iteratively adjusted the input parameters to find the combination that best matched the synthetic spectrum with the observed photometry and spectra (HST and *Spitzer*, see Sec. 3.2.1 for the full methodology). This process took into account continuum emission, atomic lines, and dust features that characterize the spectra (Sec. 3.2). We acknowledge that it is possible to develop an automated program to conduct a detailed analysis of the SED through residual analysis. However, we strongly believe that tailored models are more reliable, as they avoid leading the user to unphysical interpretations of the source structure and are less time-consuming.

Figs. 6.1–6.3 display the results of the SED analysis. The black line represents the synthetic spectrum produced using CLOUDY, while the orange line corresponds to the HST/STIS spectra (LS05), and the green line to the *Spitzer*/IRS spectra (LS07). The blue squares indicate the observed photometric data, and the red triangles indicate the synthetic photometry, which includes the contribution of the emission lines. As shown in Figs. 6.1–6.3, we successfully reproduced the main SED components for most PNe. Exceptions are due to the presence of broad unidentified dust features, such as those at 6–9, 9–13, 15–20, and 25–35 μm , and other species whose optical constants could not be included in our photoionization modeling (see Chapter 2 for details). Additionally, the dust temperature, as self-consistently derived from the photoionization code, accurately reproduced the IR peak, except for SMP LMC 4 (top panel, Fig. 6.1).

As a result of the SED analysis, we determined several key parameters for the CSs and their nebulae. These include the luminosity and effective temperature of the CSs (col. 2 and 3 in Tab. 6.3), and the thickness of the nebula, ΔR (col. 4, Tab. 6.3), which is directly linked to the nebular gaseous mass, M_{gas} (col. 5, Tab. 6.3). Additionally, we derived the chemical composition and temperature of the dust (col. 4 and 5), as well as the dust-to-gas ratio (col. 2 and 3) and the dust mass of the nebula (col. 6), retrieved as $M_{\text{dust}} = \delta[\text{C}] \cdot M_{\text{gas}}$ (Tab. 6.4), which serve as proxies for the amount of dust present in the PNe. We note that the sum of R_{in} and ΔR provides a value that agrees within 25% with the observed photometric radius of the nebulae (Shaw et al., 2001).

The CSs in our sample exhibit luminosities ranging from 2000 to 6500 L_{\odot} (col.

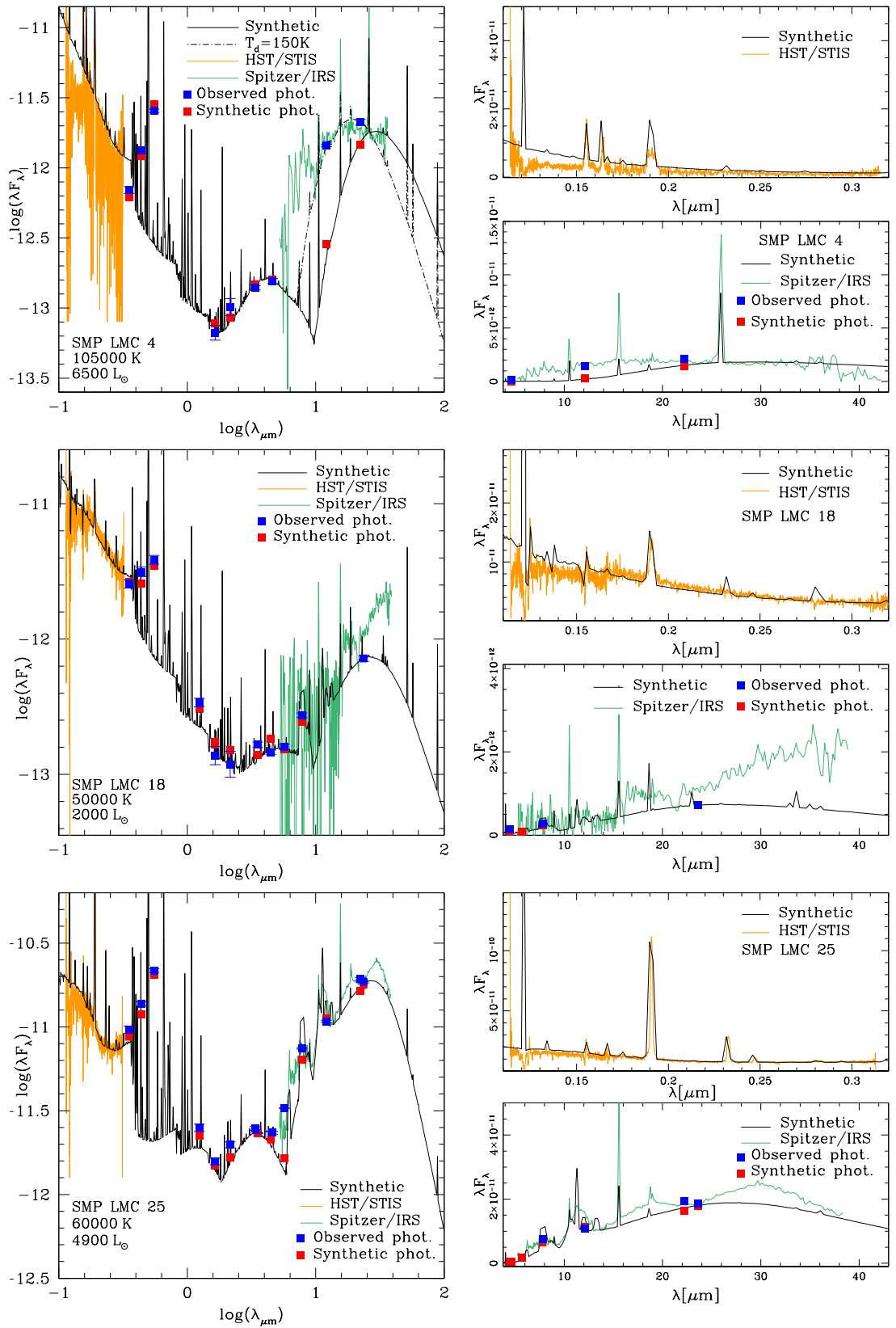


Figure 6.1: SED of the CRD PNe. The blue squares are the photometric data of Reid (2014), Cutri & et al. (2012), and Lasker et al. (2008), the orange line is the HST/STIS UV spectrum of Stanghellini et al. (2005), and the green line is the Spitzer/IRS spectrum of Stanghellini et al. (2007). The black lines and red squares indicate the synthetic spectra and photometry obtained in this work. The dotted line in the top left panel is the synthetic spectrum obtained by assuming a dust temperature of 150 K. The right panels show a zoomed view of the UV (top panel) and the IR spectra (bottom panel).

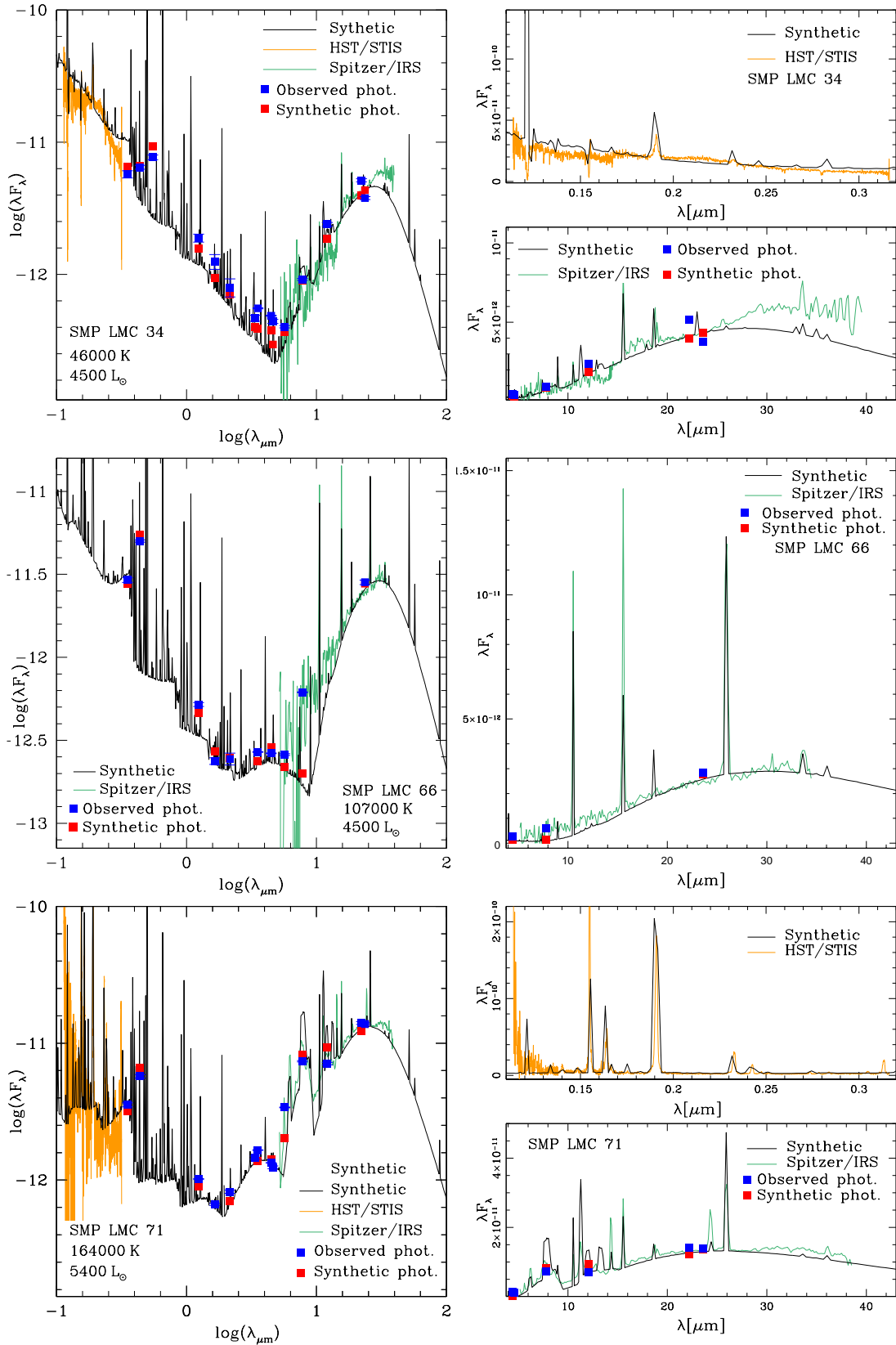


Figure 6.2: Same as Fig. 6.1

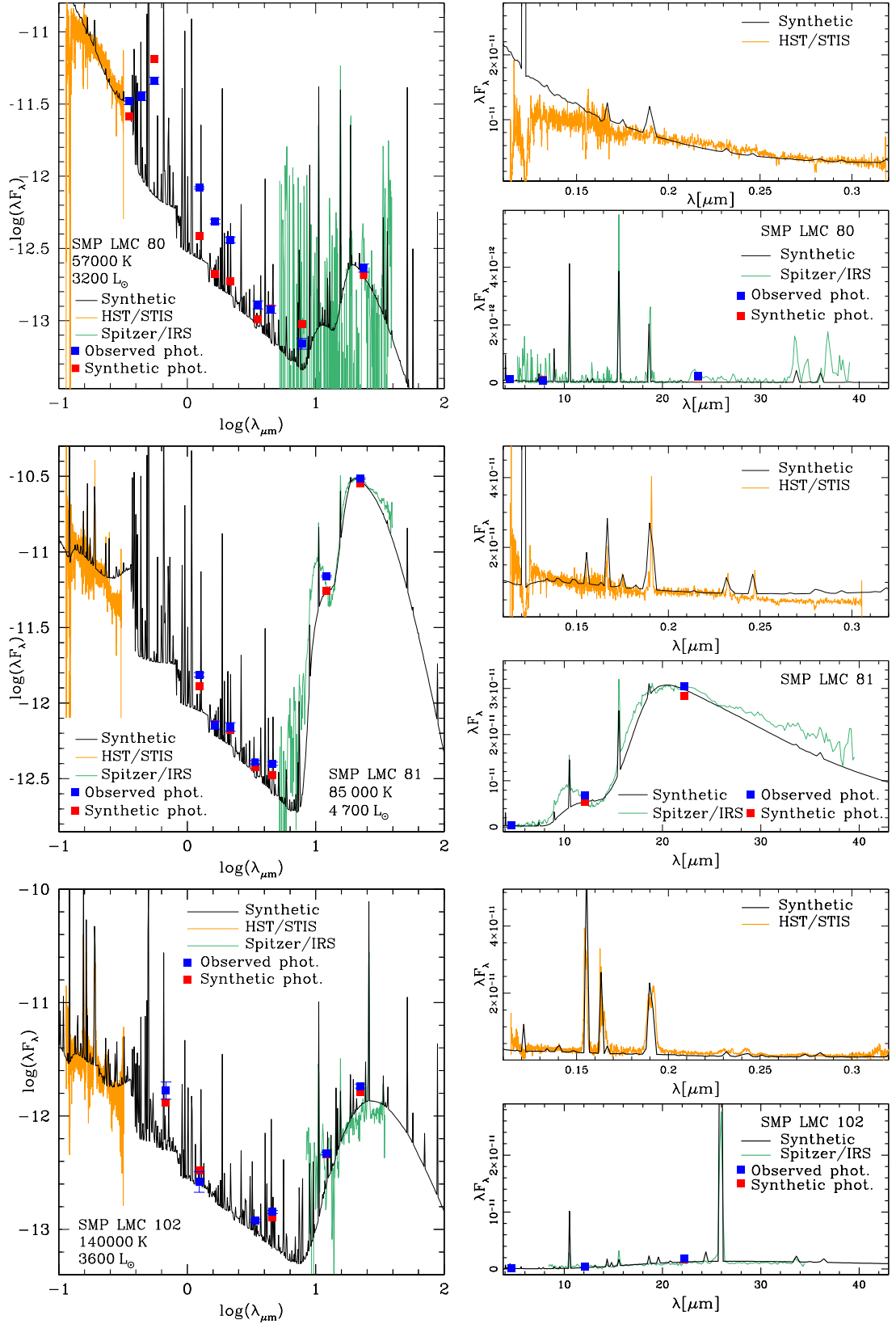


Figure 6.3: SED of a dust-free (SMP LMC 80), ORD (SMP LMC 81) and CRD (SMP LMC 102) PNe. The symbols are the same as Figs. 6.1 and 6.2.

Table 6.3: *Stellar parameter and nebula characteristics derived in the present analysis.*

ID	L/L _⊙	T _{eff} [K]	log(ΔR/[cm])	M _{gas} / M _⊙
SMP LMC 4	6500 ⁺⁶⁰⁰ ₋₁₀₀	105000 ⁺⁵⁰⁰⁰ ₋₅₀₀₀	15.68 ^{+0.03} _{-0.01}	0.034 ^{+0.002} _{-0.001}
SMP LMC 18	2000 ⁺⁷⁰⁰ ₋₅₀₀	50000 ⁺⁶⁰⁰⁰ ₋₅₀₀₀	16.37 ^{+0.08} _{-0.08}	0.086 ^{+0.020} _{-0.016}
SMP LMC 25	4900 ⁺⁴⁰⁰ ₋₂₀₀	60000 ⁺¹⁰⁰⁰⁰ ₋₁₀₀₀₀	16.45 ^{+0.01} _{-0.01}	0.110 ^{+0.003} _{-0.003}
SMP LMC 34	4500 ⁺⁸⁰⁰ ₋₆₀₀	46000 ⁺⁴⁰⁰⁰ ₋₃₀₀₀	16.95 ^{+0.01} _{-0.04}	0.282 ^{+0.009} _{-0.035}
SMP LMC 66	4500 ⁺²⁰⁰⁰ ₋₁₅₀₀	107000 ⁺⁵⁰⁰⁰ ₋₇₀₀₀	16.76 ^{+0.07} _{-0.06}	0.205 ^{+0.041} _{-0.028}
SMP LMC 71	5400 ⁺⁴⁰⁰ ₋₁₀₀	164000 ⁺⁹⁰⁰⁰ ₋₄₀₀₀	16.15 ^{+0.01} _{-0.02}	0.065 ^{+0.002} _{-0.005}
SMP LMC 80	3200 ⁺⁹⁰⁰ ₋₁₁₀₀	57000 ⁺⁵⁰⁰⁰ ₋₃₀₀₀	16.45 ^{+0.04} _{-0.04}	0.051 ^{+0.007} _{-0.005}
SMP LMC 81	4700 ⁺¹²⁰⁰ ₋₈₀₀	80000 ⁺⁴⁰⁰⁰⁰ ₋₁₅₀₀₀	16.77 ^{+0.02} _{-0.02}	0.129 ^{+0.006} _{-0.009}
SMP LMC 102	3600 ⁺⁹⁰⁰ ₋₈₀₀	140000 ⁺⁹⁰⁰⁰ ₋₁₀₀₀₀	17.29 ^{+0.03} _{-0.06}	0.370 ^{+0.042} _{-0.064}

Notes: 1– source ID; 2,3– luminosity and effective temperature of the CS; 4, 5– thickness and mass of the gas of the nebula.

Table 6.4: *Dust properties derived in the present analysis.*

CRD					
ID	$\log(\delta[\text{C}])$	$\log(\delta[\text{PAHs}])$	$T_d[\text{C}]$ [K]	$T_d[\text{PAHs}]$ [K]	$M_{\text{dust}}/M_{\odot}$
SMP LMC 4	$-2.20^{+0.07}_{-0.12}$	–	85^{+20}_{-19}	–	2.14×10^{-4}
SMP LMC 18	$-3.61^{+0.38}_{-0.01}$	$-5.04^{+0.22}_{-0.38}$	103^{+27}_{-25}	181^{+10}_{-10}	2.11×10^{-5}
SMP LMC 25	$-2.58^{+0.15}_{-0.17}$	$-3.77^{+0.30}_{-0.10}$	134^{+32}_{-30}	227^{+10}_{-10}	2.89×10^{-4}
SMP LMC 34	$-3.58^{+0.21}_{-0.10}$	$-4.89^{+0.28}_{-0.23}$	131^{+10}_{-48}	221^{+10}_{-10}	7.42×10^{-5}
SMP LMC 66	$-3.13^{+0.12}_{-0.13}$	–	102^{+38}_{-24}	–	1.52×10^{-4}
SMP LMC 71	$-2.21^{+0.15}_{-0.10}$	$-3.46^{+0.09}_{-0.19}$	114^{+23}_{-24}	197^{+10}_{-10}	4.01×10^{-4}
SMP LMC 102	$-3.52^{+0.12}_{-0.20}$	–	90^{+22}_{-21}	–	1.12×10^{-4}
ORD					
ID	$\log(\delta[\text{C}])$	$\log(\delta[\text{PAHs}])$	$T_d[\text{C}]$ [K]	$T_d[\text{PAHs}]$ [K]	$M_{\text{dust}}/M_{\odot}$
SMP LMC 81	$-2.47^{+0.09}_{-0.10}$	–	102^{+22}_{-20}	–	4.37×10^{-4}

Notes: 1– source ID; 2, 3 – logarithmic dust-to-gas mass ratio of carbon or silicate dust and PAHs; 4– carbon or silicate dust temperature; 5– PAH temperature; 6– dust mass.

2, Tab. 6.3) and effective temperatures between 46000 and 164000 K (col. 3, Tab. 6.3). The diverse morphology and structure of the nebulae result in a wide range of nebular thicknesses, with $15.68 \leq \log(\Delta R/\text{cm}) \leq 17.29$ (col. 4, Tab. 6.3). Consequently, the gas mass ranges from $0.034 M_{\odot}$ to $0.370 M_{\odot}$.

Furthermore, in the SED of five CRD PNe (SMP LMC 4, SMP LMC 18, SMP LMC 25, SMP LMC 66, and SMP LMC 71), we highlight the presence of a near-IR bump spanning wavelengths $3 \mu\text{m} \lesssim \lambda \lesssim 8 \mu\text{m}$. This distinctive feature cannot be reproduced when the dust temperature is determined self-consistently within the photoionization model.

To characterize the near-IR bump, we conducted a two-step process:

1. In the first iteration, we identified the parameters of the CS, nebula, and dust that best reproduce the SED (as detailed in Chapter 2), allowing the photoionization model to determine the dust temperature in a self-consistent manner. The resulting synthetic spectrum successfully reproduces the observed SED in the UV, optical, and mid-IR, but not the near-IR bump. The dust temperatures in this model range between 85 and 135 K.
2. Next, we ran a second model using the same parameters from the previous run but imposing a dust temperature that better matches the near-IR photometry. We assumed a pure amorphous carbon mineralogy. This second model indicates that the near-IR bump is compatible with a “hot dust” component with temperatures ranging between 600 and 800 K (see the discussion of each PN below reported for more details).

In the following paragraphs, we report the most relevant information available in the literature regarding the photometry, UV, and IR spectra used for this investigation. When available, we compare the effective temperatures derived from the SED analysis with those obtained by Villaver et al. (2003, EV03) using the Zanstra method[†]. Additionally, we describe the scheme of the synthetic models used for the SED analysis, with input parameters detailed in Tab. 6.2 and main outputs in Tab.s 6.3–6.4. It is important to note that for a few PNe, the HST and *Spitzer* spectra are noisy. This introduces challenges in the modeling process, as we must rely mainly on the photometric data.

[†]The Zanstra method, developed by Harman & Seaton (1966), assumes a stellar SED, which in EV03 is modeled as a blackbody. This method derives the total ionizing flux of the star by comparing the flux of a nebular recombination line of hydrogen or helium with the stellar continuum flux in the V-band. Specifically, it assumes that all photons above the Lyman limit of H or He+ are absorbed within the nebula and that each recombination results in a Balmer series photon. Therefore, when the He II 4686 Å line flux is available, the Zanstra method provides the stellar temperature.

SMP LMC 4

SMP LMC 4 is a moderately high excitation nebula (LS05) characterized by an elliptical shape and a faint halo (LS07). The HST spectrum is quite noisy in the region between 1500 Å and 1732 Å and shows an emission line of C III] at 1908 Å. The *Spitzer* spectrum presents nebular atomic emission lines characteristic of a very high excitation (LS07). Notable features include the [OIV] line at 26 μm and very weak emission at 11.3 μm, which could be of interstellar nature or remnants of evaporated dust (LS07; see the top panel of our Fig. 6.1).

We find an $T_{\text{eff}} = 105000^{+2000}_{-5000}$ K, in good agreement with the Zanstra temperature (HeII) reported in EV03 ($T_{\text{eff}}^{\text{HeII}} = 89900 \pm 7200$ K). For the dust, LS07 claimed a featureless spectrum, which we modeled using only amorphous carbon, obtaining a dust temperature $T_d = 85^{+20}_{-19}$ K. SMP LMC 4 is the only case in our sample where the dust temperature self-consistently calculated by CLOUDY is too low to reproduce the IR peak (see Fig. 6.1). By imposing a dust temperature, the best agreement with the observational data is obtained if $T_d = 150$ K and $\log(\delta[\text{C}]) = -3.27^{+0.04}_{-0.09}$. Furthermore, to match the mid-IR photometry, it is necessary to add a near-IR bump composed of amorphous carbon with a temperature $T_d = 630$ K. The electron temperature is $1.24 \times 10^4 < T_e[\text{K}] < 1.35 \times 10^4$.

SMP LMC 18

SMP LMC 18 is a low-excitation nebula (LS05) characterized by a round shape (LS07). The HST spectrum is quite noisy between 1500 Å and 1732 Å and shows an emission line of C III] at 1908 Å. Additionally, LS07 suggested the possible presence of broad 15 – 20 and 30 μm features (see the middle panel of Fig. 6.1).

The effective temperature of SMP LMC 18 is found to be $T_{\text{eff}} = 50000^{+6000}_{-5000}$ K. Since this value is outside the Rauch atmosphere grid (Rauch, 2003), we used the Pauldrach et al. (2001) models of atmosphere. Using these parameters, we obtained an effective temperature close to that reported in LS05, which was calculated from the UV continuum using a black body ($T_{\text{eff}}^{\text{BB}} \sim 40000$ K). Regarding the dust continuum, LS07 described a weak featureless spectrum, which we modeled using amorphous carbon and graphite. Despite the absence of PAH signatures in the noisy *Spitzer* spectrum, we included their contribution to better match the photometric point at 8 μm, finding that the best fit was achieved with $\log(\delta[\text{PAH}]) = -5.04^{+0.22}_{-0.38}$. Additionally, to reproduce the mid-IR photometry, it was necessary to add a near-IR bump composed of amorphous carbon at a temperature of $T_d = 500$ K. Finally, we found the electron temperature to be $1.17 \times 10^4 < T_e[\text{K}] < 1.21 \times 10^4$.

SMP LMC 25

SMP LMC 25 is an intermediate-excitation nebula (LS05) characterized by a round shape (LS07). The HST spectrum shows strong emission lines of C III] at 1908 Å and C II] at 2325–2329 Å (LS05). The *Spitzer* spectrum displays peaks at 6.2 and 7.7 μm, likely proto-PAH features, and a SiC emission at 11.3 μm (LS07). IR observations reveal fullerene emissions (mainly C₆₀) at 7.0, 8.5, 17.4, and 18.9 μm (García-Hernández et al., 2012) and a broad unidentified 15–20 μm feature that could be due to large PAHs or PAH clusters. SMP LMC 25 was also studied by Sloan et al. (2014), confirming the presence of fullerenes and a structure between 6 and 9 μm usually associated with PAHs. Additionally, there are two further bumps: one centered at 15–20 μm and another at 30 μm, probably due to MgS dust (Sloan et al., 2014).

We adopted a dust model based on amorphous carbon, graphite, and SiC, consistent with the carbon dust features observed in SMP LMC 25 as claimed by LS07. We also included the contribution of PAHs, with $\log(\delta[\text{PAH}]) = -3.77^{+0.30}_{-0.10}$, in agreement with Van Kerckhoven et al. (2000). Due to the strong emission at 6.2 μm (Sloan et al., 2014, see the bottom panel of our Fig. 6.1), we believe that different optical constants for PAHs (not currently available in CLOUDY) could explain the discrepancy between our synthetic photometric data at 5.6 μm and the observed data. Furthermore, to match the mid-IR photometry, it was necessary to add a near-IR bump composed of amorphous carbon with a temperature of $T_d = 780$ K. The electron temperature was found to be $7.34 \times 10^3 < T_e[\text{K}] < 1.41 \times 10^4$.

SMP LMC 34

SMP LMC 34 is a low-excitation nebula (LS05) characterized by an elliptical shape (LS07). The HST spectrum is noisy between 1500 Å and 1732 Å and shows an emission line of C III] at 1908 Å. The IR spectrum reveals a broad unidentified 30 μm feature that could be linked to MgS dust (Sloan et al., 2014) and the emission of [NeIII] at 15.6 μm (see the top panel of Fig. 6.2).

The effective temperature of SMP LMC 34 is found to be $T_{\text{eff}} = 46000^{+4000}_{-3000}$ K. Because this value is lower than 50000 K, we used Pauldrach et al. (2001) atmosphere models for the fitting. This effective temperature is lower than the EV03 measurement calculated with the Zanstra method for HeII ($T_{\text{eff}}^{\text{HeII}} = 67800 \pm 3600$ K). LS05 also highlighted this divergence and suggested a lower effective temperature around 40000 K, which aligns better with our results.

To reproduce the IR continuum, we used a combination of amorphous carbon and graphite, consistent with the featureless spectrum reported by LS07. The *Spitzer* spectrum is too noisy between 5.5 and 13 μm to confirm or rule out the presence of PAHs, but we included their contribution to better fit the photometric

data at $8\ \mu\text{m}$, finding $\log(\delta[\text{PAH}]) = -4.89^{+0.28}_{-0.23}$.

Given the large error bar on the oxygen abundance ($12 + \log(\text{O}/\text{H}) = 8.46^{+0.4}_{-0.4}$), a C/O ratio around 1 or slightly lower cannot be excluded. Therefore, we explored the SED analysis by adding silicate grains, remnants of the oxygen-rich phase, to the previous dust mixture (amorphous carbon, graphite, and PAHs). We found that the model remains reliable with $\delta[\text{C}] = 2.24 \times 10^{-4}$ and $\delta[\text{Sil}] = 4.04 \times 10^{-5}$, suggesting a possible mixed chemistry for the dust in SMP LMC 34[‡]. However, assuming pure amorphous silicate dust results in a synthetic spectrum that disagrees with the *Spitzer* spectrum and most of the observed IR photometry. For the electron temperature, we derive $8.44 \times 10^3 < T_e[\text{K}] < 1.30 \times 10^4$.

SMP LMC 66

SMP LMC 66 is a high-excitation nebula with an elliptical shape (LS07). The *Spitzer* spectrum is dominated by emission lines of [SIV] at $10.3\ \mu\text{m}$, [NeIII] at $15.6\ \mu\text{m}$, and [OIV] at $26\ \mu\text{m}$ (see Fig. 6.3). Notably, the HST spectrum and the V magnitude are absent due to the poor quality of measurements by Zaritsky et al. (2004).

To model the dust emission, we used amorphous carbon and graphite, following LS07's claim of a featureless spectrum. We found a discrepancy between the observed and synthetic photometric data at $8\ \mu\text{m}$. We believe that PAH emission at $7.85\ \mu\text{m}$, commonly observed in many PNe (Sloan et al., 2014), could help bridge this gap (see the middle panel of Fig. 6.2). This nebula also exhibits a near-IR bump, which we modeled by including amorphous carbon with a temperature of $T_d = 550\ \text{K}$. For the electron temperature, we find $1.28 \times 10^4 < T_e[\text{K}] < 1.46 \times 10^4$.

SMP LMC 71

SMP LMC 71 is a high-excitation nebula characterized by an elliptical shape (LS07). The HST spectrum shows emission lines of C III] at $1908\ \text{\AA}$ (see the bottom panel of Fig. 6.2). LS05 initially claimed a moderately high-excitation nature of the nebula based on the UV spectrum, but another scenario becomes evident when examining the *Spitzer* spectrum, which reveals a very high excitation (LS07). The IR spectrum contains a forest of emission lines, including a broad, unidentified feature at $6\text{--}9\ \mu\text{m}$, possibly due to small grain clusters, superimposed on narrow features at 6.2 , 7.7 , and $8.6\ \mu\text{m}$, characteristic of classical PAHs (LS07). In agreement with LS07, we also see a possible $30\ \mu\text{m}$ feature (see

[‡]Several observations have identified the presence of mixed-chemistry dust in PNe (Górny & Tylenda, 2000; García-Hernández & Górny, 2014). However, its origin remains a subject of debate (Perea-Calderón et al., 2009; Guzman-Ramirez et al., 2014).

the middle-right panel of Fig. 6.2) that could be due to MgS dust (Sloan et al., 2014). The V magnitude is absent due to the poor quality flag of the measurement by Zaritsky et al. (2004) (see the middle-left panel of Fig. 6.2).

The effective temperature is found to be $T_{\text{eff}} = 164000^{+9000}_{-4000}$ K, which is higher than the Zanstra method value for He II given in EV03 ($T_{\text{eff}}^{\text{HeII}} = 83400 \pm 5200$ K). This discrepancy is reasonable since their measurement is based on a lower limit in the V magnitude (see Tab. 3 of EV03). For the dust, LS07 noted the presence of carbon dust features superimposed on the dust continuum emission, aligning with our description using amorphous carbon, graphite, PAHs, and other components. We believe our choice of optical constants might not be optimal for reproducing the central peak of the dust. To achieve the photometric point at $5.6 \mu\text{m}$, it would be necessary to use new optical constants beyond those built into CLOUDY. Specifically, we think the PAH emission at $6.2 \mu\text{m}$, recognized in SMP LMC 25 (Sloan et al., 2014), could help fill the gap in that region (see the top panel of Fig. 6.3). However, using the mineralogy described above, we find $\log(\delta[\text{C}]) = -2.21^{+0.15}_{-0.10}$ and $\log(\delta[\text{PAH}]) = -3.46^{+0.09}_{-0.19}$. This nebula shows a near-IR bump reproduced by including amorphous carbon with temperature of $T_d = 680$ K. From the SED analysis, we also find $1.4 \times 10^4 < T_e[\text{K}] < 1.5 \times 10^4$.

SMP LMC 80

SMP LMC 80 is a low-excitation nebula (LS05) characterized by a round shape (LS07). The HST spectrum is quite noisy in the region between 1077 \AA and 1732 \AA . The *Spitzer* spectrum shows intermediate-excitation emission lines (LS07), with strong emission of [NeIII] at $15.6 \mu\text{m}$ and [SIII] at $18.7 \mu\text{m}$ (see the top panel of Fig. 6.3).

We struggled to align our model with most of the photometric data, possibly due to the nebula's ring shape, visible in [NII] (Shaw et al., 2001). For the dust, we confirm the featureless spectrum reported by LS07, modeling the *Spitzer*/IRS spectrum with a negligible amount of amorphous silicate dust. The current T_{eff} is much higher than those typical of the AGB phase when the dusty layer forms; therefore, we suggest that the already low amount of dust formed during its evolution could have been completely destroyed in the PN phase. Additionally, we find $1.25 \times 10^4 < T_e[\text{K}] < 1.34 \times 10^4$.

SMP LMC 81

SMP LMC 81 is an intermediate-excitation nebula (LS05) characterized by a round shape (LS07). The HST spectrum is quite noisy between 1077 \AA and 1732 \AA and shows emission lines of C III] at 1908 \AA and HeII at 1640 \AA . The *Spitzer* spectrum reveals nebular emission lines of intermediate excitation (LS07)

and distinct amorphous silicate features at approximately 9.8 and 18 μm (see the middle panel of Fig. 6.3). Using the built-in CLOUDY optical constants, we cannot perfectly model the amorphous silicate feature at around 9.8 μm . However, this does not affect the determination of the primary parameters of the central star, nebula, and dust, which is the main goal of this work.

Regarding the dust, LS07 identified an ORD chemistry, which we model to be amorphous silicates. From the SED analysis, we derive $8.28 \times 10^3 < T_e[\text{K}] < 1.61 \times 10^4$.

SMP LMC 102

SMP LMC 102 is a high-excitation nebula (LS05) with a round shape (LS07). The HST spectrum prominently features emission lines of CIV at 1548 Å, HeII at 1640 Å, and C III] at 1908 Å. In the *Spitzer* spectrum, a significant emission line from [OIV] at 26 μm was observed (see the lower-right panel of Fig. 6.3). Photometric data from *Spitzer* and the U, B, V measurements from Reid (2014) are not available (see the bottom panel of Fig. 6.3).

The effective temperature is found to be $T_{\text{eff}} = 140\,000^{+2\,300}_{-2\,000}$ K, consistent with the Zanstra temperature for HeII reported by EV03 ($T_{\text{eff}}^{\text{HeII}} = 131\,800 \pm 12\,400$ K). For the dust, LS07 identified a featureless spectrum, which we modeled using only amorphous carbon. From the SED analysis, we derive an electron temperature of $1.39 \times 10^4 < T_e[\text{K}] < 1.71 \times 10^4$.

In conclusion, we found that the IR excess of the PN sources of our sample can be modeled primarily in terms of carbonaceous dust for all but three PNe in our sample. The exceptions are SMP LMC 80, which shows no evidence of dust emission, SMP LMC 81, which displays a clear signature of silicate dust, and SMP LMC 34, for which the presence of a small quantity of silicate dust, in addition to carbonaceous dust, cannot be ruled out. The IR spectra of the seven CRD PNe in our sample show the presence of amorphous carbon, graphite, and in some sources, unidentified IR features, fullerenes, as well as emissions attributable to SiC and PAHs (see Sec. 6.1).

According to Sloan et al. (2014), PAHs are grouped into three different classes. Class B PAHs, which Peeters et al. (2002) identified as the most frequent in PNe, are characterized by emissions at 7.85 μm (Sloan et al., 2014). In alignment with this classification, we find that most of our CRD PNe exhibit signatures indicative of the presence of class B PAHs. This includes SMP LMC 25 and SMP LMC 71, which have been previously studied for their PAH features by Stanghellini et al. (2007). Despite noisy *Spitzer* spectra at wavelengths $5.5 < \lambda [\mu\text{m}] < 13$, SMP

LMC 18 and SMP LMC 34 also appear to show traces of PAH emission. Including the contribution from PAHs in our models provides a better fit to the photometric point at $8\ \mu\text{m}$.

Furthermore, as noted by Sloan et al. (2014), we observe the presence of the $6.2\ \mu\text{m}$ PAH feature in SMP LMC 25, which could explain the deviation seen in the photometric filter at $5.6\ \mu\text{m}$ (see Fig. 6.1). We believe SMP LMC 71 also exhibits this emission, which helps reconcile the differences between synthetic and observed photometry at $5.6\ \mu\text{m}$ (see Fig. 6.2). Three sources (SMP LMC 18, SMP LMC 25, and SMP LMC 34) exhibit an unidentified broad $26\text{--}30\ \mu\text{m}$ feature (the $30\ \mu\text{m}$ feature), which could be explained by MgS dust (for details, see Sloan et al., 2014). Additionally, for these objects, we observe another unidentified broad IR feature around $15\text{--}20\ \mu\text{m}$ (for details on each PN and comparisons with the literature, see next the description of each PN below).

6.2 Understanding the progenitor’s mass

We aim to reconstruct the evolutionary history of stellar targets from the AGB to the PN phase. To achieve this, we have expanded the ATON model library (see Sec. 1.4), including new evolutionary tracks that extend to the PN phase. This expansion provides a more comprehensive set of tracks covering a broader range of masses and metallicities. Specifically, our models range from 0.6 to $2.5\ M_{\odot}$ with metallicities from $Z = 10^{-3}$ to $Z = 8 \times 10^{-3}$. These mass values are defined at the beginning of the AGB phase, to mitigate potential issues related to uncertainties in mass-loss during the red giant branch phase, which is particularly important for determining the initial masses of stars with $M \lesssim 1.2\ M_{\odot}$ (see Sec. 1.1 for more details). To achieve a robust derivation of the progenitor’s mass of each CS, we conducted a two-step method:

1. We first characterized the sources by comparing the observed C and O abundance measurements (see Tab. 6.2) with the surface chemical abundances predicted by ATON models for various masses and metallicities. In Tab. 6.5 we present a grid of models specifically calculated for this analysis, refining the grid for those values of metallicity and mass that were most consistent with the observational constraints. This comparison is illustrated in Fig. 6.4, where we plot the C/H vs O/H abundances in spectroscopic notation. Here, the observed data are represented by gray diamonds, while the ATON model results are shown with colored symbols, each shape corresponding to a different metallicity. The ATON abundances are taken at the end of the AGB evolution, while the progenitor masses are those at the beginning of the AGB phase. In Fig. 6.4, the dashed line indicates $C/O = 1$, with

Table 6.5: *ATON models of different metallicities ($Z=8\times 10^{-3}$, 4×10^{-3} , 2×10^{-3} , and 1×10^{-3}).*

Progenitor's mass [M_{\odot}]	12+log(C/H)	12+log(O/H)
$Z=8\times 10^{-3}$		
2.5	9.18	8.65
2.0	8.87	8.62
1.5	8.66	8.59
$Z=4\times 10^{-3}$		
1.5	8.79	8.33
1.25	8.66	8.31
1.0	8.62	8.31
0.9	8.46	8.29
0.8	7.73	8.26
0.7	7.74	8.26
0.6	7.72	8.26
$Z=2\times 10^{-3}$		
1.25	8.96	8.11
1.0	8.59	8.05
0.9	8.35	8.04
0.85	8.20	8.02
0.8	8.21	8.02
$Z=1\times 10^{-3}$		
0.8	8.70	7.84
0.75	6.96	7.69
0.7	6.94	7.69

Notes: *The progenitor's mass is expressed at the beginning of the AGB phase; the abundances of carbon and oxygen are those at the end of the AGB phase.*

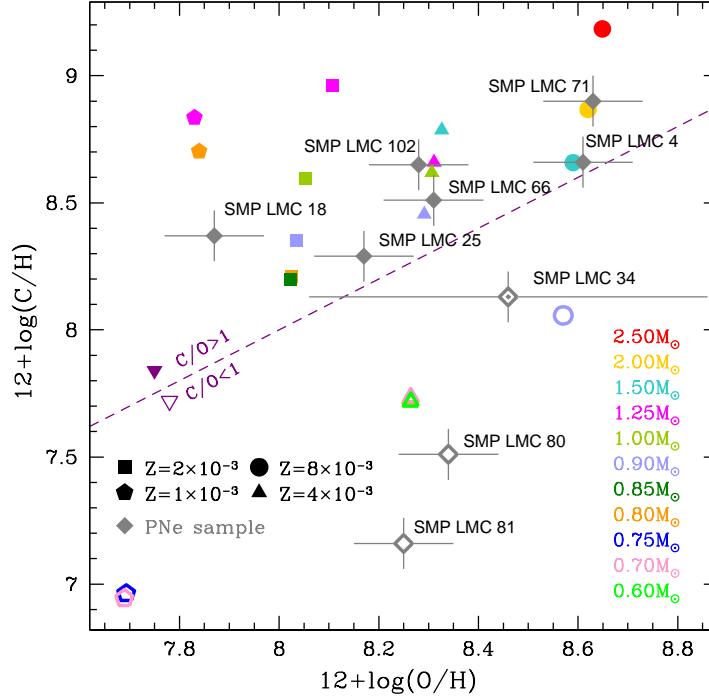


Figure 6.4: Comparison of the carbon and oxygen abundances observed for the PN sample (gray diamonds) and those computed with the ATON code at the end of the AGB evolution (colored symbols). Different shapes of the model represent different metallicities. Full and open symbols refer to C/O ratios greater and smaller than unity, respectively. The C/O of SMP LMC 34 is undefined due to the large oxygen error bars. The dashed line separates the oxygen-rich from the carbon-rich sources.

carbon-rich sources placed above this line. Due to the significant error bar for oxygen, the C/O ratio for SMP LMC 34 is undefined (see Tab. 6.2); it is depicted with an open symbol containing a central dot.

By comparing the observed data and model predictions in the C/H versus O/H plane, we can infer the nature of the PN progenitors. In the mass regime below $4 M_{\odot}$, carbon abundance is a crucial indicator for determining progenitor’s mass of post-AGB stars and PNe (Fig. 1.4). Indeed, stars with higher masses ($2\text{--}3 M_{\odot}$) end their AGB phase with a higher surface carbon fraction compared to their lower-mass counterparts, due to the greater number of TDU episodes they undergo before completely losing their envelopes. Consistent with previous findings of Ventura et al. (2015), we conclude that, given the strong agreement among different evolutionary codes regarding the final surface carbon mass fraction in the low-mass regime (Ventura et

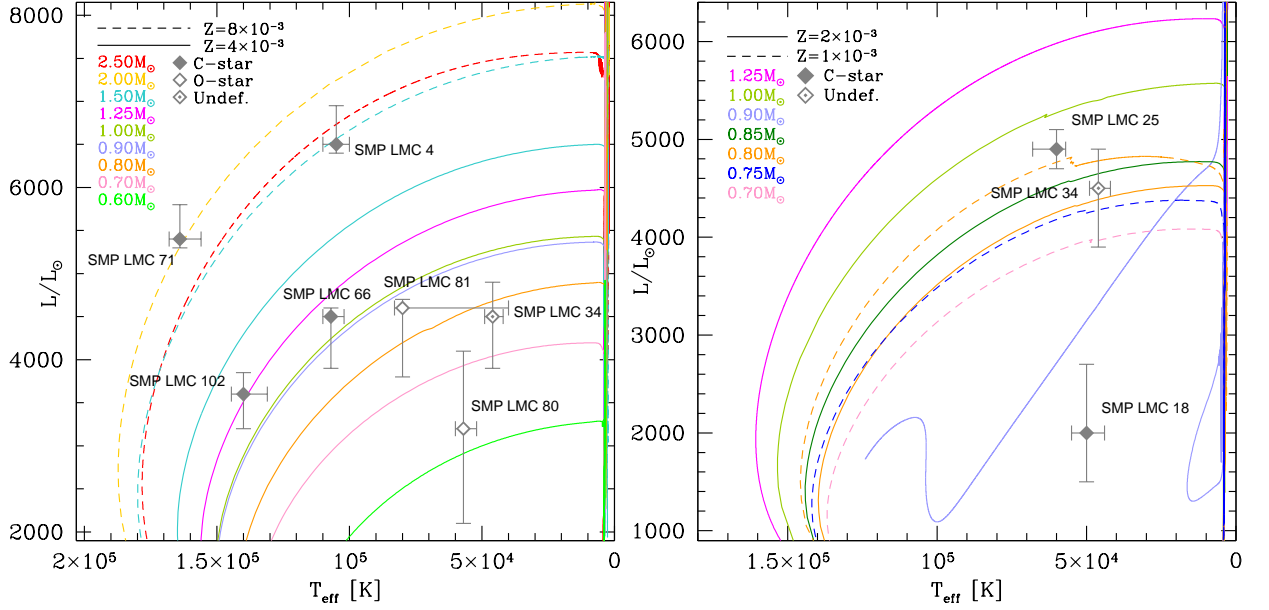


Figure 6.5: Evolutionary tracks calculated with the stellar evolution code ATON (Ventura et al., 1998) for different masses (different colors), expressed at the beginning of the AGB phase. The solid lines are the $Z = 4 \times 10^{-3}$ (left panel) and $Z = 2 \times 10^{-3}$ (right panel) and the dashed lines are the $Z = 8 \times 10^{-3}$ (left panel) and $Z = 1 \times 10^{-3}$ (right panel). The gray diamonds are the PN sample with the luminosities and effective temperatures derived in this paper. Full and open symbols refer to C/O ratios greater and less than unity, respectively. Due to the large oxygen error bar, the C/O of SMP LMC 34 is undefined.

al., 2018; Fishlock et al., 2014) and the small uncertainties in the C/H measurements, carbon abundances provide robust constraints for characterizing the progenitor mass (see also Fig. 1.4).

We determined the metallicity of each PN by comparing its oxygen abundance with the theoretical abundances from different sets of ATON models with varying metallicities. The results of this comparison are shown in Fig. 6.4. We observed that the oxygen surface abundance is slightly enhanced during the TDU episodes experienced by LIMSSs, as illustrated in the lower right panel of Fig. 1.4. However, this variation is minor (less than 0.1 dex) compared to the differences between the metallicities (greater than 0.2 dex). The accuracy of the measured oxygen abundance is sufficient to distinguish between different metallicities, with the exception of SMP LMC 34, which is discussed in detail in Sec. 6.2.

2. After identifying the progenitor mass and metallicity of each target based

on the chemical abundances, we compared the luminosity and effective temperature derived from the SED modeling of each PN with the ATON evolutionary tracks of the corresponding metallicity. This comparison is depicted in Fig. 6.5, where we plot the results of each PN in the H–R diagram, displaying the PN phase and variations in metallicity (reported with different line shapes). This comparison is fundamental for two reasons:

- It highlights the consistency between the physical parameters derived from the SED analysis and the progenitor mass determined from the carbon and oxygen measurements.
- It identifies the track that best reproduces the evolutionary history of each target, thereby creating a link to their previous evolution in the AGB phase.

In agreement with the discussion presented in Sec. 1.3.2, Fig. 6.5 shows that for a fixed metallicity and effective temperature, higher luminosities generally correspond to higher masses. However, this trend does not apply to stars experiencing LTP, where the late ignition of the helium shell leads to lower luminosities compared to standard post-AGB evolution (Sec. 1.3.1). For instance, the $0.9 M_{\odot}$ model at $Z = 2 \times 10^{-3}$ shows this behavior when reaching effective temperatures of around 15000 K (see the right panel of Fig. 6.5). Similarly, the $2.5 M_{\odot}$ model at $Z = 4 \times 10^{-3}$ also deviates from the expected luminosity-mass correlation (see the left panel of Fig. 6.5). This deviation can be explained from Fig. 6.6, where we illustrate the variation in surface carbon abundance (left panel) and core mass (right panel) as functions of the current stellar mass for three models: 1.5, 2.0, and $2.5 M_{\odot}$. Indeed, for the $2.5 M_{\odot}$ model, when the star’s mass is approximately $2 M_{\odot}$, the depth of the convective envelope during the TDU episode significantly reduces the core mass, making it lower than that of the $2 M_{\odot}$ model. This reduction causes the $2.5 M_{\odot}$ star to evolve at a lower luminosity compared to its $2 M_{\odot}$ counterpart. The surface carbon and oxygen abundances at the end of the AGB phase for all models are detailed in Tab. 6.5.

The combination of all the information from Figs. 6.5 and 6.4 enables the determination of the progenitor mass for each PN, which are reported along with the metallicities in Tab. 6.6. The uncertainties in the progenitor mass determination are primarily constrained by the chemical abundance studies, which, as shown in Fig. 6.4, allow for a precise estimation of the progenitor mass, with uncertainties of approximately $\leq 0.5 M_{\odot}$. The detailed analysis for each PN is discussed in the following subsections.

Table 6.6: *Progenitor mass at the beginning of the AGB phase and the metallicity obtained for each PN in the sample studied.*

ID	M/M _⊙	Z
SMP LMC 4	1.5	8×10^{-3}
SMP LMC 18	0.8–0.9	$1 - 2 \times 10^{-3}$
SMP LMC 25	0.9	2×10^{-3}
SMP LMC 34	0.8 – 0.9	$2 - 4 \times 10^{-3}$
SMP LMC 66	0.9– 1.0	4×10^{-3}
SMP LMC 71	2.0	8×10^{-3}
SMP LMC 80	$\lesssim 0.8$	4×10^{-3}
SMP LMC 81	$\lesssim 0.8$	4×10^{-3}
SMP LMC 102	1.25	4×10^{-3}

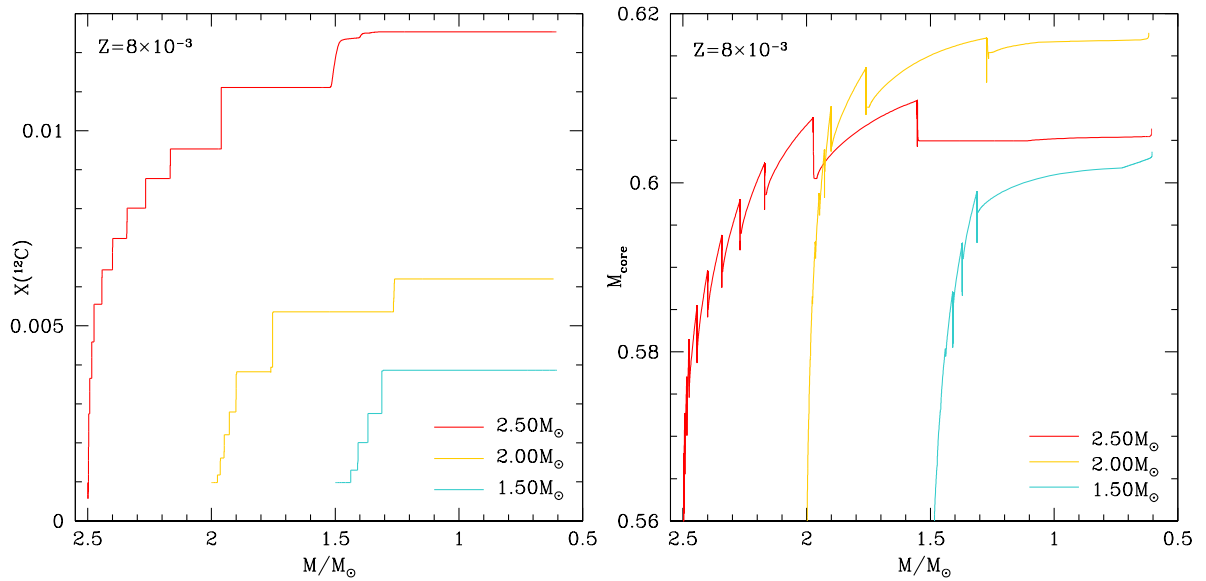


Figure 6.6: Evolution of stellar parameters as a function of the current mass of the CS, for three models at $Z = 8 \times 10^{-3}$. The left panel displays the surface carbon mass fraction for the $2.5 M_\odot$ model (red), $2.0 M_\odot$ (yellow), and $1.5 M_\odot$ (cyan). The right panel shows the core mass variation for the same models reported in the left panel.

Carbon-rich, intermediate-mass stellar progenitors

As illustrated in Fig. 6.4, oxygen measurements indicate that SMP LMC 71 and SMP LMC 4 have a metallicity of $Z = 8 \times 10^{-3}$. Our SED analysis has determined that their CSs have effective temperatures of 164000 K and 105000 K, respectively. These sources are the most luminous in the sample, with SMP LMC 71 reaching $5400 L_\odot$ and SMP LMC 4 reaching $6500 L_\odot$ (see Tab. 6.3). Due to their high luminosities, they are positioned in the upper region of the H-R diagram (left panel, Fig. 6.5), corresponding to progenitor masses of approximately $2.0 M_\odot$ for SMP LMC 71 and approximately $1.5 M_\odot$ for SMP LMC 4. These estimates align with those derived from the carbon and oxygen abundances presented in Fig. 6.4.

This characterization suggests that SMP LMC 71 and SMP LMC 4 are intermediate-mass stars that experienced several TDU episodes, enriching their surfaces with carbon and promoting the formation of carbon dust. Additionally, SMP LMC 71 and SMP LMC 4 exhibit the highest dust-to-gas mass ratio $\delta[\text{C}]$ among the studied PNe (see Tab. 6.4), further supporting this interpretation.

Carbon-rich, low-mass stellar progenitors

SMP LMC 66 and SMP LMC 102 are two PNe with a metallicity of $Z = 4 \times 10^{-3}$ (see Fig. 6.4). The characteristics of SMP LMC 102 have been extensively discussed in Dell’Agli et al. (2023b), where a progenitor mass of $1.25 M_{\odot}$ was estimated. Consistent with this finding, our analysis of the SED reveals a luminosity of $3600 L_{\odot}$ and an effective temperature of 140000 K (see Tab. 6.3). These parameters place SMP LMC 102 on the expected evolutionary track (see the left panel of Fig. 6.5). Additionally, the progenitor’s mass of $1.25 M_{\odot}$ for SMP LMC 102 is also consistent with the carbon and oxygen surface abundances derived from our models (see Fig. 6.4).

SMP LMC 66 lacks an observed HST/STIS spectrum, resulting in greater uncertainty regarding its luminosity ($L=4500_{-1500}^{+2000} L_{\odot}$). Based on the carbon and oxygen abundances shown in Fig. 6.4, we suggest that SMP LMC 66 follows a similar evolutionary path to SMP LMC 102, with a progenitor mass range of $0.9 - 1.0 M_{\odot}$. Both SMP LMC 66 and SMP LMC 102 descend from low-mass carbon stars that experienced a few TDU episodes, allowing their progenitors to reach the carbon star ($C/O > 1$) phase.

The metallicity of SMP LMC 25 is estimated to range between 2×10^{-3} and 4×10^{-3} based on the oxygen abundance in (Leisy & Dennefeld, 2006). The most probable metallicity of SMP LMC 25 is closer to the lower limit ($Z \sim 2 \times 10^{-3}$). This inference is drawn from the discrepancy between a higher dust-to-gas ratio in SMP LMC 25 compared to SMP LMC 66 and SMP LMC 102, which would be inconsistent with a higher metallicity. If SMP LMC 25 had a metallicity closer to the upper limit, its progenitor mass would be around $\sim 0.8 M_{\odot}$ (see Fig. 6.4), contradicting the observed high dust-to-gas ratio.

Considering a luminosity of $4900 L_{\odot}$ and an effective temperature of 60000 K derived from SED analysis, the PN progenitor mass for $Z = 2 \times 10^{-3}$ is estimated to be $\sim 0.85 M_{\odot}$, consistent with the carbon and oxygen abundances presented in Fig. 6.4.

SMP LMC 34: The lower limit to the carbon-rich stellar phase

The CS of SMP LMC 34 has a luminosity of $4500 L_{\odot}$ and an effective temperature of $46,000 \text{ K}$. However, characterizing its metallicity is more challenging compared to other PNe due to the significant uncertainty in the reported oxygen abundance ($12 + \log(O/H) = 8.46_{-0.4}^{+0.4}$) as shown in Fig. 6.4.

Despite this, the presence of carbonaceous dust strongly suggests that SMP LMC 34 underwent a carbon-rich phase during its evolution. This, along with the measured carbon abundance, provides valuable constraints on the metallicity of this PN. In the AGB phase, stars with $Z = 8 \times 10^{-3}$ that reach the carbon star stage

typically have masses $M > 0.9 M_{\odot}$, resulting in PNe with higher surface carbon abundances ($12 + \log(C/H) > 8.2$) than what is measured for SMP LMC 34.

Conversely, stars with masses between $0.8 M_{\odot}$ and $0.9 M_{\odot}$ within the metallicity range of 2×10^{-3} to 4×10^{-3} are known to reach the carbon star stage during the AGB phase. Their evolution exhibits luminosities, effective temperatures, and surface carbon and oxygen abundances that are compatible with the values measured for SMP LMC 34. Therefore, the most probable metallicity for SMP LMC 34 falls within the range $2 \times 10^{-3} < Z < 4 \times 10^{-3}$.

SMP LMC 18: A late thermal pulse source

Based on its oxygen abundance, SMP LMC 18 has a metallicity between 10^{-3} and 2×10^{-3} . From the SED analysis, we determined a CS luminosity of $2000 L_{\odot}$ and an effective temperature of 50000 K . SMP LMC 18 has the lowest luminosity within the sample, suggesting an oxygen-rich progenitor star. However, the IR spectrum shows clear signatures of carbon dust presence (see the middle panels of Fig. 6.1). Additionally, the $C/O > 1$ ratio indicates that the progenitor star experienced a carbon-rich phase during its evolution.

The combination of its low luminosity and the presence of carbon-rich nebular gas and dust renders SMP LMC 18 a peculiar object. A plausible explanation for this anomaly is that this PN derives from a star experiencing a late thermal pulse episode, causing it to evolve at a lower luminosity. This scenario aligns with the evolutionary track of a star with a mass of $0.9 M_{\odot}$ and a metallicity of $Z = 2 \times 10^{-3}$, as shown in the right panel of Fig. 6.5. A progenitor with these characteristics would be consistent with the observed abundances of SMP LMC 18 (see Fig. 6.4).

The oxygen-rich sources

SMP LMC 81 and SMP LMC 80 exhibit a C/O ratio of less than 1. The metallicity, derived from the comparison of observed abundances with the surface abundances at the end of the AGB phase computed using the ATON code, is $Z = 4 \times 10^{-3}$ (see Fig. 6.4). From the SED analysis, we find their luminosities to be $4700 L_{\odot}$ and $3200 L_{\odot}$, with effective temperatures of 80000 K and 57000 K , respectively. These values position them in the lower part of the H-R diagram (right panel of Fig. 6.5), indicative of progenitor masses of $\lesssim 0.8 M_{\odot}$.

In this mass range, the envelope thickness is so low that a small variation in surface carbon could result in a significant difference in the final C/O ratio. Consequently, the derived progenitor mass is subject to greater uncertainty.

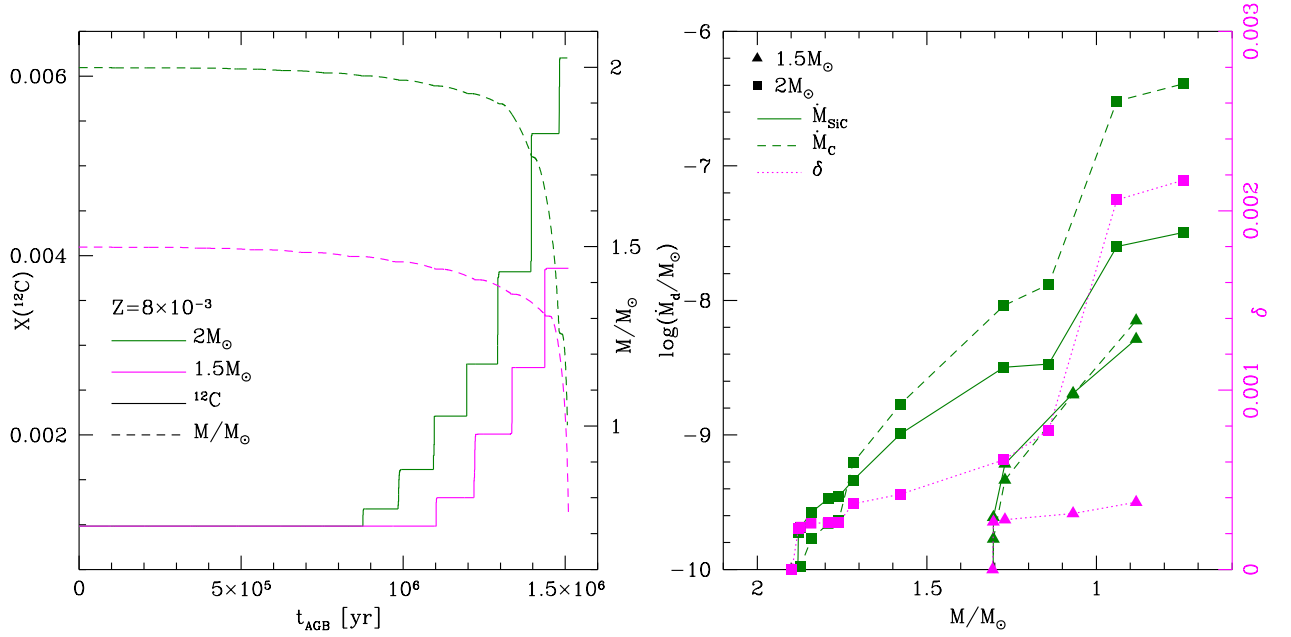


Figure 6.7: Time variation of physical properties of $1.5 M_\odot$ and $2 M_\odot$ models of $Z = 8 \times 10^{-3}$. In the left panel, the surface carbon mass fraction (left scale) is shown with a solid line, while the total mass (right scale) is represented by a dashed line. The green line corresponds to the $2M_\odot$ model, and the magenta line to the $1.5M_\odot$ model. In the right panel, the dashed line illustrates the time variation of carbon, while the solid line represents SiC. The individual points mark the inter-pulse phases, with triangles indicating the $1.5M_\odot$ model and squares representing the $2M_\odot$ model. The magenta lines and points highlight the variation of the dust-to-gas ratio (scale on the right).

6.3 PNe in the LMC and their link to their previous history of dust production

Seven of the nine PNe studied are the descendants of carbon stars, with SMP LMC 80 and SMP LMC 81 being the exceptions, as they are oxygen-rich. In this Section, we aim to explore the relationship between the properties of the whole sample of PNe, particularly their gas and dust content, and the mass and metallicity of their progenitor stars as determined in the previous Section (see Tab. 6.6). This will help us better understand the mechanisms of dust production during the late AGB phases and shed new light on the physical processes affecting the stars and their surrounding material from the AGB phase through to the PN stage.

Among the carbon-rich sources, SMP LMC 4 and SMP LMC 71 are identified as descendants of stars with masses of $1.5 M_\odot$ and $2 M_\odot$, respectively, and

metallicities of $Z = 8 \times 10^{-3}$ (Tab. 6.6). Figure 6.7 shows the evolution of key properties for these stars, derived from a combination of stellar evolution and dust formation models, as outlined in Section 2.

Specifically, in the left panel of Fig. 6.7, we observe the increasing of the surface carbon abundance following each TP and TDU event, with the final carbon mass fraction reaching approximately 4×10^{-3} for the $1.5 M_{\odot}$ star and 6×10^{-3} for the $2 M_{\odot}$ star. The evolution as a carbon star is limited to the last three inter-pulse phases for the $2 M_{\odot}$ model, whereas the $1.5 M_{\odot}$ star only becomes a carbon star during its final inter-pulse phase. The dashed lines in the figure, representing total mass, reveal a significant increase in the mass-loss rate once the stars reach the carbon-rich stage. Indeed, approximately 90% of the envelope mass is lost during this final C-star phase.

The right panel of Fig. 6.7 focuses on the dust production properties for the two model stars. It shows the evolution of the dust production rate (split between solid carbon and SiC components, reported with a green dashed and solid lines, respectively) and the dust-to-gas ratio, which is calculated as the ratio of dust formation rate to mass-loss rate (magenta line). We note that in this panel we use the current stellar mass as a time indicator.

In the early phases after the stars become carbon-rich, the formation of SiC is initially as efficient as, or even more efficient than, that of carbon dust. This is because the carbon excess relative to oxygen, a crucial factor in carbon dust formation (Ferrarotti & Gail, 2006), is initially smaller than the available silicon required to form SiC grains. However, as the AGB evolution progresses, the contribution of SiC to the total dust production decreases due to the repeated TDU events, which continue to increase the surface carbon abundance.

For the models presented here, the dust-production rate (DPR) during the final AGB phases reaches approximately 10^{-8} and $5 \times 10^{-7} M_{\odot}/\text{yr}$ for the $1.5 M_{\odot}$ and $2 M_{\odot}$ stars, respectively. The corresponding dust-to-gas ratios are about 5×10^{-4} for the $1.5 M_{\odot}$ star and 2×10^{-3} for the $2 M_{\odot}$ star.

As discussed in Sec. 6.2, the sources SMP LMC 66 and SMP LMC 102 have been identified as descendants of stars with a metallicity of $Z = 4 \times 10^{-3}$ and initial masses of $1 M_{\odot}$ and $1.25 M_{\odot}$, respectively. The evolutionary tracks for these stars are shown in Fig. 6.8, displaying the same quantities as Fig. 6.7. In both models, the C-star phase is confined to the final two inter-pulse phases. The final surface carbon abundances fall within the range of 3×10^{-3} to 4×10^{-3} , slightly lower than in the higher-mass cases discussed earlier, consistent with the trend of decreasing final carbon abundance as the initial stellar mass decreases (see also the lower-left panel of Fig. 1.4).

In line with this, and as covered in Sec. 1.2.4 and shown in Fig. 2.1, the DPR in these lower-mass stars is reduced compared to their higher-mass counterparts. The final dust production rates (\dot{M}_{dust}) are approximately $3 \times 10^{-9} M_{\odot}/\text{yr}$ for the

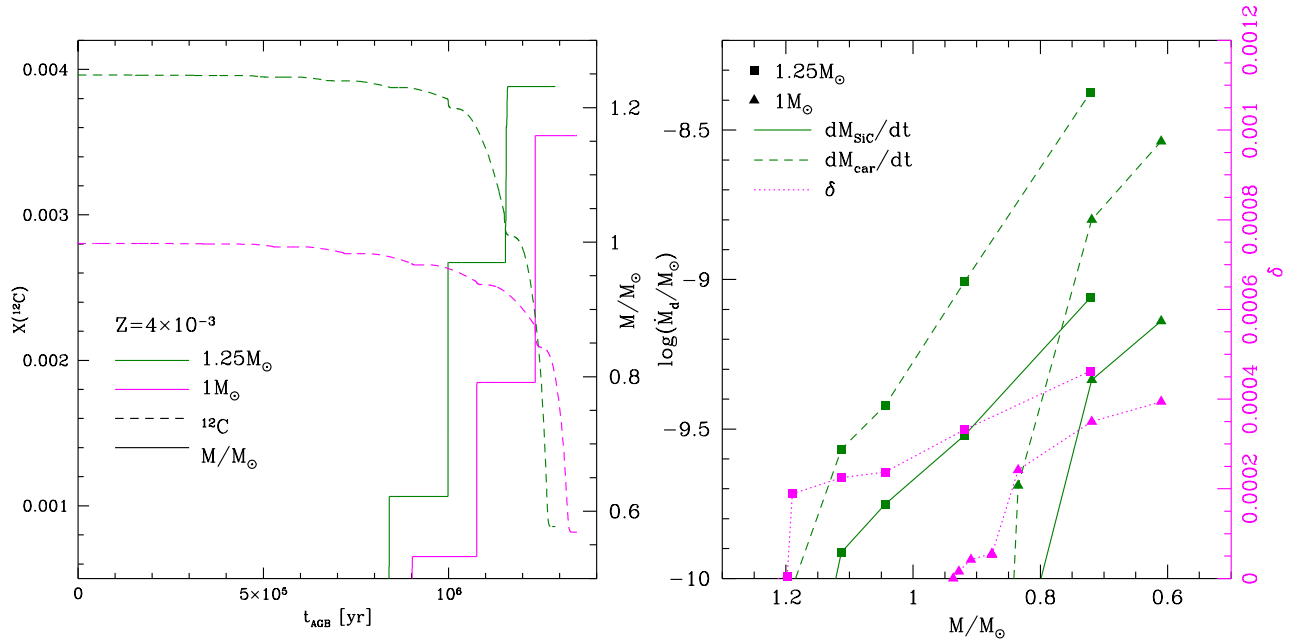


Figure 6.8: Time variation of physical properties of $1M_\odot$ (magenta lines) and $1.25 M_\odot$ (green lines) model stars with a metallicity of $Z = 4 \times 10^{-3}$. In the left panel, the surface carbon mass fraction (left scale) is shown with a dashed line, while the total mass (right scale) is represented by a solid line. In the right panel, the dashed line illustrates the time variation of carbon, while the solid line represents SiC. The individual points mark the inter-pulse phases, with triangles indicating the $1.5M_\odot$ model and squares representing the $2M_\odot$ model. The magenta lines and points highlight the variation of the dust-to-gas ratio (scale on the right)

$1 M_\odot$ star and $5 \times 10^{-9} M_\odot/\text{yr}$ for the $1.25 M_\odot$ star, assuming the carbon DPR is representative of the total dust formed. As shown in the right panel of Fig. 6.8 and detailed in Tab. 6.4, the final dust-to-gas ratio is about 4×10^{-3} for the $1 M_\odot$ star and around 5×10^{-3} for the $1.25 M_\odot$ star.

The sources SMP LMC 18, SMP LMC 25, and SMP LMC 34, discussed in the previous Section, have been linked to the evolution of low-metallicity stars ($Z \sim 0.002$) with masses around $0.9 M_\odot$. In the low-metallicity regime, these masses are just above the threshold required to transition into the C-star phase (see Fig. 6.4). The typical evolutionary track of such a star is illustrated in Fig. 6.9, where we present the evolution of surface carbon, stellar mass, and overall dust production rate. The figure shows that the majority of the envelope mass-loss occurs during the final two inter-pulse phases, coinciding with the star's evolution as a C-star. The final surface carbon abundance reaches $\sim 2 \times 10^{-3}$, while the peak dust production rate, attained near the end of the AGB phase, is approximately $2.5 \times 10^{-9} M_\odot/\text{yr}$. This is significantly lower than the dust production rates

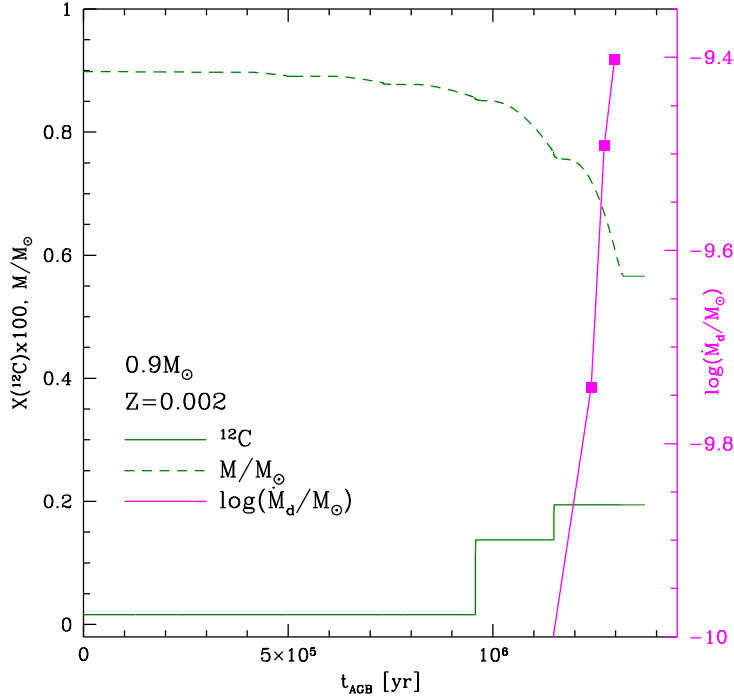


Figure 6.9: Time variation of physical properties of a $0.9 M_{\odot}$ model star of metallicity $Z = 2 \times 10^{-3}$. The green solid line represents the surface carbon mass fraction, the green dashed line indicates the total mass, and the magenta line corresponds to the dust production rate (scale on the right).

observed in higher-mass counterparts, as shown in Fig. 6.7 and Fig. 6.8.

We conclude this review of the sources studied in Sec. 6.2 with SMP LMC 80 and SMP LMC 81, which were identified as the progeny of low-mass stars that never reached the C-star phase. As detailed in Tab. 6.6, SMP LMC 81 originates from a $Z = 4 \times 10^{-3}$ progenitor with a mass of approximately $0.8 M_{\odot}$, while SMP LMC 80 descends from a $\sim 0.6 M_{\odot}$ star of similar metallicity.

Fig. 6.10 illustrates the key aspects of the evolution for these stars, showing the time evolution of both stellar mass and luminosity for each source. Dust production rates are depicted only for the higher mass object (blue line), as negligible dust production is expected for the lower mass star (Sec. 1.2.4).

As discussed e.g. in Ventura et al. (2022), the chemical composition of very low-mass stars like SMP LMC 80 and SMP LMC 81 is predominantly shaped by the first dredge-up process (and potential non-canonical mixing) that occurs during the RGB ascent (see Sec. 1.1 for further details). Neither HBB nor TDU influence the AGB evolution of these stars. The envelope is lost after only a few

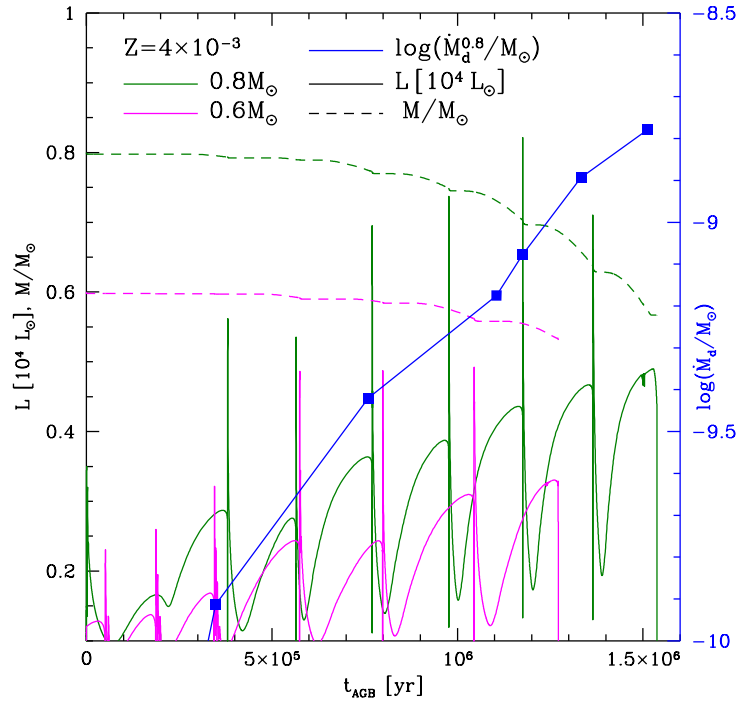


Figure 6.10: Time variation of physical properties of a $0.8 M_{\odot}$ (green line) and $0.6 M_{\odot}$ (magenta line) models of metallicity $Z = 4 \times 10^{-3}$. The magenta and green solid lines represent the time variation of luminosity, while the magenta and green dashed lines indicate the total mass. The blue line shows the DPR for the $0.8 M_{\odot}$ model star.

thermal pulses, before the stars contract and enter the post-AGB and PN phases. Consequently, dust is produced in limited quantities, with the DPR increasing to a few $10^{-9} M_{\odot}/\text{yr}$ during the final AGB phases, as shown in Fig. 6.10.

6.4 The AGB–PN connection

The analysis of the LMC sources discussed in this Chapter, as detailed in the previous Section, employs the methodologies outlined in Section 3.2.1, enabling the determination of key physical parameters that characterize the nebula surrounding the central stars. These parameters include the nebular gas mass and the dust-to-gas ratio, as summarized in Tables 6.3 and 6.4.

Focusing on the carbon-rich sources, Fig. 6.11 shows the mass of the gas (Tab. 6.3) and the dust-to-gas ratio (Tab. 6.4) of the nebulae surrounding the carbon stars in the sample investigated here. It is clear that these two quantities are anti-correlated: stars with the largest δ_C ($\sim 6 \times 10^{-3}$) are surrounded by $\sim 0.05 M_{\odot}$ of gas, whereas sources with minimal dust (δ_C on the order of a few 10^{-4}) have M_{gas}

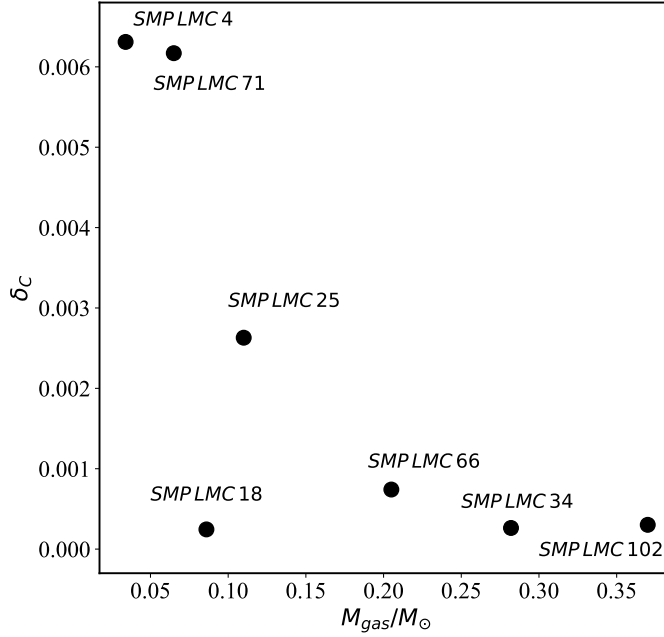


Figure 6.11: The dust-to-gas ratio, derived from SED analysis for the carbon-rich PNe examined in Sec. 1.3.2, is presented as a function of the gas mass in the nebula surrounding each source.

in the range of $\sim 0.3 - 0.35 M_{\odot}$.

Overall, the results shown in Fig. 6.11 suggest that the δ_C values derived from different sources are related not only to the dust produced during the final AGB phases and currently stored in the nebula but also to the fraction of gas lost during the AGB-post-AGB-PNe transition.

The only notable deviation from this anti-correlation is SMP LMC 18, which in Sec. 6.2 was identified as the descendant of a $\sim 0.9 M_{\odot}$ star that experienced a LTP just after entering the post-AGB phase, similar to the AGB Final Thermal Pulse (AFTP) evolution described by Blöcker (2001). The LTP caused the evolutionary track to return to the red before moving to the blue, resulting in the current stage of the star. This explains the relatively low luminosity of SMP LMC 18 ($\sim 2 \times 10^3 L_{\odot}$) compared to the other stars (see the evolutionary track of the $0.9 M_{\odot}$ star with metallicity $Z = 2 \times 10^{-3}$ in Fig. 6.5). The temporary cooling of the outer regions following the LTP likely altered the dynamics of gas and dust released during the late AGB phases, leading to the loss of additional residual gas and accounting for the anomalous position of this source in the plot shown in Fig. 6.11.

To explore how the properties of PNe relate to the stars' previous evolutionary history and how they vary with the progenitor's mass and chemical composition, we present in Fig. 6.12 the dust-to-gas ratio δ_C (left panel) and the total mass of

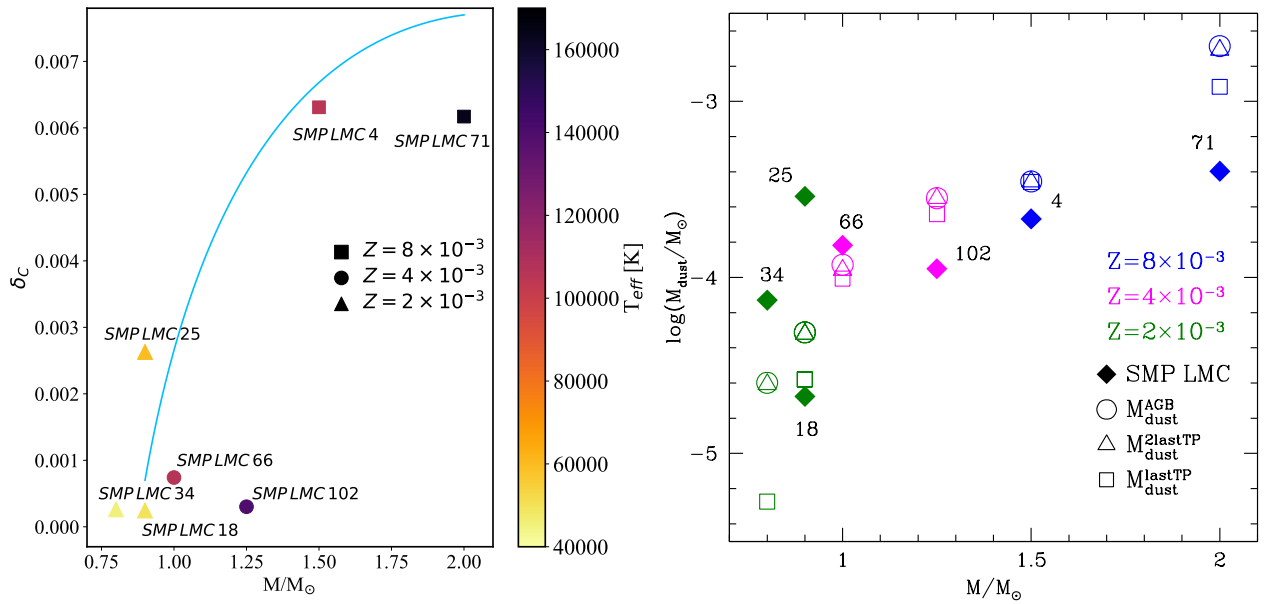


Figure 6.12: Dust and gas properties of the LMC PNe analysed in the present Chapter. The left panel shows the carbon dust-to-gas ratio (Tab. 6.4) as a function of the progenitors' mass (Tab. 6.6). Different symbols represent varying metallicities, while different colors denote effective temperatures (indicated by the vertical bar). The cyan line illustrates the approximate trend for sources with effective temperatures below 10^5 K. The right panel displays the mass of dust in the nebula (Tab. 6.4) surrounding individual sources as a function of the progenitors' mass. Filled points represent the dust mass of the PNe. Open points indicate the dust mass produced by model stars of the same mass during various phases: circles for the entire carbon star phase, triangles for the late two inter-pulse phases, and squares for the final inter-pulse phase.

Table 6.7: *Dust production rate of different ATON synthetic models*

M/M_{\odot}	Z	DPR [M_{\odot}/yr]
2.00	8×10^{-3}	5×10^{-7}
1.50	8×10^{-3}	$\sim 10^{-8}$
1.25	4×10^{-3}	5×10^{-9}
1.00	4×10^{-3}	3×10^{-9}
0.80	4×10^{-3}	$\sim 10^{-9}$
0.90	2×10^{-3}	2.5×10^{-9}

carbon dust currently stored in the nebulae (right panel) surrounding various C-rich sources. These properties are plotted against the mass of the progenitor stars, which were discussed in the previous Section.

The left panel of Fig. 6.12 shows that δ_C generally increases with the mass of the progenitor star. In agreement with Sec. 1.2.4, this trend reflects the efficiency of dust production during the final AGB phases, which is higher for more massive stars. As detailed in Tab. 6.7, the TAGB phase ranges from $\sim 5 \times 10^{-9} M_{\odot}/\text{yr}$ for the lowest mass stars ($\sim 0.9 M_{\odot}$) to $\sim 5 \times 10^{-7} M_{\odot}/\text{yr}$ for stars with $\sim 2 M_{\odot}$. The increasing trend of δ_C with progenitor mass, visible in Fig. 6.12, is thus a direct result of the larger amount of dust produced by higher mass carbon stars, which accumulates more carbon during their evolution (as discussed in Sec. 1.2.2).

Additionally, higher mass stars generally exhibit higher δ_C values because their surrounding gas disperses more rapidly. This is due to the stronger radiation pressure on newly formed dust particles, which results in faster stellar winds. Figure 6.13 illustrates this effect by showing the asymptotic velocity of the outflow during the final AGB phases for three different models. For a $\sim 2 M_{\odot}$ star (green line), the asymptotic velocity is approximately ~ 30 km/s. This velocity decreases to ~ 20 km/s for a $\sim 1 M_{\odot}$ star (magenta line) and drops slightly below ~ 10 km/s for a $\sim 0.9 M_{\odot}$ star (blue line). Consequently, Figure 6.12 shows that the sources with the lowest M_{gas} , specifically SMP LMC 4 and SMP LMC 71, exhibit the highest DPR during the final AGB phases.

The sources SMP LMC 102 and SMP LMC 71 deviate from the general trend of stellar mass versus δ_C , which is roughly outlined by the cyan line in the left panel of Fig. 6.12. We attribute this deviation to the exceptionally high effective temperatures of their central stars, exceeding 10^5 K. These high temperatures likely led to significant destruction of the surrounding dust. A similar, although less pronounced, effect might explain the behavior of SMP LMC 66.

To further investigate the sequence of events from the end of the AGB phase to the current PN state, we present in the right panel of Fig. 6.12 the dust mass surrounding the sources. This is calculated by multiplying δ_C by M_{gas} , as determined

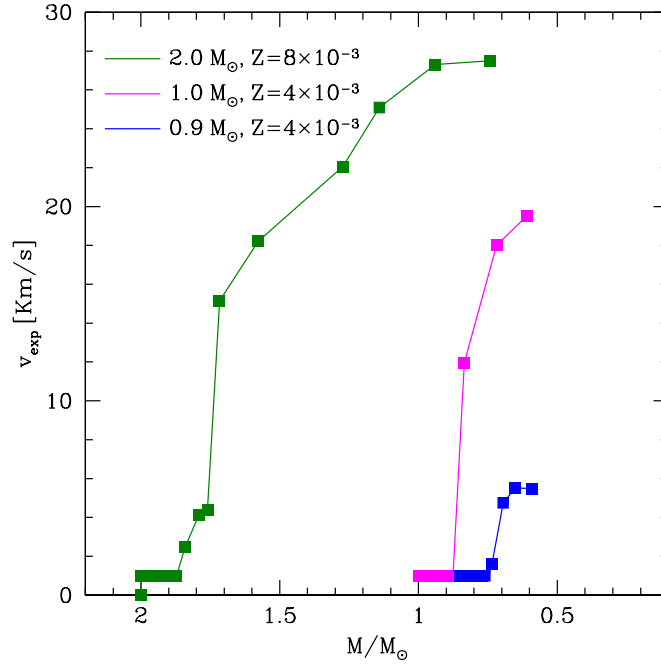


Figure 6.13: Asymptotic wind velocity during the AGB phase. The green line corresponds to the $2.0 M_{\odot}$ model with a metallicity of $Z = 8 \times 10^{-3}$. The magenta line represents the $1.0 M_{\odot}$ model with a metallicity of $Z = 4 \times 10^{-3}$, while the blue line denotes the $0.9 M_{\odot}$ model, also with a metallicity of $Z = 4 \times 10^{-3}$.

from the SED analysis (col. 6, Tab. 6.4). The progenitor’s masses reported on the abscissa are the same as in the left panel. Additionally, we display the total dust mass produced during the carbon-rich phase, as well as the dust masses released during the final inter-pulse phase and the last two inter-pulse phases. These values are derived from the dust formation modeling described in Chapter 2 and based on the time variation of the DPR shown in Figs. 6.7, 6.8, and 6.9.

For stars originating from progenitors with $M > 1 M_{\odot}$, the observed dust mass is notably lower than what dust formation models predict. This discrepancy suggests that a significant portion of the dust has been lost, potentially due to radiation pressure or vaporization by the high temperatures in the surrounding nebula. Specifically, for SMP LMC 4, the observed dust mass is approximately half of what was predicted by dust formation models. In the cases of SMP LMC 102 and SMP LMC 71, the “dust depletion factor” is about 3, indicating a more pronounced reduction in dust. This observation is consistent with earlier discussions in this Section, which noted that these two stars are among the hottest in the sample, with effective temperatures exceeding 10^5 K. Such high temperatures are conducive to the destruction of solid dust grains.

Among the sample of lower-mass progenitors, SMP LMC 25 presents an anomaly compared to higher-mass counterparts. Here, the current dust mass in the nebula, estimated at $\sim 3 \times 10^{-4} M_{\odot}$, exceeds the total dust produced during the AGB phase, which is estimated to be below $5 \times 10^{-5} M_{\odot}$. This seemingly anomalous result aligns with findings reported in Chapter 4 and 5, where we suggested that dust production by low-mass, metal-poor AGB stars might be underestimated. Specifically, higher DPRs are necessary to account for the infrared excess observed in some metal-poor, carbon-rich post-AGB stars in the MCs and MW. We highlight the importance of considering surface chemical composition, as lower metallicity stars have reduced oxygen levels, enabling the production of larger quantities of carbonaceous dust compared to their higher metallicity counterparts, as discussed also in Sec. 5.1.2. We therefore conclude that the higher dust mass observed around SMP LMC 25 compared to SMP LMC 66, despite the latter's higher initial mass, supports this interpretation.

In the case of SMP LMC 34, another low-mass progenitor, the estimated carbon dust mass from the SED analysis is $\sim 2.5 \times 10^{-5} M_{\odot}$: the lowest among the carbon stars studied. This low dust mass reflects the star's mass, which is very close to the minimum threshold required to reach the C-star stage. As a result, the carbon excess relative to oxygen, crucial for forming solid carbon dust, is minimal. Results from the previous Section indicate that SMP LMC 34 can be classified as a carbon star only when considering the lower limit of the measured oxygen abundance (see Fig. 6.4). The small dust mass and very low $\delta_{\text{C}} \sim 2.5 \times 10^{-4}$ in SMP LMC 34 are a direct result of the limited carbon excess relative to oxygen, with most carbon atoms bound in CO molecules and only a small fraction available for dust formation.

SMP LMC 18 exhibits an unusually low carbon dust mass of $\sim 2 \times 10^{-5} M_{\odot}$, significantly lower compared to other carbon stars studied. As discussed earlier, this low dust mass may be attributed to the effects of a late thermal pulse, which likely disrupted the gas and dust dynamics in the nebula and contributed to the additional loss of both gas and dust during the transition from the post-AGB to the PN phase.

In contrast, the PNe sample also includes SMP LMC 80 and SMP LMC 81, which are classified as oxygen-rich (Sec. 6.2). For SMP LMC 80, the absence of dust is consistent with the minimal dust production expected from its low-mass progenitor during the AGB phase, as discussed in Sec. 1.2.4.

However, SMP LMC 81 presents a more complex scenario. Analysis of its SED in Sec. 6.2 reveals the presence of dust, with a dust-to-gas ratio of $\sim 3.3 \times 10^{-3}$ and a total gas mass of $\sim 0.13 M_{\odot}$. If plotted in the M_{gas} vs. δ_{C} plane in Fig. 6.14, SMP LMC 81 would deviate from the general trend observed for other dusty PNe, as its dust fraction is higher than that of C-rich sources with similar gas masses. This discrepancy may arise from fundamental differences between sili-

cate and carbonaceous dust, including their extinction properties and the location of the dust relative to the central star. Further analysis involving a larger sample of oxygen-rich PNe is necessary to draw more definitive conclusions regarding the dust properties of these stars.

6.5 The evolutionary link between the AGB, Post-AGB, and PN Phases: is a comprehensive overview possible?

In this thesis, we characterized post-AGB (Chapters 4 and 5) and PN sources to assess whether the dust evolution history aligns with observations from the late LIMS evolutionary stages. Within our sample, two objects were found to have matching progenitor mass and metallicity: J050632.10-714229.8 (discussed in Chapter 4) and SMP LMC 102 (analyzed in Sec. 6.2). This Section compares these objects, aiming to establish an evolutionary link that starts from the AGB, moves through the post-AGB, and concludes in the PN phase. To support this comparison, we selected the AGB star SSID 145 from the SAGE-Spec legacy survey of the LMC (Kemper et al., 2010), previously analyzed by Marini et al. (2021) in terms of dust and CS components. Similar to our study, Marini et al. (2021) examined SSID 145’s SED using the DUSTY code (Nenkova et al., 2000, black line, Fig. 6.14), comparing it with the *Spitzer*/IRAC photometric data (blue squares, Fig. 6.14) and *Spitzer* spectrum (orange line, Fig. 6.14).

Each of the three sources corresponds to a progeny of a $1.25 M_{\odot}$ star with a metallicity of $Z = 4 \times 10^{-3}$. In the H–R diagram in Fig. 6.5, the three selected sources align along the same evolutionary model, each representing a different evolutionary stage of the same progenitor. Specifically, the figure compares ATON synthetic models for 1.0 (dashed line), 1.25 (solid line), and 1.5 (dotted line) M_{\odot} with a metallicity of $Z = 4 \times 10^{-3}$, against the effective temperatures and luminosities derived from the SED analysis (magenta triangle for SMP LMC 102, green square for J050632.10-714229.8, and orange circle for SSID 145). The determination of the progenitor’s mass and metallicity for the post-AGB and PN sources is further detailed in Chapter 4 and Sec. 6.2. The progenitor mass for SSID 145, based on SED analysis and the age-metallicity relation of the LMC, is reported in Marini et al. (2021), indicating a metallicity range of $Z = 1 - 4 \times 10^{-3}$ for stars formed 1–1.5 Gyr ago (e.g., Harris & Zaritsky, 2009).

The main quantities for creating this evolutionary link are presented in Tab. 6.8. The ATON model of a $1.25 M_{\odot}$ star with $Z = 4 \times 10^{-4}$ indicates an optical depth increasing from approximately 0.05 to about 0.35, and a dust-to-gas ratio $\delta_{\text{AGB}}^{\text{last,TP}} \sim 10^{-3}$, derived from the ratio of the dust mass produced ($4 \times 10^{-4} M_{\odot}$,

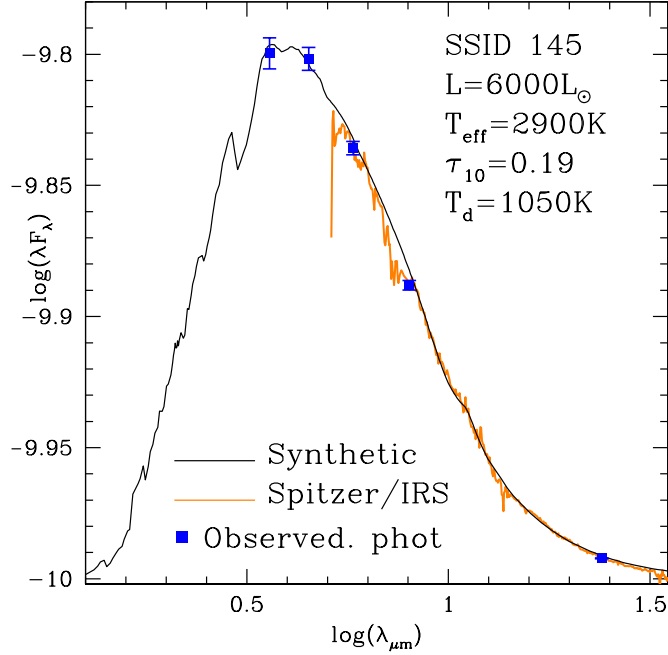


Figure 6.14: SED of SSID 145, adapted from Marini et al. (2021). The black line is the synthetic spectrum obtained using DUSTY (Sec. 3.1.1). The orange line is the Spitzer/IRS spectrum. The blue dots are the observed Spitzer/IRAC photometry.

as shown in the right panel of Fig 6.14) to the gas mass ejected into the ISM ($0.45 M_{\odot}$). Results for the post-AGB and PN phases are discussed in Chapter 4 and Sec. 6.2.

To verify if the optical depth typical of a $1.25 M_{\odot}$ star with $Z = 4 \times 10^{-4}$, scaled using Eq. 4.1, matches that derived from the SED of J050632.10-714229.8, we applied the methodology described in Sec. 4.3. Specifically, we used the optical depth from ATON, $\tau_{10}^{\text{onset}} = 0.24$, and the inner boundary radius of the dust region derived from the SED analysis, $R_{\text{in}} = 2.74 \times 10^5 R_{\odot}$ (see Tab. 4.1):

$$\tau_{10} = \tau_{10}^{\text{onset}} \times R_{\text{onset}}/R_{\text{in}} = 0.24 \times 10 R_{\star}/(2.74 \times 10^5 R_{\odot}) \sim 3 \times 10^{-3} \quad (6.1)$$

Consistent with the previous findings in Chapter 5, the observed optical depth for this low-mass and $Z = 4 \times 10^{-4}$ star is in agreement with the ATON synthetic model predictions.

Following the method outlined in Sec. 4.3, we evaluated whether the wind dynamics align with observational constraints. In Chapters 4 and 5, we found that the dust currently observed in the post-AGB phase likely formed when the effective temperature was around 3000–4000 K. Assuming a constant luminosity, the time required for the dust to reach R_{in} corresponds to the time for the effective

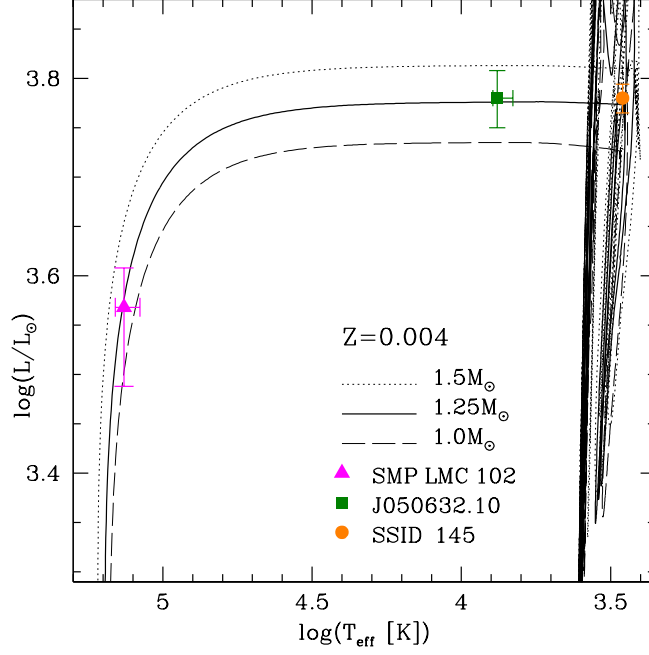


Figure 6.15: Comparison of the properties of the AGB, post-AGB and PN sources. The left panel shows the evolutionary tracks on the HR diagram of the 1.0, 1.25, and 1.5 M_{\odot} model at metallicity $Z = 4 \times 10^{-3}$, with the location of the AGB (orange solid dot), post-AGB (green solid square), and PN (magenta solid triangle) sources according to the results discussed in Marini et al. (2023), Chapter 4 and Sec.6.2.

Table 6.8: Top: parameters determined from the comparison between the observational data and the synthetic SEDs. Bottom: stellar evolution model parameters.

ATON Model	\dot{M} [$M_{\odot}\text{yr}^{-1}$]	τ_{10}^{TAGB}	$\delta_{\text{AGB}}^{\text{last TP}}$	$M_{\text{gas}}^{\text{last TP}} / M_{\odot}$
1.25 M_{\odot} , $Z=0.004$	1.7×10^{-5}	0.34	10^{-3}	0.4
ID	L / L_{\odot}	τ_{10}	δ	$M_{\text{gas}} / M_{\odot}$
SSID 145	6000 ± 150	0.19 ± 0.02	–	–
J050632.10-714229.8	6000 ± 400	0.003 ± 0.0004	–	–
SMP LMC 102	3600_{-800}^{+1000}	–	$(4.2 \pm 1) \times 10^{-4}$	$0.37 \pm 0.04^{(a)}$

Note: δ is the dust-to-gas ratio; $^{(a)}$ is the total gas mass of the nebula.

temperature to increase from 3000 K to the present estimate of 7600 K, approximately 2500 yr. Assuming a mean wind velocity of 5 km/s (see e.g., He et al., 2014), we estimate that the dust is currently at a distance of about $2.6 \times 10^5 R_{\odot}$ from the star, consistent with results in Tab. 6.8. This supports the connection between the dust produced at the end of the AGB phase and that observed in the post-AGB phase.

According to our interpretation, SMP LMC 102 represents the PN counterpart of SSID 145 and J050632.10-714229.8. We propose that the dust produced at the end of the AGB and observed in the post-AGB phase persists into the PN stage. Indeed, SMP LMC 102 (Fig. 6.3) exhibits an IR excess indicative of substantial quantities of carbonaceous dust, consistent with the findings for SSID 145 and J050632.10-714229.8. The estimated dust-to-gas ratio of SMP LMC 102, $\delta_{\text{PN}} = 4.2 \times 10^{-4}$, is approximately 2.5 times lower than the dust-to-gas ratio for the last AGB interpulse, $\delta_{\text{AGB}} \sim 10^{-3}$. As discussed in Sec. 6.4, this difference may result from dust destruction, potentially influenced by the effective temperature. Unlike the dust, the gas mass surrounding the CS ($0.4 M_{\odot}$, Tab. 6.3), aligns with the gas mass lost after the last TP, suggesting that only this gas remains in the nebula, while gas lost earlier was dissipated.

6.6 Conclusion on PNe and the evolutionary bridge

In this Chapter, we present a multiwavelength study of nine round and elliptical PNe in the LMC to examine dust production in LIMSs. Using spectra, photometric data, and abundances from the literature, we conducted an SED analysis from UV to IR via photoionization models, deriving essential physical parameters such as central star luminosity and effective temperature, nebular gas mass and radial dimensions, dust composition, and dust-to-gas ratios.

Five carbon-rich PNe (SMP LMC 4, SMP LMC 18, SMP LMC 25, SMP LMC 66, and SMP LMC 71) display a distinct near-IR bump peaking around 3–8 μm . This feature, suggesting “hot” dust with temperatures around 600–800 K, contrasts with the longer-wavelength emission from cool dust formed during the AGB phase, though its exact origin remains uncertain.

The SED analysis results were further linked through ATON evolutionary tracks extended to the PN phase. By comparing observed carbon and oxygen abundances with ATON predictions, we derived the metallicity for each PN. Additionally, comparisons between the luminosity and effective temperature obtained from SEDs and the ATON evolutionary tracks enabled us to estimate progenitor masses and metallicities for each PN.

Our analysis reveals that progenitor mass correlates inversely with nebular gas mass and directly with the dust-to-gas ratio. Specifically, as progenitor mass

increases from $0.9 M_{\odot}$ to $2 M_{\odot}$, the dust-to-gas ratio δ_C rises from $\sim 5 \times 10^{-4}$ to $\sim 6 \times 10^{-3}$. This trend reflects the fact that higher-mass carbon stars generate more dust during the AGB phase, leading to a greater dust content in the PN. Increased dust production in these stars also results in higher gas expansion velocities due to enhanced radiation pressure on the dust grains, decreasing the nebular gas mass from $\sim 0.3 - 0.35 M_{\odot}$ for $0.9 M_{\odot}$ progenitors to $\sim 0.05 M_{\odot}$ for $2 M_{\odot}$ progenitors, thereby supporting the higher observed dust-to-gas ratios.

The CS's effective temperature is also a critical factor. The hottest sources diverge from the general trend between dust-to-gas ratio and progenitor mass, likely due to intense temperatures that cause some dust to vaporize.

This Chapter also underscores the advantages of studying sources on similar evolutionary tracks but in different phases, from late AGB to the PN stage, particularly with models incorporating AGB dust formation. This approach is valuable for evaluating dust production in LIMSs. While uncertainties in TP descriptions restrict this method to the final AGB stages, this limitation is minimal for dust production studies, as most dust is formed in the late interpulse phases, especially in low-mass stars that produce substantial dust only after the final TP when they become carbon stars.

In examining the specific case of SSID 145, J050632.10-714229.8, and SMP LMC 102 discussed in this Chapter, we find that a consistent understanding of their dust history can be achieved if we consider potential dust destruction events during the PN phase, as well as reduced optical depth due to the increased distance from the central star. However, further research is necessary to confirm whether these behaviors are general or influenced by additional factors.

Addressing these open questions will require applying this methodology to a broader sample of sources with a wider range of initial masses. Extending this approach to stars with different metallicities than those in the LMC sequence, such as those in the SMC or Galactic sequences, would also be insightful.

Future observations with the JWST will significantly enhance the IR sample's variety and accuracy, offering deeper insights into dust production and destruction processes and refining our understanding of the final stages of evolution in low- and intermediate-mass stars.

Chapter 7

Conclusions

This work is centered on the mass-loss and dust production processes in LIMS, which are of critical importance in various astrophysical contexts, particularly in understanding how these stars contribute to the enrichment of the ISM with reprocessed elements, thus influencing the chemical evolution of the universe.

The methodology employed in this study involved the comparison of observational properties of post-AGB stars and PNe with theoretical models of AGB stars. The sources selected for analysis, originating from both the MCs and the MW, likely followed a single-star evolution. By examining their spectral features and modeling their SEDs, we derived the key characteristics of their central stars, as well as the dust and gas components of their circumstellar environments. The analysis, which included chemical abundances, photometric data, and multi-wavelength spectral analysis from UV to IR, enabled the determination of the progenitor mass for each source. This was achieved using ATON stellar evolutionary tracks, specifically extended up to the PN phase for this study.

Following the identification of their evolutionary path, the observed quantities of gas and dust in the post-AGB and PN stages were compared with AGB models, allowing for the evaluation and, where necessary, recalibration of the theoretical descriptions of mass-loss rates and dust production histories available in literature. This methodology offers a novel perspective for studying LIMS, overcoming the blending effects typically encountered in AGB photospheres. Moreover, it is applicable because evolutionary stages after the AGB do not significantly alter the surface chemical compositions of stars, and the dust produced during the late AGB phase remains detectable throughout the post-AGB and PN phases.

The comparison between observational data and synthetic SED models, generated using the DUSTY radiative transfer code and the CLOUDY spectral synthesis code, led to the identification of 26 post-AGB stars and seven PNe with circumstellar envelopes dominated by carbonaceous dust, 18 post-AGB stars and one PN with silicate-rich dust, and one dust-free PN.

A key outcome of this research is the clear connection between the dust properties observed in post-AGB and PN sources and their previous AGB evolutionary phase. Specifically, sources with more massive progenitors exhibit higher optical depths, which, in the case of carbon stars, can be attributed to the greater number of TDU episodes during the AGB phase. These episodes lead to increased surface carbon abundance, thereby enhancing mass-loss and promoting higher dust production. Similarly, oxygen-rich sources show greater optical depths due to higher mass-loss rates, which are driven by more intense radiation pressure. However, notable exceptions to this trend were observed in stars that experienced both TDU and HBB processes (e.g., ID 1, ID 15 in the post-AGB sample), where surface carbon was depleted by nucleosynthesis, resulting in reduced carbonaceous dust formation. In addition, in PNe, the dust-to-gas ratio relative to progenitor mass is affected by mechanisms of dust destruction. Our study indicates that these destruction mechanisms may correlate with the effective temperature of the central star. Specifically, the hottest sources exhibit significant deviations from the established trend, potentially due to elevated effective temperatures that facilitate the vaporization of dust.

Furthermore, this study reveals that in post-AGB carbon-rich stars with higher mass-loss rates, the rapid depletion of the stellar envelope leads to a quicker transition to the post-AGB phase. Consequently, the circumstellar dust remains relatively close to the photosphere. In contrast, M-type post-AGB stars, characterized by silicate-rich dust, experience longer transition timescales, allowing the dust to achieve greater distances from the star.

By analyzing the emission due to the gaseous nebula, we also assessed the amount of gas released by the star during the late AGB phases that remains trapped in the nebula. This analysis shows an anti-correlation between the nebular gas mass and the progenitor's mass, which can be explained by the fact that increased dust production in higher-mass stars leads to higher expansion velocities of the gas due to enhanced radiation pressure on the dust grains.

In addition, the SED modeling data were employed to reconstruct the evolutionary histories of these stars from the late AGB phase to their current stages, providing a valuable test of theoretical mass-loss models and highlighting the role of metallicity in dust production processes. The findings demonstrate that metallicity exerts a critical influence on the nature and quantity of dust formed around different stellar types. For instance, metal-poor stars from low-mass progenitors that did not evolve into carbon stars exhibited almost zero dust production due to a lack of silicon and aluminum. Similarly, metal-rich carbon stars, with higher initial oxygen abundances, were found to have lower carbon-to-oxygen ratios, resulting in less dust production compared to metal-poor carbon stars of similar luminosity.

Some of the most interesting results of this thesis arise from the comparison

between the observed dust content in post-AGB stars and PNe and the predicted dust production during the AGB phase. Remarkably, it was found that reproducing the observed infrared excesses requires increasing the mass-loss rates at the TP of the AGB phase for metal-poor ($[\text{Fe}/\text{H}] \lesssim -0.7$) carbon-rich low-mass stars ($M \lesssim 2 M_{\odot}$) by a factor of three to four times higher than previously suggested by the Wachter et al. (2002, 2008) prescription. Therefore, we suggest to adopt mass-loss rates of $4 - 5 \times 10^{-5} M_{\odot}/\text{yr}$ for these sources. For stars of similar mass but with higher metallicities, the expected mass-loss rates ($1 - 1.5 \times 10^{-5} M_{\odot}/\text{yr}$) were found to be in alignment with observational data. Consistent agreement was also observed for oxygen-rich stars descended from low-mass progenitors that did not become carbon-rich, for which theoretical models predict mass-loss rates of approximately $10^{-6} M_{\odot}/\text{yr}$ at the TAGB phase. However, for oxygen-rich stars that experienced HBB, the mass-loss rates from Vassiliadis & Wood (1993) provided a better match to observational data than those derived from the Blöcker (1995) prescription.

For post-AGB sources, the calibration of mass-loss rates is further supported by the comparison of the expected wind velocities and optical depths with those derived from SED modeling. Since wind velocities depend on the transitional timescales of dust release and the current effective temperature observed during the post-AGB phase, our methodology also provides insights into when the currently observed dust was ejected. The findings suggest that, contrary to common assumptions in the literature, the dust surrounding post-AGB stars was ejected after the contraction into the post-AGB phase began, with effective temperatures rising to ~ 4000 K.

For most of the stars studied, the proposed interpretation is supported by well-determined stellar distances. However, for a few Galactic post-AGBs, labeled as Q2 sources, Gaia EDR3 parallaxes are very uncertain. To reconcile observational constraints with theoretical modeling, we recommend adjusting the Bailer-Jones et al. (2021) distances of four Q2 objects (IDs 3, 4, 7, and 27).

An additional notable result for the PNe is the presence of a near-IR bump peaking around $3-8 \mu\text{m}$ in five carbon-rich PNe (SMP LMC 4, SMP LMC 18, SMP LMC 25, SMP LMC 66, and SMP LMC 71), which is currently a topic of discussion within the scientific community. This peak is distinct from the longer-wavelength emission attributed to cool dust produced during the AGB phase. The near-IR emission can be replicated by assuming the presence of “hot” dust with temperatures around $600-800$ K, though further investigation is needed to understand the formation mechanism of this feature.

This thesis develops a methodology for correlating the properties of PN with the mass, chemical composition, and dust production efficiency of their progenitor stars. The insights gained from this work help to provide a greater understanding of dust production mechanisms in LIMS during the late AGB phases and clarify

the role of AGB stars as dust manufacturers. The results presented in this thesis have been published in several peer-reviewed journals. The findings related to post-AGB stars are discussed in T22, T23 and Dell’Agli et al. (2022, 2023a), while those concerning PNe are covered in Dell’Agli et al. (2023b); Tosi et al. (2024) and Ventura et al. (2025).

To further refine these conclusions, additional investigations are required. Specifically, applying the proposed methodology to a broader sample of sources, including a greater number of oxygen-rich stars, will be essential for a more comprehensive examination. Future observations with the JWST will be instrumental in expanding and enhancing the diversity and accuracy of infrared observational data. Such observations are expected to provide more detailed insights into dust production and destruction processes, improving our understanding of the final stages of stellar evolution in low- and intermediate-mass stars. Additionally, the forthcoming release of Gaia astrometric data will be pivotal for broadening our Galactic sample of objects and verifying the results for the Q2 sources.

We are still far from achieving a detailed and robust description of the processes that lead LIMS to enrich the Universe during their final stages of their life. However, this thesis represents a step forward in that pursuit, with the hope that future data will shed more light on these enigmatic and fascinating objects in the cosmos.

Bibliography

- Abel, N. P., van Hoof, P. A. M., Shaw, G., et al. 2008, *The Astrophysical Journal*, 686, 1125
- Abia, C., Palmerini, S., Busso, M., et al. 2012, *Astronomy and Astrophysics*, 548, A55. doi:10.1051/0004-6361/201220148
- Aller, L. H. & Czyzak, S. J. 1983, *The Astrophysical Journal Supplement Series*, 51, 211.
- Bailer-Jones C. A. L., Rybizki J., Foesneau M., Demleitner M., Andrae R., 2021, *AJ*, 161, 147.
- Balick, B. & Frank, A. 2002, *Annual Review of Astronomy & Astrophysics*, 40, 439. doi:10.1146/annurev.astro.40.060401.093849
- Bandyopadhyay, R. & Das, R. 2023, *Monthly Notices of the Royal Astronomical Society*, 523, 498.
- Bell, K. R. & Lin, D. N. C. 1994, *The Astrophysical Journal*, 427, 987.
- Belokurov V., Penoyre Z., Oh S., Iorio G., Hodgkin S., Evans N. W., Everall A., et al., 2020, *MNRAS*, 496, 1922.
- Miller Bertolami, M. M. 2016, *Astronomy and Astrophysics*, 588, A25.
- Bertschinger, E., & Chevalier, R. A. 1985, *ApJ*, 167, 190
- Bladh S., Eriksson K., Marigo P., Liljegren S., Aringer B. 2019, *A&A*, 623, A119
- Bladh S., Liljegren S., Höfner S., Aringer B., Marigo P., 2019, *A&A*, 626, A100.
- Blöcker T., 1995, *A&A*, 297, 727
- Blöcker T., Schönberner D. 1991, *A&A*, 244, L43
- Blöcker, T. 2001, *Astrophysics and Space Science*, 275, 1

- Blommaert, J. A. D. L., de Vries, B. L., Waters, L. B. F. M., et al. 2014, *Astronomy and Astrophysics*, 565, A109
- Boyer, M. L., Srinivasan, S., Riebel, D., et al. 2012, *The Astrophysical Journal*, 748, 40
- Boyer M. L., McQuinn K. B. W., Barmby P., Bonanos A. Z., Gehrz R. D., Gordon K. D., Groenewegen M. A. T., et al., 2015, *ApJ*, 800, 51.
- Burbidge, E. M., Burbidge, G. R., Fowler, W. A., et al. 1957, *Reviews of Modern Physics*, 29, 547
- Buss, R. H., Tielens, A. G. G. M., Cohen, M., et al. 1993, *The Astrophysical Journal*, 415, 250
- Boothroyd, A. I., Sackmann, I.-J., & Wasserburg, G. J. 1995, *The Astrophysical Journal Letters*, 442, L21
- Bowen G. H., Willson L. A., 1991, *ApJL*, 375, L53.
- Boyer M. L., Girardi L., Marigo P., et al. 2013, *ApJ*, 774, 83
- Brown, R. L. & Mathews, W. G. 1970, *The Astrophysical Journal*, 160, 939
- Busso, M., Gallino, R., & Wasserburg, G. J. 1999, *Annual Review of Astronomy & Astrophysics*, 37, 239.
- Busso, M., Wasserburg, G. J., Nollett, K. M., et al. 2007, *The Astrophysical Journal*, 671, 802. doi:10.1086/522616
- Calura F., Palla M., Morselli L., Spitoni E., Casasola V., Verma K., Enia A., et al., 2023, *MNRAS*, 523, 2351.
- Cameron A. G. W., Fowler W. A., 1971, *ApJ*, 164, 111
- Cami, J., Bernard-Salas, J., Peeters, E., et al. 2010, *Science*, 329, 1180.
- Canuto, V. M. 1992, *The Astrophysical Journal*, 392, 218
- Canuto V. M. C., Mazzitelli I., 1991, *ApJ*, 370, 295
- Castellani, V. 1985, *Bologna : Zanichelli*, 1985. 1a ed.
- Castelli, F. & Kurucz, R. L. 2003, *modeling of Stellar Atmospheres*, 210, A20
- Cinquegrana, G. C. & Karakas, A. I. 2022, *Monthly Notices of the Royal Astronomical Society*, 510, 1557

- Cioni M.-R. L., Habing H. J. 2003, *A&A*, 402, 133
- Clayton, G. C. & De Marco, O. 1997, *The Astronomical Journal*, 114, 2679
- Cloutman, L. D. & Eoll, J. G. 1976, *The Astrophysical Journal*, 206, 548.
- Cristallo, S., Straniero, O., Gallino, R., et al. 2009, *The Astrophysical Journal*, 696, 797
- Cristallo S., Piersanti L., Straniero O., et al. 2011, *The Astrophysical Journal Supplement Series*, 197, 17
- Cristallo S., Straniero O., Piersanti L., et al. 2015, *The Astrophysical Journal Supplement Series*, 219, 40
- Cutri, R. M. & et al. 2012, *VizieR Online Data Catalog*, II/311
- Decin L., 2021, *ARA&A*, 59, 337.
- Dell’Agli, F., 2012, Master thesis, University of Rome ”Roma Tre”
- Dell’Agli F., García-Hernández D. A., Rossi C., et al. 2014a, *Monthly Notices of the Royal Astronomical Society*, 441, 1115
- Dell’Agli F., Ventura P., Garcia Hernandez D. A., et al. 2014b, *Monthly Notices of the Royal Astronomical Society*, 442, L38
- Dell’Agli F., Ventura P., Schneider R., et al. 2015a, *Monthly Notices of the Royal Astronomical Society*, 447, 2992
- Dell’Agli F., García-Hernández D. A., Ventura P., et al. 2015b, *Monthly Notices of the Royal Astronomical Society*, 454, 4235
- Dell’Agli F., Di Criscienzo M., Boyer M. L., et al. 2016, *Monthly Notices of the Royal Astronomical Society*, 460, 4230
- Dell’Agli, F., García-Hernández, D. A., Ventura, P., et al. 2018a, *Monthly Notices of the Royal Astronomical Society*, 475, 3098
- Dell’Agli F., Di Criscienzo M., Ventura P., et al. 2018, *MNRAS*, 479, 5035
- Dell’Agli F., Di Criscienzo M., García-Hernández D. A., et al. 2019, *MNRAS*, 482, 4733
- Dell’Agli F., Valiante R., Kamath D., Ventura P., García-Hernández D. A., 2019, *MNRAS*, 486, 4738.

- Dell’Agli, F., Marini, E., D’Antona, F., et al. 2021, *Monthly Notices of the Royal Astronomical Society*, 502, L35
- Dell’Agli, F., Tosi, S., Kamath, D., et al. 2022
- Dell’Agli, F., Tosi, S., Kamath, D., et al. 2023, *Astronomy and Astrophysics*, 671, A86.
- Dell’Agli, F., Tosi, S., Kamath, D., et al. 2023, *Monthly Notices of the Royal Astronomical Society*, 526, 5386
- De Smedt, K., Van Winckel, H., Kamath, D., et al. 2015, *Astronomy and Astrophysics*, 583, A56
- De Smedt, K., Van Winckel, H., Kamath, D., et al. 2016, *Astronomy and Astrophysics*, 587, A6
- Dorfi E. A., Hoefner S., 1991, *A&A*, 248, 105
- Draine B. T., 2003, *ApJ*, 598, 1017
- Draine, B. T., & Lee, H. M. 1984, *The Astrophysical Journal*, 285, 89
- Duerbeck, H. W., Liller, W., Sterken, C., et al. 2000, *The Astronomical Journal*, 119, 2360
- Eriksson, K., Nowotny, W., Höfner, S., et al. 2014, *Astronomy and Astrophysics*, 566, A95
- Ferland G. J., Chatzikos M., Guzmán F., Lykins M. L., van Hoof P. A. M., Williams R. J. R., Abel N. P., et al., 2017, *RMxAA*, 53, 385
- Ferrarotti, A. S., & Gail, H.-P. 2001, *Astronomy and Astrophysics*, 371, 133
- Ferrarotti, A. S., & Gail, H.-P. 2002, *Astronomy and Astrophysics*, 382, 256
- Ferrarotti A. S., Gail H.-P. 2006, *Astronomy and Astrophysics*, 447, 553
- Fishlock C. K., Karakas A. I., Lugaro M., Yong D., 2014, *ApJ*, 797, 44.
- Fleischer, A. J., Gauger, A., & Sedlmayr, E. 1992, *A&A*, 266, 339
- Freytag, B., Ludwig, H.-G., & Steffen, M. 1996, *Astronomy and Astrophysics*, 313, 497
- Gaia Collaboration, Brown, A. G. A., Vallenari, A., et al. 2021, *Astronomy and Astrophysics*, 649, A1

- Gail, H.-P. & Sedlmayr, E. 1985, *Astronomy and Astrophysics*, 148, 183
- Gail, H.-P. & Sedlmayr, E. 1999, *Astronomy and Astrophysics*, 347, 594
- Gail, H.-P., Wetzell, S., Pucci, A., et al. 2013, *Astronomy and Astrophysics*, 555, A119
- García-Hernández, D. A., García-Lario, P., Plez, B., et al. 2006, *Science*, 314, 1751
- García-Hernández, D. A., Manchado, A., Lambert, D. L., et al. 2009, *The Astrophysical Journal Letters*, 705, L31
- García-Hernández, D. A., Villaver, E., García-Lario, P., et al. 2012, *The Astrophysical Journal*, 760, 107
- García-Hernández, D. A. & Górný, S. K. 2014, *Astronomy and Astrophysics*, 567, A12. doi:10.1051/0004-6361/201423620
- García-Hernández, D. A., Ventura, P., Delgado-Inglada, G., et al. 2016, *Monthly Notices of the Royal Astronomical Society*, 458, L118
- García-Rojas J., Delgado-Inglada G., García-Hernández D. A., Dell'Agli F., Lugaro M., Karakas A. I., Rodríguez M., 2018, *MNRAS*, 473, 4476.
- Gehrz, R. D. & Woolf, N. J. 1971, *The Astrophysical Journal*, 165, 285.
- Gielen, C., Cami, J., Bouwman, J., et al. 2011, *Astronomy and Astrophysics*, 536, A54
- Gilman, R. C. 1969, *The Astrophysical Journal Letters*, 155, L185
- Gilman, R. C. 1972, *The Astrophysical Journal*, 178, 423
- Ginolfi, M., Graziani, L., Schneider, R., et al. 2018, *Monthly Notices of the Royal Astronomical Society*, 473, 4538
- Goebel, J. H. & Moseley, S. H. 1985, *The Astrophysical Journal Letters*, 290, L35
- Goldman, S. R., van Loon, J. T., Zijlstra, A. A., et al. 2017, *Monthly Notices of the Royal Astronomical Society*, 465, 403. doi:10.1093/mnras/stw2708
- Gordon, K. D., Clayton, G. C., Misselt, K. A., et al. 2003, *The Astrophysical Journal*, 594, 279
- Górný, S. K. & Tylenda, R. 2000, *Astronomy and Astrophysics*, 362, 1008

- Graczyk, D., Pietrzyński, G., Thompson, I. B., et al. 2020, *The Astrophysical Journal*, 904, 13
- Guandalini, R., Busso, M., Ciprini, S., et al. 2006, *Astronomy and Astrophysics*, 445, 1069. doi:10.1051/0004-6361:20053208
- Gullieuszik, M., Groenewegen, M. A. T., Cioni, M.-R. L., et al. 2012, *Astronomy and Astrophysics*, 537, A105
- Guzman-Ramirez, L., Lagadec, E., Jones, D., et al. 2014, *Monthly Notices of the Royal Astronomical Society*, 441, 364. doi:10.1093/mnras/stu454
- Harman, R. F. & Seaton, M. J. 1966, *Monthly Notices of the Royal Astronomical Society*, 132, 15
- Harris, J., & Zaritsky, D. 2009, *The Astronomical Journal*, 138, 1243
- He J. H., Szczerba R., Hasegawa T. I., Schmidt M. R., 2014, *ApJS*, 210, 26.
- Henry, R. B. C., Liebert, J., & Boroson, T. A. 1989, *The Astrophysical Journal*, 339, 872
- Herwig, F. 2005, *Annual Review of Astronomy & Astrophysics*, 43, 435
- Hofmeister, A. M., Keppel, E., & Speck, A. K. 2003, *Monthly Notices of the Royal Astronomical Society*, 345, 16.
- Hoefner S., Dorfi E. A., 1992, *A&A*, 265, 207
- Hoefner S., Feuchtinger M. U., Dorfi E. A., 1995, *A&A*, 297, 815
- Höfner, S. & Olofsson, H. 2018, *The Astronomy and Astrophysics Review*, 26, 1.
- Höfner S., Freytag B., 2019, *A&A*, 623, A158.
- Hollenbach, D. J. & Tielens, A. G. G. M. 1997, *Annual Review of Astronomy & Astrophysics*, 35, 179
- Hrivnak, B. J., Van de Steene, G., Van Winckel, H., et al. 2017, *The Astrophysical Journal*, 846, 96
- Iben, I. 1975, *The Astrophysical Journal*, 196, 525
- Iben I., 1995, *PhR*, 250, 2
- Iben, I. & Renzini, A. 1983, *Annual Review of Astronomy & Astrophysics*, 21, 271

- Iben, I., Kaler, J. B., Truran, J. W., et al. 1983, *The Astrophysical Journal*, 264, 605
- Iglesias, C. A., Rogers, F. J. 1996, *ApJ*, 464, 943
- Inno, L., Matsunaga, N., Bono, G., et al. 2013, *The Astrophysical Journal*, 764, 84.
- Jaeger, C., Mutschke, H., Begemann, B., Dorschner, J., Henning, Th. 1994, *A&A*, 292, 641
- Jones, O. C., Kemper, F., Srinivasan, S., et al. 2014, *Monthly Notices of the Royal Astronomical Society*, 440, 631
- Kamath, D., Wood, P. R., & Van Winckel, H. 2014, *Monthly Notices of the Royal Astronomical Society*, 439, 2211, K14
- Kamath, D., Wood, P. R., & Van Winckel, H. 2015, *Monthly Notices of the Royal Astronomical Society*, 454, 1468, K15
- Kamath, D. 2020, *Journal of Astrophysics and Astronomy*, 41, 42
- Kamath, D., Van Winckel, H., Ventura, P., et al. 2022, *The Astrophysical Journal Letters*, 927, L13
- Kamath, D. & Van Winckel, H. 2022, *Universe*, 8, 233
- Kamath, D., Dell'Agli, F., Ventura, P., et al. 2023, *Monthly Notices of the Royal Astronomical Society*, 519, 2169
- Käppeler, F., Gallino, R., Bisterzo, S., et al. 2011, *Reviews of Modern Physics*, 83, 157
- Karakas A. I. 2010, *Monthly Notices of the Royal Astronomical Society*, 403, 1413
- Karakas A. I., Lattanzio J. C. 2014b, *Publications of the Astronomical Society of Australia*, 31, e030
- Kemper, F., Woods, P. M., Antoniou, V., et al. 2010, *Publications of the Astronomical Society of the Pacific*, 122, 683
- Kippenhahn, R. & Weigert, A. 1990, *Stellar Structure and Evolution*, XVI, 468 pp. 192 figs. Springer-Verlag Berlin Heidelberg New York. Also *Astronomy and Astrophysics Library*, 192

- Khromov, G. S. 1989, *Space Sci. Rev.*, 51, 339.
- Klochkova V. G., Panchuk V. E., Tavalzhanskaya N. S., 2015, *AstL*, 41, 14
- Knapp, G. R. 1985, *The Astrophysical Journal*, 293, 273.
- Klochkova, V. G. & Kipper, T. 2006, *Baltic Astronomy*, 15, 395
- Kobayashi, C., Karakas, A. I., & Lugaro, M. 2020, *The Astrophysical Journal*, 900, 179
- Kwitter, K. B. & Henry, R. B. C. 2022, *Publications of the Astronomical Society of the Pacific*, 134, 022001
- Kwok, S. 2000, *The origin and evolution of planetary nebulae / Sun Kwok*. Cambridge ; New York : Cambridge University Press, 2000. (Cambridge astrophysics series ; 33)
- Kwok, S. & Zhang, Y. 2013, *The Astrophysical Journal*, 771, 5
- Kwok, S. 2007, *Physics and Chemistry of the Interstellar Medium by Sun Kwok*. University Science Books, 2007
- Kwok, S. 2022, *Frontiers in Astronomy and Space Sciences*, 9, 893061
- Lagadec, E. & Zijlstra, A. A. 2008, *Monthly Notices of the Royal Astronomical Society*, 390, L59
- Laney, C. D., Joner, M. D., & Pietrzyński, G. 2012, *Monthly Notices of the Royal Astronomical Society*, 419, 1637
- Laor, A., & Draine, B. T. 1993, *The Astrophysical Journal*, 402, 441
- Lasker, B. M., Lattanzi, M. G., McLean, B. J., et al. 2008, *The Astronomical Journal*, 136, 735.
- Leisy, P. & Dennefeld, M. 2006, *Astronomy and Astrophysics*, 456, 451.
- Limongi, M. & Chieffi, A. 2018, *The Astrophysical Journal Supplement Series*, 237, 13
- Lindgren, L., Klioner, S. A., Hernández, J., et al. 2021, *Astronomy and Astrophysics*, 649, A2.
- Lombaert, R., de Vries, B. L., de Koter, A., et al. 2012, *Astronomy and Astrophysics*, 544, L18.

- Lucy, L. B. 1971, *The Astrophysical Journal*, 163, 95. doi:10.1086/150748
- Lucy, L. B. 1976, *The Astrophysical Journal*, 205, 482. doi:10.1086/154302
- Luck, R. E., Bond, H. E., & Lambert, D. L. 1990, *The Astrophysical Journal*, 357, 188
- Marigo, P. 2002, *Astronomy and Astrophysics*, 387, 507
- Marigo P., Aringer B., 2009, *A&A*, 508, 1538
- Marini, E., Dell’Agli, F., Di Criscienzo, M., et al. 2020, *Monthly Notices of the Royal Astronomical Society*, 493, 2996
- Marini, E., Dell’Agli, F., Groenewegen, M. A. T., et al. 2021, *Astronomy and Astrophysics*, 647, A69
- Marini, E., Dell’Agli, F., Kamath, D., et al. 2023, *Astronomy and Astrophysics*, 670, A97
- Massey, P. 2002, *The Astrophysical Journal Supplement Series*, 141, 81. doi
- Matsuura, M., Woods, P. M., & Owen, P. J. 2013, *Monthly Notices of the Royal Astronomical Society*, 429, 2527.
- Mattsson, L., Wahlin, R., & Höfner, S. 2010, *Astronomy and Astrophysics*, 509, A14
- Mathis, J. S., Rumpl, W., & Nordsieck, K. H. 1977, *The Astrophysical Journal*, 217, 425
- Martin, P. G. & Rouleau, F. 1991, *Extreme Ultraviolet Astronomy*, 341
- Mazzitelli, I. 1979, *Astronomy and Astrophysics*, 79, 251
- Min, M., Jeffers, S. V., Canovas, H., et al. 2013, *Astronomy and Astrophysics*, 554, A15
- Miller Bertolami, M. M. 2016, *Astronomy and Astrophysics*, 588, A25
- Miszalski, B., Acker, A., Parker, Q. A., et al. 2009, *Astronomy and Astrophysics*, 505, 249. doi:10.1051/0004-6361/200912176
- Nanni A., Bressan A., Marigo P., et al. 2013, *Monthly Notices of the Royal Astronomical Society*, 434, 2390

- Nanni A., Bressan A., Marigo P., et al. 2014, *Monthly Notices of the Royal Astronomical Society*, 438, 2328
- Natta, A. & Panagia, N. 1981, *The Astrophysical Journal*, 248, 189
- Nenkova, M., Ivezić, Ž., & Elitzur, M. 2000, *Thermal Emission Spectroscopy and Analysis of Dust, Disks, and Regoliths*, 196, 77
- Ochsenbein, F., Bauer, P., & Marcout, J. 2000, *Astronomy and Astrophysics Supplement*, 143, 23
- Ossenkopf, V., Henning, Th., Mathis, J. S. M. 1992, *A&A*, 261, 567
- Osterbrock D. E., Ferland G. J., 2006, *Astrophysics of gaseous nebulae and active galactic nuclei*, University Science Books, Sausalito
- Paczyński, B. 1970, *Acta Astronomica*, 20, 287
- Palla M., De Looze I., Relaño M., van der Giessen S., Dayal P., Ferrara A., Schneider R., et al., 2024, *MNRAS*, 528, 2407.
- Palmerini, S., Busso, M., Maiorca, E., et al. 2009, *Publications of the Astronomical Society of Australia*, 26, 161. doi:10.1071/AS08040
- Pauldrach, A. W. A., Hoffmann, T. L., & Lennon, M. 2001, *Astronomy and Astrophysics*, 375, 161.
- Peeters, E., Hony, S., Van Kerckhoven, C., et al. 2002, *Astronomy and Astrophysics*, 390, 1089
- Pegourie, B. 1988, *Astronomy and Astrophysics*, 194, 335
- Penoyre Z., Belokurov V., Wyn Evans N., Everall A., Kuposov S. E., 2020, *MNRAS*, 495, 321.
- Pereira, C. B., Sales Silva, J. V., Chavero, C., et al. 2011, *Astronomy and Astrophysics*, 533, A51
- Pereira, C. B., Lorenz-Martins, S., & Machado, M. 2004, *Astronomy and Astrophysics*, 422, 637
- Perea-Calderón, J. V., García-Hernández, D. A., García-Lario, P., et al. 2009, *Astronomy and Astrophysics*, 495, L5. doi:10.1051/0004-6361:200811457
- Phillips, J. P. & Ramos-Larios, G. 2008, *Monthly Notices of the Royal Astronomical Society*, 383, 1029. doi:10.1111/j.1365-2966.2007.12580.x

- Pietrzyński, G., Graczyk, D., Gallenne, A., et al. 2019, *Nature*, 567, 200
- Rauch, T. 2003, *Astronomy and Astrophysics*, 403, 709.
- Reddy, B. E., Bakker, E. J., & Hrivnak, B. J. 1999, *The Astrophysical Journal*, 524, 831
- Reid W. A., 2014, *MNRAS*, 438, 2642.
- Renzini, A., & Voli, M. 1981, *Astronomy and Astrophysics*, 500, 221
- Renzini, A. 1989, *Planetary Nebulae*, 131, 391
- Reyneirs, M. 2000, PhD thesis, Institute of Astronomy, KU Leuven
- Rieke G. H., Wright G. S., Böker T., et al. 2015, *PASP*, 127, 584
- Rodríguez, L. F., Gómez, Y., & Guzmán, L. 2009, *Rev. Mexicana Astron. Astrofis.*, 45, 85.
- Romano D., Karakas A. I., Tosi M., et al. 2010, *Astronomy and Astrophysics*, 522, A32
- Rouleau, F. & Martin, P. G. 1991, *The Astrophysical Journal*, 377, 526.
- Şahin, T., Lambert, D. L., Klochkova, V. G., et al. 2011, *Monthly Notices of the Royal Astronomical Society*, 410, 612. doi:10.1111/j.1365-2966.2010.17467.x
- Schneider R., Valiante R., Ventura P., et al. 2014, *Monthly Notices of the Royal Astronomical Society*, 442, 1440
- Schneider, R., Hunt, L., & Valiante, R. 2016, *Monthly Notices of the Royal Astronomical Society*, 457, 1842
- Schneider, R. & Maiolino, R. 2024, *A&A Rev.*, 32, 2.
- Schultheis M., Rich R. M., Origlia L., et al. 2019, *Astronomy and Astrophysics*, 627, A152
- Schwab, J. 2020, *The Astrophysical Journal Letters*, 901, L18
- Schwarzschild, M. & Härm, R. 1965, *The Astrophysical Journal*, 142, 855. doi:10.1086/148358
- Sharp, C. M., & Huebner, W. F. 1990, *The Astrophysical Journal Supplement Series*, 72, 417

- Shaw, R. A., Stanghellini, L., Mutchler, M., et al. 2001, *The Astrophysical Journal*, 548, 727
- Shaw, R. A., Stanghellini, L., Villaver, E., et al. 2006, *The Astrophysical Journal Supplement Series*, 167, 201.
- Siess, L. 2007, *Astronomy and Astrophysics*, 476, 893
- Siess, L. 2010, *Astronomy and Astrophysics*, 512, A10.
- Skrutskie, M. F., Cutri, R. M., Stiening, R., et al. 2006, *The Astronomical Journal*, 131, 1163
- Sloan, G. C. & Egan, M. P. 1995, *The Astrophysical Journal*, 444, 452.
- Sloan G. C., Kraemer K. E., Price S. D., Shipman R. F., 2003, *ApJS*, 147, 379
- Sloan, G. C., Matsuura, M., Lagadec, E., et al. 2012, *The Astrophysical Journal*, 752, 140
- Sloan, G. C., Lagadec, E., Zijlstra, A. A., et al. 2014, *The Astrophysical Journal*, 791, 28
- Sloan, G. C., Kraemer, K. E., McDonald, I., et al. 2016, *The Astrophysical Journal*, 826, 44
- Speck, A. K., Barlow, M. J., & Skinner, C. J. 1997, *Monthly Notices of the Royal Astronomical Society*, 288, 431
- Speck, A. K., Corman, A. B., Wakeman, K., et al. 2009, *The Astrophysical Journal*, 691, 1202
- Stanghellini, L., Blades, J. C., Osmer, S. J., et al. 1999, *The Astrophysical Journal*, 510, 687
- Stanghellini, L., Villaver, E., Manchado, A., et al. 2002, *The Astrophysical Journal*, 576, 285.
- Stanghellini, L., Villaver, E., Manchado, A., et al. 2002, *The Astrophysical Journal*, 576, 285. doi:10.1086/341340
- Stanghellini, L., Shaw, R. A., & Gilmore, D. 2005, *The Astrophysical Journal*, 622, 294 (LS05)
- Stanghellini, L., García-Lario, P., García-Hernández, D. A., et al. 2007, *The Astrophysical Journal*, 671, 1669 (LS07)

- Stanghellini L., García-Hernández D. A., García-Lario P., et al., 2012, *ApJ*, 753, 172
- Stanghellini, L., Bucciarelli, B., Lattanzi, M. G., et al. 2020, *The Astrophysical Journal*, 889, 21
- Stanghellini L., Bushra R., Shaw R. A., Dell’Agli F., García-Hernández D. A., Ventura P., 2022, *ApJ*, 929, 148.
- Sylvester, R. J., Kemper, F., Barlow, M. J., et al. 1999, *Astronomy and Astrophysics*, 352, 587
- Tailo, M., Milone, A. P., Lagioia, E. P., et al. 2021, *Monthly Notices of the Royal Astronomical Society*, 503, 694
- Tielens, A. G. G. M. 2005, *The Physics and Chemistry of the Interstellar Medium*, by A. G. G. M. Tielens, pp. . ISBN 0521826349. Cambridge, UK: Cambridge University Press, 2005.
- Tielens, A. G. G. M. & Hollenbach, D. 1985, *The Astrophysical Journal*, 291, 722
- Toalá, J. A., Jiménez-Hernández, P., Rodríguez-González, J. B., et al. 2021, *Monthly Notices of the Royal Astronomical Society*, 503, 1543
- Tosi, S., Dell’Agli, F., Kamath, D., et al. 2022, *A&A*, 668, A22 (T22)
- Tosi, S., Kamath, D., Dell’Agli, F., et al. 2023, *Astronomy and Astrophysics*, 673, A41
- Tosi, S., Dell’Agli, F., Kamath, D., et al. 2024, *Astronomy and Astrophysics*, 688, A36
- Thorsbro B., Ryde N., Rich R. M., et al. 2020, *arXiv e-prints*, arXiv:2003.11085
- Valiante R., Schneider R., Bianchi S., et al. 2009, *Monthly Notices of the Royal Astronomical Society*, 397, 1661
- Valiante R., Giovannini L., Schneider R., Matteucci F., Dell’Agli F., Di Criscienzo M. 2017, *Memorie della Società Astronomica Italiana*, 88, 420
- van Aarle, E., Van Winckel, H., De Smedt, K., et al. 2013, *Astronomy and Astrophysics*, 554, A106
- van Hoof, P. A. M., Oudmaijer, R. D., & Waters, L. B. F. M. 1997, *Monthly Notices of the Royal Astronomical Society*, 289, 371

- van Hoof P. A. M., Van de Steene G. C., Beintema D. A., Martin P. G., Pottasch S. R., Ferland G. J., 2000, *ApJ*, 532, 384.
- van Loon, J. T. 2000, *Astronomy and Astrophysics*, 354, 125
- Van Kerckhoven, C., Hony, S., Peeters, E., et al. 2000, *Astronomy and Astrophysics*, 357, 1013
- Van Winckel, H. 1997, *Astronomy and Astrophysics*, 319, 561
- Van Winckel, H. & Reyniers, M. 2000, *Astronomy and Astrophysics*, 354, 135
- Van Winckel, H. 2003, *Annual Review of Astronomy & Astrophysics*, 41, 391
- Vassiliadis E., Wood P. R. 1993, *The Astrophysical Journal*, 413, 641
- Ventura, P., Zeppieri, A., Mazzitelli, I., D'Antona, F., 1998, *A&A*, 334, 953
- Ventura, P., D'Antona, F., & Mazzitelli, I. 1999, *The Astrophysical Journal Letters*, 524, L111
- Ventura P., D'Antona F., Mazzitelli I. 2000, *A&A*, 363, 605
- Ventura P., D'Antona F. 2005a, *Astronomy and Astrophysics*, 431, 279
- Ventura, P., D'Antona, F. 2005b, *Astronomy and Astrophysics*, 439, 1075
- Ventura P., D'Antona F., 2011, *MNRAS*, 410, 2760.
- Ventura, P., & Marigo, P. 2009, *Monthly Notices of the Royal Astronomical Society*, 399, L54
- Ventura, P. 2010, *Light Elements in the Universe*, 147
- Ventura P., Di Criscienzo M., Schneider R., et al. 2012, *Monthly Notices of the Royal Astronomical Society*, 420, 1442
- Ventura, P., D'Antona, F., Di Criscienzo, M., et al. 2012, *The Astrophysical Journal Letters*, 761, L30
- Ventura P., Di Criscienzo M., Carini R., D'Antona F., 2013, *MNRAS*, 431, 3642
- Ventura P., Dell'Agli F., Schneider R., et al. 2014, *Monthly Notices of the Royal Astronomical Society*, 439, 977
- Ventura P., Karakas A. I., Dell'Agli F., et al. 2015, *Monthly Notices of the Royal Astronomical Society*, 450, 3181

- Ventura P., Karakas A. I., Dell'Agli F., et al. 2016, *Monthly Notices of the Royal Astronomical Society*, 457, 1456
- Ventura P., Stanghellini L., Dell'Agli F., García-Hernández D. A., 2017, *MNRAS*, 471, 4648.
- Ventura P., Karakas A., Dell'Agli F., García-Hernández D. A., Guzman-Ramirez L. 2018, *MNRAS*, 475, 2282
- Ventura, P., Dell'Agli, F., Lugaro, M., et al. 2020, *Astronomy and Astrophysics*, 641, A103
- Ventura, P., Dell'Agli, F., Romano, D., et al. 2021, *Astronomy and Astrophysics*, 655, A6
- Ventura, P., Dell'Agli, F., Tailo, M., et al. 2022, *Universe*, 8, 45.
- Ventura, P., Tosi, S., García-Hernández, D. A., et al. 2025, *Astronomy and Astrophysics*, 694, A177
- Vincenzo, F., Belfiore, F., Maiolino, R., et al. 2016, *Monthly Notices of the Royal Astronomical Society*, 458, 3466
- Villaver, E., Stanghellini, L., & Shaw, R. A. 2003, *The Astrophysical Journal*, 597, 298 (EV03)
- Volk, K. & Kwok, S. 1985, *Astronomy and Astrophysics*, 153, 79
- Volk, K., Sloan, G. C., & Kraemer, K. E. 2020, *Astrophysics and Space Science*, 365, 88
- Volk K., Hrivnak B. J., Matsuura M., Bernard-Salas J., Szczerba R., Sloan G. C., Kraemer K. E., et al., 2011, *ApJ*, 735, 127.
- Wachter A., Schröder K. P., Winters J. M., Arndt T. U., Sedlmayr E., 2002, *A&A*, 384, 452
- Wachter A., Winters J. M., Schröder K. P., Sedlmayr E., 2008, *A&A*, 486, 497
- Wasserburg, G. J., Boothroyd, A. I., & Sackmann, I.-J. 1995, *The Astrophysical Journal Letters*, 447, L37. doi:10.1086/309555
- Weiss, A., & Ferguson, J. W. 2009, *Astronomy and Astrophysics*, 508, 1343
- Wegg C., Rojas-Arriagada A., Schultheis M., et al. 2019, *Astronomy and Astrophysics*, 632, A121

- Winters, J. M., Le Bertre, T., Jeong, K. S., Helling, C., & Sedlmayr, E. 2000, *A&A*, 361, 641
- Woolf, N. J. & Ney, E. P. 1969, *The Astrophysical Journal Letters*, 155, L181.
- Wright, E. L., Eisenhardt, P. R. M., Mainzer, A. K., et al. 2010, *The Astronomical Journal*, 140, 1868
- Xu, Y., Lin, Y., Zhang, J., et al. 2016, *The Astrophysical Journal*, 825, 111
- Zanstra H., 1931, *PDAO*, 4, 209
- Zamora, O., García-Hernández, D. A., Plez, B., et al. 2014, *Astronomy and Astrophysics*, 564, L4
- Zaritsky, D., Harris, J., Thompson, I. B., et al. 2004, *The Astronomical Journal*, 128, 1606
- Zhukovska S., Gail H.-P., Trieloff M. 2008, *Astronomy and Astrophysics*, 479, 453
- Zhukovska, S. & Gail, H.-P. 2009, *Cosmic Dust - Near and Far*, 414, 199
- Zijlstra, A. A., Matsuura, M., Wood, P. R., et al. 2006, *Monthly Notices of the Royal Astronomical Society*, 370, 1961
- Zinner, E. 2008, *Organic Matter in Space*, 251, 341
- Zubko, V. G., Mennella, V., Colangeli, L., et al. 1996, *Monthly Notices of the Royal Astronomical Society*, 282, 132

Ringraziamenti

In questi anni ho scoperto che fare un dottorato di ricerca non significa solo acquisire nuove competenze e conoscenze scientifiche, ma rappresenta una vera e propria esperienza di vita, in cui si collezionano ricordi e insegnamenti ben più variegati di quanto potessi immaginare.

Sin dalle elementari ci insegnano ad apprezzare i Romani, ma ammetto che mi è servito un dottorato per capirne davvero il valore. Il popolo romano si distingue per la sua immensa cultura, arricchita di volta in volta dai popoli che conquistava. È anche grazie a loro se oggi le città sono come le vediamo, con opere straordinarie come strade e acquedotti. Durante il mio dottorato, come in un poema epico, ho sentito narrare le loro gesta, sia le vittorie e sia le sconfitte (la catapultata a Siracusa!!), ma non solo. Un doveroso tributo va anche ai grandi artisti come Cavallini e Signorelli, e a capolavori incredibili come il mosaico di Santi Cosma e Damiano, che difficilmente avrei scoperto da sola.

Tutto questo è stato possibile grazie al mio mentore, Paolo, che sin dalla tesi triennale mi ha preso sotto la sua ala, insegnandomi l'amore per l'arte e la scienza (ci ha provato anche con lo sport, ma su quel fronte sono stata un terreno meno fertile). Grazie di tutto, è stato un viaggio incredibile insieme. Il mio percorso accademico non sarebbe stato lo stesso nemmeno senza Flavia. Sin dall'inizio, Paolo mi presentava a tutti come la studentessa di Flavia piuttosto che la sua tesista, e alla fine di questi anni posso dire che è stato davvero così. Inizialmente con discrezione, poi sempre più apertamente, sei stata una presenza costante nel mio dottorato, aiutandomi ogni volta che ne avevo bisogno, supportandomi e guidandomi, persino quando la tesi era ormai conclusa e dovevo trovare un postdoc. Ogni tua attenzione è stata preziosa e te ne sono profondamente grata. Un grazie sentito va anche a Devika che, nonostante la distanza, è riuscita a seguirmi e sostenermi, soprattutto nei primi tempi del dottorato, un periodo cruciale di transizione da studente a piccolo ricercatore.

Arrivo così ai miei affetti. Ognuno di voi ha contribuito, in modo diverso ma ugualmente fondamentale, alla mia serenità, al mio benessere e al mio modo di vivere. Mi siete stati vicini nei momenti di gioia (tra le giocate a D&D, giochi da tavolo e Magic) e in quelli di difficoltà, quando non stavo bene. Non ci sono abbastanza parole per esprimervi la mia gratitudine, vi voglio bene. Tra tutte le persone che adoro, mi prendo la libertà di fare un ringraziamento speciale ad Alessandra e Leonora, che da vent'anni sono le mie colonne portanti, accompagnandomi ovunque e aiutandomi più di chiunque altro. Un grazie infinito anche ai miei splendidi amici Agnese e Francesco, conosciuti grazie all'università: tra un esame e l'altro, sono diventati parte della mia vita.

Ringrazio poi la mia famiglia, che non mi ha mai fatto mancare nulla, dandomi sempre un nido sicuro in cui tornare, rilassarmi e concentrarmi. Gli insegnamenti

di mia madre sono tanti, ma quello che più mi ispira è il suo spirito di lavoratrice instancabile. Allo stesso modo, Claudia è stata tutto ciò che una sorella minore potrebbe desiderare: una protezione costante, un'amica, e persino fautrice di prese in giro che aiutano a crescere. Grazie per avermi aiutato a diventare grande.

Concludo i ringraziamenti con la persona più speciale, che da circa sei mesi è riuscita a entrare nel mio cuore e a diventare una luce immensa che mi guida nei momenti di difficoltà e mi dà tanta gioia. Sei mesi lunghissimi, che in realtà abbracciano un arco di tempo che va dalla tesi triennale fino a questa difesa di dottorato. Sei mesi, ripetuti per tanti anni, durante i quali mi hai supportato e sopportato più di chiunque altro, facendomi credere in me stessa e dandomi tutta la fiducia di cui avevo bisogno. Questa tesi è soprattutto per te, che sei parte fondamentale di me. Grazie Alessandro Foti della quinta A.

Se insisti e resisti raggiungi e conquisti
Trilussa